

PETROLOGY AND PETROGENESIS OF BASALTIC ROCKS AND THEIR INCLUSIONS:
STUDIES FROM THE RIO GRANDE RIFT, THE ROMAN COMAGMATIC PROVINCE, AND
OCEANUS PROCELLARUM

Thesis by
Warren Scott Baldrige

In Partial Fulfillment of the Requirements for the Degree of
Doctor of Philosophy

California Institute of Technology
Pasadena, California

1979

ACKNOWLEDGMENTS

Specific acknowledgment is made within each of Parts II-IV for those parts of this work. I would like to emphasize my gratitude to Prof. Arden Albee for his continuing encouragement and support and for his penetrating geologic insight, rooted in the most powerful of all arguments -- the simple ones. I also especially thank Art Chodos, whose high level of expertise with the Caltech electron microprobe facilities aided all parts of this work. T. R. McGetchin is responsible for my study of the Rio Grande rift. He and R. Riecker made the resources of Los Alamos Scientific Laboratory (LASL) available to me. Discussions with J. Murray, J. Laird, J. Everson, P. Gromet, D. DePaolo, and R. J. Bridwell have been continually stimulating and educational in various facets of this work. I gratefully acknowledge the expert typing of E. Bell, L. Cordell, H. Fabel, and B. Hahn, and the drafting skills of J. Scott, L. Smith and the graphic arts facilities of Caltech and LASL.

Financial support for the Rio Grande rift phase of this work has been provided by LASL (particularly for field work), by a grant from the Caltech Ford/Exxon Energy Research Program, by the Achievement Rewards for College Scientists Foundation, and by National Science Foundation Grant EAR75-03416-A03. This thesis was completed while holding a Postdoctoral Fellowship at the Los Alamos Scientific Laboratory.

I am particularly grateful to my wife Helen Fabel for her support and good humor through my graduate studentship.

INTRODUCTION

This thesis has as its theme the study of basalt. Basalt constitutes the most abundant igneous rock on the surface of the earth and the second most abundant rock type on the moon. Basalt has been erupted in great volume throughout geologic time. Its uniformity of composition indicates that this composition is largely controlled by the physiochemical constraints on melting. Basaltic magma therefore is a relatively direct and primitive product of its source region. As such, it is one of the most important rock types in deciphering the chemical and physical state of the mantles - in which the sources of basaltic magma lie - of the earth and moon.

This thesis consists of a series of topical studies in basalt petrology and petrogenesis, including a study of the mafic and ultramafic inclusions which sometimes occur in these magmas. Each individual study involves a separate geographical area and was motivated by its own set of questions. Each part is written as a separate individual paper. Part I is a detailed study of the petrology and petrogenesis of basaltic rocks from the central Rio Grande rift of New Mexico. This study investigates the origin and evolution of basaltic magma within a regional context. It was undertaken in order to characterize the volcanic rocks of this major but little-known continental rift zone and to compare them to rocks of other rifts and of the western United States. Part II is closely related to Part I in that it is a study of the mafic and ultramafic inclusions occurring in some of these lavas. These inclusions provide information on the mineralogy, chemistry, and thermal state of the crust and upper mantle beneath the rift.

Part III is a study of leucite-bearing basaltic lavas from the Plio-Pleistocene Roman Comagmatic Province of Italy. It was directed primarily toward defining phase relationships in the 1-atmosphere liquidus system SiO_2 - $\text{NaAlSi}_3\text{O}_8$ - KAlSi_3O_8 - $\text{CaAl}_2\text{Si}_2\text{O}_8$, which has not been experimentally investigated in its entirety. This study dealt only secondarily with the origin of these magmas. The large number of buffer assemblages present in these potassic lavas illustrates the complexity of buffering relationships between a melt and its coexisting solid phases, and demonstrates how, in principle at least, these relationships may be used to determine mixing properties of complex phases in magmas.

Part IV deals with a suite of rocks returned by the Apollo 12 mission from the eastern side of Oceanus Procellarum. This study was undertaken in order to determine how many parental magmas may have been present at the Apollo 12 site, and whether and by what process the more evolved compositions are related to the less evolved compositions. The lunar rocks illustrate many petrologic features, such as liquid immiscibility and complex pyroxene zoning, not commonly observed in terrestrial basalt.

TABLE OF CONTENTS

PART I: PETROLOGY AND PETROGENESIS OF BASALTIC ROCKS FROM THE
CENTRAL RIO GRANDE RIFT, NEW MEXICO, AND THEIR RELATION
TO RIFT STRUCTURE

ABSTRACT	2
INTRODUCTION	4
Purpose	4
Description	5
ANALYTICAL PROCEDURES	8
PLIO-PLEISTOCENE VOLCANIC ROCKS OF THE CERROS DEL RIO, SANTA ANA MESA, AND EL ALTO VOLCANIC FIELDS	13
Setting	13
Whole-rock chemistry	14
Field relations	17
Petrographic descriptions and mineral chemistry	20
Group A alkali-rich olivine tholeiite	21
Group B basaltic andesite and latite-andesite	24
Phenocryst mineralogy	28
Quantitative modeling	30
Group C basanite	33
Group D alkali olivine basalt and hawaiiite	34
Phenocryst mineralogy	38
Quantitative modeling	40
ALBUQUERQUE VOLCANOES	42
Setting	42
Whole-rock chemistry	42

Petrographic description and mineral chemistry	43
ISLETA AND WIND MESA VOLCANOES; CAT HILLS VOLCANIC FIELD	44
Setting	44
Whole-rock chemistry	45
PRE-PLIOCENE BASALTIC LAVAS	47
COMPARISON WITH BASALTIC ROCKS OF THE SOUTHWESTERN U. S.	50
PETROGENESIS	52
Evolution of rocks from the Cerros del Rio, Santa Ana Mesa, and El Alto volcanic fields	52
Basaltic andesite and latite-andesite	52
Alkali olivine basalt and hawaiiite	55
Origin of xenocrysts	56
Quartz	56
Plagioclase	60
Pyroxene	61
Possible role played by high-pressure fractional crystallization	62
Crystallization paths in the system Mg_2SiO_4 - $CaAl_2Si_2O_8$ - SiO_2 - $CaMgSi_2O_6$	63
Petrogenesis of mafic lavas	64
Comparison with experimental studies	64
Thermodynamic approach	68
Isotopic evidence regarding magma sources	73
MODEL FOR MAGMA GENESIS BENEATH THE RIO GRANDE RIFT	76
Spatial distribution of volcanic rocks - correlation with structure	76
Lithospheric structure beneath the Rio Grande rift	79

Temporal distribution of magma types	81
SUMMARY	82
REFERENCES	84
TABLE 1. Electron microprobe analyses of U. S. G. S. standard rocks compared with recommended values	91
TABLE 2. Chemical compositions (weight percent) and Barth-Niggli cation norms (cation percent) of lavas from the Cerros del Rio, Santa Ana Mesa, and El Alto volcanic field	92
TABLE 3. Chemical compositions (weight percent) and Barth-Niggli cation norms (cation percent) of basalts from the Albuquerque Volcanoes	97
TABLE 4. Chemical compositions (weight percent) and Barth-Niggli cation norms (cation percent) of basalts from Isleta Volcano, Wind Mesa Volcano, and the Cat Hills volcanic field	98
TABLE 5. Chemical compositions (weight percent) and Barth-Niggli cation norms (cation percent) of pre-Pliocene basalts from the central Rio Grande rift	99
TABLE 6. Result of least-squares modeling in weight percent	101
TABLE 7. Silica and alumina buffer reactions and activity models used in this paper	102
FIGURE CAPTIONS	
Figure 1 - Figure 6	103
Figure 7 - Figure 15	104
Figure 16 - Figure 26	105
Figure 27 - Figure 35	106
Figure 36	107
FIGURES	108
APPENDIX 1	144
Group A olivine tholeiites	144

Group B basaltic andesites and related basaltic andesites and latite-andesites	145
Group C basanites	146
Group D alkali olivine basalts and related basalts and hawaiites	147
APPENDIX 2	149
Albuquerque Volcanoes	149
Isleta	149
Wind Mesa	150
Cat Hills	150
PART II: MAFIC AND ULTRAMAFIC INCLUSION SUITES FROM THE RIO GRANDE RIFT (NEW MEXICO) AND THEIR BEARING ON THE COMPOSITION AND THERMAL STATE OF THE LITHOSPHERE	
ABSTRACT	152
INTRODUCTION	153
ANALYTICAL PROCEDURES	155
DESCRIPTION AND CHEMISTRY	157
Abiquiu locality	157
Geologic setting; host rock	157
Description of inclusions	157
Mineral chemistry	159
Cieneguilla locality	161
Geologic setting; host rock	161
Description of inclusions	162
Mineral chemistry	163

Elephant Butte locality	164
Geologic setting; host rock	164
Description of inclusions	165
Clinopyroxenite	165
Granulite	166
Spinel lherzolite	166
Mineral chemistry	167
ORIGIN OF INCLUSIONS	171
Pyroxenite and granulite	171
Megacrysts	173
Lherzolite and harzburgite	176
ESTIMATION OF GEOTHERMAL GRADIENT	177
LITHOSPHERIC STRUCTURE BENEATH THE RIO GRANDE RIFT	182
ACKNOWLEDGMENTS	184
REFERENCES	185
TABLE 1. Chemical compositions (weight %) and Barth-Niggli cation norms (cation %) of host volcanic rocks and granulite inclusion	189
TABLE 2. Representative individual chemical analyses of major phases in most abundant inclusion types	190
TABLE 3. Calculated temperatures from compositions of coexisting clinopyroxene and orthopyroxene	192
FIGURE CAPTIONS	
Figure 1 - Figure 3A, B, C	193
Figure 3D, E, F - Figure 8	194
Figure 9 - Figure 13	195
FIGURES	197

PART III: PETROLOGY OF FOUR LEUCITITES FROM THE ROMAN REGION, ITALY

ABSTRACT	211
INTRODUCTION	212
DESCRIPTION OF SAMPLES	214
NMNH-99024	215
NMNH-99055	215
NMNH-99071	216
NMNH-99097	217
ANALYTICAL TECHNIQUE	218
ANALYTICAL RESULTS	219
DISCUSSION	220
Phase relations	220
Strontium and barium partitioning in feldspar	225
Silica and alumina activity; oxygen fugacity; pyroxene components	229
PETROGENESIS	237
REFERENCES	239
TABLE 1. Chemical analyses from Washington (1906) and CIPW norms	244
TABLE 2. Comparison of "calculated modes" given by Washington (1906) with those determined in this work	245
TABLE 3. Microprobe analyses of NMNH-99024	246
TABLE 4. Microprobe analyses of NMNH-99055	252
TABLE 5. Microprobe analyses of NMNH-99071	256
TABLE 6. Microprobe analyses of NMNH-99097	260
FIGURE CAPTIONS	
Figure 1 - Figure 2	264

Figure 3 - Figure 5	265
FIGURES	266
PART IV: PETROLOGIC EVOLUTION OF APOLLO 12 OLIVINE-PIGEONITE MARE BASALTS	
ABSTRACT	272
INTRODUCTION	273
ANALYTICAL TECHNIQUES	274
PETROGRAPHY AND MINERAL CHEMISTRY	276
12015	277
12011	280
12043	282
12007	285
12072	288
COMPARATIVE PETROLOGY	291
Texture	291
Mineral crystallization trends	293
Pyroxene	293
Plagioclase	296
Olivine	298
Spinel and ilmenite	298
Modal sequence	299
GENETIC RELATIONSHIPS	299
Olivine and pigeonite basalts	299
Feldspathic basalt 12072	303
ACKNOWLEDGMENTS	304

REFERENCES	305
TABLE 1. Mode, "average" phase compositions, and bulk chemical composition of vitrophyre 12015, 15	308
TABLE 2. Mode, "average" phase compositions, and bulk chemical composition of vitrophyre 12015, 16	309
TABLE 3. Mode, "average" phase compositions, and bulk chemical composition of basalt 12011	310
TABLE 4. Mode, "average" phase compositions, and bulk chemical composition of basalt 12043	311
TABLE 5. Mode, "average" phase compositions, and bulk chemical composition of basalt 12007	312
TABLE 6. Mode, "average" phase compositions, and bulk chemical composition of basalt 12072	313
TABLE 7. Summary of whole-rock chemical and normative compositions	314
FIGURE CAPTIONS	
Figure 1 - Figure 9	315
FIGURES	316

PART I

PETROLOGY AND PETROGENESIS OF BASALTIC ROCKS
FROM THE CENTRAL RIO GRANDE RIFT, NEW MEXICO, AND
THEIR RELATION TO RIFT STRUCTURE

ABSTRACT

Mafic volcanism associated with the central Rio Grande rift is mainly of Pliocene and Pleistocene age. Volcanic rocks occur as isolated small shield volcanoes and cinder cone fields at or near the top of the graben fill. Structurally, the central Rio Grande rift consists of the Española and Albuquerque-Belen basins (grabens), offset from each other 50-60 km along the transverse Jemez lineament. The largest and most compositionally complex volcanic field (Cerros del Rio) occurs in this offset zone. On the basis of petrography and whole-rock chemistry, mafic lavas of this field can be divided into four groups: high-alkali olivine tholeiite, basaltic andesite, alkali olivine basalt, and basanite. All were erupted approximately contemporaneously. Quantitative modeling based on detailed phase chemistry shows that none of these lavas can be related to each other by any simple processes involving observed phenocryst and xenocryst phases.

Latite-andesite, also present in this field, is derived from basaltic andesite by subtraction of about 35 percent of olivine, pyroxene, and calcic plagioclase, and by addition of 17 percent of xenocrystic quartz and sodic plagioclase. Quartz and plagioclase occur as single crystals or as single phase aggregates; quartz rarely has a euhedral habit. These features suggest that quartz and plagioclase may be relict high-pressure phenocrysts. Thus, basaltic andesite magma bodies, residing in independent crustal reservoirs, may evolve by gravitative differentiation. The lighter, relict high-pressure quartz and sodic plagioclase phenocrysts are concentrated at the tops of these reservoirs by flotation simultaneously as the heavier olivine, pyroxene, and calcic plagioclase sink.

Lavas from the northern Albuquerque-Belen basin consist of lower-alkali olivine tholeiite, similar to basalt of the northern rift. Those from the central Albuquerque-Belen basin consist of olivine tholeiite, basaltic andesite, and alkali olivine basalt of relatively restricted compositional range.

Pre-Pliocene volcanism occurred mainly in the upper Oligocene/lower Miocene and in the late Miocene. The earlier phase of volcanism erupted lavas ranging in composition from olivine nephelinite to quartz tholeiite, while the later phase erupted both alkali olivine and tholeiitic basalts. Hence no well-defined change in magma composition occurred with time.

Experimental studies suggest that the olivine tholeiite was derived from >18% partial melting of spinel pyrolite at about 35 km and the alkali olivine basalt and basanite from approximately 10% partial melting at 50-70 km. Thermodynamic calculations emphasize the hazards of inferring pressure (depth) and temperature of origin from basaltic lavas which are not primitive. The distribution of parental magmas suggests a model in which a transverse shear zone taps a sub-crustal diapir and bleeds magmas from various depths between 35 and 70 km. In contrast, the "normal" genesis of basaltic magmas along the rift occurs at the top of the diapir immediately beneath the base of the crust.

INTRODUCTION

Purpose

The Rio Grande rift of New Mexico and Colorado is a major, late Cenozoic continental rift. It has been the locus of volcanism since its inception in the late Oligocene, although widespread volcanism did not occur until the Pliocene and Holocene. These volcanic rocks include tholeiitic and alkali olivine basalt, basaltic andesite, and minor nephelinite and silicic lavas. Elements of its structure and stratigraphy have been studied by several investigators since the pioneering work of Bryan and his colleagues (e.g., Bryan, 1938; Kelley, 1952, 1956; Stearns, 1953a, Chapin, 1971; Chapin and Seager, 1975). However the petrology of its volcanic rocks has received relatively less attention to date. This study was undertaken in order to characterize comprehensively the volcanic products of the rift. The approach has been: (1) to define the major basalt types on the basis of petrographic characteristics and whole-rock major-element chemistry, and (2) to obtain detailed major element chemical analyses of all phases present in selected rocks. The immediate goal of this study was (1) to determine what kinds of mafic volcanic rocks exist in the rift, (2) to characterize their distribution with respect to intra-rift structural elements and to look for systematic changes in magma compositions with age, (3) to determine the compositions of parental and "primitive" magmas, (4) to model the processes relating the magmas to each other, and (5) to estimate the conditions under which the magmas originated. The ultimate goal of this work is to define the conditions of magma generation beneath the rift and to arrive at a petrologic model for the evolution of the rift.

Description

The Rio Grande rift consists of a series of north-trending, sediment-filled, grabens arranged en echelon in a north-northeasterly direction. The term "basin" is widely used to refer to these grabens, and reflects their sediment fill and low topographic expression relative to the surrounding uplifts. The rift extends over 900 km from the upper Arkansas graben near Leadville, Colorado, to the Los Muertos basin in Chihuahua, Mexico. The individual grabens are separated from adjacent grabens by uplifts extending transversely to the axes of the basins. In part, at least, the basins may have different structural histories. The flanks of the rift are defined principally by normal faults, but in some cases the margins are high-angle reverse faults. Vertical offset of the basins, measured on the Precambrian surface, exceeds 6 km (Kelley, 1956; Chapin, 1971; Cordell, 1976). Extensional faulting, generally thought to mark the inception of rifting, probably began 25 to 29 m.y. ago (Chapin and Seager, 1975; Lipman and Mehnert, 1975).

In the present work the central part of the Rio Grande rift is considered to extend from the Tusas Mountains on the north to Socorro on the south (figure 1). This part of the rift consists of the following basins, from north to south: (1) the Española basin, (2) the small Santo Domingo basin, and (3) the Albuquerque-Belen basin. These basins are from 15 to 65 km wide. South of the Albuquerque-Belen basin, where the rift includes several parallel basins, it reaches 150 km in width.

The main occurrence of intermediate to silicic volcanic rocks is the volcanic complex with its associated resurgent caldera and ash flow

tuffs forming the present Jemez Mountains (Smith et al., 1970). This volcanic edifice is located on the western bounding faults of the Española basin. Rock types present consist primarily of andesite, dacite, quartz latite, rhyodacite, and rhyolite, with only minor basalt. They range in age from approximately 10 to 0.1 m.y. (Bailey et al., 1969; Doell et al., 1968). These rocks may be derived from remelted lower crust (Eichelberger and Gooley, 1977). Although basalts and related mafic lavas have been erupted sporadically since initiation of rifting in the late Oligocene, most were erupted in latest Pliocene and in Quaternary time. They occur as isolated volcanoes or cinder cone fields at or near the present top of the rift-filling sediments. These Pliocene and Quaternary lavas are the main subject of this study.

The northern and southern parts of the rift have erupted basaltic magmas of quite different compositions. Volcanism in the northern rift (Taos Plateau) consisted predominantly of aluminous olivine tholeiite and derivatives (Aoki, 1967; Lipman, 1969), whereas south of Socorro volcanism consisted primarily of alkali olivine basalt and related rocks (Renault, 1970; Kudo et al., 1971). Within the central Rio Grande rift, between Santa Fe and Socorro, both tholeiite and alkali olivine basalt have been erupted approximately contemporaneously (e.g., Aoki and Kudo, 1976).

The main volcanic fields of the central rift which will be discussed here are shown in figure 1. These are the El Alto basaltic field (A), located at the west side of the Española basin along the main bounding fault of the rift; the Cerros del Rio (B) and Santa Ana Mesa (C) fields, located respectively at the eastern and western margins of the small Santo Domingo basin; and the Albuquerque Volcanoes

(D), Isleta Volcano (E), Wind Mesa Volcano (F), and the Cat Hills volcanic field (G), all located along north-south fracture zones within the Albuquerque-Belen basin. The geology, petrology, mineralogy, and chemistry of rocks from these fields will be discussed in following sections.

PREVIOUS WORK

The first detailed descriptions of volcanic rocks of the central Rio Grande rift were those published by Stearns (1953b) of the Oligocene to early Miocene Espinazo Volcanics. The Espinazo Volcanics consist of volcanoclastic sediments and flows of latite and andesite cropping out along the southern margin of the Española basin. Stearns (1953b) also defined the Cieneguilla Limburgite, a group of Oligocene alkali olivine basalt, olivine tholeiite, and olivine nephelinite flows and tuffs cropping out in the same area (refer to figure 28 for location), and published an analysis of one of these flows. Sun and Baldwin (1958) presented further field and petrographic descriptions and six new analyses of these same volcanic units. Their analyses included one of a Plio-Pleistocene alkali olivine basalt flow of the southern Cerros del Rio field, where this flow laps onto the Cieneguilla Limburgite.

Aoki (1967) first published petrologic and chemical data on the basalt from the Servilleta Formation of the Taos Plateau in the southern San Luis Valley. This basalt ranges from about 4.5 to 2.0 m.y. in age (Lipman, 1977). He pointed out that this basalt, while normative tholeiite, was intermediate in its alkali content between tholeiitic and alkali olivine basalt. It also contains high Al_2O_3 (15.5-17.5 percent) and is similar to high-Al basalt of south-central

Oregon and the Cascade Range. Lipman (1969) and Lipman and Mehnert (1975) presented additional analyses of the basalt from the Servilleta Formation and of adjacent fields of alkalic basalt to the east and west. They postulated that the lateral change from tholeiitic basalt within the rift to alkali olivine basalt outside the rift reflected different depths to the zone of magma generation within the mantle. Renault (1970) presented whole-rock chemical analyses of alkali olivine basalt from the southern rift, and of olivine tholeiite from the south-central rift and from west of the rift. Aoki and Kudo (1976) presented new whole-rock chemical analyses of many previously unanalyzed basalt flows from within the rift, including flows from the Cerros del Rio and Santa Ana Mesa fields (one analysis each), the Albuquerque Volcanoes (two analyses), Isleta (one analysis), and the Cat Hills (two analyses). From these data they pointed out that, whereas basalts occurring within the northern Rio Grande rift (Servilleta Formation) are primarily olivine tholeiite, those of the southern rift are primarily alkali olivine basalt and basanite. Within the central rift (Santa Fe to Socorro), both olivine tholeiite and alkali olivine basalt are present.

ANALYTICAL PROCEDURES

Mineral analyses were performed with a Materials Analysis Corporation model 5-SA3 electron microprobe controlled by a Digital Equipment Corporation 12K PDP-8/L computer. Operating techniques were similar to those described by Chodos and Albee (1972), with an updated program (Chodos et al., 1973). Standard operating conditions were 15 kV accelerating potential, 0.05 μ A sample current on brass, and a 10- to 15-micron beam diameter, with beam current integration and pulse height

selection. For groundmass grains the sample current was reduced to 0.005 μA and the beam diameter to 2-3 microns. Analyses are accurate to 1-2 relative % for most oxides constituting 1-10% of the sample (Champion et al., 1975).

All formula compositions and elemental ratios used in the text and diagrams are in molecular proportions. Olivine compositions are reported as %Fo = $100 \times [\text{Mg}/(\text{Mg}+\text{Fe}+\text{Mn})]$. Feldspar compositions are reported as %An = $100 \times [\text{Ca}/(\text{Ca}+\text{Na}+\text{K})]$, %Ab = $100 \times [\text{Na}/(\text{Ca}+\text{Na}+\text{K})]$, %Or = $100 \times [\text{K}/(\text{Ca}+\text{Na}+\text{K})]$. Pyroxene compositions are reported as %Wo = $100 \times [\text{Ca}/(\text{Ca}+\text{Mg}+\text{Fe}+\text{Mn})]$, %En = $100 \times [\text{Mg}/(\text{Ca}+\text{Mg}+\text{Fe}+\text{Mn})]$, %Fs = $100 \times [(\text{Fe}+\text{Mn})/(\text{Ca}+\text{Mg}+\text{Fe}+\text{Mn})]$. Pyroxene formulas were calculated by normalizing the sum of the catatoms to four, assuming that $\text{Fe}^{3+} = 12 - [4(\text{Si}+\text{Ti}) + 3(\text{Al}+\text{Cr}) + 2(\text{Ca}+\text{Mg}+\text{Fe}+\text{Mn}) + \text{Na}]$, and sequentially calculating $(\text{Fe},\text{Mn})_2\text{Si}_2\text{O}_6$, $\text{NaCrSi}_2\text{O}_6$, CaCrAlSiO_6 , $\text{NaFe}^{3+}\text{Si}_2\text{O}_6$, $\text{NaAlSi}_2\text{O}_6$, $\text{CaTiAl}_2\text{O}_6$, $\text{R}^{2+}\text{Fe}^{3+}\text{AlSiO}_6$, $\text{R}^{2+}\text{Al}_2\text{SiO}_6$, $\text{Ca}_2\text{Si}_2\text{O}_6$, and $\text{Mg}_2\text{Si}_2\text{O}_6$. The components $(\text{Fe},\text{Mn})_2\text{Si}_2\text{O}_6$, $\text{Ca}_2\text{Si}_2\text{O}_6$, and $\text{Mg}_2\text{Si}_2\text{O}_6$ plot on the standard pyroxene quadrilateral and are therefore referred to as quadrilateral components. The remaining components are non-quadrilateral components. Ilmenite and spinel (including magnetite) formulas were calculated by normalizing the sum of the catatoms to two and three, respectively; assuming that the difference of $4(\text{Si}+\text{Ti}+\text{Zr}) + 3(\text{Al}+\text{Cr}+\text{Nb}) + 2(\text{Mg}+\text{Fe}+\text{Mn}+\text{Zn})$ from six and eight, respectively, was equal to Fe^{3+} ; and sequentially calculating $(\text{Mg},\text{Zn})\text{TiO}_3$ (geikielite), MnTiO_3 , FeTiO_3 (ilmenite), and Fe_2O_3 (hematite) for ilmenite, and $(\text{Mg},\text{Fe},\text{Mn})\text{Cr}_2\text{O}_4$ (spinel), and $(\text{Mg},\text{Fe},\text{Mn})\text{Fe}_2\text{O}_4$ (magnetite) for spinel. Ilmenite compositions are reported as % Ilm, % Hem, % Gi. Spinel compositions are reported as

% Sp, % Mt, % Chr. Magnetite compositions are reported as % Mt, % Ulv. Listings of all analyses may be obtained from the author.

Whole-rock major-element analyses were obtained by electron microprobe analysis of fused rock powders using a fluxless technique similar to that described by Brown (1977). This technique involves fusion in air of a small amount (10-30 mg) of sample on a 1x2.5x0.005 cm strip of iridium foil in a resistance furnace. In order to improve homogeneity, each fused bead was ground and re-fused prior to analysis. Duplicate beads were made of each rock powder. The furnace was calibrated with an optical pyrometer. Typical fusion temperatures were 1600°C; total fusion time (including re-fusion) was usually 30-60 seconds. No attempt was made to preserve the ratio $\text{Fe}^{3+}/\text{Fe}^{2+}$ during fusion of the beads because (1) the oxidation state of iron cannot be determined with the electron microprobe, and (2) the value of $\text{Fe}^{3+}/\text{Fe}^{2+}$ of the magma is commonly altered by weathering and/or by deuteric alteration.

Rock powders were obtained by splitting approximately 500-1000 cm^3 of rock into pieces 2-3 cm on a side in a hydraulic press equipped with hardened steel chisel points. All exterior and weathered pieces of the rock and all vesicles or amygdules were removed. These smaller pieces were then further reduced in size by crushing between flat surfaces of hardened steel in a hydraulic press. Hydraulic presses were used in order to eliminate lateral motion of the rock against crushing or splitting surfaces. These small (<1 to several millimeter sized) pieces were hand picked to further eliminate vesicles and secondary material. The final powders were prepared by grinding about 10 cm^3 of these small pieces in a Spex mixer/mill equipped with a tungsten carbide grinding vessel.

Operating conditions on the microprobe were 0.03 μA sample current (on brass) and 20-30 μm beam diameter for mafic to intermediate glasses ($\text{SiO}_2 < 60$ weight percent), and 0.005 μA sample current and 30 μm beam diameter for silicic glasses. Detailed tests of counts versus analysis time for K_2O and Na_2O under a variety of operating conditions showed that under these conditions no loss of K_2O or Na_2O could be detected.

In order to reduce further the risk of losing K_2O and Na_2O under the electron beam, a computer program was written to advance automatically the sample stage under the beam during analysis. Analysis of glass beads was performed as follows: Three elements were analyzed simultaneously on a given spot. After 15 s the stage was automatically moved a distance of $(x+5)$ μm , where x is the particular beam diameter selected. Ten individual spots were analyzed in a "square spiral" array. Background was automatically measured before and after each ten steps. Following analysis of the first set of three elements, the spectrometers were automatically driven to the background positions for the second set of elements. Analysis then continued outward along the square spiral for two additional groups of three elements.

The analysis performed on this square spiral, representing an "average" over an area of approximately $2-4 \times 10^{-2} \text{ mm}^2$, constitutes a single "point" analysis. Typically 3-5 analyses were performed on each bead. Homogeneity was always within microprobe error (see below). A duplicate bead was analyzed and the results for the two beads were averaged to give the whole-rock analysis.

Microprobe analyses of U.S.G.S. standard rocks W-1 (diabase), AGV-1 (andesite), and BCR-1 (basalt) are presented in table 1 along with volatile-corrected analyses of these rocks from Flanagan (1973).

The standard deviation of analyses on replicate beads is given for the microprobe analyses. The error on replicate beads for SiO_2 (~50 weight percent abundance) is about 0.5 relative percent and for Al_2O_3 (~15 percent) is ~1.4 relative percent. For oxides constituting 5-10 and 1-5 weight percent of the rock the error is ~2 and <6 relative percent, respectively. For K_2O and TiO_2 , which constitute 0.5-1 percent of the rock, the error is 6 - 10 percent. For P_2O_5 (<0.5 weight percent), the error is ~30 relative percent. These errors are approximately the same as the overall analytical accuracy of the microprobe (Champion et al., 1975). Microprobe analyses of the U.S.G.S. standard rocks are in excellent agreement with analyses of Flanagan (1973) except for silica in AGV-1. The value obtained in the present work (60.60 weight percent) is almost exactly the same as that obtained by Brown (1977) (60.64 percent) for this rock. Both numbers are about one percent higher than the values quoted in Flanagan (1973). This discrepancy, in addition to the fact that Flanagan's total is also about one percent low, suggests that his value for SiO_2 is too low.

Whole-rock analyses are presented in tables 2-5. Fe_2O_3 was calculated by setting $\text{Fe}^{3+}/\text{Fe}^{2+} = 0.1$ (atomic). This ratio yields values of Fe_2O_3 which are approximately equal to the lowest analyzed values of Fe_2O_3 in basaltic rocks from the Rio Grande rift (Aoki, 1967; Aoki and Kudo, 1976) and other continental areas (e.g., Irving and Green, 1976). The suggestion of Irvine and Baragar (1971) that Fe_2O_3 be set equal to $(\text{TiO}_2 + 1.5)$ weight percent yields unrealistically high $\text{Fe}^{3+}/\text{Fe}^{2+}$ for these rocks. The ratio $\text{Fe}_2\text{O}_3/\text{FeO}$ will be slightly higher in rocks with higher alkalis and in rocks which are more differentiated (i.e., have lower liquidus temperatures) (Carmichael et al., 1974). However, for

simplicity and lacking criteria by which to choose a more appropriate $\text{Fe}^{3+}/\text{Fe}^{2+}$ for these rocks, a uniform value of 0.1 was used for all rocks regardless of composition. Normative compositions and Mg-values $[100 \cdot (\text{Mg}/\text{Mg} + \text{Fe}^{2+})]$ were calculated after adjustment of FeO and Fe_2O_3 . To facilitate comparison, analyses from the literature were also recalculated such that $\text{Fe}^{3+}/\text{Fe}^{2+} = 0.1$. Mg-values and An/An+Ab are in cation percent. Normative compositions are Barth-Niggli norms (cation percent) unless otherwise indicated.

PLIO-PLEISTOCENE VOLCANIC ROCKS OF THE CERROS DEL RIO, SANTA ANA MESA,
AND EL ALTO VOLCANIC FIELDS

Setting

Volcanic rocks of the Cerros del Rio, Santa Ana Mesa, and El Alto volcanic fields are considered together because they occur in close proximity to each other in a similar tectonic setting within the Rio Grande rift. The Cerros del Rio and Santa Ana Mesa fields are located along the eastern and western bounding faults of the Santo Domingo basin, respectively (figure 1). The smaller El Alto field is located 40 km north of the Santo Domingo basin along the western bounding faults of the Española basin. These faults extend southward to the Santo Domingo basin. The ages of these basalts range from about 2.0-2.8 m.y. (Manley, 1976; Bachman and Mehnert, 1978).

Prior to this study only two analyses existed of the volcanic rocks of the Cerros del Rio and a single analysis of a flow from Santa Ana Mesa (included in figure 3). Accordingly, an attempt was made to sample widely and over as great a vertical distance as possible in order to determine whether different rock types were present and to

determine the range of compositions. However, not all cinder cones and flows have been sampled. The locations of samples from these fields are shown in figure 2.

Sample coverage is greatest from the Cerros del Rio volcanic field. This field is the largest in both areal and vertical extent. Over most of the Cerros field little or no vertical exposure occurs, hence only those latest flows and cinder cones can be sampled. The greatest vertical exposure occurs in White Rock Canyon along the northwest side of the field, where about 300 m of basalt and interbedded river sand and gravel crop out. The vertical sequence of flows was sampled at two localities, along Ancho Canyon, south of White Rock, and along the long-abandoned Buckman Road, directly north of White Rock.

Much of Santa Ana Mesa consists of a thin cap of basalt, a single flow unit thick, surmounted by two chains of vents. This capping flow was sampled at two localities; a cinder cone further to the north was also sampled (figure 2).

The El Alto volcanic field located 40 km to the north is the smallest in areal extent. It consists generally of poorly exposed basalt flows and small, deeply eroded cinder cones. All samples from the El Alto field are from these cinder cones, except for two samples which were taken from a sequence of two flows exposed along the northern edge of the field.

Whole-rock chemistry

Thirty-eight whole-rock chemical analyses of lavas from the Cerros del Rio, Santa Ana Mesa, and El Alto volcanic fields are presented in table 2 and are summarized on figures 3 and 4. The terminology for basaltic rocks used in this work follows that of Yoder and Tilley

(1962), where quartz tholeiite is defined as basalt with normative hypersthene and olivine, and alkali olivine basalt contains normative olivine and nepheline.

Lavas from the Cerros del Rio include both tholeiitic and alkali olivine basalts. The silica content of the lavas ranges from about 45 to 64 weight percent. Samples from the Santa Ana Mesa and El Alto fields are similar in composition to those from the Cerros del Rio; however lavas from each of these fields encompass a much more limited range in composition. Lavas from Santa Ana Mesa are restricted to olivine tholeiite. Those from El Alto consist of both hypersthene- and nepheline-normative compositions. However the total range in SiO_2 of these rocks is only 49-53 weight percent.

An important feature of the lavas from these three volcanic fields, considered collectively, is that four discrete groups of compositions can be distinguished (figures 3 and 4). Olivine tholeiite falls into two groups with different $(\text{Na}_2\text{O}+\text{K}_2\text{O})$ and SiO_2 , designated A and B on figure 3. Both groups are significantly richer in total alkalis and normative albite compared to normal olivine tholeiites (e.g., mid-ocean ridge basalts). Group A basalt has $\text{SiO}_2 = 50.5-52$ weight percent and $(\text{Na}_2\text{O}+\text{K}_2\text{O}) = 4.5\%$. It has about 55 percent normative plagioclase and $\text{An}/\text{An}+\text{Ab} \approx 0.42-0.47$ (see figure 4). The maximum Mg-value is approximately 62. Basalt within this group shows no significant variation in its composition. Group B basaltic rocks have a distinctly higher SiO_2 and $(\text{Na}_2\text{O}+\text{K}_2\text{O})$ (figure 3). The least silicic group B rocks have $\text{SiO}_2 = 53.5-54$ weight percent, $(\text{Na}_2\text{O}+\text{K}_2\text{O}) \approx 6$ percent, and a maximum Mg-value of about 64. They have about the same amount of normative plagioclase (55 percent) as group A, but this plagioclase is

significantly more sodic ($An/An+Ab \approx 0.34$). Because rocks of this group are distinctly more silicic and alkalic than the group A tholeiite, and because their normative plagioclase is much more sodic, these group B compositions are called basaltic andesite. This distinction between basalt and basaltic andesite at $SiO_2 \approx 52$ weight percent corresponds approximately to normative $100(An/An+Ab) = 40$ and is compatible with the terminology of Coats (1968), Carmichael et al. (1974), and Lipman and Mehnert (1975).

A well-defined trend originates from the least silicic group B rocks and extends with decreasing Mg-values through more silicic basaltic andesite to quartz-normative compositions (figures 3 and 4). The most silicic of these have $SiO_2 \approx 64$ weight percent and $(Na_2O+K_2O) \approx 7$ percent. These high-alkali, silica-oversaturated compositions are referred to as latite-andesite. They have about 55 percent normative plagioclase, and $An/An+Ab \approx 0.32$. Their Mg-value is about 55. The basaltic andesite with the lowest SiO_2 and total alkalis and the highest Mg-values is likely to be parental to this entire suite of basaltic andesite and latite-andesite. This parental composition is designated on figures 3 and 4 with stars.

Similarly two separate groups of nepheline-normative rocks may be distinguished, designated as C and D on figure 3. Group C lavas have $SiO_2 = 46.5-47.5$ weight percent and $(Na_2O+K_2O) = 5.5-6$ percent. In addition they have approximately 40 percent normative plagioclase, with $An/An+Ab \approx 0.50$, and relatively high normative nepheline (about 9 percent) (figure 4). The maximum Mg-value of these lavas is approximately 63. Because of their high normative nepheline content these rocks are termed basanite. This terminology is consistent with that of Green

(1970b), who distinguished basanite from alkali olivine basalt at normative nepheline contents >5 percent.

The group D lavas constitute a broad group which is distinctly higher in SiO_2 and in normative plagioclase and lower in normative nepheline than the basanite (figures 3 and 4). The lava with the highest Mg-values and the lowest SiO_2 , designated with stars on figures 3 and 4, has $\text{SiO}_2 \approx 49$ weight percent and $(\text{Na}_2\text{O}+\text{K}_2\text{O}) \approx 4.5$ percent. The normative plagioclase is more sodic in composition ($\text{An}/\text{An}+\text{Ab} \approx 0.45$) than in the basanite. The Mg-value of this basalt is 64. A broad trend in composition originates near D and extends with generally decreasing Mg-values and $\text{An}/\text{An}+\text{Ab}$ toward increasing SiO_2 , $(\text{Na}_2\text{O}+\text{K}_2\text{O})$, and normative plagioclase. On figure 4 a slight gap is present in the middle of this sequence. This gap, corresponding approximately to $\text{An}/\text{An}+\text{Ab} = 0.40$, is a convenient point at which to distinguish the mafic members of this series from the more alkalic and silicic members. The rocks with the lowest silica and total alkalis, characterized by $\text{An}/\text{An}+\text{Ab} > 0.40$, are alkali olivine basalt. Those rocks with $\text{An}/\text{An}+\text{Ab} < 0.40$ have generally higher normative plagioclase and are termed hawaiite. Collectively the alkali olivine basalt and hawaiite of group D constitute a diverse suite of compositions, many of which cannot be simply related to each other by fractional crystallization.

Field relations

Group A olivine tholeiite occurs in the Cerros del Rio, El Alto, and Santa Ana Mesa fields. Within the Cerros, this basalt occurs as flows exposed along White Rock Canyon. They comprise the uppermost of four flows in the Buckman Road section and the upper two flows of a section of basalt exposed in Ancho Canyon. The uppermost flow in the

Buckman Road section (Sample -232) was also sampled 4 km to the north (-049). These two samples are identical in composition. Group A olivine tholeiite has not yet been found further to the south or southeast in the Cerros. This occurrence along White Rock Canyon may suggest that such basalt was restricted to vents localized in this part of the Cerros.

All samples from Santa Ana Mesa belong to group A. Two samples (-057 and -058) from different levels within a single flow exposed along the mesa edge have identical compositions. A third sample taken from 3 km to the west may also be from this same flow. The cinder cone that was sampled, one of a chain of cinder cones, may be the source of the Santa Ana Mesa flow. Samples of the group A tholeiites from El Alto are all from cinder cones.

Basaltic andesite and latite-andesite have been found only in the Cerros del Rio field. Most occur in White Rock Canyon, where they constitute the lowermost two flows exposed along Buckman Road and the two lowermost flows of an undetermined number of flows along the Ancho Canyon section. The lowermost flow in Ancho Canyon has been dated at 2.6 ± 0.4 m.y. by Manley (1976). Basaltic andesite also comprises at least one cinder cone within the Cerros field. Latite-andesite occurs in at least three localities within the Cerros field. It constitutes the highest flow at the southern end of White Rock Canyon (mapped as the Tank Nineteen basaltic andesite by Smith et al., 1970) as well as a cinder cone in this same area (figure 2).

The flows of Ortiz Mountain, a broad, low shield cone in the northeast corner of the Cerros field, are also latite-andesite. All three of the most silicic latite-andesite compositions (figure 3) are from

massive flows associated with Ortiz Mountain. A dike exposed in Ancho Canyon is also latite-andesite. Two rocks intermediate in SiO_2 and in total alkalis lying between the group A olivine tholeiite and the group B basaltic andesite (figure 3) are from the El Alto field.

Basanite comprises an extensive flow capping the south and southeast side of the Cerros del Rio field (La Bajada Mesa) and at least one cinder cone within the Cerros field. This occurrence of basanite is compatible with its being late in the eruptive cycle. The group C alkali olivine basalt and hawaiite occur in both the El Alto and the Cerros del Rio fields. In the El Alto field alkali olivine basalt comprises two cinder cones immediately adjacent to cinder cones of group A olivine tholeiite composition. A sequence of two flows of hawaiite are exposed at the northern margin of this field. The lower of these two flows (-F212) is the Mesa de Abiquiu flow, which contains a suite of pyroxenite, plagioclase, and orthopyroxene inclusions (Baldrige, 1979b). Many of the cinder cones within the Cerros del Rio field consist of alkali olivine basalt or hawaiite. These cinder cones occur adjacent to, and approximately contemporaneously with, cones of basaltic andesite and of basanite. In addition, a flow exposed in the middle of the Buckman Road section consists of hawaiite. The uppermost flow exposed on the west side of the Rio Grande, southwest of the Tank Nineteen basaltic andesite, consists of alkali olivine basalt, as does the eroded vent complex comprising the most northerly outlier of the Cerros field (figure 2).

In summary, all basalt types occur as late cinder cones and/or flows within these three fields. The earliest flows, exposed along White Rock Canyon, consist of basaltic andesite. Geographically the

basalt types are not distributed systematically. Within both the El Alto and Cerros del Rio fields lavas of different composition have been erupted from adjacent vents approximately contemporaneously. Hence in general no well-defined correlation of composition with either geographic location or with age can be discerned among the rocks of the Cerros del Rio, Santa Ana Mesa, and El Alto volcanic fields.

Petrographic descriptions and mineral chemistry

The major groups of basaltic rocks from the Cerros del Rio, Santa Ana Mesa, and El Alto volcanic fields have many textural features in common. Most rocks are at least slightly porphyritic (commonly glomeroporphyritic) and vesicular, although vesicularity varies from flow to flow and within a given flow. The most mafic rocks have an intergranular texture, rarely grading to subophitic in the coarser-grained rocks. The more silicic and/or alkalic rocks (the basaltic andesite and hawaiite) have textures which are pilotaxitic or transitional between pilotaxitic and intergranular. The latite-andesite is characterized by hyaloophitic or hyalopilitic textures. Most of the mafic lavas contain a few (<5) percent phenocrysts of olivine and of plagioclase. Olivine contains inclusions of Cr-rich spinel. Clinopyroxene is a minor phenocryst or microphenocryst phase (0-3 percent). None of the tholeiitic lavas show the olivine to low-Ca pyroxene reaction relationship typical of tholeiitic rocks from many areas. All of the rocks contain at least a few percent of interstitial glass in their groundmass. Although only fresh samples were chosen for analysis, most samples show at least a small amount of alteration. Most commonly the interstitial groundmass glass is devitrified and/or altered to a fine-grained mixture of clay minerals and cannot be analyzed. Magnetite grains are commonly

surrounded by rims of hematite or are completely altered to hematite. Less commonly, olivine grains are surrounded by rims of iddingsite or serpentine; rarely groundmass olivine is completely altered to iddingsite or serpentine. Occasionally, vesicles are filled with carbonate.

However, some significant differences in petrographic characteristics exist among these mafic rocks, even where the overall textures are similar. These differences correlate with the various groups defined on the basis of major element chemistry. For example, all rocks of the group B basaltic andesite are characterized by the presence of partially resorbed xenocrysts of quartz and of plagioclase. The texture of these rocks is pilotaxitic or transitional between intergranular and pilotaxitic. Rocks of the group A olivine tholeiite have an intergranular (or rarely subophitic) texture, and none contain quartz or partially resorbed plagioclase. Pyroxene of both the groups A and B basaltic rocks is very pale green in color and only weakly zoned. Lavas of the group C basanite and group D alkali olivine basalt also have an intergranular texture whereas the hawaiites have a pilotaxitic texture. Both the alkali olivine basalt and hawaiite contain rare xenocrysts of partially resorbed plagioclase and/or quartz. The pyroxene of these silica-undersaturated rocks is pale brown in color, slightly pleochroic, and more strongly zoned. These petrographic features are discussed in more detail in the following sections.

Group A alkali-rich olivine tholeiite

This group of basalts (figures 3 and 4 and table 2) is characterized by 3-5 percent of euhedral, commonly skeletal, olivine phenocrysts <4 mm, and <1 to 5 percent of euhedral plagioclase phenocrysts <2 mm in size. In certain rocks the olivine phenocrysts and larger

groundmass grains are partly or completely altered to iddingsite, which is overgrown by a jacket of olivine. This texture has also been described in basalt from the western Grand Canyon region by Best and Brimhall (1970). Clinopyroxene is a subordinate phenocryst phase, absent in some rocks but present in small amounts (approximately one percent) in others. Where present it occurs as small (<2 mm), zoned, colorless to pale green, euhedral to subhedral phenocrysts or microphenocrysts. Microphenocrysts of magnetite <0.2 mm are also present. The groundmass consists of plagioclase microlites with interstitial granular olivine, clinopyroxene, and magnetite; and acicular ilmenite and apatite. A few percent of devitrified brownish glass forms the residuum. The groundmass of most of these rocks is characterized by an intergranular texture (figure 5A). Coarser-grained rocks (0.2-0.5 mm) may display a partial ophitic texture, in which augite oikocrysts are separated by areas with intergranular texture (figure 5B). This texture is interpreted as resulting from an interruption in the growth of the oikocrysts caused by more rapid cooling.

The composition of olivine occurring in these basalts is shown in figure 6. Phenocrysts are zoned over a range of about 10 mole percent. These phenocrysts contain abundant euhedral inclusions <50 μm of Cr-rich spinel. Groundmass olivine ranges in composition from about Fo_{74} to Fo_{33} .

The compositions of clinopyroxene occurring in these lavas are also shown in figure 6. The average pyroxene composition is about $\text{Wo}_{39}\text{En}_{43}\text{Fs}_{18}$. The maximum range of zoning in a single grain is about 4 mole percent, and the maximum range in a single rock about 9 mole percent. Pyroxene contains about 2-3.5 weight percent Al_2O_3 , 0.5-1.5 percent

TiO_2 , and <0.5 percent Na_2O and Cr_2O_3 . The minor-element content of the pyroxene is shown as insets in figure 6. Arrows indicate the direction of crystallization. The most magnesian pyroxene has the highest Cr_2O_3 . Increasing crystallization is accompanied by a decrease in Cr and Al and an increase in Ti. The most Fe-rich pyroxene has $\text{Al}/\text{Ti} \approx 2$, indicating that Al and Ti are present in pyroxene dominantly as $\text{CaTiAl}_2\text{O}_6$. Pyroxenes of -087, which has the coarsest grain size of the group A tholeiites (0.2-0.5 mm), shows the least range in either $\text{Fe}/\text{Mg}+\text{Fe}$ or in Al/Ti (figure 6). This limited range may be due to the fact that the slower cooling rate has allowed the pyroxene to equilibrate more completely to the groundmass temperature.

Plagioclase compositions are shown in figure 7. In general the most calcic phenocrysts are about $\text{An}_{69}\text{Ab}_{30}\text{Or}_1$. However one relict core in -087 has a composition of $\text{An}_{84}\text{Ab}_{15}\text{Or}_1$. Groundmass plagioclase ranges to $\text{An}_{25}\text{Ab}_{60}\text{Or}_{15}$. No sanidine is present in the groundmass.

The compositions of oxide minerals are shown in figure 8. Spinel occurs only as inclusions in olivine phenocrysts. Its composition varies significantly in Al, ranging from $\text{Sp}_{57}\text{Mt}_{15}\text{Chr}_{28}$ to $\text{Sp}_{42}\text{Mt}_{25}\text{Chr}_{33}$. The TiO_2 of spinel is 1-3 weight percent. The groundmass oxide phases are titaniferous magnetite and ilmenite. The composition of magnetite averages $\text{Mt}_{35}\text{Ulv}_{65}$ and ranges from Mt_{20} to Mt_{41} . Compositions become more Ti-rich with increasing crystallization. Average Al_2O_3 is ~0.5-2 weight percent. The composition of groundmass ilmenite is also shown in figure 8. It contains about 5 mole percent of MgTiO_3 and 6-8 mole percent of Fe_2O_3 .

Interstitial glass is commonly devitrified or altered. However, unaltered glass in -087 is approximately: SiO_2 70.1, TiO_2 0.9, Al_2O_3

13.7, CaO 1.7, MgO 0.1, FeO 2.5, Na₂O 3.3, K₂O 7.0, and BaO 0.6 weight percent. The normative composition of this glass is: quartz 18.9, orthoclase 41.9, albite 30.0, anorthite 1.9, wollastonite 0.2, diopside 5.9, and ilmenite 1.3.

Group B basaltic andesite and latite-andesite.

This group includes basaltic andesite ($\text{SiO}_2 \sim 53.5\text{-}57$ weight percent) and the related, more silicic rocks trending toward higher ($\text{Na}_2\text{O}+\text{K}_2\text{O}$) and SiO_2 (figures 3 and 4 and table 2). The most distinguishing petrographic feature of this group is the presence of resorbed quartz grains in all rocks of this group, and of resorbed, sodic plagioclase in all but the most silicic latite-andesite. The most magnesian rock, designated with a star on figure 3, is characterized by approximately 2-4 percent of euhedral to subhedral olivine phenocrysts <2.5 mm; 4-5 percent of rounded and embayed quartz grains <5 mm, surrounded by fine-grained granular reaction rims of clinopyroxene (figure 5C, left); and <1 percent of rounded, highly resorbed plagioclase grains <1.5 mm (figure 5D). No clinopyroxene is present as phenocrysts or microphenocrysts. A single quartz grain from rock -231 has a nearly perfectly euhedral, hexagonal form (figure 5C, right).

The groundmass consists of microlites of plagioclase, with interstitial olivine, clinopyroxene, magnetite, ilmenite, and a few percent of anhedral, devitrified residual glass. The groundmass texture is pilotaxitic or transitional between intergranular and pilotaxitic.

In the more silicic basaltic andesite ($\text{SiO}_2 = 55\text{-}57$ weight percent), 1-2 percent of plagioclase phenocrysts <1.5 mm and about a percent of colorless to pale green, zoned augite phenocrysts <0.7 mm are present in addition to olivine and to resorbed plagioclase and quartz.

In the latite-andesite, both clino- and orthopyroxene are abundant as phenocrysts. They range in size to about 3 mm and constitute about 4 percent of the rock. Olivine is present only as sparse, resorbed cores in orthopyroxene. As in the basaltic andesite, both resorbed quartz and resorbed plagioclase are present, each constituting up to about 3 percent of the rock. Small (<0.3 mm) rounded grains of hornblende occur rarely. The composition of this hornblende is approximately $(\text{Na}_{0.7}\text{K}_{0.1})\text{Ca}_{1.7}(\text{Mg}_{3.1}\text{Fe}^{2+}_{1.6}\text{Fe}^{3+}_{0.1}\text{Al}_{0.2})(\text{Si}_{6.2}\text{Al}_{1.7}\text{O}_{22})(\text{OH}_{0.6}\text{F}_{0.1})$. Where present these are surrounded by opaque black rims of fine-grained reaction material. Microphenocrysts of plagioclase <0.4 mm may be present, except in the most silicic latite-andesite ($\text{SiO}_2 \approx 64$ percent); and microphenocrysts of magnetite and of ilmenite may also occur.

The groundmass is comprised of plagioclase; clinopyroxene and orthopyroxene; olivine, except in the most silicic rocks; and glass. Textures are hyalopilitic to hyaloophitic. In some rocks glass may constitute 20 to 50 percent of the groundmass (figure 5E).

Olivine compositions are shown in figure 9. The composition of the most magnesian phenocrysts in -230 and -045 is Fo_{85} and Fo_{87} , respectively. The phenocrysts range to about Fo_{77} . More iron-rich olivine (to Fo_{52}) occurs as a groundmass phase. The composition of olivine phenocrysts in -044 cannot be accurately measured because of alteration to serpentine. No olivine occurs in -063 or -036.

The compositions of pyroxene in these rocks are shown in figure 9. In the basaltic andesite (-230) the average pyroxene composition is $\text{Wo}_{43}\text{En}_{44}\text{Fs}_{13}$. The total range toward more Fe-rich compositions is about 10 mole percent. A slight decrease of non-quadrilateral components

(mainly Al) correlates with increasing Fe. The pyroxene is slightly more calcic than pyroxene of the group A tholeiite (cf. figures 9 and 6), but is very similar in Al_2O_3 (1-4.5 weight percent), TiO_2 (1-1.5 percent), Na_2O (~ 0.5 percent), and Cr_2O_3 (< 0.5 percent). The minor element content of the pyroxene is shown as insets. With increasing crystallization Al/Ti decreases and approaches a value of 2. Essentially no change in Cr occurs.

For -045 and -044, the more intermediate members of this series, the composition of clinopyroxene for both quadrilateral and non-quadrilateral components is approximately the same. The more silicic members of the series (-063 and -036) contain no olivine. In these, orthopyroxene is present in addition to clinopyroxene. The clinopyroxene is more magnesian than in the mafic, olivine-bearing members of the series. For -063 clinopyroxene is about $\text{Wo}_{43}\text{En}_{46}\text{Fs}_{11}$ and orthopyroxene about $\text{Wo}_3\text{En}_{79}\text{Fs}_{18}$; for -036, clinopyroxene is $\text{Wo}_3\text{En}_{80}\text{Fs}_{17}$ to $\text{Wo}_5\text{En}_{65}\text{Fs}_{30}$. TiO_2 is much lower (< 0.7 weight percent). A distinctly different trend in minor elements occurs in -063 and -036 in contrast to more magnesian members of this series. Cr is much higher in both clino- and orthopyroxene relative to Al and Ti, due probably to the absence of olivine. In -063, Cr/Cr+Al+Ti decreases with increasing crystallization; separate trends can be distinguished for clinopyroxene and for orthopyroxene. In -036 clinopyroxene exhibits a trend similar to that in -063. However, orthopyroxene shows a poorly-defined trend toward decreasing Al/Ti.

Feldspar compositions are shown in figure 10. In -230 the most calcic plagioclase (An_{43-51}) is a single partially resorbed phenocryst displaying oscillatory zoning. A continuous range in composition exists

through sodic plagioclase to sanidine. Zoned, partially resorbed plagioclase phenocrysts are more abundant in -045. While the maximum range of zoning of these resorbed grains (An_{65} , cores, to An_{28} , rims) is about the same as that of the unresorbed phenocrysts and microphenocrysts, these resorbed grains are on the average somewhat more sodic.

Sample -044 has approximately 15 volume percent of plagioclase phenocrysts (figure 5F) of composition An_{40-45} . This rock has probably undergone accumulation of plagioclase (discussed further in a later section). Both sodic plagioclase and sanidine occur in the groundmass. Plagioclase occurring in the more silicic members of the series (-063 and -036) is also relatively calcic (An_{30-55}). Sanidine is not present as a groundmass phase in the rocks; instead abundant glass is present.

The compositions of oxide phases are shown in figure 11. Spinel occurring as inclusions in olivine phenocrysts is $Sp_{65}Mt_{15}Chr_{20}$ to $Sp_{70}Mt_{10}Chr_{20}$. Magnetite ranges from $Mt_{40}Ulv_{60}$ to $Mt_{85}Ulv_{15}$. Compositions become more titaniferous with increasing crystallization. Al_2O_3 ranges from approximately 1.5-6 weight percent. The aluminum contents of both the spinel and magnetite are substantially higher than in the group A tholeiite, presumably reflecting the higher bulk rock alumina content. Ilmenite contains about 10-15 mole percent $MgTiO_3$ and 10-20 mole percent Fe_2O_3 .

Interstitial glass in -036 has the composition: SiO_2 71.7, TiO_2 0.9, Al_2O_3 12.6, CaO 0.6, MgO 0.1, FeO 2.9, Na_2O 2.8, K_2O 5.9, BaO 0.0, and Cr_2O_3 0.0 weight percent. The normative composition of this glass is: quartz 29.0, corundum 0.6, orthoclase 36.6, albite 25.8, anorthite 3.0, hypersthene 3.7, and ilmenite 1.3.

Phenocryst mineralogy. The minerals occurring as phenocrysts in these basaltic andesite and latite-andesite lavas are summarized in figure 12. The group B basaltic andesite is characterized by phenocrysts of olivine containing inclusions of Cr-rich spinel. Quartz is present in abundance (~5 percent) as partially resorbed single grains and polygranular aggregates surrounded by rims of fine-grained augite. Plagioclase occurs only as partially resorbed grains sparsely distributed throughout the rocks. The composition of the most magnesian olivine in -230 is Fo₈₅ (figure 9). In figure 13 the composition of the most magnesian olivine in each rock is plotted against the whole-rock Mg-value. Olivine of Fo₈₅ is approximately in equilibrium with a melt of the composition of -230. The equilibrium value of K_d^{Fe-Mg} is assumed to be approximately 0.30 (Roeder and Emslie, 1970). Values of K_d calculated after the experimental determination of Longhi (1977) give slightly higher results (0.32-0.35); these may be valid only for very low-alkali compositions. The partially resorbed plagioclase in this rock ranges from An₄₀ to An₅₀. In the more silicic basaltic andesite (SiO₂ ≈ 55.5-56.5 weight percent), both plagioclase (as euhedral laths) and augite are present as phenocrysts or microphenocrysts. The most magnesian olivine in -045 is Fo₈₇. This composition is very slightly more magnesian than -230, which may indicate that this composition has been affected by loss of olivine.

In the latite-andesite (SiO₂ > 59 weight percent) hypersthene is present as a phenocryst phase in addition to augite and plagioclase, and both titaniferous magnetite and ilmenite are microphenocryst phases. Olivine is not present as phenocrysts. Rare, small phenocrysts of

amphibole occur in some rocks. The composition of augite phenocrysts in the latite-andesite is slightly more magnesian than in the basaltic andesite (see figure 9). The more magnesian composition may result from the fact that, since olivine is not a phenocryst phase, the Mg/Fe ratio of the melt is higher when augite begins to crystallize.

For the most silicic rocks ($\text{SiO}_2 > 60$ percent) the large, partially resorbed laths of plagioclase are not present. For rocks with > 62 percent SiO_2 plagioclase is not present as a phenocryst phase, and olivine does not occur in the groundmass. Quartz occurs in all of these rocks as resorbed single grains and as polygranular aggregates.

The compositions of spinel, occurring as inclusions in olivine phenocrysts, and of groundmass and microphenocryst Ti-magnetite and ilmenite overlap for all of these rocks (figure 11), hence no regular progression of compositions is apparent.

In figure 14 the composition of the most magnesian olivine and pyroxene phenocrysts in each rock is plotted against the composition of the most calcic plagioclase phenocrysts. Rock -230, in which the most magnesian olivine is Fo_{85} , is not plotted, since it contains no plagioclase as phenocrysts. Rock -044, which contains about 15 percent of plagioclase phenocrysts, has probably undergone accumulation of plagioclase. Hence its correct position along this series is uncertain. Possibly the composition of its plagioclase and clinopyroxene accurately reflect crystallization from a single melt composition. Clinopyroxene shows a strong decrease in Mg-value with decreasing $\text{An}/(\text{An}+\text{Ab})$ in plagioclase for three of these rocks. Clinopyroxene in -045 is more iron-rich and does not fall on this trend. This clinopyroxene may have

lower Mg/Mg+Fe because it occurs as a microphenocryst phase, hence crystallized at a lower temperature from a melt richer in iron. Orthopyroxene, which occurs only in -063 and -036, shows almost no difference in composition. Hence these data cannot be unambiguously interpreted, yet suggest that decreasing Mg-values of mafic phases (especially clinopyroxene) correlate with decreasing anorthite component of coexisting plagioclase.

Quantitative modeling. Variation diagrams for this suite of rocks are presented in figure 15. The phases indicated by arrows are all observed as phenocrysts or as xenocrysts. For all phases except quartz the arrows indicate 5% subtraction of that phase. For quartz the arrow (dashed) shows 5% addition. All rock compositions fall on smooth curves except for a single point (rock -044).

Figure 15 shows that for the most mafic basaltic andesite subtraction of olivine (Fo_{84}) and addition of plagioclase (An_{46}) and quartz will adequately model the evolution of these rocks to more intermediate compositions. These three phases are present as phenocrysts and/or xenocrysts in the basaltic andesites. In the more intermediate members of this series, subtraction of olivine (Fo_{84-86}), clinopyroxene ($\text{Wo}_{40}\text{En}_{45}\text{Fs}_{15}$), and plagioclase (An_{58}), and addition of quartz will drive the melt to latite-andesite compositions. In the most silicic end of the series the evolution of these melts is controlled by subtraction of clinopyroxene, orthopyroxene ($\text{Wo}_3\text{En}_{79}\text{Fs}_{18}$), and plagioclase (An_{50}), and by the continued addition of quartz.

Rock -044 falls consistently off the trends defined on these diagrams. This rock contains about 15 percent of plagioclase phenocrysts.

Figure 15 shows that its composition is explained by addition of plagioclase to a melt of basaltic andesite composition. The low MgO and high FeO* result from the complete alteration of olivine to iddingsite.

The evolution of this series has been quantitatively modeled using the least-squares technique of Reid et al. (1973). The key feature in using such a technique is that measured compositions of phenocrysts and/or xenocrysts actually present in the rocks are fit to a change in bulk composition. If the bulk compositions cannot be related by the phases actually present, then a genetic relationship between these compositions is in serious question. In the following models, all solutions were overdetermined, i.e., the number of phases (variables) solved for was always less than the number of oxides (constraints). Criteria used in determining "good" fits were a low sigma squared, and approximately equal numbers of positive and negative residuals, whose mean value was about zero (Reid et al., 1973). In addition, two important "modal" criteria were, first, that the amounts of the various phases solved for by the least-squares fit approximated the modal amounts of those phases, and second, that the solution was "stable", i.e., that adding or subtracting a phase or changing the compositions of the phases did not radically change the amounts of other phases in the solution. In all cases the best solution resulted from fitting all phenocryst and/or xenocryst phases in a particular rock.

This series was first modeled as a single step, using the most magnesian rock -230 as the starting composition and the most silicic rock -036 as the derivative composition (table 6). Actual phenocryst

phases and their measured compositions were used. This model was designed primarily to determine whether, in addition to adding quartz, removal of olivine and clinopyroxene yields a significantly better fit to these compositions than removal of either clinopyroxene or olivine alone. Solutions involving olivine and quartz, with and without plagioclase; and clinopyroxene and quartz, with and without plagioclase, gave unsatisfactory results. Solutions with olivine, clinopyroxene, and quartz, with and without plagioclase, yielded significantly better results. The best fit was obtained using all of the observed phenocryst phases: olivine, clinopyroxene, plagioclase, magnetite, and ilmenite (Cr-spinel was ignored; orthopyroxene appears as olivine + quartz). The phase compositions used and the results of this best model are summarized in table 6.

Next, this series was divided into three steps in order to more closely model this series. Actual phenocryst phases and their measured compositions were used in relating successive rock compositions to each other. The results of this modeling are presented in table 6. Briefly, to derive the most silicic basaltic andesite ($\text{SiO}_2 \approx 55$ percent) from the most magnesian basaltic andesite ($\text{SiO}_2 \approx 53$ -54 percent) requires subtraction of olivine (Fo_{84}) and Cr-spinel and addition of sodic plagioclase (An_{46}) and quartz. The more mafic latite-andesite ($\text{SiO}_2 \approx 59$ -60 percent) is derived from the silicic basaltic andesite by subtraction of olivine (Fo_{86}), plagioclase (An_{58}), augite, and minor titaniferous magnetite and ilmenite; and by addition of quartz. Net subtraction of more calcic plagioclase occurs because plagioclase becomes a major phenocryst phase at $\text{SiO}_2 \approx 54.5$ percent. This

plagioclase component actually represents the sum of subtraction of calcic plagioclase phenocrysts ($An > 58$) and addition of partially resorbed sodic plagioclase ($An \approx 46$). Derivation of the most silicic latite-andesite ($SiO_2 \approx 64$ percent) from the mafic latite-andesite requires subtraction of plagioclase (An_{50}), augite, hypersthene, and minor titaniferous magnetite and ilmenite; and by continued addition of quartz. The final amount (by weight) of the most evolved latite-andesite is 80% of the initial amount of magnesian basaltic andesite. A striking feature of these calculations, anticipated from the modal compositions of the rocks and from their variation diagrams (figure 15), is the large amount (12 percent) of quartz required to adequately model the evolution of this compositional series. The origin of this quartz will be discussed in a later section.

Group C basanite

This group consists of only two samples, distinguished by their high normative nepheline content (>5 percent). These rocks are characterized by approximately 4-5 percent of euhedral, skeletal olivine phenocrysts <3 mm and 2 percent of euhedral, green to brownish green, sector-zoned clinopyroxene phenocrysts <1.2 mm. One sample (-034) contains ~4 percent of euhedral plagioclase microphenocrysts <0.6 mm. Olivine phenocrysts contain abundant inclusions <0.1 mm of Cr-spinel. The groundmass consists of plagioclase, olivine, clinopyroxene, magnetite, apatite, and a small amount of glass, with an intergranular texture.

The composition of olivine in basanite -269 is shown in figure 16. Olivine phenocrysts range from Fo_{83} to Fo_{73} . The range of zoning in

individual phenocrysts is ~5 mole percent. Groundmass olivine has a range of Fo_{73-61} .

Pyroxene composition is also shown in figure 16. The pyroxene is distinctly different in composition from that of either the group A or group B basaltic rocks. It contains a much higher content of non-quadrilateral components, particularly $CaAl_2SiO_6$ and $CaTiAl_2O_6$. The average pyroxene composition in -269 is about $Wo_{48}En_{38}Fs_{14}$. Al_2O_3 averages about 3.5-8 weight percent, TiO_2 is 1-2.5 percent, and Na_2O and Cr_2O_3 < 0.5 percent. A slight trend toward increasing non-quadrilateral components is evident in figure 16. The minor element composition of the pyroxene is shown in the triangular inset. No systematic change in these elements is apparent.

Feldspar compositions are shown in figure 17. A wide range of composition is present in the groundmass, from calcic plagioclase ($An_{61}Ab_{37}Or_2$) to K-rich sanidine ($An_2Ab_{36}Or_{62}$). The compositions of adjacent plagioclase and sanidine grains are tentatively connected by a tie line (dashed line) in figure 17.

The composition of titaniferous magnetite in this rock, given in figure 18, is very similar to Ti-magnetite of the group D basalt and related hawaiiite, hence is not distinguished on this figure.

Group D alkali olivine basalt and hawaiiite

The group D alkali olivine basalt together with the hawaiiite constitute a diverse group of nepheline-normative rocks (figures 3 and 4). The basalt is taken as those rocks with the highest Mg-values (~63) and the lowest (Na_2O+K_2O) (~4.5 weight percent) and SiO_2 (~49 percent).

The alkali olivine basalt is characterized by 3-4 percent of euhedral olivine phenocrysts <2.5 mm, containing inclusions <50 μm of Cr-spinel, and 3-4 percent of euhedral zoned plagioclase phenocrysts <1.8 mm. A small amount (1-2 percent) of euhedral, green to brownish-green clinopyroxene phenocrysts <1 mm is present in some rocks. Partially resorbed quartz grains <2 mm and/or resorbed plagioclase grains <2 mm occur in some samples, but are not ubiquitous as they are in the basaltic andesite and the latite-andesite. Also euhedral titaniferous magnetite microphenocrysts may be present. These rocks are characterized by an intergranular texture. Groundmass phases consist of plagioclase, olivine, augite, magnetite, apatite, and a small amount of brownish glass. Ilmenite is not present.

Olivine compositions are shown in figure 16. Phenocrysts range from Fo_{82} to Fo_{79} . This limited range is probably due to the relatively small number of analyses. Groundmass compositions extend to Fo_{50} .

Pyroxene compositions are similar to those of the group C basanite (figure 16). The average pyroxene composition is $\text{Wo}_{47}\text{En}_{40}\text{Fs}_{13}$. Al_2O_3 ranges from 2.5-7.5 weight percent, TiO_2 0.5-2.5 percent, and Na_2O and Cr_2O_3 < 0.5 percent. The minor element content of pyroxene is shown in the triangular inset. A well-defined trend exists of decreasing Al/Ti (approaching 2) with increasing degree of crystallization. This trend differs from that of the group A tholeiite in that little or no change in Cr is present.

Feldspar compositions are presented in figure 17. They are similar to those in basanite -269. The most calcic phenocrysts have a

composition of about $An_{68}Ab_{31}Or_1$. Both plagioclase and sanidine are present in the groundmass.

The compositions of groundmass magnetite are given in figure 18. Magnetite compositions overlap for all samples of the basanite, alkali olivine basalt, and hawaiite. The range is $Mt_{25}Ulv_{75}$ to $Mt_{60}Ulv_{40}$. Al_2O_3 is between 1 and 2 weight percent.

Interstitial glass in -061 has the composition: SiO_2 56.5, TiO_2 2.1, Al_2O_3 19.0, CaO 0.6, MgO 0.4, FeO 5.4, Na_2O 8.3, K_2O 6.3, BaO 0.1, and Cr_2O_3 0.0 weight percent. Its normative composition is: orthoclase 36.6, albite 32.4, nepheline 19.5, sodium metasilicate (Na_2SiO_3) 2.3, diopside 2.5, olivine 3.9, and ilmenite 2.8.

The hawaiite is petrographically somewhat diverse. It is characterized by up to 5 percent phenocrysts of olivine <2.5 mm, except in the most silica- and alkali-rich hawaiite where olivine is absent, and by up to 3 percent of brownish green, zoned clinopyroxene phenocrysts <2 mm. In the hawaiite with lower SiO_2 (~51 weight percent) plagioclase is restricted to the groundmass, or is rarely present as microphenocrysts. Lavas with higher SiO_2 (52-53 percent) consistently contain sparse (~1 percent) phenocrysts or microphenocrysts of plagioclase <1.5 mm. In addition, rare, highly resorbed plagioclase phenocrysts <4 mm are present in some samples. Embayed quartz grains <2 mm surrounded by clinopyroxene reaction rims are also rarely present.

Detailed microprobe data have been obtained for -283. Although its (Na_2O+K_2O) and SiO_2 (~6 and 50 weight percent, respectively) suggest that it is more differentiated than the alkali olivine basalt, its

Mg-value (66) is the highest of all the samples examined in this study. This rock consists of 5 percent of euhedral (skeletal) to subhedral olivine phenocrysts <2.7 mm, containing abundant inclusions <0.1 mm of Cr-spinel, and 1 percent of zoned phenocrysts of brownish green clinopyroxene <1 mm. The larger pyroxene phenocrysts are ragged in outline and are heavily resorbed. Plagioclase is not a phenocryst phase. The groundmass consists of plagioclase laths surrounded by granular olivine, pyroxene, magnetite, apatite, and limonite minerals. A small amount (2-3 percent) of interstitial, devitrified glass is present.

Olivine compositions are presented in figure 16. Phenocrysts range from Fo₈₄ to Fo₇₇, which is also the maximum range of zoning in a single phenocryst. Groundmass olivine extends to Fo₆₃. Pyroxene compositions are given on figure 16. The composition of the larger, resorbed phenocrysts is more magnesian (Wo₄₄En₄₅Fs₁₁) than that of the smaller, unresorbed phenocrysts and groundmass pyroxenes (Wo₄₄En₄₃Fs₁₃ to Wo₄₈En₃₈Fs₁₄). In general the pyroxene composition is very similar to that of -061. Olivine poikilitically enclosed within a resorbed phenocryst is Fo₇₇₋₇₈. The minor element composition of pyroxene is shown in the triangular inset. The large, resorbed, Mg-rich phenocrysts have the highest Al/Ti. As for group C basalt -061, increasing crystallization correlates with decreasing Al/Ti. The composition of groundmass plagioclase is An₂₅ to An₆₀ (figure 17). Spinel included in olivine is Sp₄₅Mt₂₀Chr₃₅; groundmass magnetite ranges from Mt₂₅Ulv₇₅ to Mt₄₅Ulv₅₅, with Al₂O₃ from 1.8-2.7 weight percent.

Microprobe analyses have also been obtained for hawaiite -F212. This rock is the host rock for a suite of pyroxenite, plagioclase, and

orthopyroxene inclusions (Baldrige, 1979b). It consists of about 5 percent of euhedral to subhedral phenocrysts of olivine <0.5 mm, 1 percent of euhedral laths of plagioclase <1.5 mm, and <1 percent of euhedral to subhedral microphenocrysts of brownish green augite <0.2 mm. The groundmass consists of plagioclase laths, with granular olivine, augite, titaniferous magnetite, apatite, and interstitial potassium feldspar and glass; the texture is transitional between intergranular and pilotaxitic. A small amount of secondary hematite is present.

Olivine compositions are shown in figure 16. Phenocryst compositions range from Fo₇₈ to Fo₇₀. The range of zoning in individual phenocrysts is ~4 mole percent. Olivine phenocrysts characteristically contain abundant inclusions of Cr-spinel. Groundmass olivine has not been analyzed.

The composition of pyroxene is also shown in figure 16. The pyroxene is very similar to that of -283 in both major- and minor-element composition. Al₂O₃ ranges from 1.5-7 weight percent, TiO₂ is 1-2 percent, and Cr₂O₃ and Na₂O <0.5 percent.

Feldspar compositions are presented in figure 17. These are very similar to feldspar of -061 and -283. The most calcic phenocrysts are An₆₆Ab₃₃Or₁. The composition of groundmass magnetite (figure 18) ranges from Mt₄₁₋₇₄; Al₂O₃ is between 0.8 and 3.5 weight percent.

Phenocryst mineralogy. The minerals occurring as phenocrysts in the alkali olivine basalt and hawaiiite are summarized in figure 12. The lavas with the lowest MgO, SiO₂, and (Na₂O+K₂O) (e.g., -061) are characterized by phenocrysts of olivine (with Cr-rich spinel inclusions) and plagioclase. Some have a small amount (<2 percent) of augite

phenocrysts. Microphenocrysts of titaniferous magnetite may be present. In -061 the most magnesian olivine phenocryst is Fo_{82} . Olivine of this composition is slightly too iron-rich to be in equilibrium with a melt of the composition of -061 (figure 13). It is displaced in a direction consistent with resorption of the earliest formed olivine phenocrysts. The most calcic plagioclase phenocrysts are about $\text{An}_{68}\text{Ab}_{31}\text{Or}_1$. In the more silicic alkali olivine basalt (e.g., -029 and -281) the phenocryst assemblage is the same; in addition a small amount (1-2 percent) of partially resorbed quartz and/or plagioclase may be present.

Plagioclase is not present as a phenocryst phase in most of the hawaiitic lavas. The line separating alkali olivine basalt, with plagioclase phenocrysts, from hawaiite is labeled as the plagioclase-absent line of figure 12. In the hawaiite, phenocrysts consist of olivine and augite. A small amount (1 percent) of partially resorbed quartz is present in some rocks. The most magnesian olivine in hawaiite -283 is Fo_{84} , slightly more magnesian than in the alkali olivine basalt. However this rock also has the highest Mg-value of any of the lavas (65.9), hence olivine of Fo_{84} is slightly too iron-rich to be in equilibrium with a melt corresponding in composition to -283 (figure 13). It is displaced in a direction consistent with either resorption of the early-formed olivine phenocrysts or addition of augite phenocrysts. This rock is petrographically distinct from all other alkalic lavas in that it contains large, partially resorbed phenocrysts of titaniferous augite. These resorbed phenocrysts are slightly more magnesian than the stable augite phenocrysts occurring in this rock and also than

augite phenocrysts in the alkali olivine basalt. Addition of these phenocrysts would substantially increase the Mg-value of this rock.

In the more silica-rich ($\text{SiO}_2 \approx 52$ weight percent) hawaiitic lavas, phenocrysts consist of olivine (except in the most silicic), Ti-rich augite, and a small amount (<1 percent) of plagioclase. In -F212 the most magnesian olivine phenocrysts are Fo_{78} . These are also substantially too iron-rich to be in equilibrium with a melt corresponding in composition to -F212 (figure 32). Since this rock is the host for a suite of megacrysts and pyroxenite inclusions (Baldrige, 1979b) it is possible that this whole-rock composition reflects addition of some pyroxene. The most calcic plagioclase phenocrysts are $\text{An}_{66} \text{Ab}_{33} \text{Or}_1$.

Quantitative modeling

Variation diagrams for the group D alkali olivine basalt and hawaiite are shown in figure 19. These compositions do not fall on single, well-defined trends as for the basaltic andesite and latite-andesite (figure 15). On certain diagrams, for example, SiO_2 vs. MgO and FeO^* vs. MgO , parallel trends are evident. Compositions in one trend cannot be related to compositions in the other by addition or subtraction of phases actually present as phenocrysts. Therefore instead of a single quantitative model relating all of these compositions to each other, smaller sets of compositions can be related. Parental (i.e., the most magnesian) compositions are indicated on figure 19 by stars. The solid star is -061, representative of the parental alkali olivine basalt. Open stars are the two parental hawaiitic compositions (-028 and -213). Within each set, lavas with higher Na_2O and K_2O , and

lower MgO can be related to these parental compositions by subtraction of some combination of olivine, clinopyroxene, and plagioclase. Rock -283, shown in figure 19 as a solid square, lies off these trends. The high Mg-value of this rock and the presence of large, partially resorbed clinopyroxene phenocrysts, suggest that this rock has undergone accumulation of clinopyroxene. On figure 12 the compositions that are related by addition or removal of these phases are shown by arrows.

The results of quantitative modeling are presented in table 6. These least-squares calculations show that the five basaltic compositions can be related by subtraction of olivine (Fo_{81}), augite ($\text{Wo}_{45}\text{En}_{42}\text{Fs}_{13}$), plagioclase (An_{65}), and a trace of Cr-spinel. About 22 percent by weight of these phases are removed from the initial basalt to derive the final composition. The two sets of hawaiitic compositions evolve by subtraction of olivine (Fo_{74-82}), augite, and trace amounts of Cr-spinel. Plagioclase is either a very minor phenocryst or microphenocryst phase in the hawaiite or is absent altogether. Approximately 5-8 percent of these phases are subtracted from the hawaiite melts to derive the final compositions.

Small amounts of partially resorbed quartz and plagioclase occur in some of the alkalic lavas. Quartz was included as a phase in these least-squares calculations. However, within the limits of error, neither addition nor subtraction of quartz was required to fit the end member compositions. Similarly, no addition of sodic plagioclase was required. However, it is probably impossible to distinguish the addition of a small amount of this plagioclase to a composition from which plagioclase is a major fractionating phase.

ALBUQUERQUE VOLCANOES

Setting

The Albuquerque Volcanoes, located in the northern Albuquerque-Belen basin (figure 1), consist of five large cinder cones and several smaller vents, as well as an apron of basalt flows spreading laterally from the bases of the cones. This field covers some 60 square km. The cinder cones are aligned approximately north-south along two en echelon fractures (Kelley and Kudo, 1978). The age of these flows is about 190,000 yrs. (Bachman and Mehnert, 1978). Sample localities are shown in figure 20. Samples were obtained from the major cinder cones and from the apron of flows capping the adjacent mesa in order to test for vertical and lateral variations in composition.

Whole-rock chemistry

Whole-rock chemical analyses of lavas from the Albuquerque Volcanoes are presented in table 3. These compositions are plotted in terms of $(\text{Na}_2\text{O}+\text{K}_2\text{O})$ vs. SiO_2 in figure 21, and in figure 22 they are represented in terms of normative plagioclase, olivine, and hypersthene. These lavas are normative olivine tholeiites, and are very uniform in bulk composition.

However, in spite of this uniformity, a very slight trend toward higher SiO_2 and lower normative olivine occurs (figures 21 and 22). Kelley and Kudo (1978) state that the stratigraphically higher flows are progressively more differentiated than the lower flows. However, data presented here indicate that the relationship is not so simple. The flows with lower SiO_2 (approximately 50 weight percent) occur as the upper of two flows which cap the mesa in two places along the

southern edge of the Albuquerque Volcanoes field (e.g., -093 and -110; see figure 20). The lower of these two flows plus the mesa-capping flow further north and the more northerly cinder cones, are slightly more silicic ($\text{SiO}_2 \approx 51$ percent). This relationship suggests that one or more of the southerly vents was extruding very slightly more mafic lavas.

Petrographic description and mineral chemistry

These lavas are petrographically rather uniform. The variation that is present within this group is related mainly to the degree of crystallinity. These rocks consist of 3-5 percent of euhedral, skeletal olivine phenocrysts <3 mm and 3-10 percent of zoned, euhedral laths of plagioclase <4 mm. In contrast to lavas from the Cerros del Rio, Santa Ana Mesa, and El Alto, augite is not present as a phenocryst or microphenocryst phase.

The groundmass is characterized generally by an intergranular texture, although texture may range from hyaloophitic to subophitic depending on cooling rate. The groundmass consists of plagioclase micro-lites surrounded by granular olivine, augite, low-Ca pyroxene, magnetite, ilmenite, apatite, and a few percent of interstitial glass. The presence of low-Ca pyroxene, which is difficult or impossible to detect without the electron microprobe, is distinctive and is the only petrographic indication that these rocks are tholeiitic. The relationship of groundmass olivine and low-Ca pyroxene will be discussed in more detail below.

Sample -093 is representative of these lavas and has been analyzed in detail. Olivine compositions are presented in figure 23. Phenocryst compositions range from Fo_{79} to Fo_{71} . The maximum range of

zoning in phenocrysts is about 7 mole percent. Groundmass compositions range to Fo_{37} . Pyroxene compositions are also shown in figure 23. The composition of groundmass augite ranges from $Wo_{37}En_{46}Fs_{17}$ to $Wo_{35}En_{38}Fs_{27}$. Low-Ca pyroxene ranges from $Wo_{11}En_{51}Fs_{38}$ to $Wo_8En_{46}Fs_{46}$. The Fe/Mg+Fe ratio of low-Ca pyroxene is much higher than for augite, suggesting that low-Ca pyroxene is a very late-crystallizing groundmass phase. The minor element composition of the pyroxene is shown in the triangular inset. A distinct trend of decreasing Al/Ti (to ~2:1) with increasing crystallization is present in augite. In low-Ca pyroxene Al/Ti is approximately 2:1, and no systematic variation is apparent.

The composition of feldspar in -093 is presented in figure 24. Plagioclase phenocrysts range from $An_{69}Ab_{30}Or_1$ to about $An_{62}Ab_{37}Or_1$. Groundmass feldspar ranges to anorthoclase ($An_{13}Ab_{66}Or_{21}$).

The compositions of titaniferous magnetite and ilmenite in -093 are given in figure 25. Magnetite is Mt_{58} , and contains about 1.8 weight percent Al_2O_3 ; ilmenite is $Il_{84-64}Hem_{10-30}Gi_6$.

ISLETA AND WIND MESA VOLCANOES; CAT HILLS VOLCANIC FIELD

Setting

Isleta Volcano, Wind Mesa Volcano, and the Cat Hills volcanic field constitute three separate volcanic fields of different ages. They will be treated together here because (1) the lavas are similar in composition and (2) these fields, while separate, are located in close proximity to one another (figures 1 and 26). All three fields can be enclosed in an area equal to about one-half the area occupied by the Cerros del Rio volcanic field. Isleta Volcano is a broad, low cone,

70-150 m high and <2 km in diameter, consisting of several ash and flow units. Wind Mesa Volcano is a small shield volcano 150 m high covering an area of 10 square km. It too consists of several flow and ash units (Kelley and Kudo, 1978). Both volcanoes are of late Pliocene or Pleistocene age (Dane and Bachman, 1965). The Cat Hills volcanic field consists of a broad apron of basalt flows which is capped by 23 cinder cones. This field covers an area of approximately 65 square km. These cones are aligned approximately north-south along fissures. The Cat Hills basalt is approximately 140,000 years old (Kudo, 1976). Sample localities for these three fields are shown in figure 26. Reconnaissance whole-rock analyses have been obtained on samples from these fields in order to determine what lava types are present and their range of compositions. No microprobe analyses of these lavas exist presently.

Whole-rock chemistry

Whole-rock chemical analyses of lavas from Isleta and Wind Mesa Volcanoes and from the Cat Hills volcanic field are given in table 4. Figure 27 presents $(\text{Na}_2\text{O} + \text{K}_2\text{O})$ vs. SiO_2 for these analyses. The range of compositions is relatively restricted, with SiO_2 ranging from 48.5 to 53 weight percent. While compositions from Wind Mesa Volcano are generally the most silicic, lavas from all three volcanic fields overlap in composition. Both hypersthene-normative and nepheline-normative basaltic rocks are present. The silica content of most of the tholeiitic rocks is between 49 and 52 weight percent and the Mg-value between 53.5 and 60. They are similar in composition to the group A olivine tholeiite of the Cerros del Rio, Santa Ana Mesa, and El Alto volcanic fields.

The most magnesian of these rocks is indicated on figure 22 with a star. A few tholeiitic flows from Wind Mesa with higher silica ($\text{SiO}_2 = 52.2 - 53.5$ weight percent) also have higher Mg-values (61.5 - 62.5) and may constitute a separate group. Two of these compositions are also shown with stars on figure 27.

The nepheline-normative rocks have $\text{SiO}_2 = 48.5 - 50.5$ and $(\text{Na}_2\text{O} + \text{K}_2\text{O}) = 5-6$. The most magnesian of these lavas are those reported by Kelley and Kudo (1978), with an Mg-value of 60 (designated with a star on figure 27). The nepheline-normative basalt is similar to the hawaiite of the Cerros del Rio, Santa Ana Mesa, and El Alto volcanic fields (figure 3).

Hence these analyses suggest that several distinct parental lavas of relatively restricted compositional range are present. Additional analyses, both whole-rock and microprobe, are required to clarify the chemical and petrologic relations among these lavas and to compare their genesis to other lavas of the Rio Grande rift.

The olivine tholeiite contains 2-5 percent of euhedral to skeletal olivine phenocrysts <3 mm and 1-5 percent euhedral phenocrysts of plagioclase <3 mm. Up to 3 percent phenocrysts of microphenocrysts of colorless to pale green augite <1 mm are present in some rocks. Olivine phenocrysts contain inclusions of euhedral Cr-spinel <60 μm . In the most mafic rocks rare phenocrysts of partially resorbed plagioclase are present. These consist of irregularly-shaped cores, which are nearly opaque due to tiny ($\sim 3 \mu\text{m}$) inclusions of silicate phases and of magnetite, overgrown by clear rims of plagioclase. The groundmass is characterized by an intergranular texture, or by a hyalopilitic

texture in more quickly cooled rocks. It consists of plagioclase microlites, clinopyroxene, olivine, magnetite, ilmenite, apatite, and interstitial glass. Both magnetite and ilmenite may be skeletal. Slight alteration of olivine to iddingsite and of glass to clay minerals(?) is common. Some hematite is also present in the groundmass.

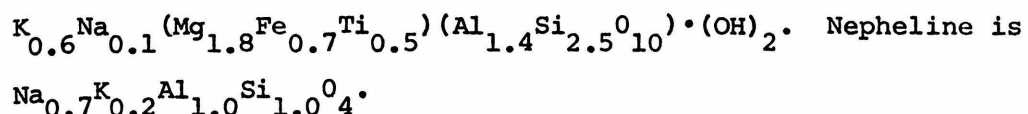
The basaltic andesite is similar to the olivine tholeiite in that it contains about 5 percent phenocrysts of olivine <3 mm (with inclusions of Cr-spinel), 5 percent phenocrysts of plagioclase <1.5 mm, and 2-3 percent of clinopyroxene microphenocrysts. Plagioclase is characterized by a strongly seriate texture, with a continuous range in grain size from phenocrysts to groundmass microlites. The groundmass has a pilotaxitic texture. The same groundmass phases are present as in the olivine tholeiite. The nepheline-normative rocks contain phenocrysts of olivine, plagioclase, and clinopyroxene and are distinguished petrographically from the tholeiite lavas by the deeper brownish green color and stronger zoning of the augite phenocrysts and by the absence of ilmenite as a groundmass phase.

PRE-PLIOCENE BASALTIC LAVAS

While by far the greatest volume of basalt in the Rio Grande rift is Pliocene (<5 m.y.) and Quaternary in age, lesser quantities of basaltic lava have been erupted since inception of crustal extension in the late Oligocene. These older lavas generally occur as isolated flows, dikes, or plugs of very limited areal extent (figure 29). Eruption of the pre-Pliocene lavas occurred mainly during two intervals of time: lower Miocene/upper Oligocene and late Miocene (figure 30).

Reconnaissance chemistry obtained on many of the lavas (table 5) shows that both hypersthene- and nepheline-normative compositions are present (figures 31 and 32). While some of the early lavas are olivine nephelinite, no systematic change in composition with time is present.

The oldest group of lavas (upper Oligocene and lower Miocene) includes the Cieneguilla Limburgite, the nephelinitic lava of Cerro Negro, the tholeiitic flows of the Jarita Formation, and the flows occurring along the east side of the Española basin (figure 29). The Cieneguilla Limburgite (Stearns, 1953a; Sun and Baldwin, 1958), which is about 25 m.y. old (Baldrige, Damon, and Bridwell, unpublished data), crops out in the offset region between the southern Española and northern Albuquerque-Belen basins (figure 29). These rocks are comprised of flows and interbedded tuffs of alkali olivine basalt, olivine tholeiite, and olivine nephelinite of late Oligocene to early Miocene age. One of these nephelinitic lavas (-A271) is the host rock for a suite of harzburgite, clinopyroxene, magnetite, and (rare) granulite inclusions (Baldrige, 1979b). This olivine nephelinite consists of about 10 percent of euhedral (commonly skeletal) olivine phenocrysts <1.5 mm and 5 percent of euhedral to subhedral clinopyroxene phenocrysts <1.1 mm in a non-vesicular, granular groundmass of olivine, tabular clinopyroxene, magnetite, biotite, and interstitial nepheline and zeolites (natrolite and gonnardite). The compositions of olivine and clinopyroxene phenocrysts are shown in figure 33. Olivine phenocrysts are Fo_{85-87} . Clinopyroxene phenocrysts average $Wo_{51}En_{38}Fs_{11}$. The total range of zoning is about 4 mole percent. Groundmass biotite has the composition



Cerro Negro, a small volcanic plug with an associated lava flow located in the northern Española basin (figure 29), is 19 m.y. old (Baldrige, Damon, and Bridwell, unpublished data). It also is olivine nephelinite (table 5, figures 31, 32). However the basalt flows of the Jarita Formation, which occur in the southern Tusas Mountains and northern Española basin, are quartz tholeiite. These basalt flows (22-25 m.y. old; Baldrige, Damon, and Bridwell, unpublished data) are interbedded with the Miocene Abiquiu Formation (J. May, unpublished map). The basalt flows occurring at Cundiyo and Bishop's Lodge, along the east side of the Española basin, lie stratigraphically below the Santa Fe Group sediments, and are approximately equivalent in age to the Abiquiu Formation (Galusha and Blick, 1971). The Cundiyo flow is a tholeiite, whereas the Bishop's Lodge flow is alkali olivine basalt (figures 31, 32).

Basaltic lavas erupted during the late Miocene consist of olivine tholeiite and alkali olivine basalt. These lavas include the flow at Chili and the Rio del Oso dikes, located in the northern central Española basin, and the Lobato Basalt on the northeastern edge of the Jemez Mountains. The Chili flow (9.6 m.y.; Baldrige, Damon, and Bridwell, unpublished data) is interbedded in the Chamita Formation (Hemphillian) of the Santa Fe Group (Galusha and Blick, 1971). The Rio del Oso Dikes (9.7 m.y.; Baldrige, Damon, and Bridwell, unpublished data) belong to the same intrusive episode. A sill extending from one of these dikes intrudes the Chama-El Rito Formation of the Santa Fe

Group. The Lobato Basalt has been dated by Bailey et al. (1969) at 7.4 m.y. The Lobato Basalt and the flow occurring at Chili are both olivine tholeiite, whereas the Rio del Oso sill is slightly nepheline normative.

In summary, lavas extruded during latest Oligocene and early Miocene range in composition from olivine nephelinite to quartz tholeiite. Very undersaturated lavas (nephelinite) occur at the northern and southern margins of the Española basin. Flows within the basin or near its eastern margin are both tholeiite and alkali olivine basalt. Late Miocene lavas also consist of both tholeiite and alkali olivine basalt. Hence no well-defined trend in composition exists over the time during which rifting has occurred. Differences in composition may perhaps be related to local structural environment. All of the pre-Pliocene lavas are generally lower in alkalis than the later lavas of the Cerros del Rio, Santa Ana Mesa, and El Alto.

COMPARISON WITH BASALTIC ROCKS OF THE SOUTHWESTERN U.S.

Many of the Plio-Pleistocene basalts of the central Rio Grande rift are characteristic of the late Cenozoic basalts from other structural provinces of the southwestern U.S. For example, basaltic andesite similar in composition to that occurring in the Cerros del Rio and Wind Mesa is widespread throughout the Basin-and-Range province (Leeman and Rodgers, 1970). It also occurs in the western Grand Canyon region (Best and Brimhall, 1970) and in the San Juan Mountains (Lipman and Mehnert, 1975). In neither the Basin-and-Range province nor the western Grand Canyon region are there rocks similar to the latite-andesite that is here associated with the basaltic andesite, although such rocks are

reported from the San Juan Mountains (Lipman and Mehnert, 1975).

Basanite, alkali olivine basalt, and hawaiite similar to those of the central Rio Grande rift characterize the late Cenozoic volcanism of the Basin-and-Range province (Leeman and Rodgers, 1970). Similar lavas also are dominant in the western Grand Canyon region (Best and Brimhall, 1970) and are widespread throughout the southern Rocky Mountains, where they are included as silicic alkali basalts by Lipman and Mehnert (1975).

Basalt similar to the group A olivine tholeiites occurs at various places within the southern Rocky Mountains, specifically at Los Mogotes Volcano in the southern San Juan Mountains and from the Cimarron Mountains and the High Plains of northeastern New Mexico (e.g., Lipman and Mehnert, 1975). This basalt is called "silicic alkalic basalt" by Lipman and Mehnert (1975) in recognition of its high $(\text{Na}_2\text{O}+\text{K}_2\text{O})$. This high-alkali olivine tholeiite is not characteristic of the Basin-and-Range province nor of the Colorado Plateau.

Lavas of the Albuquerque Volcanoes have a composition which is unique to the rift. They are distinct from the lavas of the Cerros del Rio, Santa Ana Mesa, and El Alto fields in their significantly lower $(\text{Na}_2\text{O}+\text{K}_2\text{O})$ and generally lower SiO_2 (~ 3.5 and 50-51 weight percent, respectively). Also they are 5-10% lower in modal plagioclase and $\sim 10\%$ higher in modal hypersthene than either the group A tholeiite or the group B basaltic andesite. Rocks from the Albuquerque Volcanoes are most similar to olivine tholeiite from the Servilleta Formation of the Taos Plateau, although they have slightly higher alkalis and lower Al_2O_3 than the Servilleta basalts (Aoki, 1967; Lipman, 1969; Lipman and Mehnert, 1975).

Of the pre-Pliocene lavas, the olivine nephelinite is distinctive. Similar lavas are not known from other regions of the southwestern U.S. Within the rift these lavas were erupted only during the earlier phase of volcanism (19-25 m.y.) and are not characteristic of the pre-Pliocene volcanism in general.

PETROGENESIS

Evolution of rocks from the Cerros del Rio, Santa Ana Mesa, and El Alto volcanic fields

Of the four major groups of rocks occurring in the Cerros del Rio, Santa Ana Mesa, and El Alto volcanic fields, two of these, the group B basaltic andesite and latite-andesite and the group D alkali olivine basalt and hawaiite, show a large compositional and petrographic variation. The origin of the variation within these two groups is discussed with reference to the one-atmosphere liquidus tetrahedron anorthite-forsterite-SiO₂-diopside (figure 34), which is analogous to the saturated and oversaturated part of normative basalt tetrahedron of Yoder and Tilley (1962).

Basaltic andesite and latite-andesite

The most distinctive compositional trend shown by the lavas from the central Rio Grande rift is that extending from the group B basaltic andesite to the latite-andesite. This series of rocks is very unusual in that SiO₂ changes by a very large amount between the two end members relative to the amount of change in other components. This large variation in SiO₂ is reflected in the large amount of quartz (about 12 percent) that must be added to a melt with the composition of -230 in order

to reach a composition corresponding to -036. In addition, a minimum of 6 percent of sodic plagioclase must also be added. This amount of quartz and plagioclase corresponds to about one-third of the total amount of material which must be added to and subtracted from -230 to reach -036 (table 6). Hence it is clear that in very large measure this series of rocks evolved by assimilation of these phases.

However the variation diagrams (figure 15) and least-squares modeling (table 6) show that other phases must be removed from -230 in order to derive a composition equivalent to -036. Removal of these phases could be accomplished in two alternate ways, yielding different results. In the first case, batches of magma with the composition of -230 could assimilate different amounts of quartz (plus a small amount of sodic plagioclase). The compositions of these magmas would thus lie at various points along a mixing line toward (quartz + plagioclase). At each point fractional crystallization would begin, and the melt composition would move away from whatever phase or phases were on the liquidus. In the second case, fractionation of phases occurs concomitantly with assimilation of quartz and plagioclase. The melt composition descends (with falling temperature) along phase boundaries, defining a path similar to that produced by normal fractional crystallization. Several lines of evidence suggest that the series of compositions from -230 to -036 represents assimilation of quartz and plagioclase and concomitant fractional crystallization in the liquidus system represented by figure 34. First, a mixing line between -230 and quartz (plus a small amount of plagioclase) will cross the olivine and pyroxene liquidus fields. Therefore (ignoring spinel), olivine would be the

first phase to crystallize in the most magnesian liquids--those which have assimilated only a small amount of quartz. From liquids which have assimilated more quartz and whose compositions therefore lie in the pyroxene field, pyroxene rather than olivine would be the first phase to crystallize. These liquids could not have had olivine component subtracted from them. However the least-squares modeling (described in a previous section) indicates that the silicic members of this series have undergone fractionation of both clinopyroxene and olivine.

Second, the presence of olivine, plagioclase, and clinopyroxene coexisting as phenocrysts in the basaltic andesite indicate that the melt was multiply saturated, hence crystallized along phase boundaries. A mixing line is likely to traverse single phase fields, hence crystallization would produce only a single phenocryst phase, at least until each batch had crystallized far enough for the melt compositions to reach phase boundaries.

These considerations suggest that this sequence does not represent a mixing line but rather that assimilation in combination with fractional crystallization has occurred. For this particular liquidus system and for a composition similar to -230, this case could give rise to a sequence of liquid compositions indistinguishable from that produced by fractional crystallization alone. The sequence of phases observed as phenocrysts in the basaltic andesite and latite-andesite (see figure 12) is compatible with fractional crystallization in this basaltic system. For example, petrographic observations indicate that spinel is an early (probably the first) phase to crystallize, followed closely by olivine and plagioclase. Intermediate compositions lie approximately

along the forsterite-anorthite-diopside and anorthite-diopside-enstatite (isobaric) univariant lines (figure 34). These positions are in agreement with the presence of augite and hypersthene phenocrysts and the absence of olivine in the intermediate members of this series. Concomitant assimilation of either solid rock or magma and fractional crystallization would be expected to add components other than those of quartz and sodic plagioclase. Yet least-squares modeling can explain the evolution of these rocks totally in terms of the observed solid phases.

Hence in summary, a major factor in the evolution of the basaltic andesite and latite-andesite trend is assimilation of quartz and sodic plagioclase. The heat required to assimilate this material was probably derived from the concomitant crystallization of other (mafic) phases from the melts, such that both assimilation and fractional crystallization occurred simultaneously with decreasing temperature.

Alkali olivine basalt and hawaiite

The lavas of the group D alkali olivine basalt and hawaiite constitute at least three separate sets of compositions (figure 19) rather than a single, well-defined series as do the basaltic andesite and latite-andesite. Least-squares calculations (table 6) show that within each set the rocks evolve by removal of olivine, plagioclase, and clinopyroxene (the observed phenocrysts). Though partially resorbed grains of quartz may be present in some of these rocks, it is not measurably required in the evolution of these rocks. The fact that many compositions cannot be related to each other by addition or subtraction of these phases, and in particular that none of the hawaiitic lavas can be

related to individual alkali olivine basaltic lavas suggests that other phases (at depth) are being added to or subtracted from these melts in processes such as crustal contamination or high pressure fractional crystallization.

The observed phenocryst mineralogy is compatible with fractional crystallization in the basaltic liquidus tetrahedron (figure 34). For example, spinel is the earliest phase to crystallize, followed by olivine and plagioclase. As crystallization continues the liquid proceeds to the plagioclase-olivine-clinopyroxene univariant line, where clinopyroxene becomes a phenocryst phase. Hence, although individual sets of compositions cannot be related by low pressure fractional crystallization, the compositions within each set can be.

Origin of xenocrysts

The importance of the xenocrysts which are present in the lavas of the Cerros del Rio, Santa Ana Mesa, and El Alto fields has already been emphasized. The quartz and sodic plagioclase xenocrysts play a major role in the evolution of the group B basaltic andesite and latite-andesite. In addition, large, partially resorbed magnesian Ti-augite grains occur in one of the hawaiite lavas (-283). The origin of these xenocrysts is a difficult problem, one which has not been satisfactorily solved.

Quartz. Quartz is a common "xenocryst" phase in basalt, basaltic andesite, and andesite from many parts of the world and from different tectonic environments (see, for example, Carmichael et al., 1974; Eichelberger, 1978). Quartz-bearing mafic lavas are a particularly common feature of the western United States (e.g., Doe et al., 1969;

Lipman, 1969; Leeman and Rodgers, 1970; Best and Brimhall, 1970; Lipman and Mehnert, 1975; Stormer, 1972). Opinions differ as to whether the quartz is a high-pressure phenocryst phase, or a contaminant "xenocryst" phase.

Arguments favoring a contaminant origin attribute the quartz either to silicic crustal rocks which were incorporated into the melt or to phenocrysts from a silicic magma which was mixed into the basaltic magma. The first argument is extrapolated from the existence of rare xenoliths of granitic rocks in some of these lavas. For example, Doe et al. (1969) postulated that lower crustal granitic rocks or upper crustal Precambrian or Paleozoic rocks had been assimilated to explain a correlation between the presence of quartz and plagioclase xenocrysts and relatively unradiogenic lead for the southern Rocky Mountains. However, subsequent work (Everson, personal communication) for the Basin-and-Range province and Colorado Plateau does not substantiate such a correlation. The second argument is based on disequilibrium phenocryst assemblages and on the fact that in some rocks the quartz contains inclusions of rhyolite glass (e.g., Eichelberger, 1978).

Arguments favoring a high-pressure cognate origin for the quartz are based on the fact that: (1) quartz usually occurs as discrete, single grains; where it occurs in polygranular aggregates, these aggregates are composed solely of quartz; (2) though nearly always embayed and jacketed by acicular clinopyroxene, some grains have a distinct bipyramidal habit (Best and Brimhall, 1970); (3) thermodynamic calculations by Nicholls et al. (1971) and by Marsh and Carmichael (1974) show that quartz could be in equilibrium with basalt and basaltic andesite

melts at elevated pressures (18-27 kb at 1100°C); (4) experiments show that quartz is an intermediate liquidus phase in high-Al olivine tholeiite and calc-alkaline andesite at high pressure (>10 kb; Green and Ringwood, 1968; Green, 1972).

In this present study several additional observations have been made which bear on the origin of modal quartz in these rocks. First, although the quartz is usually deeply embayed, rare grains are euhedral in shape (figure 5C). Second, within these rocks, the presence of quartz is restricted to certain compositions. Quartz occurs mainly in the group B basaltic andesite (and related latite-andesite), which have high Na_2O , K_2O , SiO_2 , and normative albite compared to other basaltic rocks of the central rift. Quartz also occurs sparsely in some of the group D alkali olivine basalt and related hawaiite, which also have high Na_2O and normative albite. Modal quartz is never found in the group A olivine tholeiite or in lavas from the Albuquerque Volcanoes, Isleta, Wind Mesa, or the Cat Hills. Best and Brimhall (1970) also found that, in the western Grand Canyon region, the presence of modal quartz was restricted entirely to the basaltic andesite (Middleton basalts) highest in alkalis and silica. The fact that the occurrence of quartz is not uniformly or randomly distributed over the various compositional groups suggests that the formation of quartz is a sensitive function of bulk composition at some temperature and/or pressure. If these compositions are high in silica and alkalis because they are contaminated, then the composition of the uncontaminated, parental basalts from which they are derived is unknown. It cannot be group A, since contamination of group A basalt with quartz and plagioclase will not yield group B compositions.

Also, no quartz or resorbed sodic plagioclase grains are observed in the group A lavas. Derivation of the quartz by assimilating variable amounts of either silicic rock or magma into a magma with the composition of -230 is excluded on the basis of mass balance constraints, i.e., the variation diagrams (figure 15) do not support two-component mixing. Similarly, a combination of mixing and fractional crystallization is not likely to result in removal of the required phases or in a correct mass balance, as discussed in a previous section. Hence on the basis of these observations and those of previous investigators it is suggested that modal quartz in these basaltic rocks may be a high-pressure phenocryst phase. As such it would be cognate in the most magnesian basaltic andesite but xenocrysts in the more evolved rocks of this series. A significant uncertainty remains with the experimental data, however. First, quartz and magnesian olivine cannot coexist stably in a melt at any pressure or temperature. If quartz is a stable phenocryst phase under certain conditions, then olivine cannot be. Since the most plausible source rock for these basalts includes major amounts of magnesian olivine, these basalts must be capable of coexisting in equilibrium with mantle olivine under some conditions. However they need not be capable of precipitating olivine under all pressure or temperature conditions, or even under the conditions of their original formation if removed from their residual material. If olivine in the source rock melts incongruently or is in reaction relationship with melt such that $\text{Mg-olivine} + \text{liquid}_A \rightarrow \text{clinopyroxene} + \text{liquid}_B$, the derivative liquid will not be capable of precipitating olivine under identical conditions if removed from the residual phases. Indeed such

reaction relationships probably occur in formation of basaltic liquids, as discussed by Green (1970) and in detail by Yoder (1976, chap. 8).

Even in basaltic compositions where quartz is precipitated at high pressure, quartz is never the first phase (or the second phase after plagioclase) to appear on the liquidus (Green and Ringwood, 1968; Green, 1972). Quartz in equilibrium with these melts coexists with plagioclase and with either clinopyroxene or garnet. Only in compositions as silicic as dacite is quartz the first phase to appear on the liquidus. If this quartz is a high-pressure phenocryst phase, then either the clinopyroxene (or garnet) that coexists with it has not been recognized in those rocks or the higher density clinopyroxene (or garnet) phenocrysts have been separated from the quartz and feldspar gravitatively as the magma ascended to the surface. An additional possibility is that in basaltic andesite of the composition of -230 quartz appears earlier on the liquidus at high pressure than in the compositions investigated by Green and Ringwood (1968) and Green (1972).

In summary, arguments may be cited favoring both the assimilation and the high-pressure phenocryst origin for the quartz and none are conclusive. However the bulk of the evidence, both textural and chemical, seems to indicate that the quartz xenocrysts are high-pressure phenocrysts.

Plagioclase. Partially resorbed, tabular grains of sodic plagioclase commonly accompany quartz grains in basalts from the western United States (e.g., Doe et al., 1969; Lipman, 1969; Stormer, 1972). In the basaltic rocks from the central Rio Grande rift, sodic plagioclase (typically An_{30-50}) is abundant, along with quartz, in the

basaltic andesite and occurs sparsely, with or without quartz, in the alkali olivine basalt and hawaiite. These plagioclase grains are rounded and embayed. They are wormy or cloudy due to numerous minute inclusions where the grains were invaded by the host melt, which has subsequently crystallized to groundmass pyroxene, plagioclase, and magnetite.

Experimental work (e.g., Green and Ringwood, 1967a; Green, 1967) shows that plagioclase crystallizing from basaltic magma becomes increasingly sodic with increasing pressure (up to the stability limit of plagioclase at 20-25 kb), as aluminum enters pyroxene via the reaction $\text{CaAl}_2\text{Si}_2\text{O}_8 = \text{CaAl}_2\text{SiO}_6 + \text{SiO}_2$. In addition, other evidence such as the lack of accompanying xenolithic aggregates and the fact that these xenocrysts invariably occur as single crystals also suggests that they are high-pressure phenocrysts rather than contaminating material (see also Stormer, 1972). Hence it is likely that this plagioclase, as well as the quartz which it typically accompanies, is a relict high-pressure phenocryst phase. This plagioclase is in the process of reacting with the melt to yield plagioclase of a more calcic composition.

Pyroxene. Large, partially resorbed grains of augite occur in one hawaiitic lava (-283). These are rounded and embayed, and wormy due to abundant inclusions of groundmass material. Compositionally, this augite is aluminous and titaniferous ($\text{Al}_2\text{O}_3 \approx 3.91$ weight percent; $\text{TiO}_2 \approx 0.83$), similar to the augite phenocrysts in this rock; its Mg/Mg+Fe is slightly greater than but overlaps with that of the phenocrysts (see figure 16). No other inclusions occur in this rock to suggest that this melt has undergone contamination. Experiments show that at pressures

greater than about 12 kb clinopyroxene appears on the liquidus of olivine tholeiite and alkali olivine basalt earlier than olivine (e.g., Green and Ringwood, 1967b). Hence this augite, too, is interpreted as a relict high-pressure phenocryst phase.

Possible role played by high-pressure fractional crystallization

Since a series of rock compositions does not exist which is unambiguously derived by high-pressure fractional crystallization, it is difficult to assess the overall role of high-pressure fractional crystallization in the evolution of these basalts. The presence of phases which may be relict high-pressure phenocrysts argues that at least some may have occurred. In these lavas the effect of possible high-pressure phenocrysts is seen most clearly in the addition of these phases to the lavas. For example, it seems very likely that hawaiite -283 owes its high Mg-value to the presence of these (high-pressure) magnesian augite phenocrysts. The effect of removing this augite component from -283 is shown in figure 12 (dashed arrow).

If the quartz and sodic plagioclase originate as high-pressure phenocrysts, then the effect of high-pressure phases is greatest in the group B basaltic andesite and related latite-andesite. The minimum amount of quartz and feldspar that must be added to the basaltic andesite to derive the most silicic latite-andesite is equal to about 17% of the original amount of basaltic andesite. This amount is about one-third of the total amount of material that is added to or subtracted from the melt. Hence the effect of possible high-pressure phases on the overall range of bulk compositions present is great.

Crystallization paths in the system Mg_2SiO_4 - $CaAl_2Si_2O_8$ - SiO_2 - $CaMgSi_2O_6$

An important feature of most of the olivine tholeiite from the central Rio Grande rift is the absence of the olivine-low-Ca pyroxene reaction relationship. Lavas of the Albuquerque Volcanoes constitute the exception to this feature in that, while olivine is a stable phenocryst phase, both augite and a low-Ca pyroxene are present in the groundmass. Consideration of crystallization paths in the 1-atmosphere basalt liquidus system Mg_2SiO_4 - $CaAl_2Si_2O_8$ - SiO_2 - $CaMgSi_2O_6$ (figure 34) suggests an explanation for the absence of this reaction. The early crystallization of spinel is followed by the crystallization of olivine and plagioclase as described previously. Crystallization proceeds along the forsterite-anorthite surface, then continues along the forsterite-anorthite-diopside isobaric univariant line until the rock is quenched. Probably the melt never reaches the forsterite-anorthite-diopside-enstatite invariant point, where reaction of olivine to low-Ca pyroxene would occur.

Tholeiitic lavas from the Albuquerque Volcanoes are slightly lower in normative anorthite relative to normative forsterite plus SiO_2 than other (higher alkali) tholeiitic lavas from the central Rio Grande rift (cf. figures 4 and 21). This difference, though slight, is probably very significant for the modal mineralogy. These lavas follow a similar crystallization path to that described above. However, because of their slightly different starting compositions, the liquid composition actually proceeds to the forsterite-anorthite-diopside-enstatite isobaric invariant point where orthopyroxene crystallizes as a late groundmass phase. For crystallization to proceed further olivine must become

unstable. This reaction is the characteristic olivine + Si-rich melt = low-Ca pyroxene reaction of tholeiitic basalt. For the more alkali-rich tholeiitic lavas whose compositions lie farther from the forsterite-anorthite-diopside-enstatite invariant point, crystallization seldom or never reaches this point. Hypersthene might be present only under conditions where slower cooling rates obtain such that all the melt crystallizes and none remains as glass.

Petrogenesis of mafic lavas

Comparison with experimental studies

Two approaches will be used to attempt to determine the conditions of origin of these magmas: (1) comparison with relevant experimental studies, and (2) thermodynamic calculations of the silica and alumina activities of the melts, and of the depth at which these melts could be in equilibrium with mantle phases.

In trying to relate these lavas to experimental studies two significant problems arise. First, none of the lavas is primitive. A primitive (or primary) magma is one which has been generated by partial melting of the upper mantle and has been erupted to the earth's surface without further modification. A generally-used major-element criterion of primitive composition is $Mg/Mg+Fe^{2+} = 0.68-0.72$ (Irving and Green, 1976). Most mafic lavas which, from experiments, are known to be in equilibrium with pyrolite at depth have approximately these Mg-values (Ringwood, 1975).

Primitive magmas are relatively rare on the earth's surface, since fractional crystallization (at both high and low pressure) and other processes readily modify the original composition during ascent. Since

none of the rocks from the central Rio Grande rift has Mg-values greater than about 65, none is genuinely primitive in composition; all have undergone at least some compositional modification. Hence the most mafic (i.e., parental) lavas of each group are used in comparison with experimental data.

The second problem is that experimental studies have not been done on compositions closely similar to those of basalts from the central Rio Grande rift. Experiments to date on basaltic rocks have focussed generally on rocks from ocean basins. These are characterized by lower SiO_2 , higher $\text{Mg}/\text{Mg}+\text{Fe}$, lower Al_2O_3 , and lower alkalis. Experiments on more silicic rocks (basaltic andesite, andesite, dacite, etc.) have concentrated on calc-alkalic and related magmas, which are higher in Al and Ca and lower in alkalis than the Rio Grande rift lavas. Hence extrapolation from these experiments must of necessity be general.

The experiments by Green and Ringwood (1967b) set the framework for discussing the origin of tholeiite and alkali olivine basalt. They found that partial melting of dry pyrolite at pressures of 5-10 kb gives rise to high-Al basalt. With less than about 18 percent partial melting these melts are alkali olivine basalt; with greater partial melting they are olivine tholeiite (see, for example, Green and Ringwood, 1967b; Green, 1970a, b). At higher pressures (10 to 20 kb), alkali olivine basalt is produced by about 5-15 percent partial melting, and olivine tholeiite (with alkalic affinities) with >15 percent melting. At still greater pressures, the melts produced are strongly picritic, and are undersaturated except for large amounts of partial melting (>30 percent). Probably the mantle contains about 0.1 weight percent of water

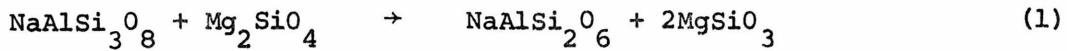
(Ringwood, 1975). The principle effect of this water at depths less than about 75 km is an expansion and depression of the temperature over which melting of pyrolite occurs. For example, for an average tholeiitic melt, the H_2O content of the melt would be <0.5 weight percent. This water content would depress the tholeiite liquidus <50°C below the anhydrous liquidus. Hence no significant effect on melting equilibria occurs, and the sequence discussed above is not changed.

Thompson (1974) has conducted anhydrous melting experiments on an alkali olivine basalt and a nepheline-normative, aluminous "transitional basalt" from Skye. The alkali olivine basalt is somewhat closer in composition to the group C and D basalts from the Rio Grande rift. This composition, though low in SiO_2 (46.12 weight percent), has higher Al_2O_3 (13.94 percent) and alkalis (3.68 percent), and lower normative nepheline (2.8 percent) than the alkali olivine basalts used by Green and Ringwood (1967b). This basalt is in equilibrium with olivine, low-Ca pyroxene, and high-Ca pyroxene at about 17 kb. Spinel was not present near the liquidus, probably due to the low f_{O_2} of the experimental charges. Thompson (1974) concluded that this basalt could be derived from partial melting of Fe-rich spinel pyrolite at a pressure of about 17 kb. This result is in reasonable agreement with the studies of Green and Ringwood (1967b). The transitional basalt is similar to the alkali olivine basalt but is lower in magnesium. It has olivine, plagioclase, and clinopyroxene on the liquidus at about 11 kb, and could have been derived from the alkali olivine basalt by fractionation of these phases.

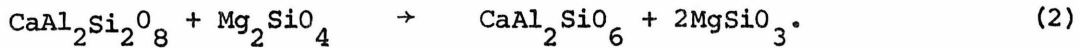
The composition of the volatile phase (i.e., CO_2 and H_2O) in the mantle has a major effect on the composition of melts generated within the mantle. In particular, a high $\text{CO}_2/(\text{CO}_2 \text{ and } \text{H}_2\text{O})$ results in the formation of liquids which are significantly more silica-poor than liquids derived in the absence of volatiles or in the presence of H_2O alone (Eggler, 1978). However, the effect of the volatile phase on basaltic magmas is insignificant and will probably not change these depth ranges (Eggler, 1978).

Hence the results of these experimental studies indicate that the tholeiitic rocks most likely originate from greater than 18 percent partial melting of pyrolite at a pressure of 10 kb (35 km) or perhaps slightly greater. The source rock is likely to be spinel pyrolite rather than plagioclase pyrolite. The alkali olivine basalt and basanite may be derived from approximately 10 percent partial melting of spinel pyrolite at pressures of about 15-20 kb (50-70 km). The lower limits of these ranges are the preferred pressures (depths) for the following reasons. In general the Al-content of the experimental melts is greatest with low pressures and smaller amounts of partial melting. At pressures <10 kb, aluminum in pyrolite is contained in plagioclase, which is the first phase to melt completely. Melting under these conditions yields high-Al basalt such as mid-ocean ridge basalt (e.g., Green and Ringwood, 1967b). Since the crust-mantle boundary is probably at a depth of about 35 km (10 kb) under the Rio Grande rift, plagioclase pyrolite is probably not present. Above about 10 kb Al exists mainly in spinel. However, the transition from plagioclase- to spinel-pyrolite is not sharp.

The following equilibria obtain:



albite forsterite jadeite enstatite



anorthite forsterite Ca-Tschermak's
molecule enstatite

Since these phases are solid solutions, these equilibria occur over a finite pressure interval. Therefore, even though at pressure >10 kb spinel is the dominant Al-bearing phase, diminishing amounts of plagioclase may be present. Even where plagioclase is not present, melts are preferentially enriched in Al over the residual solid material because spinel and high-Ca pyroxene are the first phases to melt completely. With greater degrees of partial melting, progressively larger fractions of low-Ca pyroxene and of olivine enter the melt (e.g., Green and Ringwood, 1967b; Mysen and Kushiro, 1977).

The experimental data are not complete enough to attempt to resolve the various tholeiite groups (e.g., groups A and B, the Albuquerque Volcanoes, etc.) or the nepheline-normative groups from each other in terms of depth of origin or amount of partial melting.

Thermodynamic approach

A second approach used to estimate the depth of origin of these magmas is based on the activities of silica and alumina of the melt and their extrapolation to mantle pressure and temperature (Nicholls et al., 1971; Nicholls and Carmichael, 1972). This approach depends on

the fact that the activity of a component in a melt can be defined by the mineral assemblage with which it is in equilibrium.

The activity of a component i in a melt may be expressed as

$$(\log a_i)^{P,T} = \log X_i + \frac{\phi_i}{T} + \frac{V_i - V_i^{\circ}}{2.303RT} (P-1), \quad (3)$$

where X_i is the mole fraction of i in the melt, V_i is the molar volume of i in the melt, V_i° is the molar volume of pure liquid i , R is the gas constant in calories per mole per degree, and T is temperature in degrees Kelvin. The term ϕ_i is derived from the activity coefficient of i in the melt and is defined by

$$\log a_i - \log X_i = \log V_i = \frac{\phi_i}{T}. \quad (4)$$

The activity of component i in the melt is defined by the composition of the minerals with which it is in equilibrium. For example, for the reaction Mg_2SiO_4 (olivine) + SiO_2 (melt) = $2MgSiO_3$ (pyroxene) the activity of SiO_2 as a function of P and T is given by

$$\begin{aligned} (\log a_{SiO_2}^{melt})^{P,T} &= \frac{(\Delta G_{reaction}^{\circ})^{1 \text{ atm.}}}{2.303RT} + \frac{\Delta V_{reaction}^{\circ}}{2.303RT} (P-1) \\ &+ 2 \log a_{MgSiO_3}^T - \log a_{Mg_2SiO_4}^T. \end{aligned} \quad (5)$$

If ΔC_p is zero for this reaction, then

$$\frac{\Delta G_r^P}{2.303RT} = \frac{\Delta G_r^{\circ} + \Delta V_r^{\circ}}{2.303RT} (P-1).$$

This term is a linear function of $1/T$ and may be expressed as

$$\frac{\Delta G_R^P}{2.303RT} = \frac{A}{T} + B + \frac{C(P-1)}{T} .$$

A and B are constants derived by least-squares analysis of the variation of $\Delta G_R^P/2.303RT$ with temperature for each reaction at one atmosphere pressure. C is equal to $\Delta V_r^O/2.303R$ at 1 atmosphere and 298°C. The reactions used in this study are listed in table 7 together with the values of their constants A, B, and C determined by Nicholls and Carmichael (1972) and Bacon and Carmichael (1973). The activity models used for the various phases are also given in table 7.

Calculation of the unique pressure and temperature at which a given component i could be in equilibrium with a given mantle assemblage at depth requires first the calculation of a_i of the melt from the appropriate buffer assemblage at 1 bar pressure. In practice, SiO_2 and Al_2O_3 are the best choices of components since thermodynamic data are available for the appropriate phases. Once a_{SiO_2} and $a_{\text{Al}_2\text{O}_3}$ have been determined, ϕ_{SiO_2} and $\phi_{\text{Al}_2\text{O}_3}$ can be calculated. Then $(\log a_{\text{SiO}_2})^{P,T}$ and $(\log a_{\text{Al}_2\text{O}_3})^{P,T}$ may be expressed by equation 3. Expressions for $(\log a_{\text{SiO}_2})^{P,T}$ and $(\log a_{\text{Al}_2\text{O}_3})^{P,T}$ are also derived from the appropriate mantle assemblages by means of equation 5. The two sets of equations for SiO_2 and Al_2O_3 may then be solved simultaneously for the unique pressure and temperature at which the melt equilibrated with the mantle refractory phases.

This approach has not had satisfactory results for these rocks. Two significant problems are inherent in the application of this method.

First, the activities of silica and alumina can only be determined for the groundmasses of these rocks, since the appropriate phases for the buffer reactions are not present as phenocrysts. The compositions of these groundmass phases, and the activities of coexisting SiO_2 and Al_2O_3 , reflect the increased amount of crystallization. Second, and more seriously, even the most parental rocks are not primitive. Significant fractional crystallization has probably occurred before the melts reached the surface, driving the melt compositions to higher silica and alumina activities.

The activities of silica and alumina were calculated for rock -087, which is typical of the group A olivine tholeiite. Values of T and f_{O_2} , given in a previous section, are 1051°C and $10^{-10.2}$. These are necessarily groundmass values, since coexisting opaque phases do not occur as phenocrysts. Additional input data were: $\Delta G_r^{\text{O}} = 22387 \text{ cal.}$, $a_{\text{fay}} = 0.235$, and $a_{\text{mt}} = 0.376$. The resulting value of a_{SiO_2} is 0.896. With this value for the activity of silica, the activity of alumina can be calculated from equation 2. Additional input data are $\Delta G_r^{\text{O}} = -25,453$, $a_{\text{an}} = 0.518$, and $a_{\text{di}} = 0.501$. The resulting $a_{\text{Al}_2\text{O}_3}$ is 3.54×10^{-5} .

These values for the activities of silica and alumina can be used to derive the constants ϕ_{SiO_2} and $\phi_{\text{Al}_2\text{O}_3}$. Even though a_{SiO_2} and $a_{\text{Al}_2\text{O}_3}$ were derived from groundmass compositions and groundmass temperature, a more realistic temperature for calculation of ϕ would be that before significant crystallization occurred. Hence a temperature of 1175°C was obtained for -087 from the composition of olivine phenocrysts by the method of Roeder and Emslie (1970). Their method assumes that

olivine is the only phase coexisting with the melt. For -087 this assumption is not strictly valid, since a small amount of Cr-spinel occurs as inclusions within olivine and since plagioclase phenocrysts coprecipitate with olivine. However this temperature is probably more realistic for calculation of ϕ than the groundmass temperature derived from coexisting magnetite and ilmenite. Using $X_{\text{SiO}_2} = 0.546$, $X_{\text{Al}_2\text{O}_3} = 0.100$, and $T = 1175^\circ\text{C}$, the computed value of ϕ_{SiO_2} is 312 and of $\phi_{\text{Al}_2\text{O}_3}$ is -5000. For SiO_2 and Al_2O_3 , equations 3 have the form

$$\log a_{\text{SiO}_2}^{P,T} = \log X_{\text{SiO}_2} + \frac{\phi_{\text{SiO}_2}}{T} + \left(-\frac{0.0047}{T} + 1.34 \times 10^{-6}\right) \cdot (P-1) \quad (6)$$

and

$$\log a_{\text{Al}_2\text{O}_3}^{P,T} = \log X_{\text{Al}_2\text{O}_3} + \frac{\phi_{\text{Al}_2\text{O}_3}}{T} + \left(\frac{0.1806}{T} - 0.67 \times 10^{-4}\right) \cdot (P-1). \quad (7)$$

The final step is to assume that -087 equilibrated with a mantle assemblage of olivine, orthopyroxene, clinopyroxene, and spinel. The activities of silica and alumina are defined by reactions 3 and 4, table 7. These reactions yield

$$\log a_{\text{SiO}_2}^{P,T} = -\frac{1034}{T} + 0.597 - \frac{0.0424}{T} (P-1) + 2 \log a_{\text{en}} - \log a_{\text{fo}} \quad (8)$$

and

$$\log a_{\text{Al}_2\text{O}_3}^{P,T} = -\frac{8131}{T} + 2.632 + \left(\frac{0.1344}{T} - 0.723 \times 10^{-4}\right) (P-1) + \log a_{\text{en}} + \log a_{\text{Sp}} - \log a_{\text{fo}}. \quad (9)$$

The activities of these phases are $a_{fo} = 0.81$, $a_{en} = 0.90$, and $a_{sp} = 0.75$. Equation 8 may be set equal to equation 6, and equation 9 equal to equation 7 to solve for the loci of pressures and temperatures at which -087 could have been in equilibrium with this mantle assemblage. The intersection of the a_{SiO_2} and $a_{Al_2O_3}$ equilibrium lines defines the unique P and T at which this magma could have equilibrated with the mantle assemblage. For Al_2O_3 the resulting values are 724°C at 8 kb and 828°C at 15 kb. For SiO_2 , $T = 1666^\circ C$ at 8 kb. These values for Al_2O_3 are unrealistically low, and the values for SiO_2 are far too high. The intersection of these two equilibrium lines occurs at negative pressure.

This approach would give a more reasonable solution if a SiO_2 were significantly lower (about 0.28). The high silica activity may be due to the fractionated bulk composition of -087 and to the fact that the activity was determined from groundmass phases. These calculations are not useful in placing pressure and temperature constraints on the origin of this magma. They do illustrate the difficulty of this approach and the extreme care that should be exercised in the interpretation of thermodynamic data.

Isotopic evidence regarding magma sources

Isotopic data on volcanic rocks from the Rio Grande rift are at present sparse. Strontium abundances and isotopic compositions of basalts from several structural provinces within New Mexico, including the Rio Grande rift, were measured by Kudo et al. (1971). These data show that $^{87}Sr/^{86}Sr$ of nepheline-normative rocks ranges from 0.7028-0.7044 and strontium abundance from 380-1400 ppm. $^{87}Sr/^{86}Sr$ for the

tholeiitic rocks ranges from 0.7029-0.7078 and Sr abundances are generally lower (200-600 ppm). Their data may suggest that many of the hypersthene-normative basalts are derived from a mantle source with higher $^{87}\text{Sr}/^{86}\text{Sr}$ than the nepheline-normative basalts. Within the Rio Grande rift, tholeiitic rocks are generally confined to the northern and central portions of the rift, whereas nepheline-normative rocks occur in the central and southern parts.

Doe et al. (1969) found for the southern Rocky Mountains that lead isotopic ratios of basalts containing xenocrysts of partially-resorbed plagioclase and quartz were less radiogenic than basalts free of these megacrysts. This correlation was interpreted to result from assimilation either of lower crustal granitic rocks or of upper crustal Precambrian or Paleozoic rocks. However, more recent work does not confirm that the xenocryst-bearing lavas are consistently less radiogenic than the xenocryst-free lavas (J. Everson, personal communication). Therefore the lead isotopic data do not suggest a simple assimilation model for these basalts.

The lead data of Everson and Silver (1978) show that late Cenozoic basaltic rocks from the rift north of Socorro and along the international border lie on Colorado Plateau regression lines, suggesting that they were derived from Precambrian continental lithosphere. These rocks north of Socorro are relatively unradiogenic ($^{206}\text{Pb}/^{204}\text{Pb} = 17.3-18.5$). Between Socorro and Las Cruces the isotopic compositions are among the most radiogenic in the southwestern U.S. ($^{206}\text{Pb}/^{204}\text{Pb} = 19.2-19.6$) and lie off the Colorado Plateau isochrons. They have been derived from sources similar to alkalic oceanic island basalts and very

different from those yielding basalts in the rift to the north and south, and from the adjacent Colorado Plateau and High Plains. These data suggest that "ocean"-like deeper mantle material is upwelling and penetrating the lithosphere between Socorro and Las Cruces.

Both $^{87}\text{Sr}/^{86}\text{Sr}$ and $^{143}\text{Nd}/^{144}\text{Nd}$ were measured on a group D alkali olivine basalt from El Alto (74-005) by DePaolo and Wasserburg (1976). The value of $^{87}\text{Sr}/^{86}\text{Sr}$ is 0.70436 ± 12 , which is at the very uppermost end of the range for nepheline-normative basalts determined by Kudo et al. (1971). Nd-Sm data yield a value $\epsilon_I^{\text{CHUR}} = 0.2 \pm 0.7$. This value is typical of continental basalts and suggests that this magma was derived from an ancient mantle source with chondritic Sm/Nd abundances. These Nd- and Sr-isotopic values fall exactly on the empirical ϵ_I^{CHUR} vs. initial $^{87}\text{Sr}/^{86}\text{Sr}$ line, indicating that no contamination of this magma with crustal radiogenic strontium has occurred.

Hence the limited amount of isotopic data available for the Rio Grande rift suggests that the mantle source beneath the central rift is ancient continental lithosphere characterized by chondritic REE abundance ratios. Between Socorro and Las Cruces this continental lithosphere may be intruded by material with more "ocean"-like lead and strontium isotopic compositions.

Two important tests have yet to be performed to better delineate the isotopic characteristics of the mantle beneath the rift. First, both $^{87}\text{Sr}/^{86}\text{Sr}$ and Nd-Sm need to be obtained on an alkali olivine basalt and a tholeiite from the same volcanic field to determine what variations are present in a single location and whether the different

magma types are derived from different source materials. Strontium isotope and Nd-Sm measurements on a tholeiitic basalt from the El Alto field would thus complement the analysis of -005 by DePaolo and Wasserburg (1976). Second, although Kudo et al. (1971) analyzed $^{87}\text{Sr}/^{86}\text{Sr}$ from the entire Rio Grande rift, their data were not presented according to regions within the rift. Strontium isotopic and Nd-Sm measurements should be obtained on basaltic rocks from the various parts of the rift. When compared to Everson and Silver's (1978) Pb-isotopic data, these data may characterize different chemical regimes within the mantle beneath the rift.

MODEL FOR MAGMA GENESIS BENEATH THE RIO GRANDE RIFT

Spatial distribution of volcanic rocks - correlation with structure

An important feature of the volcanism of the central Rio Grande rift is the penecontemporaneous eruption of both alkali olivine basalt and tholeiitic basalt, in some cases from adjacent vents within a single volcanic field. In terms of both the variety of parental compositions and the overall range of compositions present, the volcanic fields with the greatest complexity are (collectively) the Cerros del Rio, Santa Ana Mesa, and El Alto fields. The Cerros del Rio and Santa Ana Mesa fields occupy an area of great structural complexity in a direction transverse to the main rift lineation (figure 1). This transverse zone is a major shear zone that has been the locus of large-scale crustal disruption. In this area the southern Española basin shallows and ramps out against the Cerrillos and Ortiz uplifts. The rift is stepped westward a distance of 50-60 km through the small

Santo Domingo basin to the main Albuquerque-Belen basin by a series of en echelon faults (Stearns, 1953b; Kelley, 1956; Woodward et al. 1975). Gravity modeling indicates that the Santo Domingo basin is extremely deep (-3 km). The basin is 2-3 km deeper than the adjacent parts of the Española and Albuquerque-Belen basins and is separated from them by very steep gravity gradients, which presumably indicate steeply-dipping fault zones (Cordell, 1976). The Cerros del Rio and Santa Ana Mesa volcanic fields are located directly over the eastern and western boundaries, respectively, of the Santo Domingo basin; hence it is likely that the fault zones bounding the basin have served as conduits for the lavas. In addition, structures adjacent to the rift are also disrupted along the strike of this transverse zone. For example, the southern extension of the Sierra Nacimiento uplift strikes obliquely into the Albuquerque-Belen basin at the latitude of this transverse zone.

Numerous lines of evidence indicate that this transverse zone has been a major zone of crustal weakness intermittently since the Precambrian. First, on a small scale, both the northern and southern margins of the Santo Domingo structural basin are aligned in a northeast-southwest direction; this direction parallels, on a large scale, the overall strike of the entire transverse zone. Numerous investigators (e.g., Cordell, 1976; King, 1977; Shoemaker et al., 1974; Ramberg et al., 1978; Warner, 1978) have pointed out that this northeast-southwest lineation is part of the Precambrian structural grain. Second, the Sierra Nacimiento is a structure of Laramide age (King, 1978). If its southern terminus has been influenced by this transverse zone, then

this zone has played a tectonic role since at least late Laramide time. Third, in Eocene and Oligocene time, just prior to crustal extension preceding rifting, this transverse zone was the locus of extensive intrusion and extrusion of quartz monzonite, andesite, and latite (Stearns, 1953b; Sun and Baldwin, 1958).

This transverse shear zone is actually a part of a much more major crustal structure, the Jemez lineament, extending from Springerville in eastern Arizona to the southeastern corner of Colorado (Mayo, 1958; Chapin et al., 1978). When viewed on a large scale, the intersection of this transverse zone with the Rio Grande rift includes much of the Española basin. The Jemez lineament is only one of several transverse lineaments intersecting the rift, but has been the most active lineament magmatically during the past 5 m.y. (Chapin et al., 1978).

Volcanic rocks occurring adjacent to this transverse zone to the north and immediately to the south are compositionally distinct from those occurring within this zone. Aoki (1967), Lipman (1969), and Lipman and Mehnert (1975) have presented descriptions and whole-rock major- and minor-element analyses of the basaltic rocks from the Taos Plateau (figure 1). These consist predominantly of relatively low-alkali, high-Al olivine and quartz tholeiite with minor, more silicic calc-alkaline andesite. The Albuquerque Volcanoes are located immediately to the south of this transverse zone. These lavas consist uniformly of lower-alkali olivine tholeiite. They are compared in figure 35 with basalt of the Taos Plateau and of the Cerros del Rio, Santa Ana Mesa, and El Alto volcanic fields. Hence, as was suggested by Baldrige (1978), a correlation may exist between transverse

structural zones (specifically, the Jemez lineament) and both alkaline magmatism and a multiplicity of parental compositions. Lavas of the Isleta, Wind Mesa, and Cat Hills volcanic fields may possibly complicate this correlation, since both hypersthene- and nepheline-normative lavas are present. However, the available data on these lavas indicate that the diversity of compositions, such as characterizes lavas of the transverse zone, is not present.

A similar and better-defined correlation between alkaline volcanism and transverse tectonics was observed by Barberi and co-workers (Barberi et al., 1974; Barberi and Varet, 1977, 1978) in Afar. Here it was found that transverse structures were usually characterized by nepheline-normative alkalic basalt, typically containing peridotite xenoliths. In addition these basalts commonly contain Al-rich augite and oligoclase megacrysts interpreted as high-pressure phases. A suggestion that such a relationship between transverse structures (transform faults) and alkaline magmatism exists within ocean basins has been made by Thompson and Melson (1972).

Lithospheric structure beneath the Rio Grande rift

To date no explanation has been advanced for the relationship between alkaline magmatism and transverse tectonics in areas of rifting, either oceanic or continental. A possible model to explain this relationship is schematically presented in figure 36. This model incorporates a thinned lithosphere beneath the rift due to intrusion into the lithosphere of buoyant, low-density mantle. Gravity and seismic data suggest that this diapir extends to the base of the crust, approximately 27-35 km beneath the rift, and may be at least 400 km in

width (Bridwell, 1976; McCullar and Smithson, 1977; Olsen et al., 1977; Ramberg et al., 1978). Unreversed seismic refraction profiles suggest that a "pillow" of anomalous mantle exists directly beneath the crust in the southern Rio Grande rift (McCullar and Smithson, 1977). The Jemez lineament, a transverse fracture zone, is shown on figure 36 as a plane cutting the upper lithosphere and extending into the diapir.

Away from this fracture zone, within basins, separation of magma from the mantle occurs from near or at the top of this diapir, at a depth of approximately 35-40 km (10-12 kb). These magmas correspond to the olivine tholeiite of the Albuquerque Volcanoes and of the Taos Plateau. The transverse fracture zone is a zone of lithospheric weakness. Where it extends into the diapir it provides an escape route to the surface for pockets of melt trapped at deeper levels within the diapir (50-70 km). These lavas correspond to the basanite and alkali olivine basalt occurring in the Cerros del Rio and El Alto volcanic fields. The diversity of compositions present in this location results from the fact that magmas at various levels within the diapir, from the base of the crust to about 70 km, are tapped by the fracture zone. Many of these magmas move directly and rapidly to the surface with only moderate alteration of their compositions by crystal fractionation. Others collect in reservoirs in the crust, where extensive fractional crystallization may occur, before continuing to the surface. The importance of olivine and plagioclase as fractionating phases indicates that this fractionation occurs at depths shallower than about 35 km (10 kb). This depth is compatible with the seismic data of Sanford and co-workers (summarized in Chapin et al., 1978) which suggest that magma chambers

are present at 18-22 km and at about 5 km beneath Socorro. If, as postulated here, the quartz and resorbed plagioclase which occur mainly in the basaltic andesite, alkali olivine basalt, and hawaiite, are high-pressure phenocrysts, much resorption of these must also occur in these crustal chambers. The quartz and feldspar may be concentrated by flotation near the tops of these chambers.

The mechanism by which such shear zones may exist within the deep crust and mantle, and particularly by which they may continue to exist over such a long interval of time, is unknown. Although they exist as fractures and faults near the earth's surface, they cannot do so at depth. They may be zones across which differences in composition and/or physical properties exist. Also the mechanism by which they influence magma genesis is unknown. Perhaps tectonic activity which is focussed along such zones leads locally to pressure decreases, causing melting. Or perhaps such zones, being weaker, simply facilitate the "kneading out" of magmas already present (Yoder, 1976).

Temporal distribution of magma types

It was considered a possibility in the beginning of this work that a systematic change in magma composition with time might be present in the volcanic rocks of the Rio Grande rift. Such a relationship has been observed in the lavas of the Kenya rift (Baker et al., 1978; Williams, 1978) and attributed to tapping of magmas from successively shallower depths from a progressively rising mantle diapir (Baker et al., 1978). The sparsity of older (>5 m.y.) lavas in the Rio Grande rift makes it difficult to generalize about magma production with time. The late Oligocene to early Miocene nephelinite of the Cieneguilla

Limburgite and Cerro Negro in the southern and northern Española basin, respectively, is similar to early magmas occurring in the Kenya rift (Baker et al., 1978). However, hypersthene-normative rocks of about the same age are also present in relatively close proximity to this nephelinite. Late Miocene volcanic rocks are both nepheline- and hypersthene-normative. Therefore, with respect to the few volcanic rocks of late Oligocene and of Miocene age that occur in the central rift, no general trend from more to less alkaline or undersaturated compositions is present.

SUMMARY

1. The main Pliocene and Pleistocene volcanic fields of the Rio Grande rift (the Cerros del Rio, Santa Ana Mesa, and El Alto fields) are located along a major transverse shear zone at the offset between the Española and Albuquerque-Belen basins. On the basis of bulk chemistry and detailed phase petrology, four compositional groups can be distinguished: low-alkali olivine tholeiite (group A), basaltic andesite and latite-andesite (group B), basanite (group C), and alkali olivine basalt and hawaiite (group D).
2. Volcanic rocks of the northern Albuquerque-Belen basin (Albuquerque Volcanoes) are low-alkali tholeiite.
3. Volcanic rocks of the central Albuquerque-Belen basin (Isleta, Wind Mesa, Cat Hills) are olivine tholeiite, basaltic andesite, and alkali olivine basalt.

4. Latite-andesite from the Cerros del Rio was derived from basaltic andesite by removal of olivine, plagioclase, clino- and orthopyroxene, and minor Cr-spinel, magnetite, and ilmenite; and by addition of quartz and sodic plagioclase. It is suggested that basaltic andesite magma, containing quartz and sodic plagioclase xenocrysts of possible high pressure origin, resided temporarily in crustal magma chambers. Quartz and sodic plagioclase may have been gravitatively concentrated near the tops of these chambers and resorbed as olivine, pyroxene, calcic plagioclase, and opaque minerals were removed by fractional crystallization. Some of the alkali olivine basalt and hawaiite compositions from the Cerros del Rio and El Alto can be related to each other by fractional crystallization of olivine, plagioclase, and clinopyroxene.
5. Comparison with experiments suggests that the tholeiitic lavas were derived from about 35 km depth and the alkalic magmas from 50-70 km. The apparent correlation of more alkaline chemistry with the transverse shear zone may indicate that such transverse zones tap magmas at greater depths than along adjacent regions of the rift.
6. Mafic lavas of the lower Miocene and/or upper Oligocene range in composition from olivine nephelinite to quartz tholeiite. Late Miocene lavas are alkali olivine basalt and olivine tholeiite. Hence in the central Rio Grande rift no systematic variation of magma composition with time has occurred.

REFERENCES

- Aoki, K., 1967. Petrography and petrochemistry of latest Pliocene olivine-tholeiites of Taos area, northern New Mexico, U.S.A. *Contr. Mineral. Petrol.*, 14: 190-203.
- Aoki, K., and Kudo, A. M., 1976. Major-element variations of late Cenozoic basalts of New Mexico. *New Mex. Soc. Spec. Publ.*, 5: 82-88.
- Bachman, G. O., and Mehnert, H. H., 1978. New K-Ar dates and the late Pliocene to Holocene geomorphic history of the central Rio Grande region, New Mexico. *Geol. Soc. Amer. Bull.*, 89: 283-292.
- Bacon, C. R., and Carmichael, I. S. E., 1973. Stages in the P-T path of ascending basalt magma: An example from San Quintin, Baja California. *Contr. Mineral. Petrol.*, 41: 1-22.
- Bailey, R. A., Smith, R. L., and Ross, C. S., 1969. Stratigraphic nomenclature of volcanic rocks in the Jemez Mountains, New Mexico. *U.S. Geol. Surv. Bull.*, 1274-P.
- Baker, B. H., Crossley, R., and Goles, G. G., 1978. Tectonic and magmatic evolution of the southern part of the Kenya rift valley. Pp. 29-50 in *Petrology and geochemistry of continental rifts* (eds. Neumann, E.-R., and Ramberg, I. B.) Reidel, Dordrecht.
- Baldrige, W. S., 1978. Petrology of Plio-Pleistocene basaltic rocks from the central Rio Grande rift (New Mexico, USA) and their relation to rift structure. Pp. 71-78 in *Petrology and geochemistry of continental rifts* (eds. Neumann, E.-R., and Ramberg, I. B.) Reidel, Dordrecht.
- Baldrige, W. S., 1979a. Petrology and petrogenesis of Plio-Pleistocene basaltic rocks from the central Rio Grande rift, New Mexico, and their relation to rift structure. In *Rio Grande Rift: Tectonics and Magmatism*, R. Riecker (Editor). *Amer. Geophys. Union Spec. Publ.* (in press).
- Baldrige, W. S., 1979b. Mafic and ultramafic inclusion suites from the Rio Grande rift (New Mexico) and their bearing on the composition and thermal state of the lithosphere. *Subm. to J. Volcan. Geotherm. Res.*
- Barberi, F., Bonatti, E., Marinelli, G., and Varet, J., 1974. Transverse tectonics during the split of a continent: Data from the Afar rift. *Tectonophys.*, 23: 17-29.
- Barberi, F., and Varet, J., 1977. Volcanism of Afar: Small-scale plate tectonics implications. *Geol. Soc. Amer. Bull.*, 88: 1251-1266.

- Barberi, F., and Varet, J., 1978. The Afar rift junction. Pp. 55-69 in *Petrology and geochemistry of continental rifts* (eds. Neumann, E.-R., and Ramberg, I. B.) Reidel, Dordrecht.
- Berggren, W. A., and Van Couvering, J. A., 1974. The late Neogene. *Palaeogeography, Palaeoclimatology, Palaeoecology*, 16: 1-216.
- Best, M. G., and Brimhall, W. H., 1970. Late Cenozoic basalt types in the western Grand Canyon region. In *The Western Grand Canyon District*, W. K. Hamblin and M. G. Best (Editors). *Utah Geol. Surv., Guidebook Geol. Utah*, 23.
- Bridwell, R. J., 1976. Lithospheric thinning and the late Cenozoic thermal and tectonic regime of the northern Rio Grande rift. *New Mexico Geol. Soc. Guidebook, 27th Field Conf.*: 283-292.
- Brown, R. W., 1977. A sample fusion technique for whole rock analysis with the electron microprobe. *Geochim. Cosmochim. Acta*, 41: 435-438.
- Bryan, K., 1938. Geology and ground-water conditions of the Rio Grande depression in Colorado and New Mexico. In *Rio Grande Joint Investigations in the Upper Rio Grande Basin in Colorado, New Mexico and Texas*: Washington, National Resources Commission, Regional Planning, pt. 6: 196-225.
- Butler, A. P., Jr., 1971. Tertiary volcanic stratigraphy of the eastern Tuzas Mountains, southwest of the San Luis Valley, Colorado-New Mexico. *New Mex. Geol. Soc. Guidebook, 22nd Field Conf.*: 289-300.
- Carmichael, I. S. E., 1964. The Petrology of Thingmuli, a Tertiary volcano in eastern Iceland. *J. Petrol.*, 5: 435-460.
- Carmichael, I. S. E., Turner, F. J., and Verhoogen, J., 1974. *Igneous petrology*. McGraw-Hill, New York, 739 pp.
- Champion, D. E., Albee, A. L., and Chodos, A. A., 1975. Reproducibility and operator bias in a computer-controlled system for quantitative electron microprobe analysis. *Proc. 10th Ann. Microbeam Anal. Soc. Conf.*: 55A-55F.
- Chapin, C. E., 1971. The Rio Grande rift, Part I: Modifications and additions. *New Mex. Geol. Soc. Guidebook, 22nd Field Conf.*: 191-201.
- Chapin, C. E., and Seager, W. R., 1975. Evolution of the Rio Grande rift in the Socorro and Las Cruces areas. *New Mex. Geol. Soc. Guidebook, 26th Field Conf.*: 297-321.

- Chapin, C. E., Chamberlin, R. M., Osburn, G. R., White, D. W., and Sanford, A. R., 1978. Exploration framework of the Socorro geothermal area, New Mexico. *New Mex. Geol. Soc. Spec. Publ.*, 7: 114-129.
- Chodos, A. A., and Albee, A. L., 1972. Automated microprobe analysis and applications to analysis of exotic lunar phases. *Proc. 6th Internat. Conf. X-ray Optics and Microanalysis*: 779-784.
- Chodos, A. A., Albee, A. L., Gancarz, A. J., and Laird, J., 1973. Optimization of computer-controlled quantitative analysis of minerals. *Proc. 8th Nat. Conf. Electron Probe Anal.*: 45A-45C.
- Coats, R. R., 1968. Basaltic andesites. In *Basalts*, H. H. Hess and A. Poldervaart (Editors). Interscience, New York, pp. 689-736.
- Cordell, L., 1976. Aeromagnetic and gravity studies of the Rio Grande graben in New Mexico between Belen and Pilar. *New Mex. Geol. Soc., Spec. Publ.*, 6: 62-70.
- Dane, C. H., and Bachman, G. O., 1965. Geologic map of New Mexico. *U.S. Geol. Surv. Map*.
- DePaolo, D. J., and Wasserburg, G. J., 1976. Inferences about magma sources and mantle structure from variations of $^{143}\text{Nd}/^{144}\text{Nd}$. *J. Geophys. Res. Letts.*, 3:743-746.
- Doe, B. R., Lipman, P. W., Hedge, C. E., and Kurawawa, H., 1969. Primitive and contaminated basalts from the southern Rocky Mountains, U.S.A. *Contr. Mineral. Petrol.*, 21: 142-156.
- Doell, R. R., Dalrymple, G. B., Smith, R. L., and Bailey, R. A., 1968. Paleomagnetism, potassium-argon ages, and geology of rhyolites and associated rocks of the Valles Caldera, New Mexico. Pp. 212-248 in *Studies in geology* (eds. Coats, R. L., Hay, R. L., and Anderson, C. A.) *Geol. Soc. Amer. Mem.* 116.
- Eggler, D. H., 1978. The effect of CO_2 upon partial melting of peridotite in the system $\text{Na}_2\text{O}-\text{CaO}-\text{Al}_2\text{O}_3-\text{MgO}-\text{SiO}_2$ to 35 kb, with an analysis of melting in a peridotite- $\text{H}_2\text{O}-\text{CO}_2$ system. *Amer. J. Sci.*, 278: 305-343.
- Eichelberger, J. C., 1978. Andesitic volcanism and crustal evolution. *Nature*, 275: 21-27.
- Eichelberger, J. C., and Gooley, R., 1977. Evolution of silicic magma chambers and their relationship to basaltic volcanism. Pp. 57-77 in *The Earth's Crust* (eds. Heacock, J. G., Keller, G. V., Oliver, J. E., and Simmons, G.) *Amer. Geophys. Union Mono.*, 20.
- Everson, J. E., and Silver, L. T., 1978. Lead systematics of late Cenozoic basalts from the Rio Grande rift (abstr.). *Int. Symp. on the Rio Grande Rift*, Oct. 8-17, 1978, Santa Fe, New Mexico Los Alamos Scien. Lab. Rep. LA-7487-C: 36-37.

- Flanagan, F. J., 1973. 1972 values for international geochemical reference samples. *Geochim. Cosmochim. Acta*, 37: 1189-1200.
- Galusha, T., and Blick, J. C., 1971. Stratigraphy of the Santa Fe Group, New Mexico. *Bull. Amer. Mus. Nat. History*, 144: 1-128.
- Green, D. H., 1970a. A review of experimental evidence on the origin of basaltic and nephelinitic magmas. *Phys. Earth Planet. Int.*, 3: 221-235.
- Green, D. H., 1970b. The origin of basaltic and nephelinitic magmas. *Trans. Leicester Liter. Philosoph. Soc.*, 64: 28-54.
- Green, D. H., and Ringwood, A. E., 1967a. An experimental investigation of the gabbro to eclogite transformation and its petrological applications. *Geochim. Cosmochim. Acta*, 31: 767-833.
- Green, D. H., and Ringwood, A. E., 1967b. The genesis of basaltic magmas. *Contr. Mineral. Petrol.*, 15: 103-190.
- Green, T. H., 1967. An experimental investigation of sub-solidus assemblages formed at high pressure in high-alumina basalt, kyanite eclogite and grosspydrite compositions. *Contr. Mineral. Petrol.*, 16: 84-114.
- Green, T. H., 1972. Crystallization of calc-alkaline andesite under controlled high-pressure hydrous conditions. *Contr. Mineral. Petrol.*, 34: 150-166.
- Green, T. H., and Ringwood, A. E., 1968. Genesis of the calc-alkaline igneous rock suite. *Contr. Mineral. Petrol.*, 18: 105-162.
- Irvine, T. N., and Baragar, W. R. A., 1971. A guide to the chemical classification of the common volcanic rocks. *Canad. J. Earth Sci.*, 8: 523-548.
- Irving, A. J., and Green, D. H., 1976. Geochemistry and petrogenesis of the newer basalts of Victoria and South Australia. *J. Geol. Soc. Australia*, 23, Pt. 1: 45-66.
- Kelley, V. C., 1952. Tectonics of the Rio Grande depression of central New Mexico. *New Mex. Geol. Soc. Guidebook*, 3rd Field Conf.: 93-103.
- Kelley, V. C., 1956. The Rio Grande depression from Taos to Santa Fe. *New Mex. Geol. Soc. Guidebook*, 7th Field Conf.: 109-114.
- Kelley, V. C., 1978. Geology of Española Basin, New Mexico. *New Mex. Bur. Mines Min. Res. Geol. Map* 48.

- Kelley, V. C., and Kudo, A. M., 1978. Volcanoes and related basalts of Albuquerque-Belen basin, New Mexico. New Mex. Bur. Mines Miner. Res. Circ., 156, 30 p.
- King, P. B., 1977. The evolution of North America. (Revised ed.) Princeton Univ. Press, Princeton, 197 pp.
- Kudo, A. M., 1976. Volcanism within the Rio Grande rift (abstr.). Abstracts with Programs, Geol. Soc. Am. Rocky Mtn. Sec. Ann. Mtg., 8: 597.
- Kudo, A. M., Aoki, K., and Brookins, D. G., 1971. The origin of Pliocene-Holocene basalts of New Mexico in the light of strontium-isotope and major-element abundances. Earth Planet. Sci. Lett., 13: 200-204.
- Leeman, W. P., and Rodgers, J. J. W., 1970. Late Cenozoic alkali-olivine basalts of the Basin-Range province, U.S.A. Contr. Mineral. Petrol., 25: 1-24.
- Lipman, P. W., 1969. Alkalic and tholeiitic basaltic volcanism related to the Rio Grande depression, southern Colorado and northern New Mexico. Geol. Soc. Amer. Bull., 80: 1343-1354.
- Lipman, P. W., 1977. The Taos Plateau volcanic field, northern Rio Grande rift, New Mexico (abstr). Second Inter-team Mtg. Basaltic Volcan. Study Proj., Houston, TX, 20-23 Sept. 1977. Lunar Sci. Inst. Stud. Proj., BVSP Contr. 7: 41-43.
- Lipman, P. W., and Mehnert, H. H., 1975. Late Cenozoic basaltic volcanism and development of the Rio Grande depression in the southern Rocky Mountains. Geol. Soc. Amer. Mem., 144: 119-154.
- Longhi, J., 1977. Magma oceanography 2: Chemical evolution and crustal formation. Proc. Lunar Sci. Conf. 8th: 601-621.
- MacDonald, G. A., and Katsura, T., 1964. Chemical composition of Hawaiian lavas. J. Petrol., 5: 82-133.
- Manley, K., 1976. K-Ar age determinations on Pliocene basalts from the Española basin, New Mexico. Isochron/West, No. 16: 28-30.
- Marsh, B. D., and Carmichael, I. S. E., 1974. Benioff zone magmatism. J. Geophys. Res., 79: 1196-1206.
- Mayo, E. B., 1958. Lineament tectonics and some ore districts of the southwest. Mining Engin., 10: 1169-1175.
- McCullar, D. B., and Smithson, S. B., 1977. Unreversed seismic crustal refraction profile across the southern Rio Grande rift (abstr.). EOS, Trans. Amer. Geophys. Union, 58: 1184.

- Mysen, B. O., and Kushiro, I., 1977. Compositional variations of coexisting phases with degree of melting of peridotite in the upper mantle. *Amer. Min.*, 62: 843-865.
- Nicholls, J., Carmichael, I. S. E., and Stormer, J. C., Jr., 1971. Silica activity and P_{total} in igneous rocks. *Contr. Mineral. Petrol.*, 33: 1-20.
- Nicholls, J., and Carmichael, I. S. E., 1972. The equilibrium temperature and pressure of various lava types with spinel- and garnet peridotite. *Amer. Min.*, 57: 941-959.
- Olsen, K. H., Keller, G. R., Stewart, J. N., Homuth, E. F., Cash, D. J., and Newton, C. A., 1977. A seismic refraction study of crustal structure in the central Rio Grande rift, New Mexico (abstr.). *EOS, Trans. Amer. Geophys. Union*, 58: 1184.
- Presnall, D. C., 1976. Alumina content of enstatite as a geobarometer for plagioclase and spinel lherzolites. *Amer. Min.*, 61: 582-588.
- Ramberg, I. B., 1976. Gravity interpretation of the Oslo graben and associated igneous rocks. *Norges Geol. Unders.*, 325: 1-94.
- Ramberg, I. B., Cook, F. A., and Smithson, S. B., 1978. Structure of the Rio Grande rift in southern New Mexico and West Texas based on gravity interpretation. *Geol. Soc. Amer. Bull.*, 89: 107-123.
- Reid, M. J., Gancarz, A. J., and Albee, A. L., 1973. Constrained least-squares analysis of petrologic problems with an application to lunar sample 12040. *Earth Planet. Sci. Lett.*, 17: 433-445.
- Renault, J., 1970. Major-element variations in the Potrillo, Carrizozo, and McCartys basalt fields, New Mexico. *New Mex. Bur. Mines Miner. Res. Circ.*, 113, 22 p.
- Ringwood, A. E., 1975. Composition and petrology of the earth's mantle. McGraw-Hill, New York, 618 pp.
- Roeder, P. L., and Emslie, R. F., 1970. Olivine-liquid equilibrium. *Contr. Mineral. Petrol.*, 29: 275-289.
- Shoemaker, E. M., Squires, R. L., and Abrams, M. J., 1974. The Bright Angel and Mesa Butte fault systems of northern Arizona. Pp. 355-391 in *Geology of northern Arizona, Part I--Regional studies*. *Geol. Soc. Amer. Rocky Mtn. Sec. Ann. Mtg.*, Flagstaff, Arizona.
- Smith, R. L., Bailey, R. A., and Ross, C. S., 1970. Geologic map of the Jemez Mountains. *U.S. Geol. Surv. Map*, No. I-571.

- Spiegel, Z., and Baldwin, B., 1963. Geology and water resources of the Santa Fe area, New Mexico. U.S. Geol. Surv. Water-Supply Paper, 1525, 258 p.
- Stearns, C. E., 1953a. Early Tertiary vulcanism in the Galisteo-Tonque area, north-central New Mexico. Amer. J. Sci., 25: 415-452.
- Stearns, C. E., 1953b. Tertiary geology of the Galisteo-Tonque area, New Mexico. Geol. Soc. Amer. Bull., 64: 459-508.
- Stormer, J. C., Jr., 1972. Mineralogy and petrology of the Raton-Clayton volcanic field, northeastern New Mexico. Geol. Soc. Amer. Bull., 83: 3299-3322.
- Sun, M., and Baldwin, B., 1958. Volcanic rocks of the Cienega area, Santa Fe County, New Mexico. New Mex. Bur. Mines Min. Res. Bull., 54, 80 p.
- Thompson, G., and Melson, W. G., 1972. The petrology of oceanic crust across fracture zones in the Atlantic Ocean: Evidence of a new kind of sea-floor spreading. J. Geol., 80: 526-538.
- Thompson, R. N., 1974. Primary basalts and magma genesis. I. Skye, north-west Scotland. Contr. Mineral. Petrol., 45: 317-341.
- Warner, L. A., 1978. The Colorado lineament: A middle Precambrian wrench fault system. Geol. Soc. Amer. Bull., 89: 161-171.
- Williams, L. A. J., 1978. The volcanological development of the Kenya rift. Pp. 101-121 in Petrology and geochemistry of continental rifts (eds. Neumann, E. -R., and Ramberg, I. B.) Reidel, Dordrecht.
- Woodward, L. A., Callender, J. F., and Zilinski, R. E., 1975. Tectonic map of the Rio Grande rift, New Mexico. Geol. Soc. Amer. Map and Chart Ser., MC-11.
- Yoder, H. S., Jr., 1976. Generation of basaltic magma. Nat. Acad. Sci., Washington, D. C., 265 pp.
- Yoder, H. S., and Tilley, C. E., 1962. Origin of basaltic magmas: an experimental study of natural and synthetic rock systems. J. Petrol., 3: 342-532.

TABLE 1. Electron microprobe analyses of U. S. G. S. standard rocks compared with recommended values. *Total iron as FeO.

	W-1			AGV-1			BCR-1		
	a	s.d.	b	a	s.d.	b	a	s.d.	b
SiO ₂	52.77	±0.27	53.00	60.60	±0.22	59.61	55.24	±0.53	55.37
TiO ₂	1.07	0.09	1.08	1.17	0.03	1.05	2.21	0.04	2.24
Al ₂ O ₃	14.99	0.21	15.10	17.62	0.24	17.43	13.68	0.18	13.83
FeO*	10.13	0.21	10.05	6.26	0.09	6.17	12.17	0.28	12.30
MgO	6.79	0.10	6.67	1.65	0.09	1.55	3.65	0.08	3.52
CaO	10.78	0.10	11.04	4.94	0.07	4.95	6.87	0.01	7.03
Na ₂ O	2.32	0.12	2.16	4.27	0.10	4.30	3.50	0.01	3.32
K ₂ O	0.62	0.04	0.64	2.91	0.06	2.92	1.73	0.03	1.73
P ₂ O ₅	0.11	0.03	0.14	0.40	0.11	0.50	0.37	0.00	0.37
SUM	99.58		99.88	99.82		98.48	99.42		99.71
No. beads	10			4			2		

a. Average microprobe analyses obtained on glass beads. s.d. indicates standard deviation on replicate beads.

b. Analyses from Flanagan (1973), corrected for H₂O and CO₂ losses.

TABLE 2

Chemical compositions (weight percent) and Barth-Niggli cation norms (cation percent) of lavas from the Cerros del Rio, Santa Ana Mesa, and El Alto volcanic fields. *Fe₂O₃ calculated from Fe³⁺/Fe²⁺ + Fe³⁺ = 0.1. Mg-value = 100(Mg/Mg + Fe²⁺).

	Group A olivine tholeiites									
	-004	-009	-049	-057	-058	-064	-065	-087	-232	-261
SiO ₂	51.08	50.78	51.21	51.34	51.36	51.29	51.39	51.37	51.73	51.42
TiO ₂	1.51	1.56	1.51	1.38	1.40	1.51	1.51	1.49	1.45	1.48
Al ₂ O ₃	16.53	16.13	16.10	15.81	15.97	16.36	16.29	16.04	16.14	16.20
Fe ₂ O ₃ *	1.71	1.79	1.91	1.94	1.92	1.84	1.74	1.92	1.90	1.90
FeO	7.78	8.15	8.69	8.86	8.75	8.38	7.92	8.75	8.64	8.64
MgO	6.93	6.71	7.35	6.28	6.64	6.33	7.20	6.64	7.01	6.63
CaO	9.23	9.14	8.71	9.39	9.09	9.25	8.67	8.83	8.78	8.92
Na ₂ O	3.65	3.74	3.28	3.56	3.60	3.46	3.65	3.44	3.28	3.52
K ₂ O	1.00	1.08	1.00	0.88	0.96	1.05	1.24	1.09	1.01	0.96
P ₂ O ₅	0.39	0.39	0.31	0.28	0.27	0.27	0.33	0.25	0.22	0.29
TOTAL	99.81	99.47	100.07	99.72	99.96	99.74	99.94	99.82	100.16	99.96
Mg-value	61.3	59.5	60.1	55.8	57.5	57.4	61.8	57.5	59.1	57.8
Q	0.00	0.00	0.00	0.00	0.00	0.00	0.00	0.00	0.00	0.00
or	5.89	6.39	5.90	5.22	5.67	6.22	7.28	6.45	5.96	5.67
ab	32.66	33.63	29.39	32.10	32.30	31.15	32.58	30.95	29.39	31.60
an	25.69	24.08	26.21	24.68	24.58	26.09	24.28	25.17	26.30	25.58
ne	0.00	0.00	0.00	0.00	0.00	0.00	0.00	0.00	0.00	0.00
di	13.92	15.02	11.91	16.22	14.98	14.53	13.08	13.67	12.60	13.42
hy	6.32	3.59	14.57	9.79	8.65	10.20	6.50	11.65	16.13	11.71
ol	10.85	12.44	7.29	7.45	9.30	7.22	11.69	7.49	5.17	7.23
mt	1.77	1.86	1.99	2.03	2.00	1.92	1.80	2.00	1.98	2.74
ilm	2.10	2.18	2.10	1.93	1.95	2.11	2.09	2.08	2.02	2.81
ap	0.81	0.82	0.65	0.59	0.56	0.57	0.69	0.52	0.46	0.70

TABLE 2 (continued)

	Group B basaltic andesites and related latite-andesites						
	-001	-021	-023	-D031	-036	-038	-A039
SiO ₂	54.89	53.24	52.93	53.82	64.12	63.77	64.17
TiO ₂	1.28	1.22	1.26	1.25	0.75	0.80	0.82
Al ₂ O ₃	15.40	16.98	16.87	15.78	16.20	16.43	16.42
Fe ₂ O ₃ *	1.33	1.50	1.53	1.41	0.84	0.88	0.91
FeO	6.04	6.85	6.98	6.41	3.81	4.03	4.13
MgO	5.73	5.49	5.75	6.21	2.74	2.87	2.54
CaO	7.49	8.27	8.46	7.82	4.78	4.85	4.84
Na ₂ O	4.29	3.86	3.81	4.37	4.17	4.09	4.42
K ₂ O	2.38	1.59	1.60	1.84	2.83	2.84	2.51
P ₂ O ₅	0.84	0.39	0.38	0.54	0.37	0.38	0.34
TOTAL	99.67	99.39	99.57	99.45	100.61	100.94	101.10
Mg-value	62.8	58.8	59.5	63.3	56.2	55.9	52.3
Q	0.00	0.00	0.00	0.00	13.16	12.64	12.84
or	13.97	9.40	9.44	10.80	16.59	16.60	14.64
ab	38.28	34.69	34.17	39.00	37.15	36.32	39.19
an	15.65	24.35	24.19	17.91	17.00	17.90	17.34
ne	0.00	0.00	0.00	0.00	0.00	0.00	0.00
di	12.66	11.34	12.21	13.72	3.30	2.76	3.34
hy	10.35	12.66	10.40	5.27	10.12	10.97	9.88
ol	4.20	3.48	5.46	9.01	0.00	0.00	0.00
mt	1.37	1.56	1.59	1.45	0.87	0.92	0.95
ilm	1.77	1.70	1.75	1.73	1.04	1.10	1.13
ap	1.75	0.82	0.79	1.12	0.77	0.79	0.70

TABLE 2 (continued)

Group B basaltic andesites and related latite-andesites

	-044	-045	-062	-063	-230	-231	-262
SiO ₂	56.54	55.00	61.10	59.34	53.46	53.95	58.79
TiO ₂	1.59	1.41	0.94	0.94	1.52	1.45	0.97
Al ₂ O ₃	18.89	16.28	16.25	16.54	15.38	15.25	16.27
Fe ₂ O ₃ *	1.54	1.39	1.05	1.06	1.52	1.48	1.15
FeO	7.01	6.31	4.78	4.82	6.94	6.76	5.22
MgO	1.89	5.59	3.21	4.02	7.25	6.73	4.42
CaO	6.20	7.37	5.45	6.29	7.39	7.70	6.29
Na ₂ O	4.27	4.11	3.79	4.04	3.79	4.06	4.63
K ₂ O	1.98	2.01	2.73	2.40	2.11	2.02	2.10
P ₂ O ₅	0.12	0.45	0.37	0.37	0.57	0.56	0.45
TOTAL	100.03	99.92	99.67	99.82	99.93	99.96	100.29
Mg-value	32.4	61.2	54.5	59.8	65.1	64.0	60.1
Q	4.67	0.00	10.66	6.68	0.00	0.00	3.80
or	11.76	11.80	16.20	14.14	12.36	11.82	12.26
ab	38.55	36.66	34.18	36.17	33.74	36.12	41.07
an	26.69	19.92	19.36	19.86	18.57	17.27	17.21
ne	0.00	0.00	0.00	0.00	0.00	0.00	0.00
di	2.76	10.79	4.30	7.08	11.27	13.57	8.57
hy	11.47	15.95	12.11	12.90	11.77	9.24	13.65
ol	0.00	0.57	0.00	0.00	7.44	7.29	0.00
mt	1.62	1.43	1.10	1.10	1.57	1.53	1.19
ilm	2.23	1.95	1.32	1.31	2.10	2.00	1.33
ap	0.25	0.93	0.78	0.77	1.18	1.16	0.93

TABLE 2 (continued)

	Group C basanites		Group D alkali olivine basalts and related hawaiites				
	-034	-269	-005	-006	-024	-028	-029
SiO ₂	46.54	47.54	49.01	51.10	50.85	50.64	49.84
TiO ₂	2.09	1.89	1.48	1.34	1.55	1.51	1.79
Al ₂ O ₃	16.52	15.74	15.90	16.51	17.05	16.39	18.09
Fe ₂ O ₃ *	1.83	1.91	1.93	1.51	1.72	1.58	1.86
FeO	8.32	8.70	8.80	6.88	7.83	7.18	8.45
MgO	7.14	8.14	8.63	4.91	3.96	6.58	4.24
CaO	10.18	8.97	9.06	10.13	8.78	8.64	8.94
Na ₂ O	3.63	4.21	3.65	4.48	4.68	4.19	4.28
K ₂ O	2.01	1.73	0.89	1.61	1.92	1.77	1.26
P ₂ O ₅	1.17	0.97	0.28	1.05	1.00	0.87	0.60
TOTAL	99.43	99.80	99.63	99.52	99.34	99.35	99.35
Mg-value	60.5	62.5	63.6	56.0	47.4	62.0	47.2
Q	0.00	0.00	0.00	0.00	0.00	0.00	0.00
or	11.87	10.11	5.23	9.49	11.39	10.42	7.50
ab	18.08	22.28	29.34	33.00	34.85	33.31	35.26
an	22.86	18.75	24.23	20.15	19.93	20.62	26.63
ne	8.70	9.08	1.94	4.28	4.40	2.50	2.06
di	16.00	15.21	14.90	18.52	13.79	13.14	11.28
hy	0.00	0.00	0.00	0.00	0.00	0.00	0.00
ol	15.23	18.00	19.74	8.94	9.59	14.49	11.56
mt	1.89	1.97	2.00	1.56	1.79	1.63	1.94
ilm	2.91	2.60	2.05	1.86	2.17	2.10	2.51
ap	2.45	2.00	0.58	2.19	2.10	1.81	1.26

TABLE 2 (continued)

Group D alkali olivine basalts and related hawaiites

	-042	-061	-281	-283	-F212	-213	-233
SiO ₂	49.64	49.15	49.72	50.06	52.25	51.89	52.62
TiO ₂	1.62	1.48	1.71	1.52	1.48	1.36	1.49
Al ₂ O ₃	16.55	15.71	17.58	16.23	16.80	16.34	17.80
Fe ₂ O ₃ *	1.80	1.85	1.79	1.63	1.54	1.55	1.64
FeO	8.18	8.43	8.15	7.45	7.02	7.05	7.47
MgO	6.96	8.43	6.34	8.08	5.84	6.37	4.86
CaO	9.46	9.59	8.39	8.43	8.45	8.94	8.21
Na ₂ O	3.92	3.70	4.06	4.46	4.46	4.19	4.28
K ₂ O	1.19	1.03	1.41	1.57	1.53	1.52	1.76
P ₂ O	0.39	0.65	0.79	0.75	0.64	0.77	0.57
TOTAL	99.71	100.02	99.94	100.18	100.01	99.98	100.70
Mg-value	60.2	64.0	58.1	65.9	59.7	61.7	53.7
Q	0.00	0.00	0.00	0.00	0.00	0.00	0.00
or	7.00	6.02	8.28	9.09	8.95	8.89	10.27
ab	29.64	28.85	33.90	29.65	38.46	36.74	37.96
an	23.95	22.99	25.44	19.25	21.10	21.10	23.88
ne	3.23	2.42	1.40	5.76	0.71	0.31	0.00
di	16.19	15.92	8.64	13.56	13.01	14.28	10.14
hy	0.00	0.00	0.00	0.00	0.00	0.00	1.81
ol	15.07	18.50	16.48	17.40	12.82	13.60	11.01
mt	1.86	1.01	1.85	1.68	1.59	1.60	1.70
ilm	2.25	2.04	2.37	2.08	2.04	1.88	2.05
ap	0.81	1.35	1.64	1.54	1.32	1.59	1.18

TABLE 3

Chemical compositions (weight percent) and Barth-Niggli cation norms (cation percent) of basalts from the Albuquerque Volcanoes. *Fe₂O₃ calculated from $\text{Fe}^{3+}/\text{Fe}^{2+} + \text{Fe}^{3+} = 0.1$. Mg-value = $100(\text{Mg}/\text{Mg} + \text{Fe}^{2+})$.

	-093	-095	-105	-106	-108	-110
SiO ₂	50.10	51.08	51.09	51.18	51.18	50.37
TiO ₂	1.52	1.41	1.46	1.40	1.47	1.51
Al ₂ O ₃	14.64	15.02	15.05	15.11	14.85	15.14
Fe ₂ O ₃ *	2.03	1.94	1.96	1.98	1.99	2.05
FeO	9.25	8.83	8.95	9.01	9.07	9.34
MgO	8.86	8.90	8.32	8.40	8.45	8.85
CaO	9.50	9.03	9.48	9.56	9.44	9.42
Na ₂ O	2.97	2.94	2.83	2.79	2.99	2.88
K ₂ O	0.55	0.61	0.56	0.49	0.52	0.52
P ₂ O ₅	0.22	0.22	0.20	0.19	0.21	0.23
TOTAL	99.64	99.98	99.90	100.11	100.17	100.23
Mg-value	63.1	64.2	62.4	62.4	62.4	62.8
or	3.26	3.59	3.31	2.89	3.07	3.06
ab	26.73	26.33	25.45	25.04	26.79	25.07
an	25.06	25.93	26.77	27.26	25.52	27.14
di	16.59	13.86	15.23	15.13	15.88	14.37
hy	13.81	19.83	21.43	22.38	19.02	18.29
ol	9.86	6.04	3.30	2.89	5.17	7.34
mt	2.11	2.02	2.05	2.06	2.08	2.14
ilm	2.12	1.96	2.04	1.95	2.04	2.10
ap	0.46	1.46	0.42	0.40	0.44	0.48

TABLE 4 Chemical compositions (weight percent) and Barth-Niggli cation norms (cation percent) of basalts from Isleta Volcano, Wind Mesa Volcano, and the Cat Hills volcanic field. *Fe₂O₃ calculated from Fe³⁺/Fe²⁺ + Fe²⁺ + Fe³⁺ = 0.1. Mg-value = 100(Mg/Mg + Fe²⁺).

	Isleta		Wind Mesa				Cat Hills				
	-111	-114	-116	-122	-129	-131	-132	-133	-135	-136	-140
SiO ₂	51.13	50.29	51.72	52.75	50.51	53.05	50.50	50.46	51.15	51.05	51.54
TiO ₂	2.18	2.14	1.78	1.41	2.10	1.51	1.70	1.77	1.70	1.87	1.83
Al ₂ O ₃	16.95	16.54	15.65	15.65	15.47	16.25	16.01	16.16	16.70	16.53	16.33
Fe ₂ O ₃ *	1.74	1.76	1.72	1.55	1.90	1.53	1.90	1.84	1.79	1.83	1.80
FeO	7.94	8.04	7.84	7.04	8.66	6.98	8.67	8.39	8.17	8.34	8.20
MgO	6.09	5.42	6.29	6.58	5.56	6.56	7.28	6.28	6.03	5.36	5.81
CaO	8.89	9.20	8.67	8.56	9.25	8.31	9.20	9.24	9.12	9.14	9.22
Na ₂ O	3.37	4.05	3.96	4.05	3.82	3.93	3.53	3.65	3.79	3.73	3.69
K ₂ O	1.40	1.56	1.65	1.55	1.95	1.51	0.97	1.31	1.20	1.32	1.23
P ₂ O ₅	0.17	0.54	0.46	0.56	0.62	0.35	0.34	0.42	0.37	0.38	0.27
TOTAL	99.86	99.54	99.74	99.70	99.84	99.98	100.10	99.52	100.02	99.55	99.92
Mg-value	57.7	54.6	58.9	62.5	53.4	62.6	59.9	57.2	56.8	53.4	55.8
or	8.29	9.25	9.73	9.11	11.56	8.85	5.71	7.77	7.07	7.85	7.28
ab	30.32	32.91	35.50	36.17	31.13	35.00	31.57	32.90	33.95	33.72	33.17
an	27.06	22.43	20.03	19.85	19.39	22.08	24.89	23.95	24.96	24.64	24.40
ne	0.00	2.15	0.00	0.00	1.98	0.00	0.00	0.00	0.00	0.00	0.00
di	12.83	15.86	15.93	15.00	18.09	13.25	14.69	15.46	14.21	14.81	15.71
hy	9.74	0.00	1.05	5.59	0.00	8.99	5.30	1.95	3.72	5.07	6.55
ol	6.55	11.45	12.53	9.56	11.63	7.43	12.80	12.69	11.09	8.58	7.89
mt	1.82	1.84	1.79	1.60	1.99	1.59	1.98	1.92	1.87	1.91	1.88
ilm	3.04	2.99	2.48	1.95	2.94	2.09	2.36	2.48	2.36	2.62	2.55
ap	0.36	1.13	0.96	1.16	1.30	0.73	0.71	0.88	0.77	0.80	0.57

TABLE 5. Chemical compositions (weight percent) and Barth-Niggli cation norms (cation percent) of pre-Pliocene basalts from the central Rio Grande rift. *Fe₂O₃ calculated from Fe³⁺/Fe²⁺ + Fe³⁺ = 0.1. Mg-value = 100(Mg/Mg+Fe²⁺).

	Cieneguilla	Cerro Negro		Jarita basalt	
	-A271	-A286	-A287	-290	-293
SiO ₂	42.46	40.60	42.14	53.29	52.71
TiO ₂	1.88	2.57	2.60	1.99	1.51
Al ₂ O ₃	11.40	12.61	12.78	15.51	14.05
Fe ₂ O ₃ *	1.98	2.62	2.36	1.88	2.04
FeO	9.03	11.95	10.77	8.57	9.29
MgO	15.54	11.45	11.00	5.43	7.35
CaO	12.98	11.90	11.87	8.97	8.79
Na ₂ O	3.09	3.81	3.55	3.47	3.17
K ₂ O	0.81	1.02	0.73	0.32	0.53
P ₂ O ₅	1.01	1.39	1.47	0.27	0.19
TOTAL	100.18	99.92	99.27	99.70	99.63
Mg-value	75.4	63.1	64.5	53.0	58.5
Q	0.00	0.00	0.00	3.80	1.35
or	0.00	3.80	4.31	1.91	3.16
ab	0.00	0.00	7.98	31.54	28.72
an	14.41	14.15	16.79	26.13	22.76
ne	16.15	20.33	14.33	0.00	0.00
lc	3.71	1.73	0.00	0.00	0.00
di	32.60	28.26	25.99	13.71	16.00
hy	0.00	0.00	0.00	17.56	23.35
ol	26.26	22.57	21.46	0.00	0.00
cs	0.28	0.00	0.00	0.00	0.00
mt	2.01	2.71	2.44	1.98	2.14
ilm	2.54	3.55	3.62	2.81	2.12
ap	2.05	2.88	3.07	0.57	0.40

TABLE 5 (continued)

	OTHER				
	Cundiyo flow	Bishop's Lodge flow	Rio del Oso dike	Lobato basalt	Chili flow
	-273	-274	-278	-011	-226
SiO ₂	50.99	47.95	48.50	49.51	49.36
TiO ₂	1.84	1.85	1.50	1.57	1.58
Al ₂ O ₃	12.44	12.55	16.75	17.47	16.63
Fe ₂ O ₃ *	1.99	2.13	1.95	1.98	1.90
FeO	9.04	9.71	8.88	9.01	8.67
MgO	9.88	8.27	8.08	5.31	7.63
CaO	10.66	12.99	9.65	10.23	9.73
Na ₂ O	2.59	2.92	3.42	3.57	3.26
K ₂ O	0.30	0.79	0.76	0.70	0.62
P ₂ O ₅	0.37	0.45	0.33	0.28	0.34
TOTAL	100.10	99.61	99.82	99.63	99.72
Mg-value	66.1	60.3	61.8	51.2	61.1
Q	0.00	0.00	0.00	0.00	0.00
or	1.77	4.71	4.47	4.17	3.66
ab	23.26	19.16	28.40	32.29	29.27
an	21.45	18.97	27.99	29.81	28.92
ne	0.00	4.37	1.30	0.00	0.00
lc	0.00	0.00	0.00	0.00	0.00
di	23.23	34.44	14.02	15.59	13.70
hy	22.36	0.00	0.00	1.04	6.07
ol	2.51	12.58	19.05	12.24	13.48
cs	0.00	0.00	0.00	0.00	0.00
mt	2.07	2.23	2.02	2.07	1.98
ilm	2.56	2.60	2.08	2.20	2.20
ap	0.77	0.95	0.69	0.59	0.71

Table 6. Result of least-squares modeling in weight percent. Sample numbers and mineral compositions are those used in calculations. "Amount" refers to amount of derivative melt at each stage relative to the initial composition.

Group B basaltic andesite to latite-andesite series:

-230 $\xrightarrow{\hspace{15em}}$ -036
Amount: 1.00 Amount: 0.75
Subtr: 6% ol (Fo₈₄)
 15% Cpx (Wo₄₀En₄₅Fs₁₅)
 10% plag (An₄₆Ab₅₂Or₂)
 2% mt
 2% ilm
Add: 10% qtz

-230 $\xrightarrow{\hspace{3em}}$ -045 $\xrightarrow{\hspace{3em}}$ -063 $\xrightarrow{\hspace{3em}}$ -036
Amount: 1.00 Amount: 1.05 Amount: 0.95 Amount: 0.80
Subtr: 3% ol (Fo₈₄) Subtr: 6% cpx (Wo₄₀En₄₅Fs₁₅) Subtr: 6% cpx (Wo₄₂En₄₇Fs₁₁)
 0.1% Cr-spinel 5% plag (An₅₈Ab₄₀Or₂) 10% plag (An₅₀Ab₄₈Or₂)
 6% plag (An₄₆Ab₅₂Or₂) 2% ol (Fo₈₄) 2% opx (Wo₃En₇₉Fs₁₈)
 2% qtz 1% mt 1% mt
1% ilm 0.5% ilm
Add: 5% qtz Add: 4% qtz

Group D alkali olivine basalt:

-061 $\xrightarrow{\hspace{10em}}$ -029
Amount: 1.00 Amount: 0.78
Subtr: 9% ol (Fo₈₁)
 9% cpx (Wo₄₅En₄₂Fs₁₃)
 4% plag (An₆₅Ab₃₄Or₁)

Group D hawaiite

-028 $\xrightarrow{\hspace{10em}}$ -024 $\xrightarrow{\hspace{10em}}$ -213 $\xrightarrow{\hspace{10em}}$ -233
Amount: 1.00 Amount: 0.92 Amount: 1.00 Amount: 0.95
Subtr: 5% ol (Fo₈₂) Subtr: 4% cpx (Wo₄₃En₄₄Fs₁₃)
 3% cpx (Wo₄₄En₄₅Fs₁₁) 0.5% ol (Fo₇₄)

Table 7. Silica and alumina buffer reactions and activity models used in this paper.

Reaction	A	B	C
1) $2/3 \text{Fe}_3\text{O}_4 + \text{SiO}_2 = \text{Fe}_2\text{O}_3 + 1/3 \text{O}_2$	8,270	-2.81	-0.0406
2) $\text{CaMgSi}_2\text{O}_6 + 1/2 \text{SiO}_2 + \text{Al}_2\text{O}_3 = \text{CaAl}_2\text{Si}_2\text{O}_8 + 1/2 \text{Mg}_2\text{SiO}_4$	-6,776	0.859	0.2157
3) $\text{Mg}_2\text{SiO}_4 + \text{SiO}_2 = 2 \text{MgSiO}_3$	-1,034	0.597	-0.0424
4) $\text{Mg}_2\text{SiO}_4 + \text{Al}_2\text{O}_3 = \text{MgSiO}_3 + \text{MgAl}_2\text{O}_4$	-8,131	2.633	0.1344

Activity Models

$$a_{\text{Fe}_3\text{O}_4}^{\text{mt}} = X_{\text{Fe}}^{\text{A}} \cdot (1/2 X_{\text{Fe}}^{\text{B}})^2$$

$$a_{\text{MgAl}_2\text{O}_4}^{\text{SP}} = X_{\text{MgAl}_2\text{O}_4}^{\text{SP}}$$

$$a_{\text{Fe}_2\text{SiO}_4}^{\text{ol}} = (X_{\text{Fe}_2\text{SiO}_4}^{\text{ol}})^2$$

$$a_{\text{CaAl}_2\text{Si}_2\text{O}_8}^{\text{plag}} = X_{\text{CaAl}_2\text{Si}_2\text{O}_8}^{\text{plag}}$$

$$a_{\text{MgSiO}_3}^{\text{opx}} = X_{\text{MgSiO}_3}^{\text{opx}}$$

$$a_{\text{CaMgSi}_2\text{O}_6}^{\text{cpx}} = X_{\text{Ca}}^{\text{M}_2} \cdot X_{\text{Mg}}^{\text{M}_1}$$

FIGURE CAPTIONS

- Figure 1. Generalized structure map of the central Rio Grande rift. Letters A-G indicate major Plio-Pleistocene volcanic fields discussed in this work. Modified from Woodward et al. (1975).
- Figure 2. Sample localities for the Cerros del Rio, Santa Ana Mesa, and El Alto volcanic fields. Stars indicate samples from cinder cones. Geology is generalized from Smith et al. (1970), Stearns (1953b), and Kelley (1978).
- Figure 3. Alkalis vs. silica diagram for lavas of the Cerros del Rio, Santa Ana Mesa, and El Alto volcanic fields. Stars labelled B and D are most magnesian basaltic andesite and alkali olivine basalt, respectively. Empirical line dividing tholeiite from alkali olivine basalt in Hawaii (MacDonald and Katsura, 1964) is shown for reference. MOR indicates composition of average mid-ocean ridge tholeiite (Carmichael et al., 1975).
- Figure 4. Normative mineralogy of volcanic rocks from the Cerros del Rio, Santa Ana Mesa, and El Alto volcanic fields. Catatom percent. Dashed line for groups C and D lavas separates hawaiite with $An/(An+Ab) < 40$ from alkali basalt with $An/(An+Ab) > 40$. Stars indicate most magnesian basaltic andesite and alkali olivine basalt.
- Figure 5. Photomicrographs. Length of bar is 1 mm unless otherwise indicated.
- A. Intergranular texture in group A olivine tholeiite (-058). Length of bar is 0.2 mm.
- B. Partial ophitic texture in group A olivine tholeiite (-087). Right side of photograph shows single pyroxene grain enclosing laths of plagioclase (ophitic texture). Left side shows intergranular texture. Partly crossed nicols. Length of bar is 0.5 mm.
- C. Left. Partially resorbed quartz xenocryst surrounded by reaction rim of clinopyroxene (-230). Right. Nearly euhedral quartz xenocryst, also surrounded by reaction rim of clinopyroxene (-231).
- D. Partially resorbed plagioclase xenocrysts (-045). Partly crossed nicols. For photograph on right, length of bar is 0.5 mm.
- E. Hyalopilitic texture in latite-andesite (-036). Length of bar is 0.2 mm.
- F. Cumulate plagioclase in basaltic andesite -044. Length of bar is 5 mm.
- Figure 6. Pyroxene and olivine compositions of group A olivine tholeiite.

- Figure 7. Feldspar compositions of group A olivine tholeiite.
- Figure 8. Compositions of spinel, titaniferous magnetite, and ilmenite of group A olivine tholeiite.
- Figure 9. Pyroxene and olivine compositions of group B basaltic andesite and latite-andesite.
- Figure 10. Feldspar compositions of group B basaltic andesite and latite-andesite.
- Figure 11. Compositions of spinel, titaniferous magnetite, and ilmenite of group B basaltic andesite and latite-andesite.
- Figure 12. Phenocryst phases present in lavas of the Cerros del Rio, Santa Ana Mesa, and El Alto volcanic fields. Groups A-D same as figure 3. Group A tholeiite contains phenocrysts of olivine, plagioclase, and minor clinopyroxene. The group C basaltic lava with lower total alkalis contains phenocrysts of olivine and plagioclase. For groups B and D, the most magnesian (least evolved) compositions are shown by stars. These rocks contain phenocrysts of olivine. Compositional sequences for groups B and D are shown by arrows. Within each sequence, heavy lines indicate change in phenocryst mineralogy. Mineral name beside line indicates presence of the phase as phenocrysts in rocks on that side of line. Absence of phase is also indicated. Dashed arrow marked CPX is clinopyroxene control line showing addition of clinopyroxene to composition indicated.
- Figure 13. $100 \cdot (\text{Mg}/\text{Mg}+\text{Fe}^{+2})_{\text{olivine}}$ of the most magnesian phenocrysts vs. $100 \cdot (\text{Mg}/\text{Mg}+\text{Fe}^{+2})_{\text{whole rock}}$ for lavas of the Cerros del Rio, Santa Ana Mesa, and El Alto volcanic fields. Stippled region indicates equilibrium values of $K_{\text{D}}^{\text{Fe-Mg}}_{\text{Olivine-Liquid}} = 0.30$ (Roeder and Emslie, 1970).
- Figure 14. $100 \cdot \text{Mg}/(\text{Mg}+\text{Fe})$ vs. $\text{An}/(\text{An}+\text{Ab})$ for phenocrysts and microphenocrysts of the group B basaltic andesite and latite-andesite.
- Figure 15. Variation diagrams (weight percent) for the group B basaltic andesite and latite-andesite. FeO^* is total iron as FeO . Subtraction of phases (except quartz) present as phenocrysts or xenocrysts is indicated by arrows. For quartz, arrow (dashed) indicates addition. Length of arrow represents 10 percent subtraction/addition of phase. Composition with highest Mg-value (-230) is indicated by star.

- Figure 16. Pyroxene and olivine compositions of group C basanite and group D alkali olivine basalt and hawaiiite.
- Figure 17. Feldspar compositions of group C basanite and group D alkali olivine basalt and hawaiiite.
- Figure 18. Compositions of titaniferous magnetite and spinel of group C basanite and group D alkali olivine basalt and hawaiiite.
- Figure 19. Variation diagrams (weight percent) for the group D alkali olivine basalt and hawaiiite. FeO* is total iron as FeO. Subtraction of phases present as phenocrysts is indicated by arrows. Length of arrow represents 10 percent subtraction of phase. Star represents alkali olivine basalt (-061) with highest Mg-value and lowest SiO₂ and (Na₂O+K₂O). Solid and open triangles represent specific hawaiiites (-028 and -213, respectively) which can be related by fractional crystallization to other hawaiiites. Solid square is -283, which has accumulated clinopyroxene.
- Figure 20. Sample localities for the Albuquerque Volcanoes. Stippled area is basalt. Star indicates sample from cinder cone. Geology is generalized from Kelley and Kudo (1978).
- Figure 21. Alkalis vs. silica diagram for lavas of the Albuquerque Volcanoes. Empirical line dividing tholeiite from alkali olivine basalt in Hawaii (MacDonald and Katsura, 1964) is shown for reference. MOR indicates composition of average mid-ocean ridge tholeiite (Carmichael et al., 1974).
- Figure 22. Normative mineralogy of lavas of the Albuquerque Volcanoes. Catatom percent.
- Figure 23. Pyroxene and olivine compositions of Albuquerque Volcanoes olivine tholeiite -093.
- Figure 24. Feldspar compositions of Albuquerque Volcanoes olivine tholeiite -093.
- Figure 25. Compositions of titaniferous magnetite and ilmenite for Albuquerque Volcanoes olivine tholeiite -093.
- Figure 26. Sample localities for the Wind Mesa and Cat Hills (left) and Isleta (right) volcanic fields. Broadly-ruled pattern indicates older basalt (late Pliocene and/or Pleistocene) of Wind Mesa; finely-ruled pattern indicates Pleistocene basalt (140,000 yrs.). Broadly-stippled pattern indicates Plio-Pleistocene basalt of Isleta Volcano; finely-stippled pattern is basaltic tuff. Stars indicate samples from cinder cones. Geology is generalized from Kelley and Kudo (1978).

- Figure 27. Alkalis vs. silica diagram for lavas of Isleta Volcano, Wind Mesa Volcano, and the Cat Hills volcanic field. Empirical line dividing tholeiitic from alkali olivine basalt in Hawaii (MacDonald and Katsura, 1964) is shown for reference. MOR indicates composition of average mid-ocean ridge tholeiite (Carmichael et al., 1974). Stars indicate rocks with high Mg-values, which are possible parental compositions.
- Figure 28. Normative mineralogy of volcanic rocks of Isleta and Wind Mesa Volcanos and the Cat Hills volcanic field. Symbols same as figure 27. Catatom percent.
- Figure 29. Sample localities for pre-Pliocene lavas of the central Rio Grande rift.
- Figure 30. Composite stratigraphic column for Cenozoic rocks of the Española and Santo Domingo basins. Compositions of analyzed basaltic rocks shown by symbols. Time scale after Berggren and VanCouvering (1974). Data compiled from Galusha and Blick (1971), Stearns (1953b), Sun and Baldwin (1958), Bailey et al. (1969), Butler (1971), Spiegel and Baldwin (1963), and Manley (1976).
- Figure 31. Alkalis vs. silica diagram for pre-Pliocene lavas of the central Rio Grande rift. Empirical line dividing tholeiitic from alkali olivine basalt in Hawaii (MacDonald and Katsura, 1964) is shown for reference.
- Figure 32. Normative mineralogy of pre-Pliocene lavas of the central Rio Grande rift. Symbols same as figure 29. Catatom percent.
- Figure 33. Pyroxene and olivine compositions of Cieneguilla limburgite -271.
- Figure 34. One-atmosphere liquidus phase diagram for the system $\text{CaMgSi}_2\text{O}_6$ - $\text{CaAl}_2\text{Si}_2\text{O}_8$ - Mg_2SiO_4 - SiO_2 (after Presnall, 1976).
- Figure 35. Alkalis vs. silica diagram for Servilleta basalt of Taos Plateau. Data from Aoki (1967), Lipman (1969), and Lipman and Mehnert (1975). Field of Albuquerque Volcanoes shown for comparison. Empirical line dividing tholeiite from alkali olivine basalt in Hawaii (MacDonald and Katsura, 1964) is indicated. MOR indicates composition of average mid-ocean ridge tholeiite (Carmichael et al., 1974).

Figure 36. Schematic diagram of central Rio Grande rift. Low velocity zone (LVZ) diapir modeled after Lipman (1969), Bridwell (1976), and Ramberg et al. (1978), and by analogy with other continental rift zones (e.g., Ramberg, 1976; Baker et al., 1978). Jemez lineament modeled after Mayo (1958) and Chapin et al. (1978). Model shows tholeiitic and alkalic magmas of the Cerros del Rio, El Alto, and Santa Ana Mesa volcanic fields, which are located along transverse offset of rift (shown here as Jemez lineament), originating from various depths (35-70 km) within diapir; and tholeiites of the Albuquerque Volcanoes from near top of diapir (approximately 35 km).

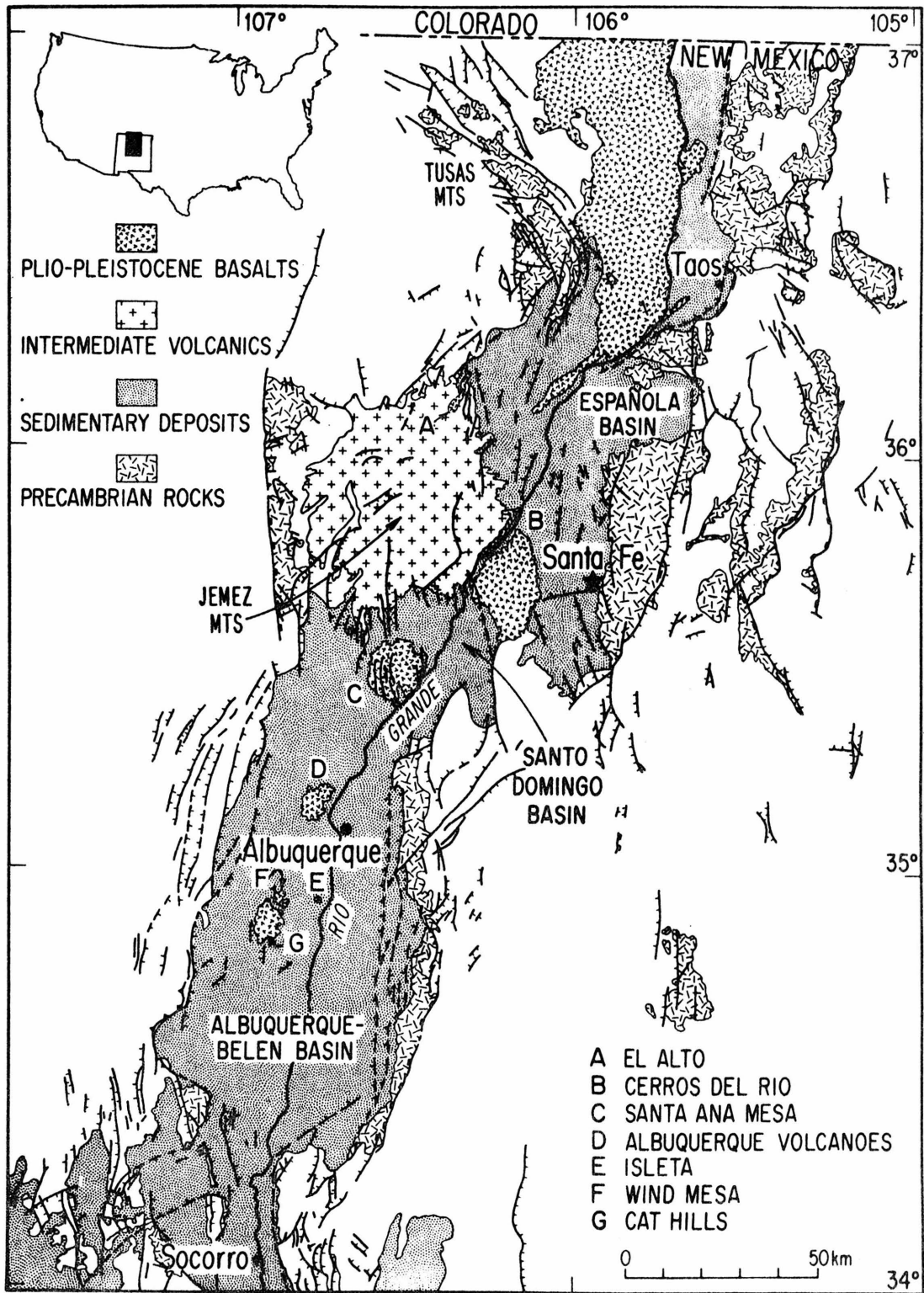


Figure 1

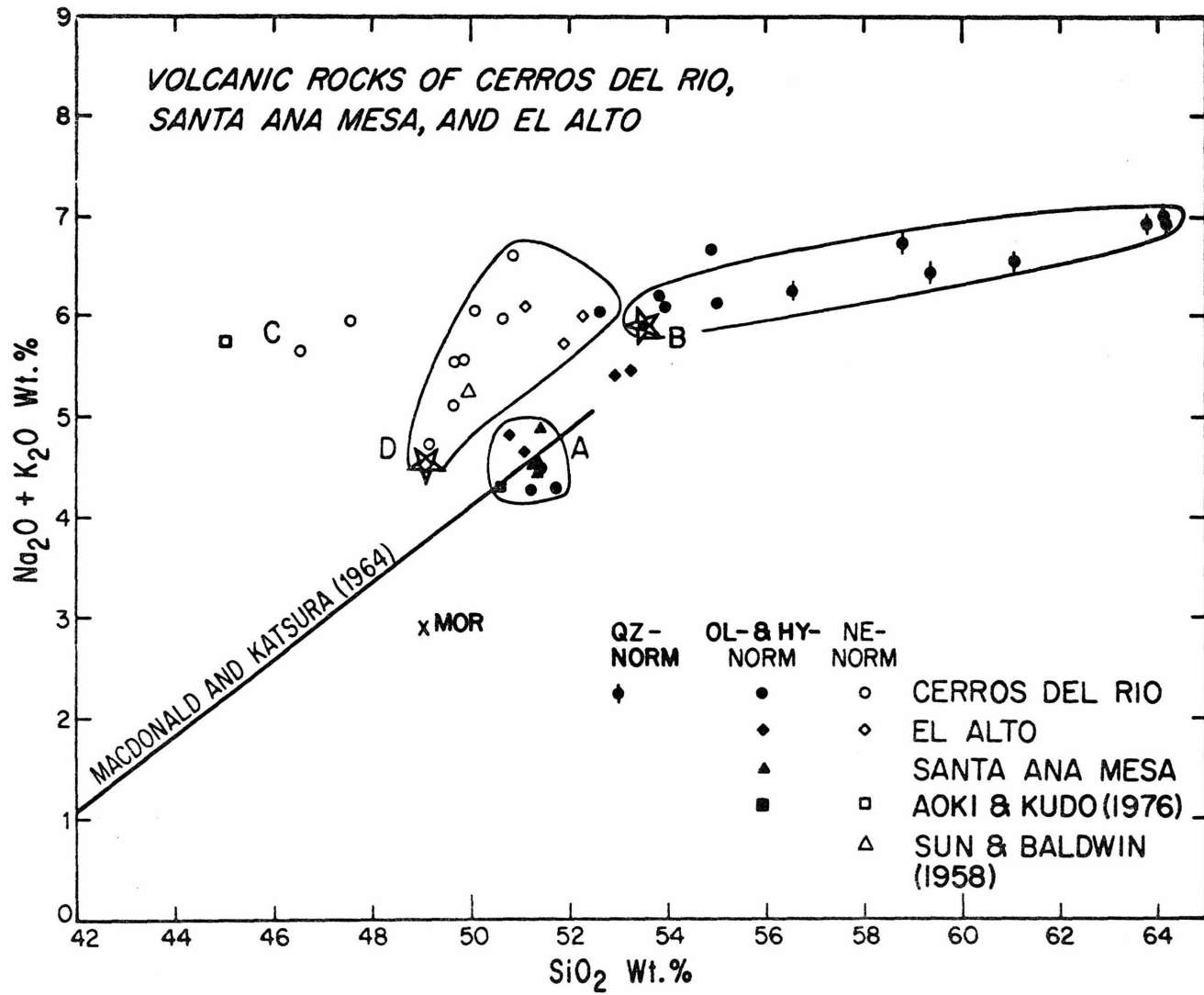


Figure 3

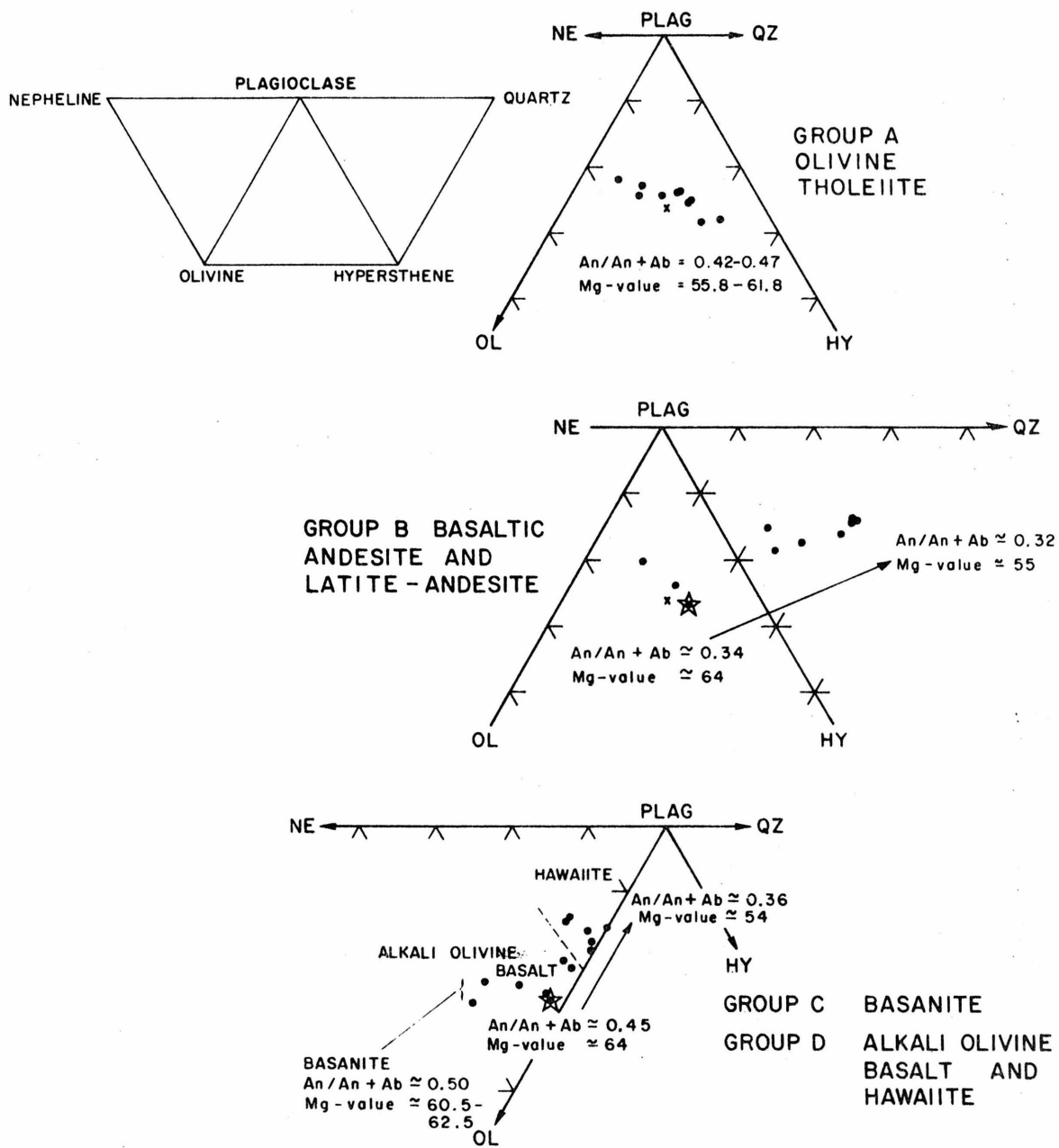


Figure 4

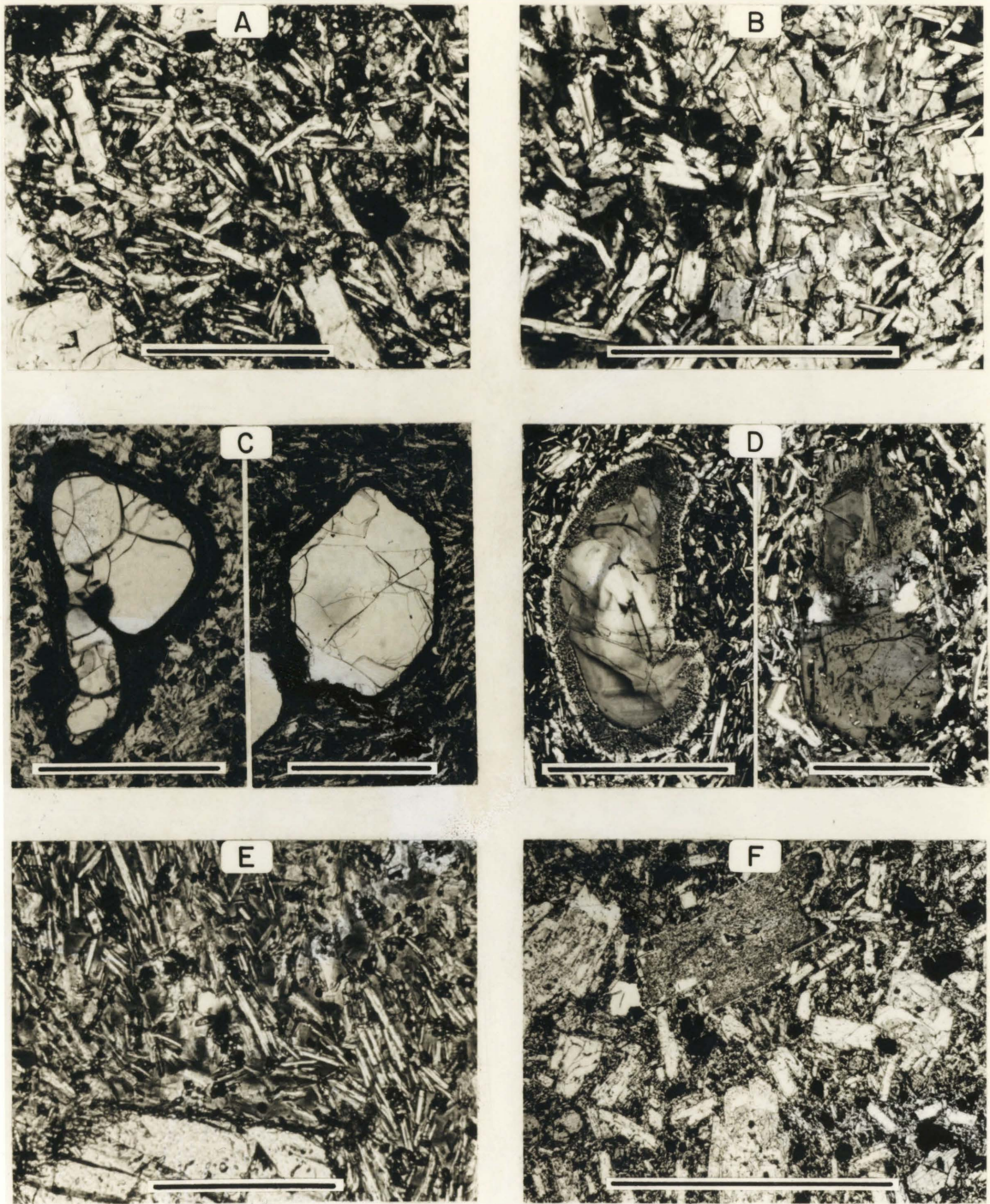


Figure 5

GROUP A OLIVINE THOLEIITE

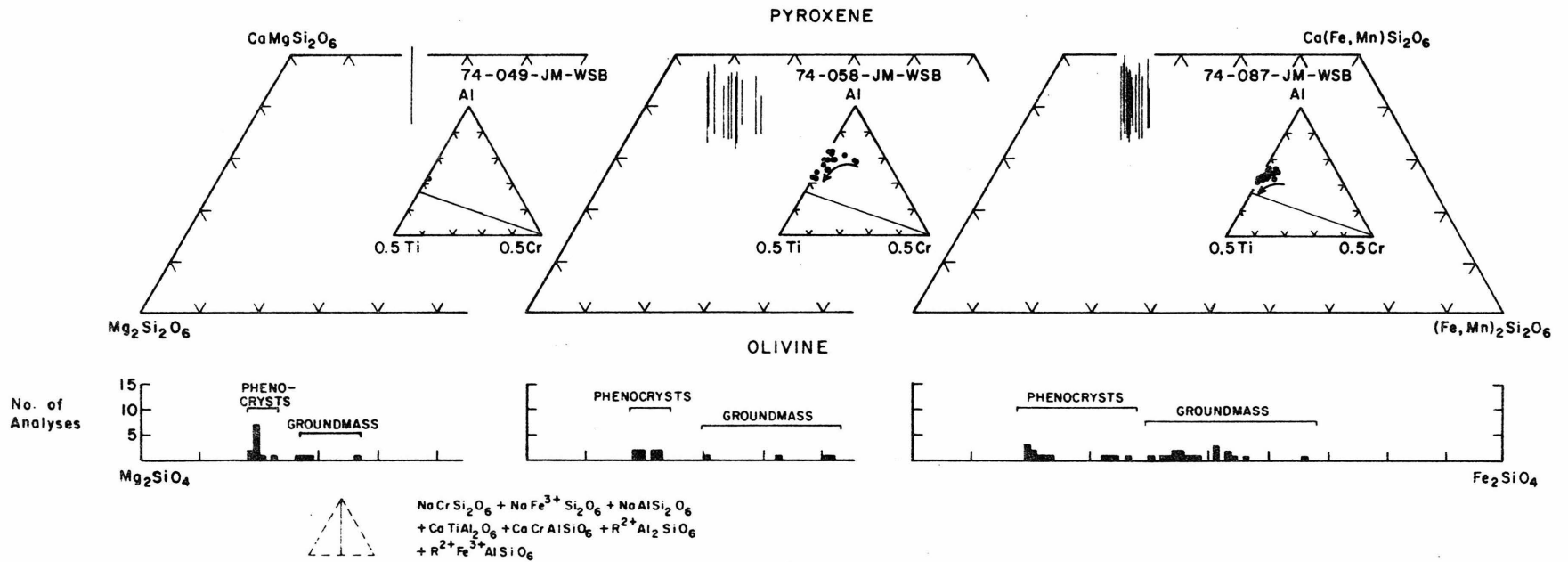


Figure 6

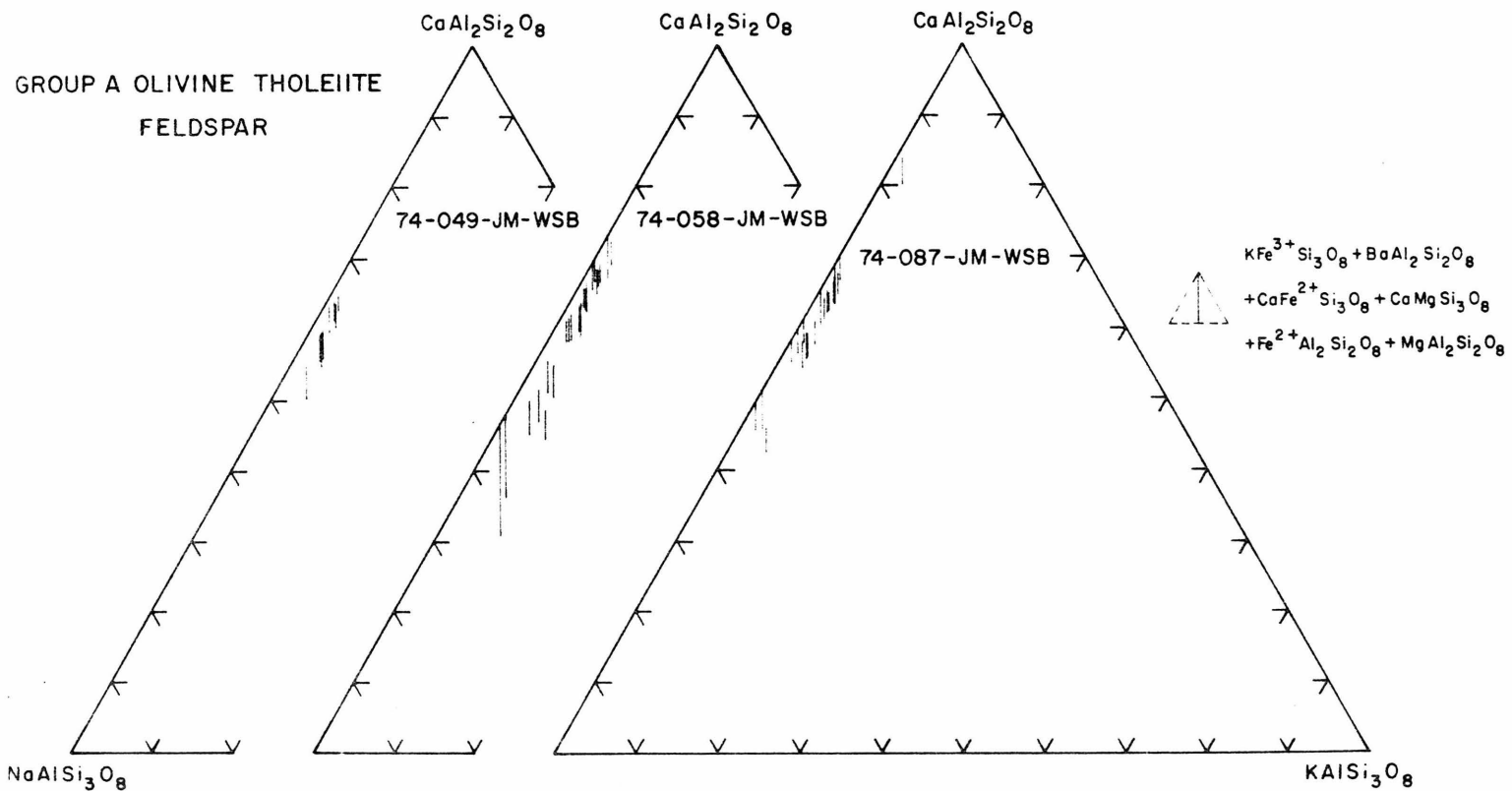


Figure 7

GROUP A OLIVINE THOLEIITE
OXIDE MINERALS

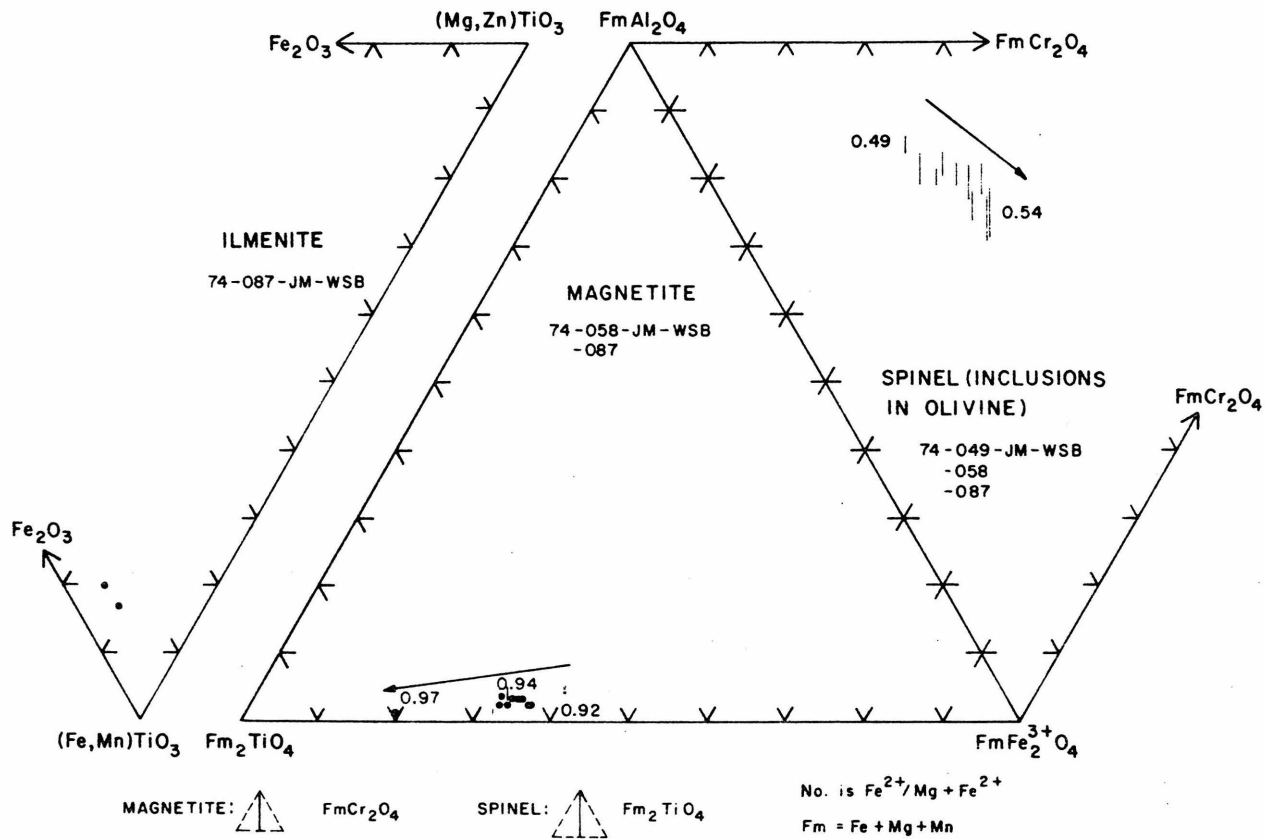


Figure 8

GROUP B BASALTIC ANDESITE & LATITE-ANDESITE

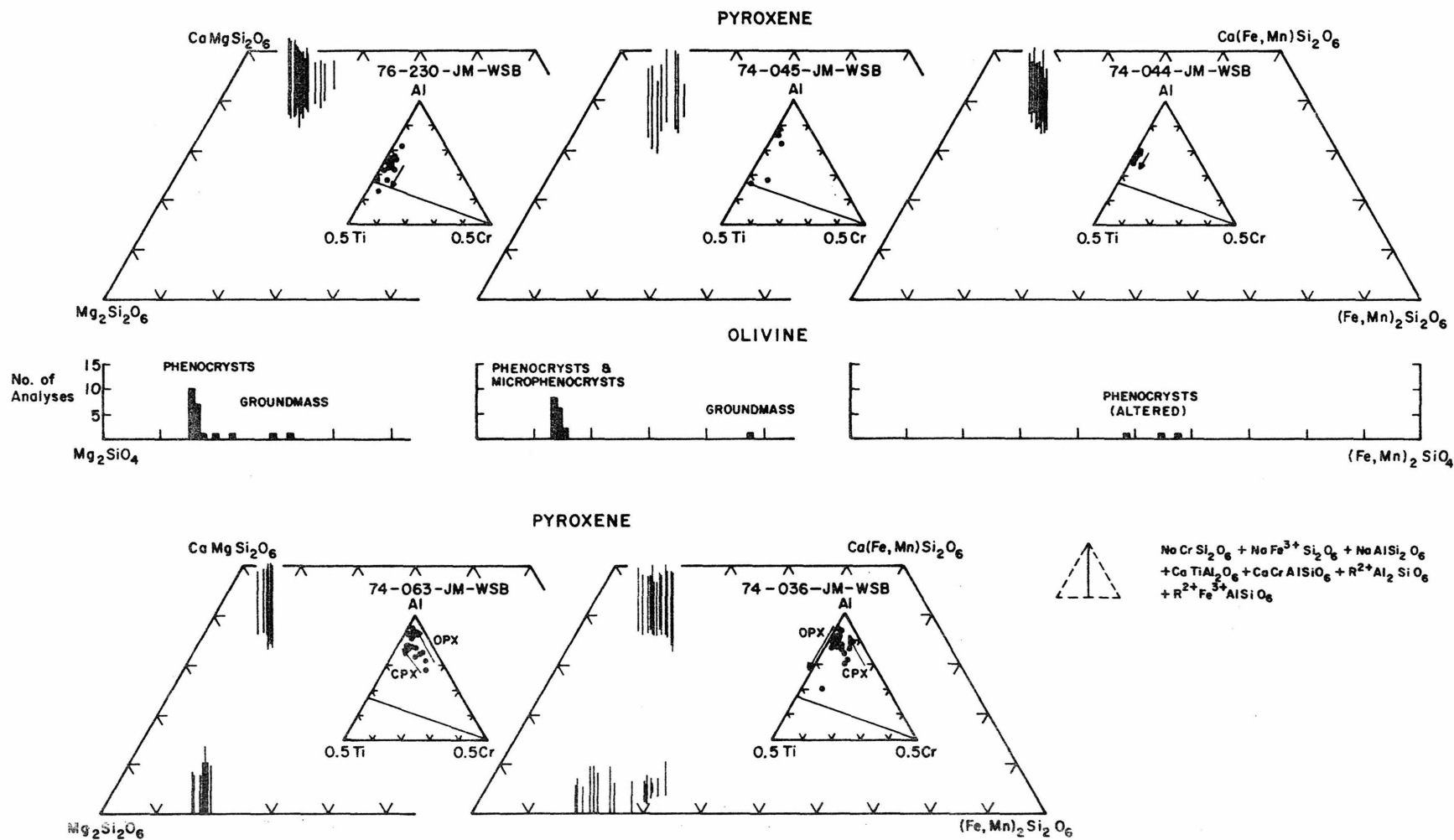


Figure 9

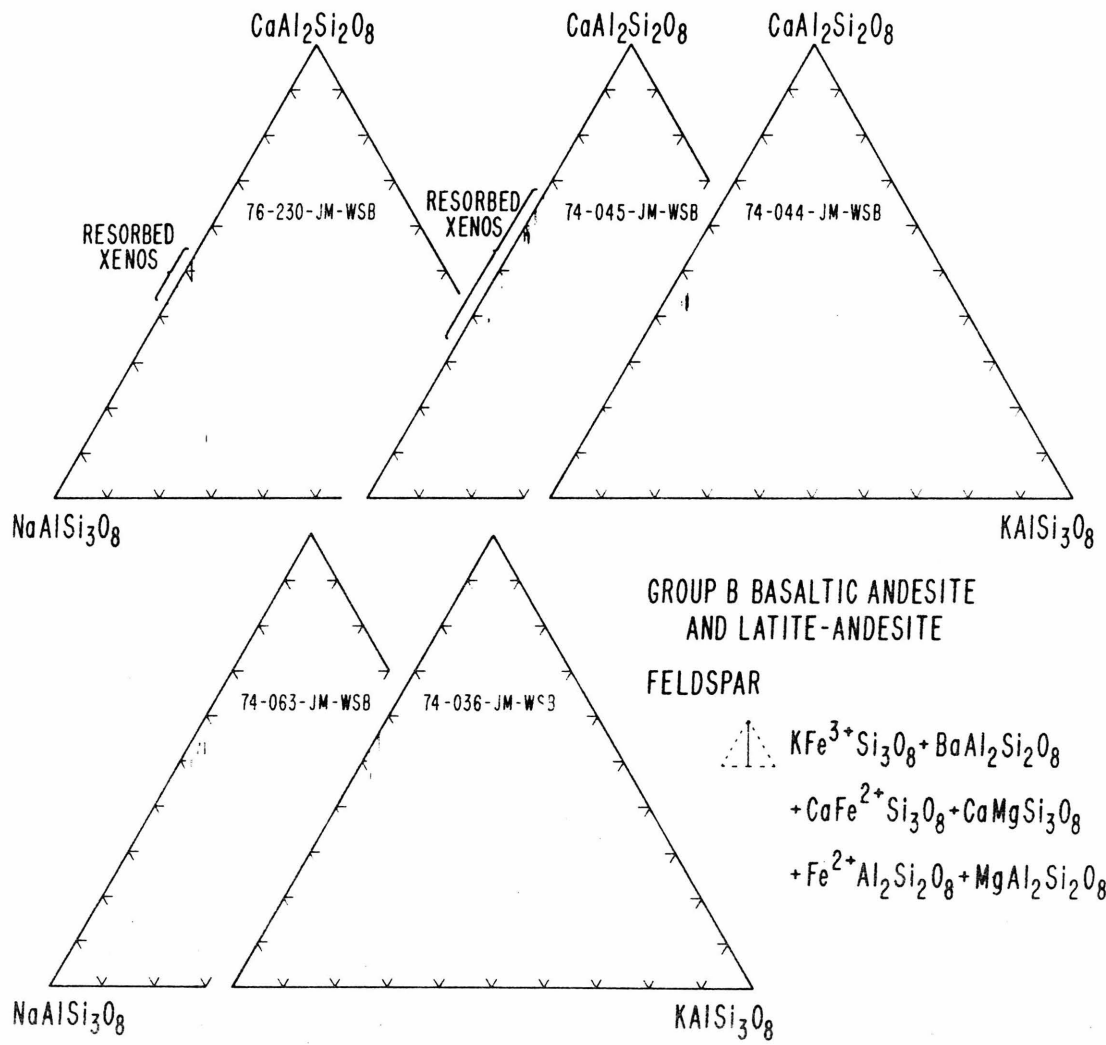


Figure 10

GROUP B BASALTIC ANDESITE & LATITE - ANDESITE

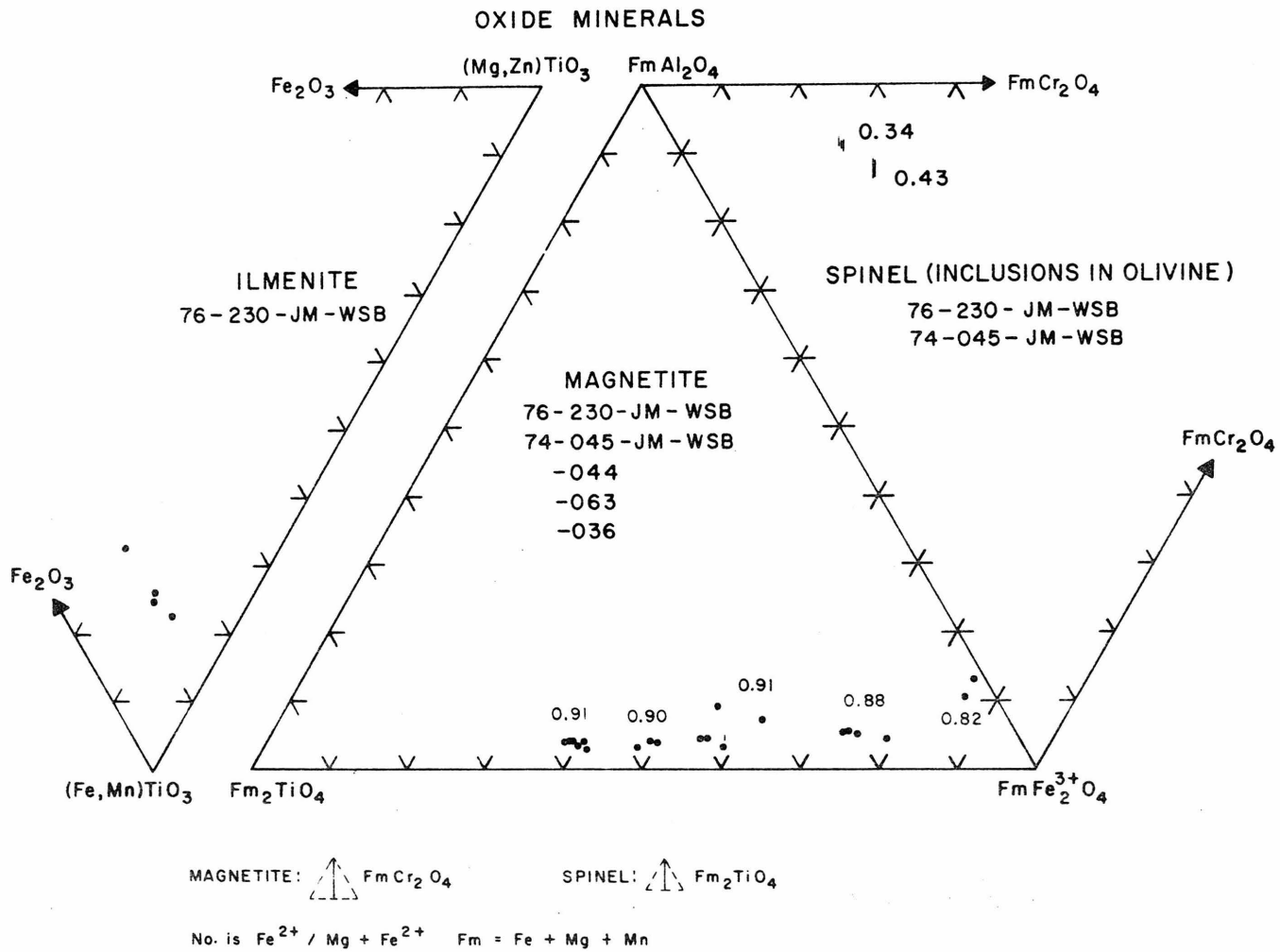


Figure 11

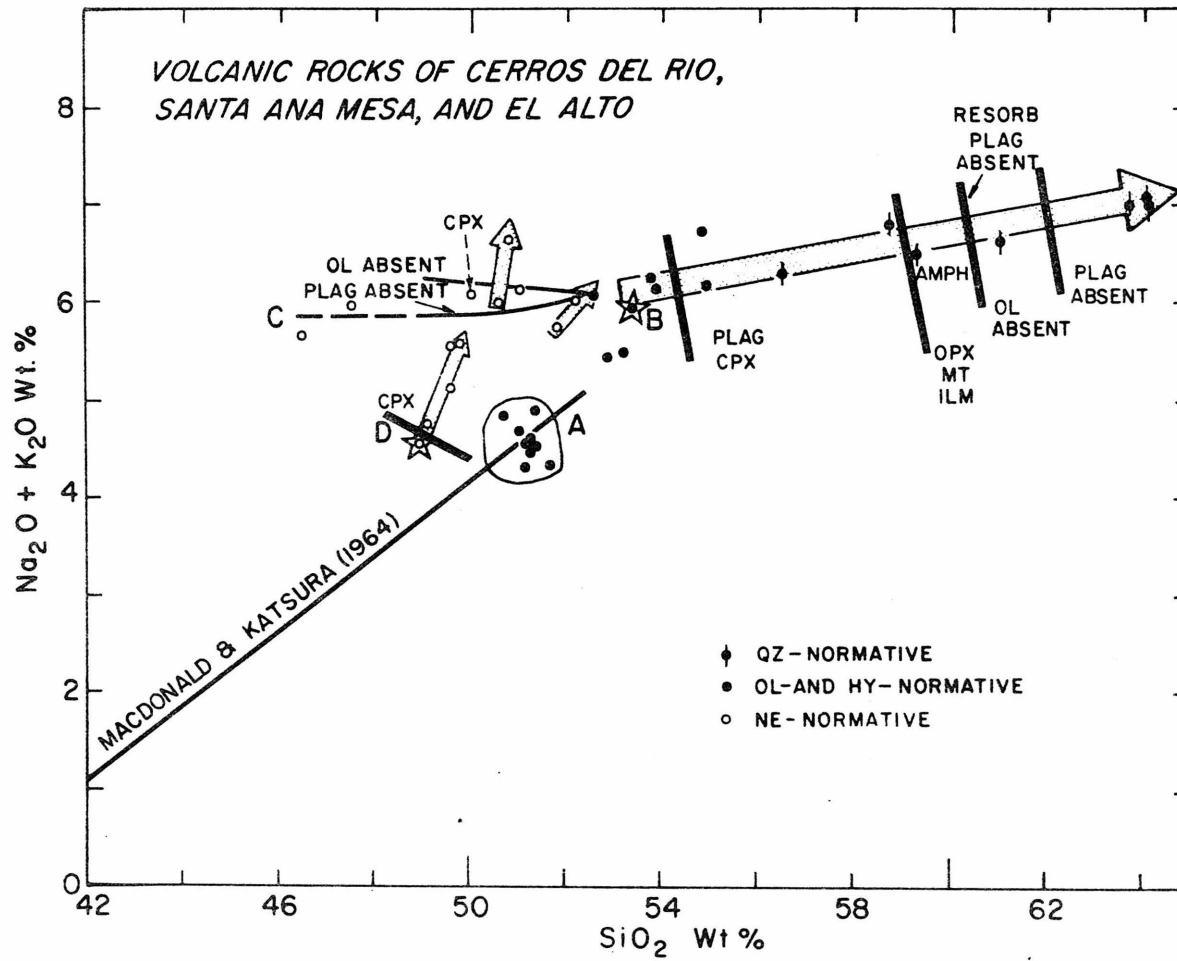


Figure 12

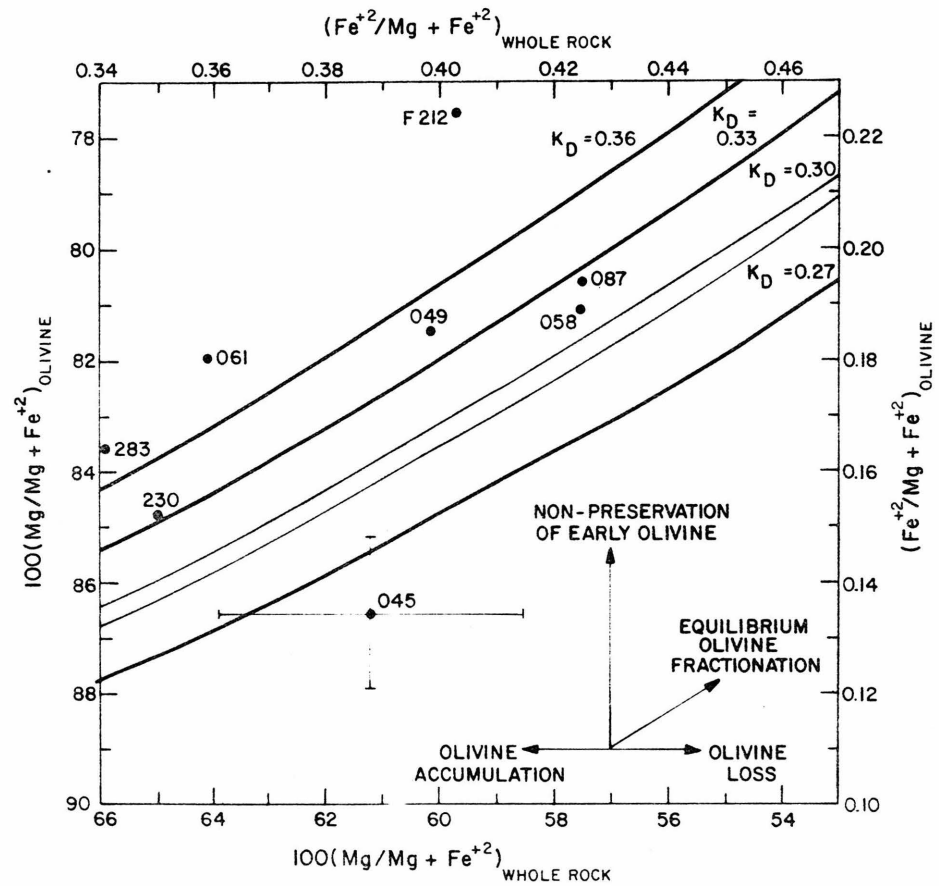
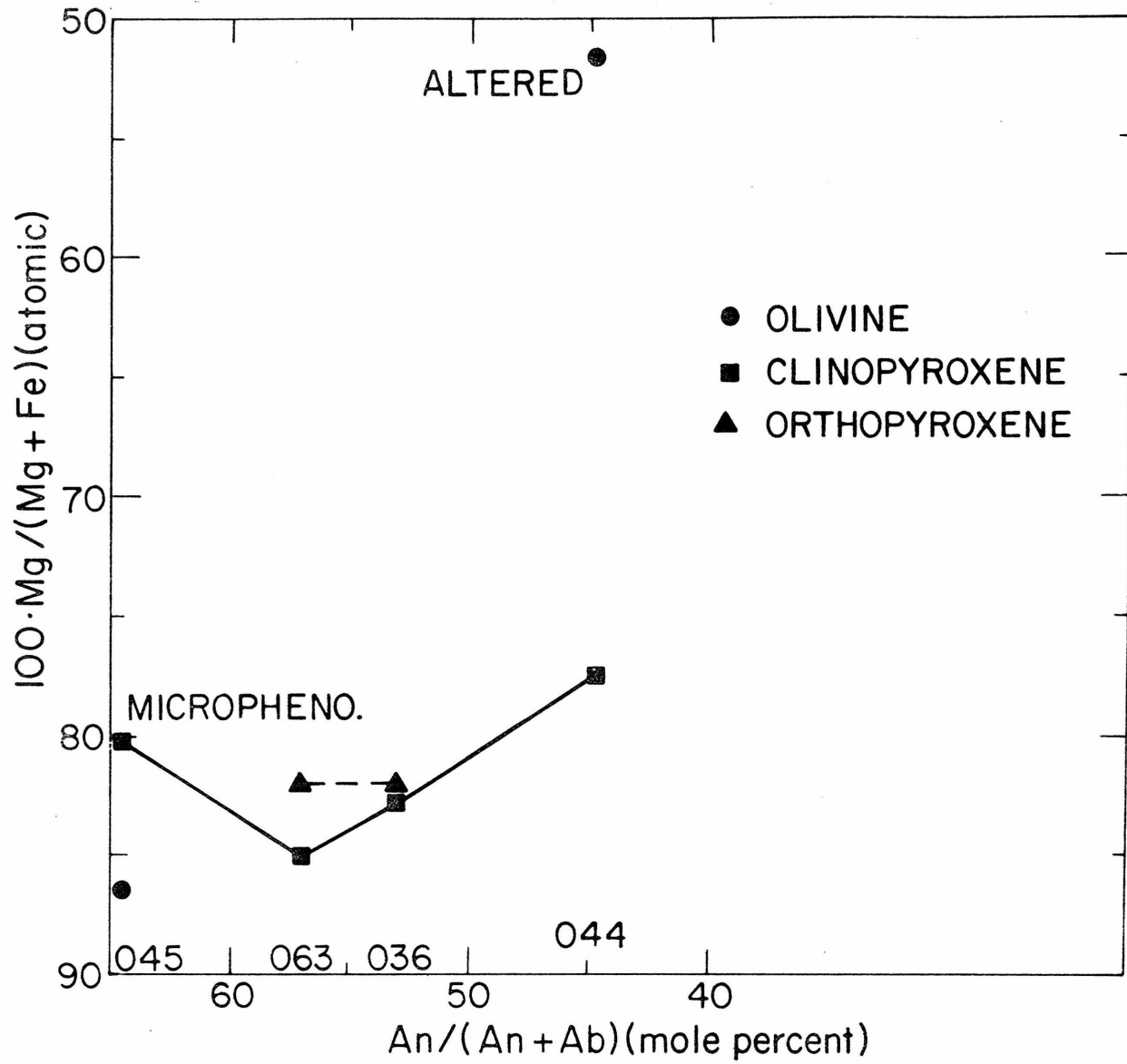


Figure 13

Figure 14



GROUP B BASALTIC ANDESITE AND LATITE-ANDESITE

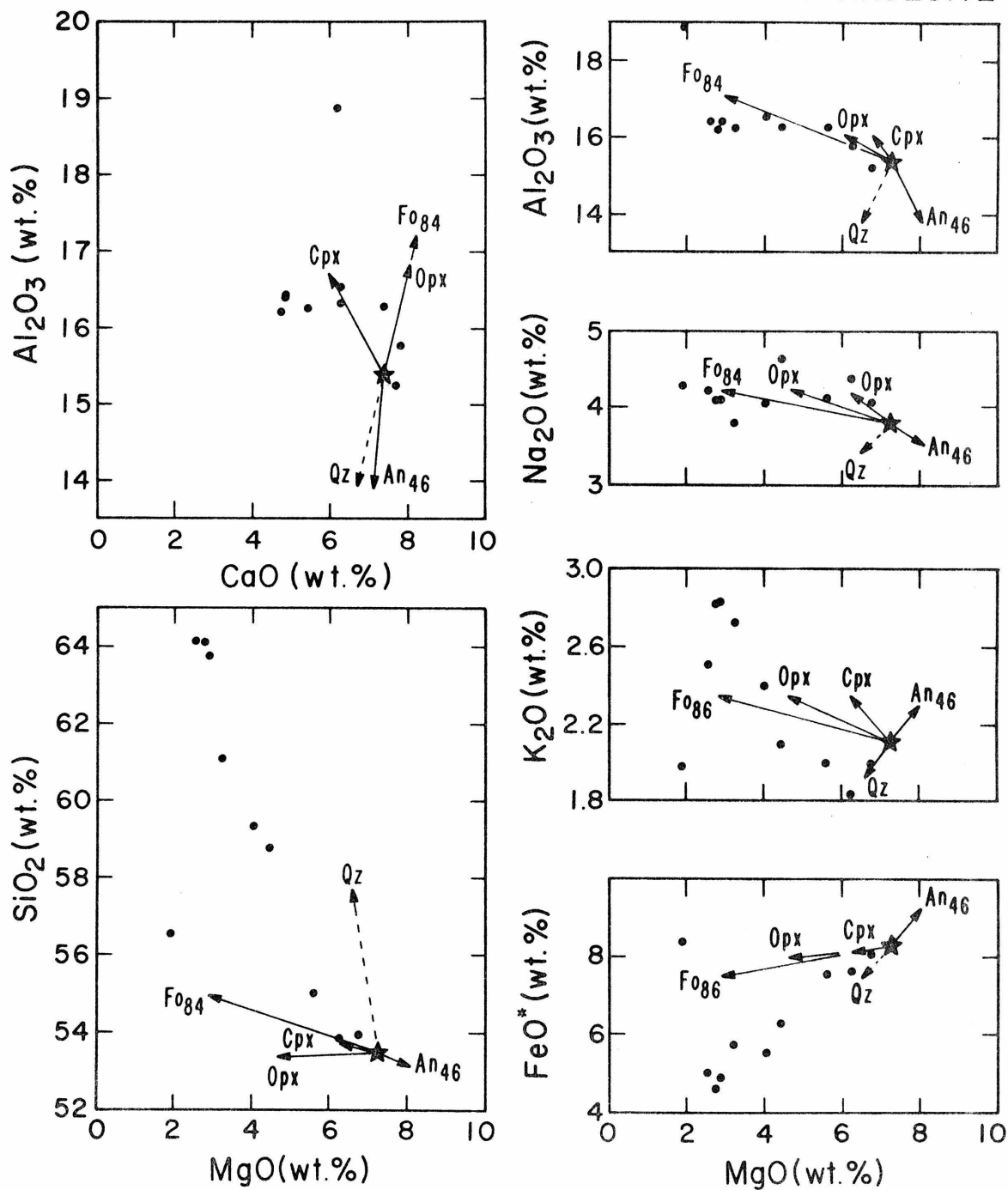


Figure 15

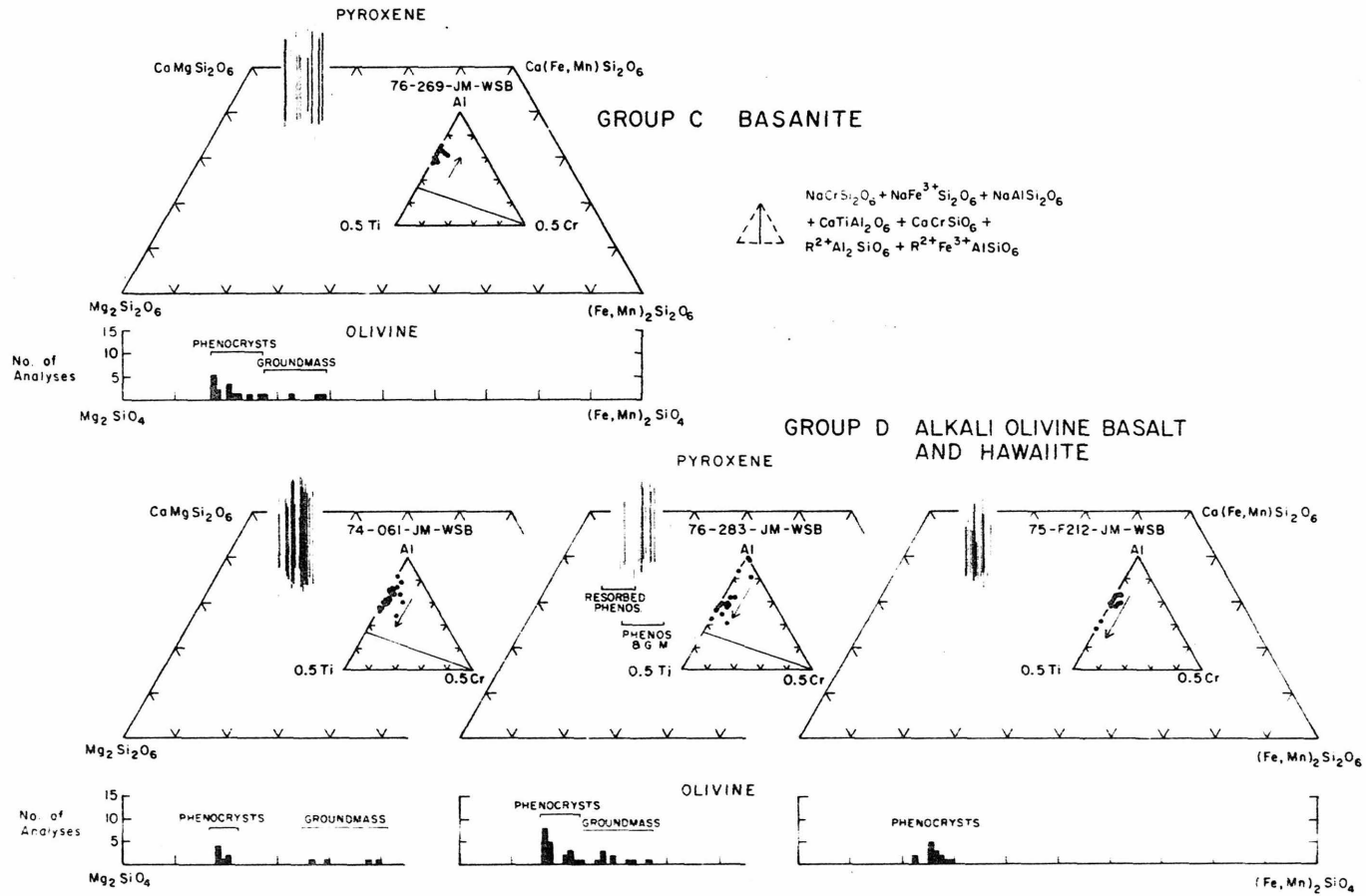


Figure 16

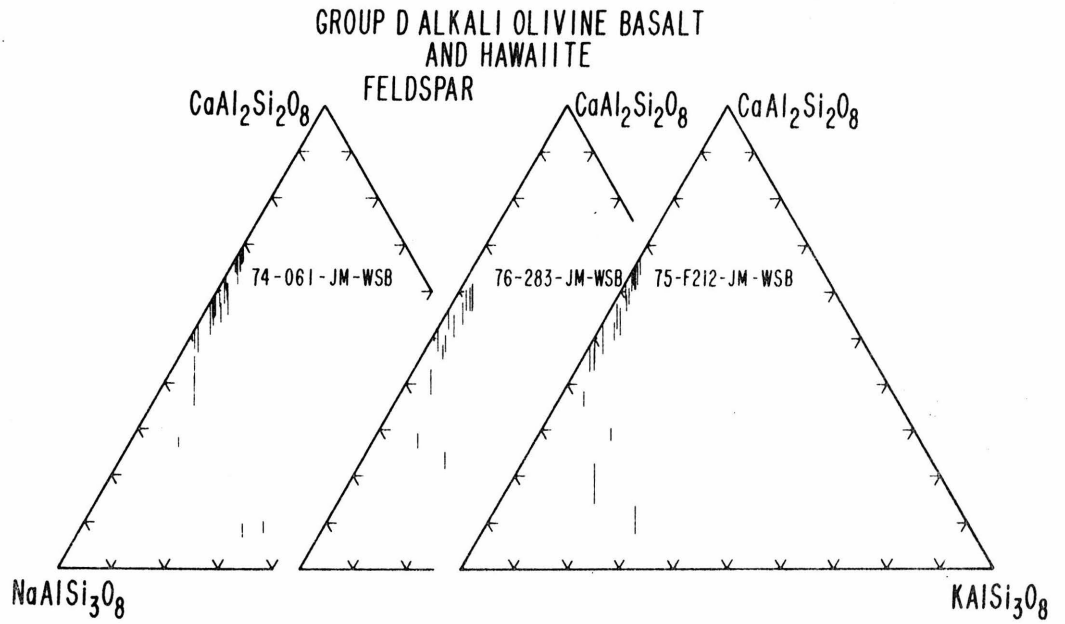
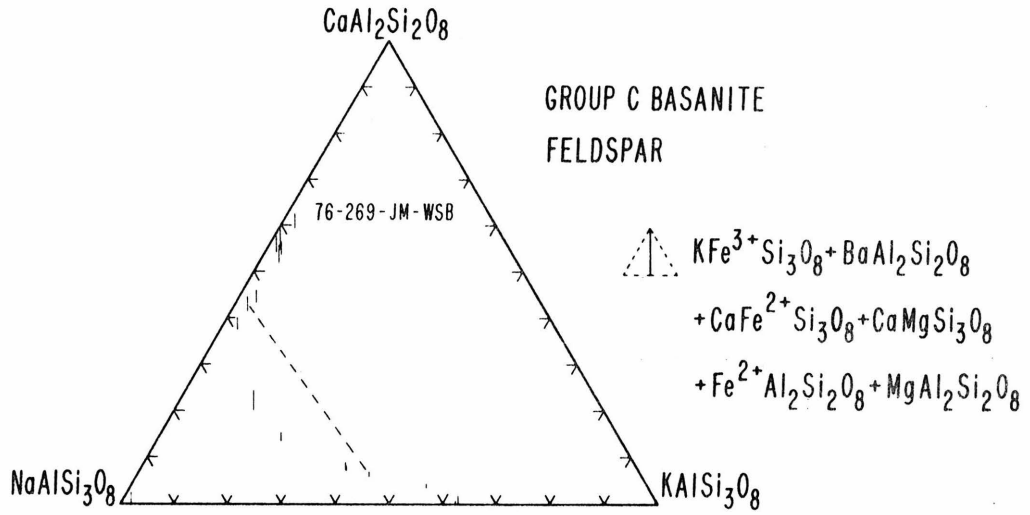


Figure 17

GROUPS C & D { BASANITE
 ALKALI OLIVINE BASALT
 HAWAIIITE

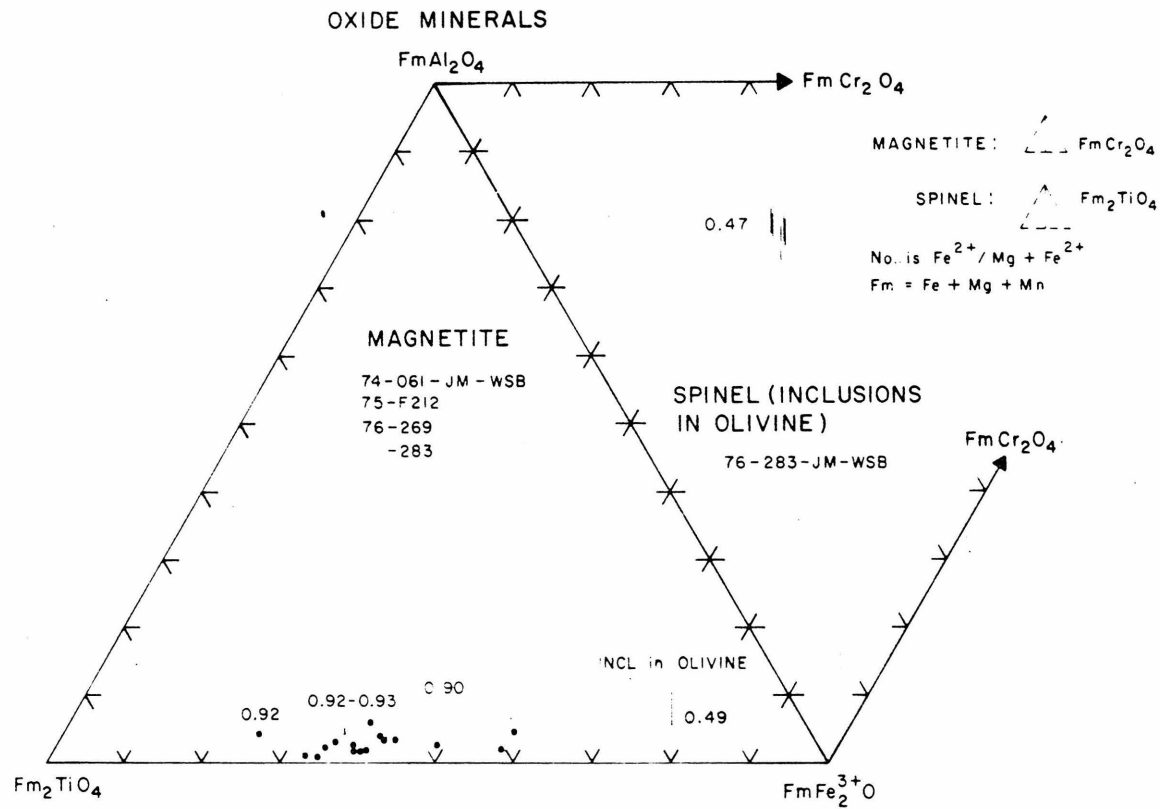


Figure 13

GROUP D ALKALI OLIVINE BASALT AND HAWAIIITE

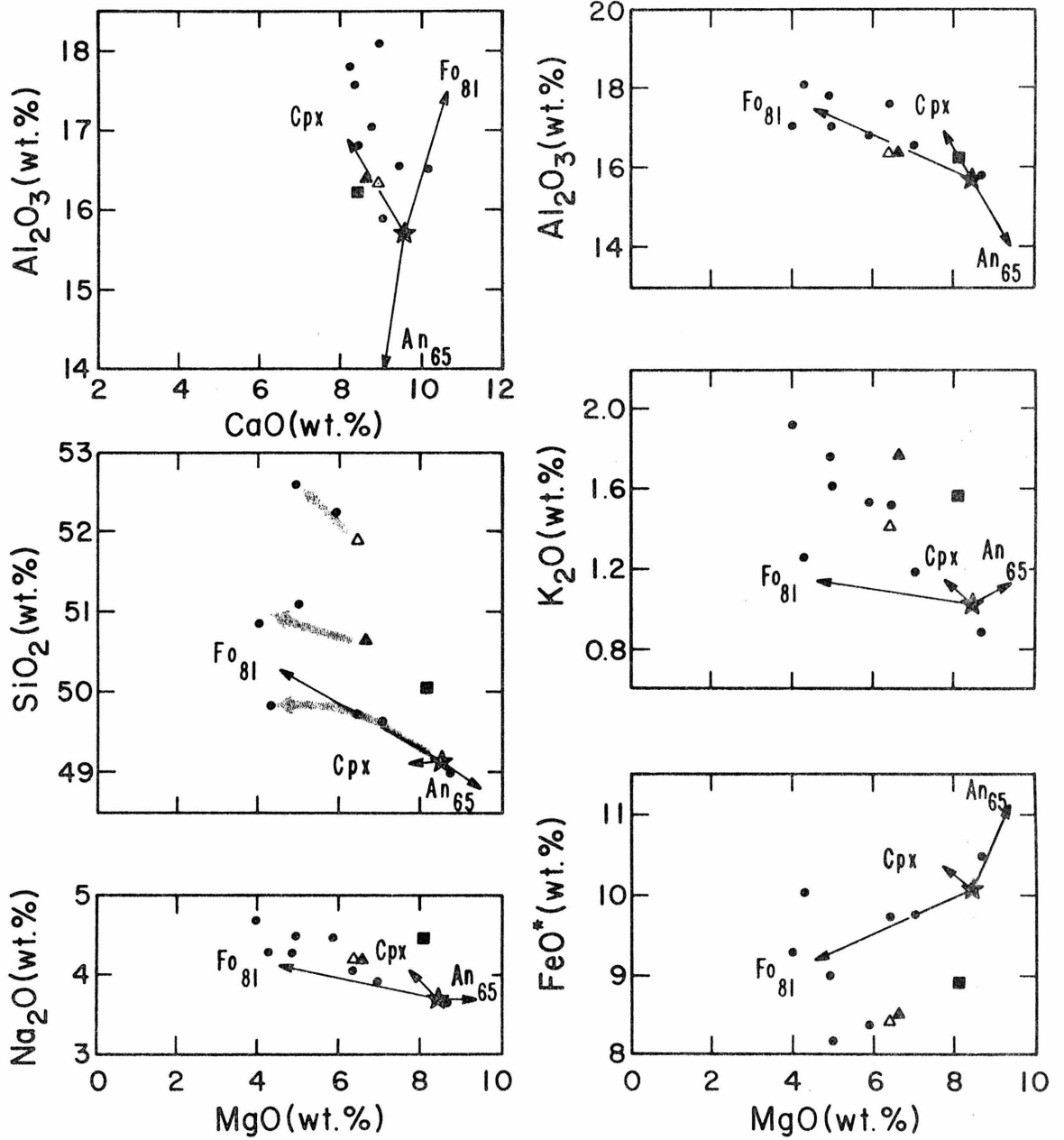


Figure 19

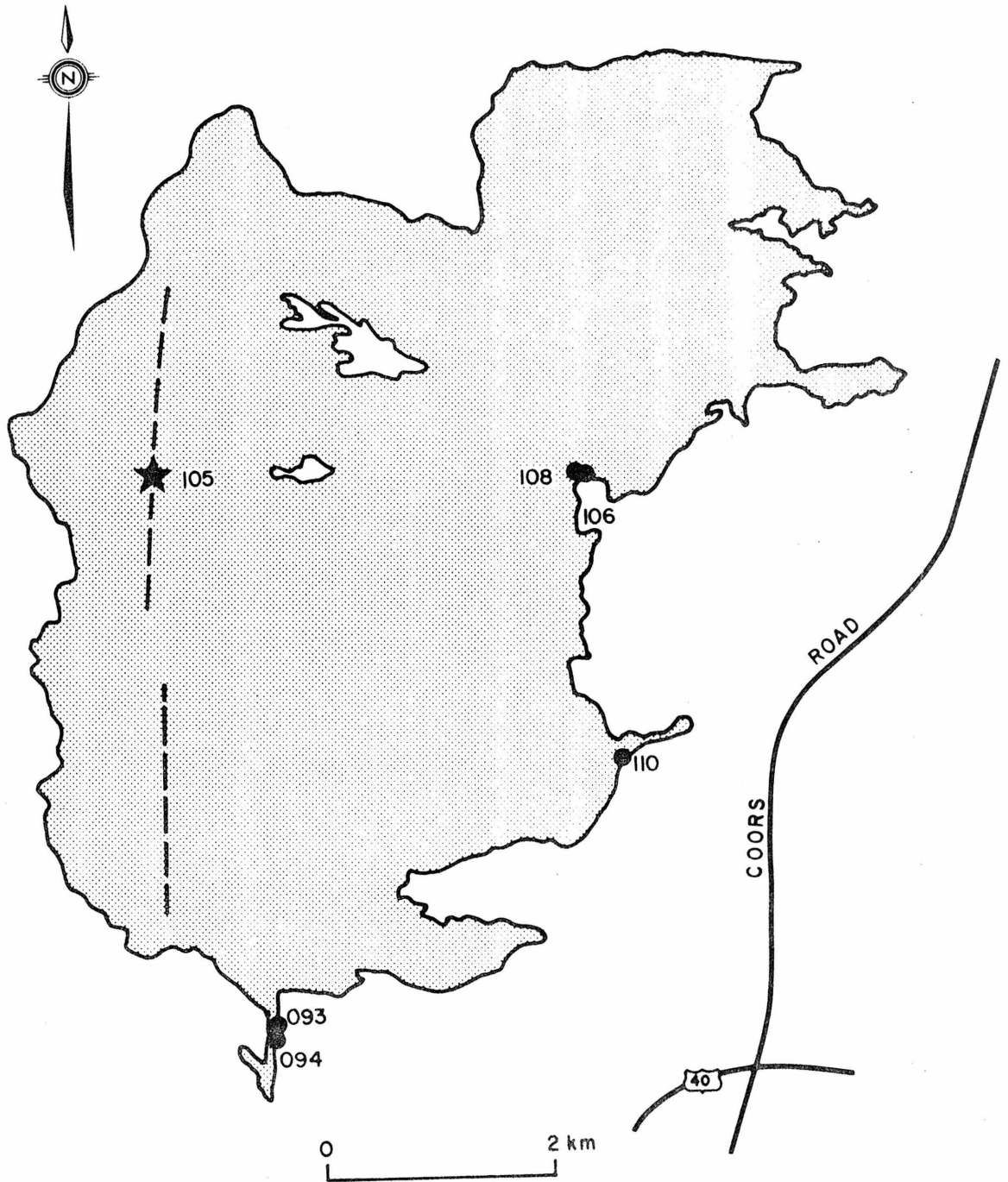


Figure 20

Figure 21

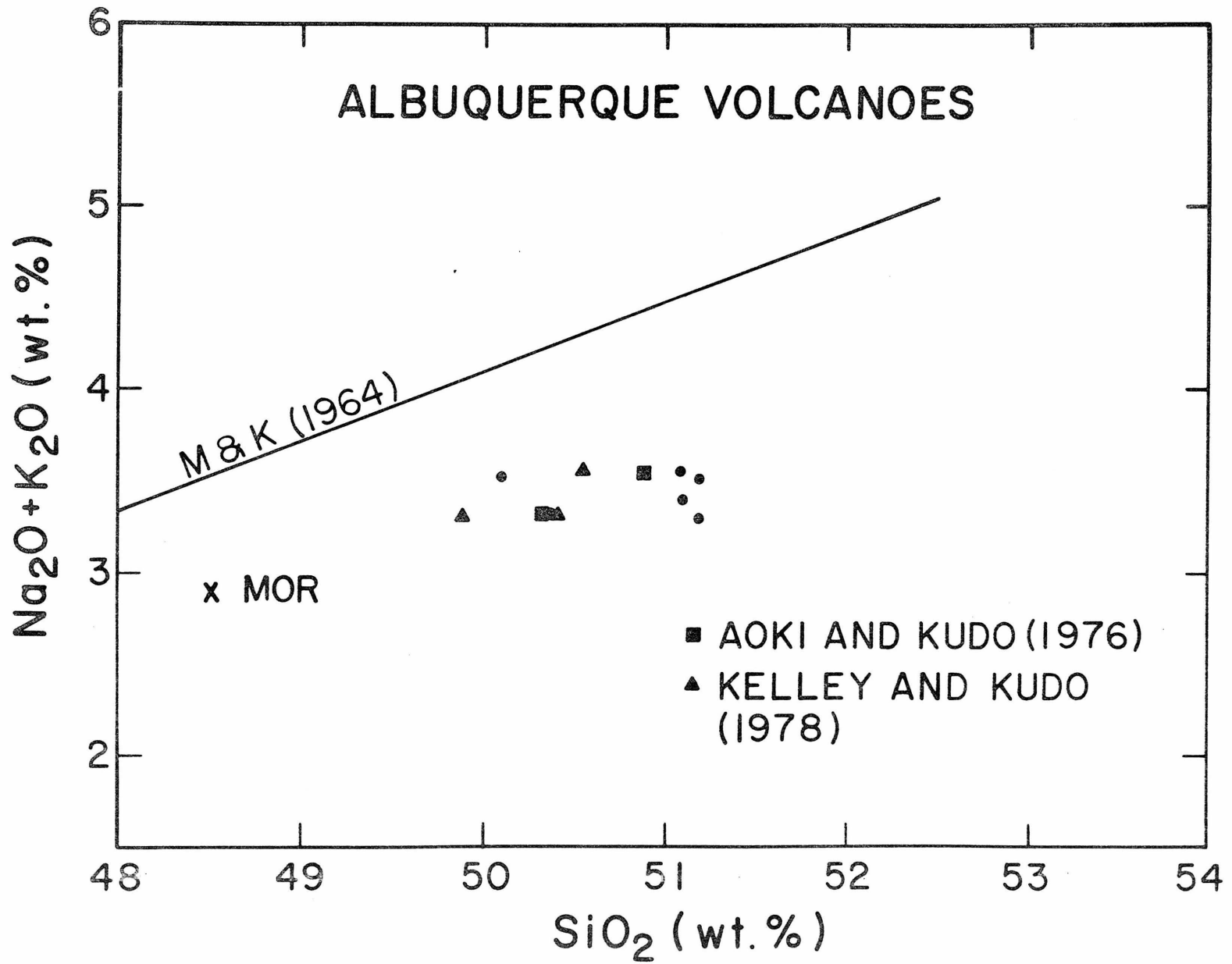
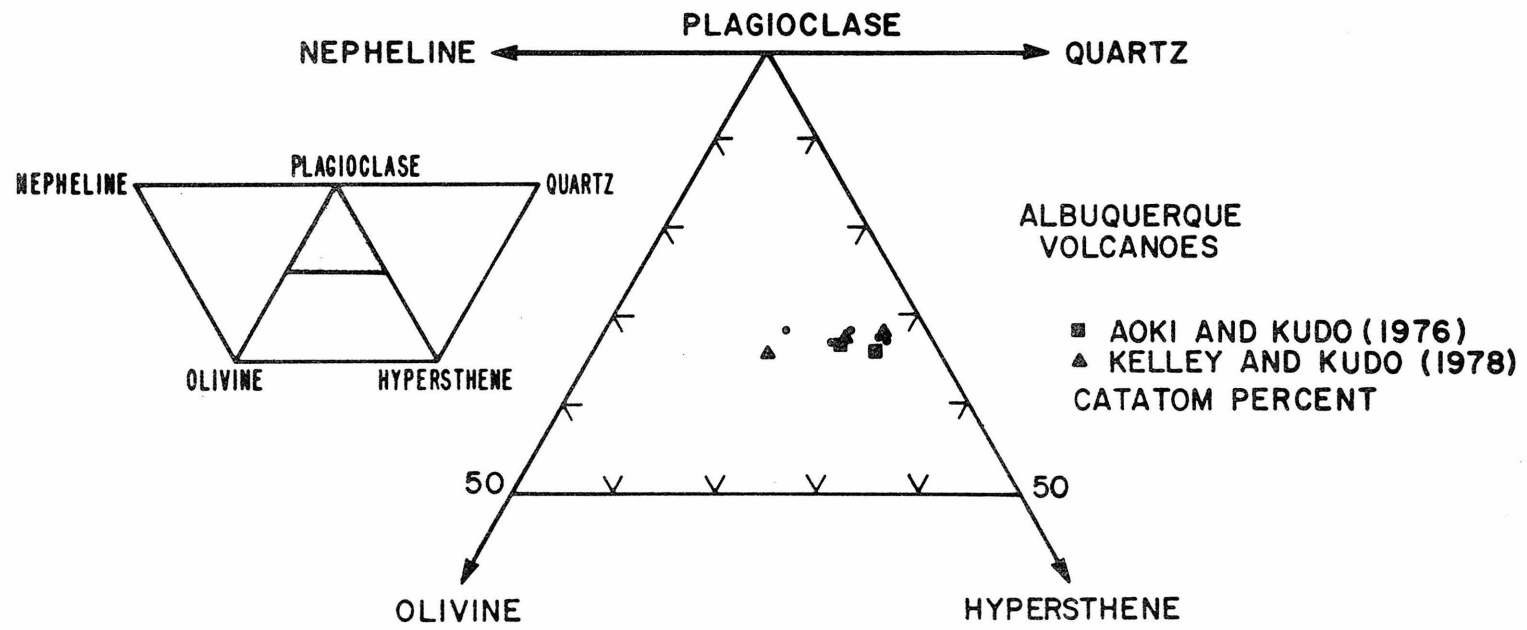


Figure 22



ALBUQUERQUE VOLCANOES

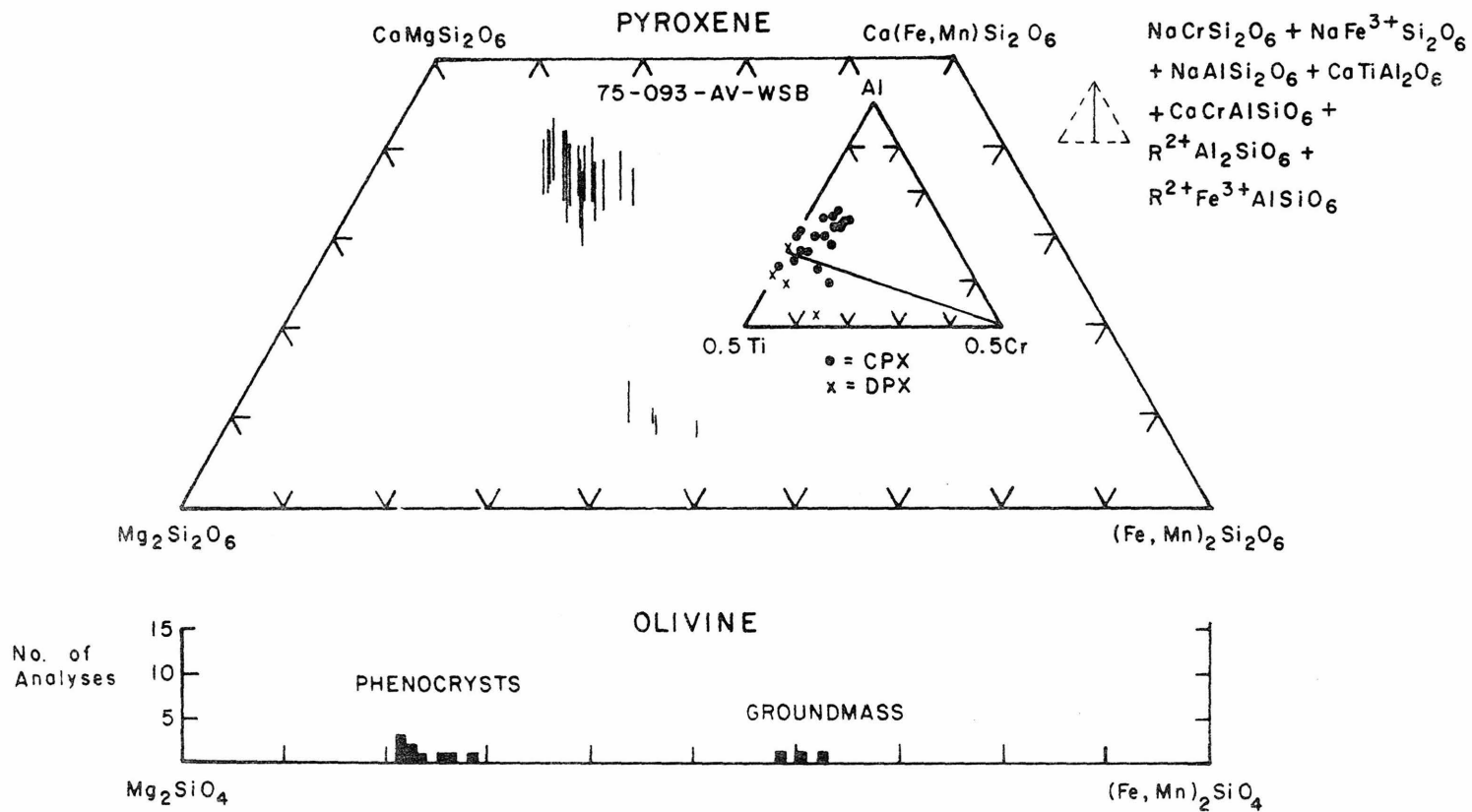


Figure 23

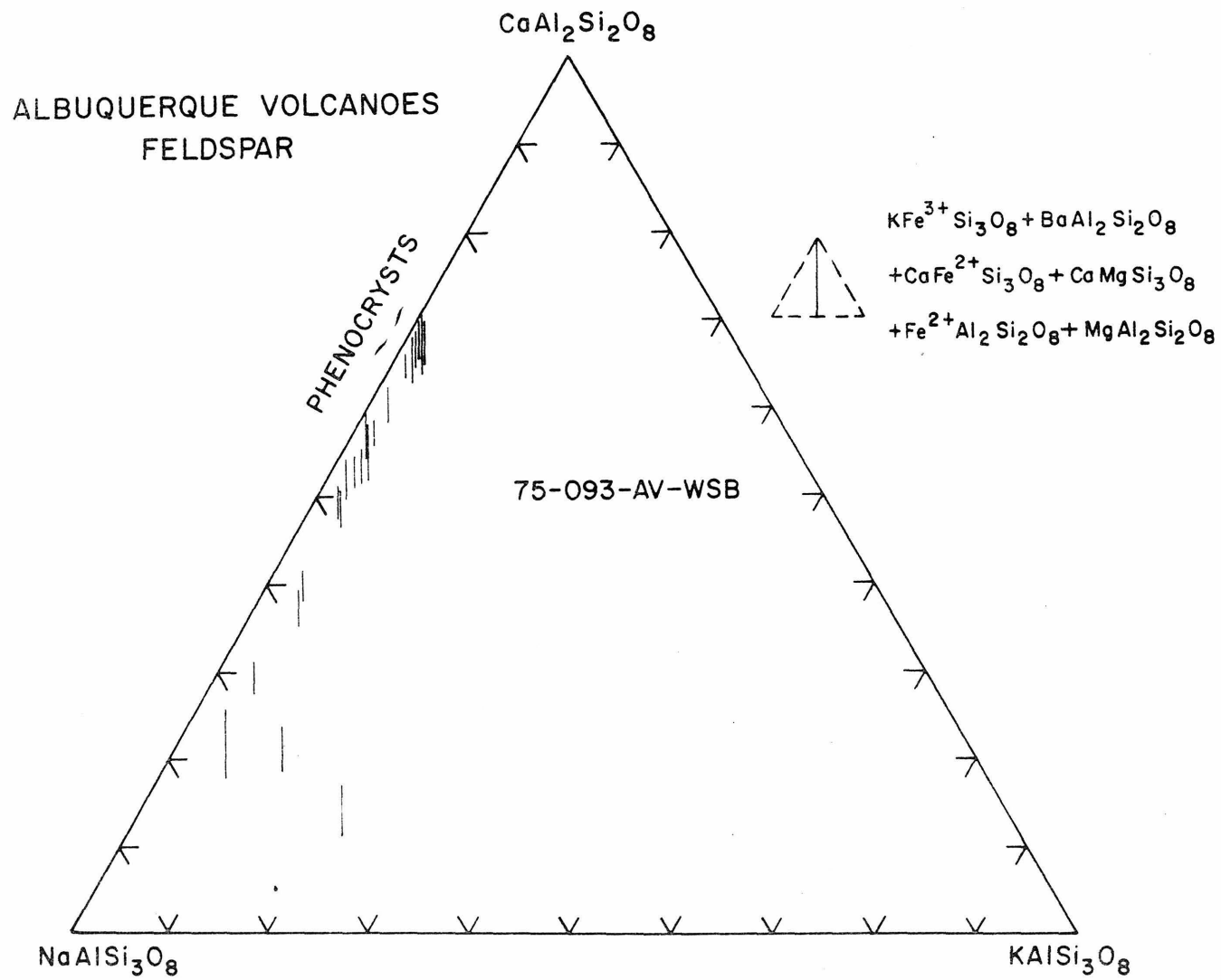


Figure 24

ALBUQUERQUE VOLCANOES

OXIDE MINERALS

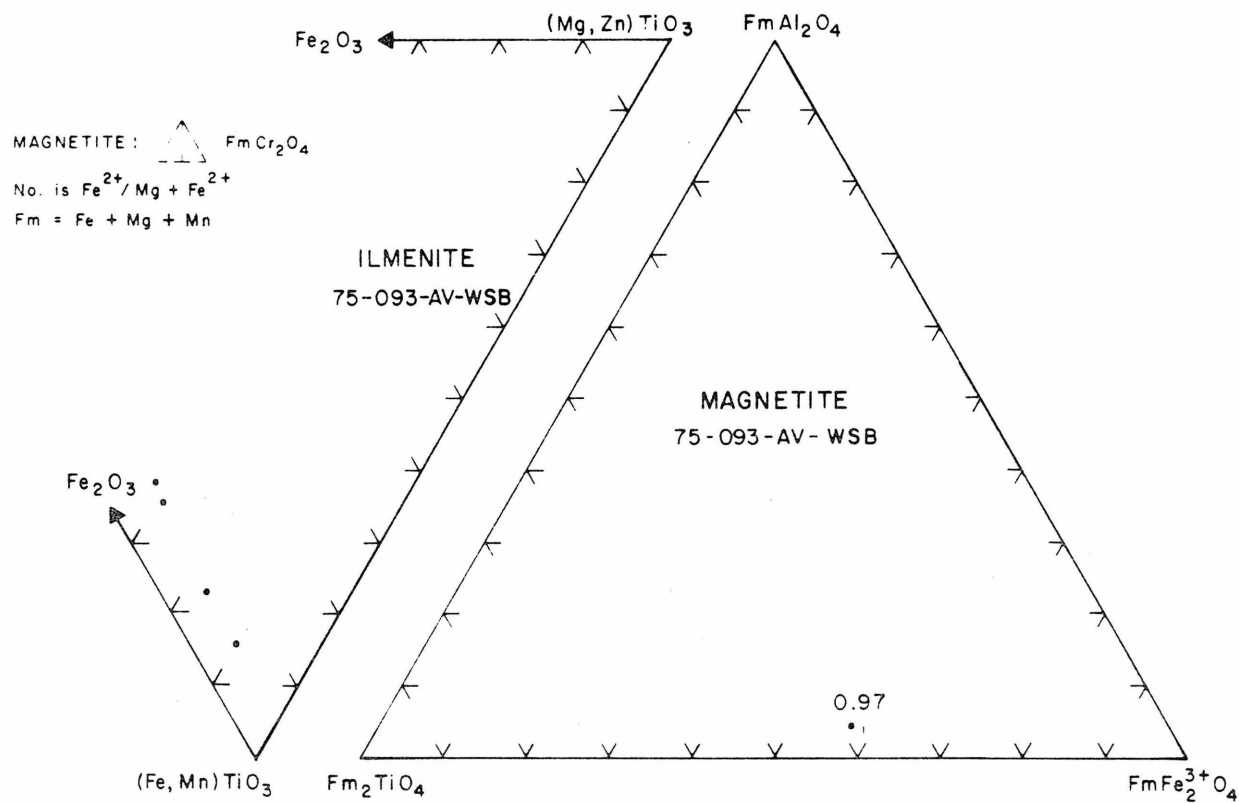
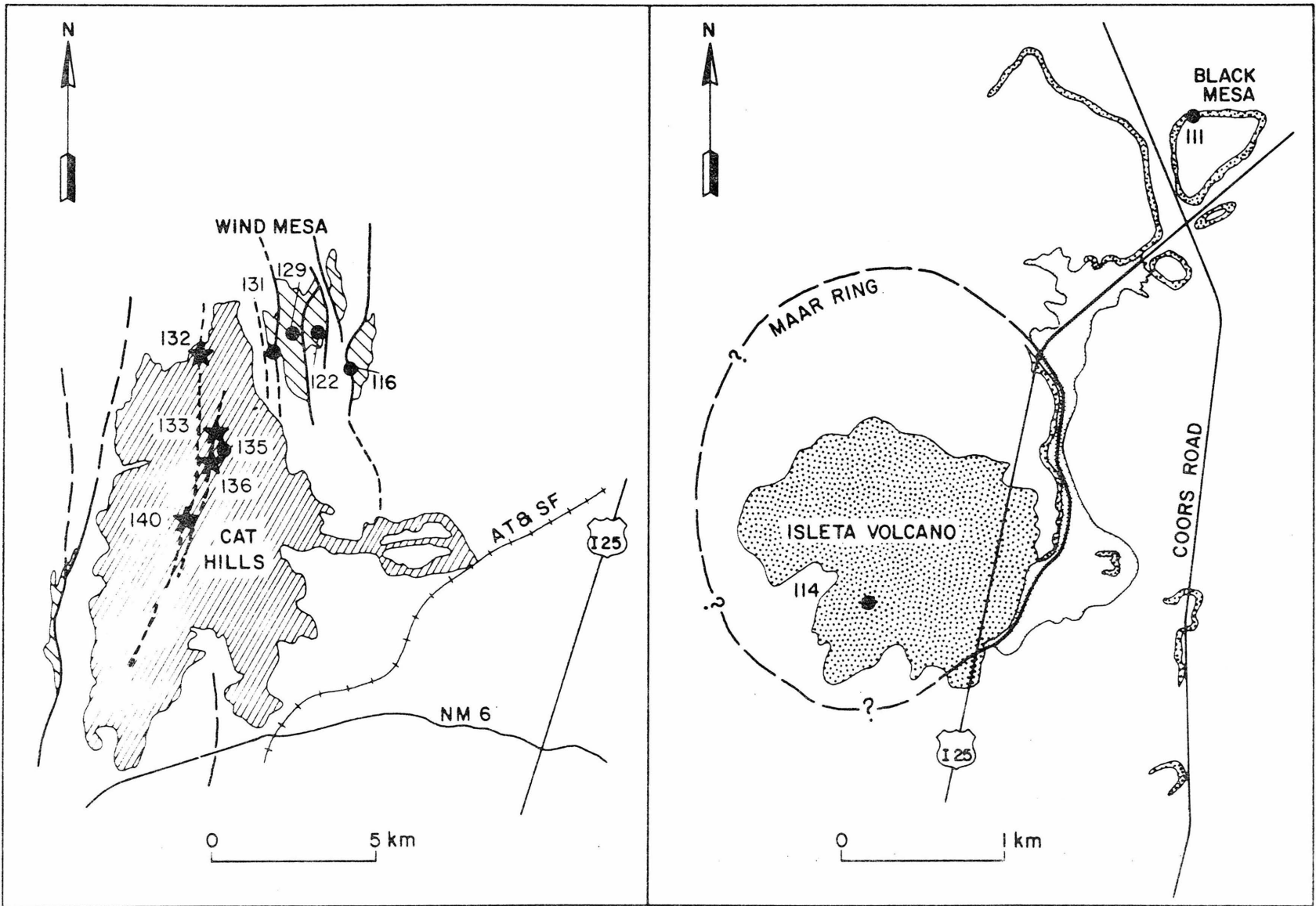


Figure 25

Figure 26



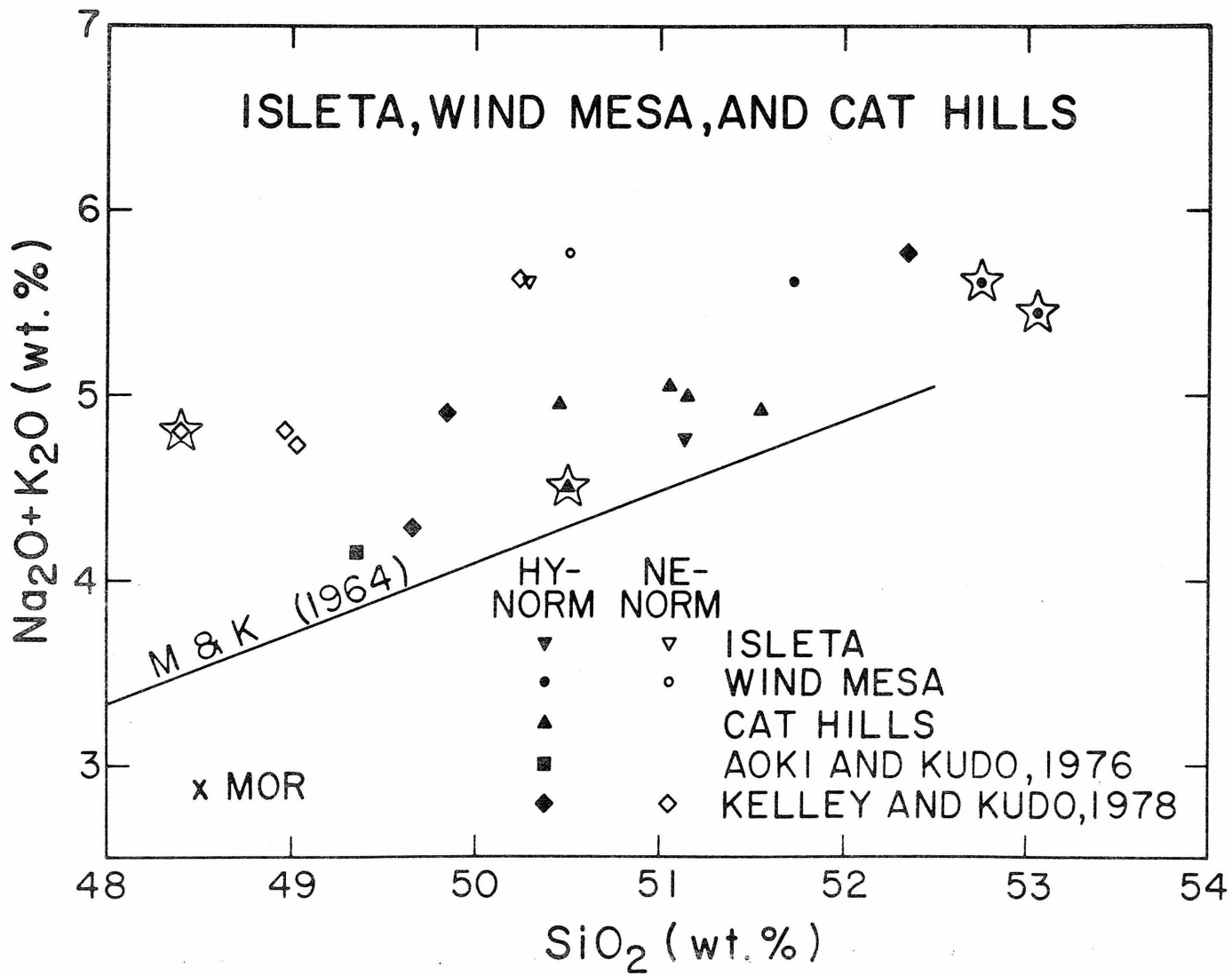
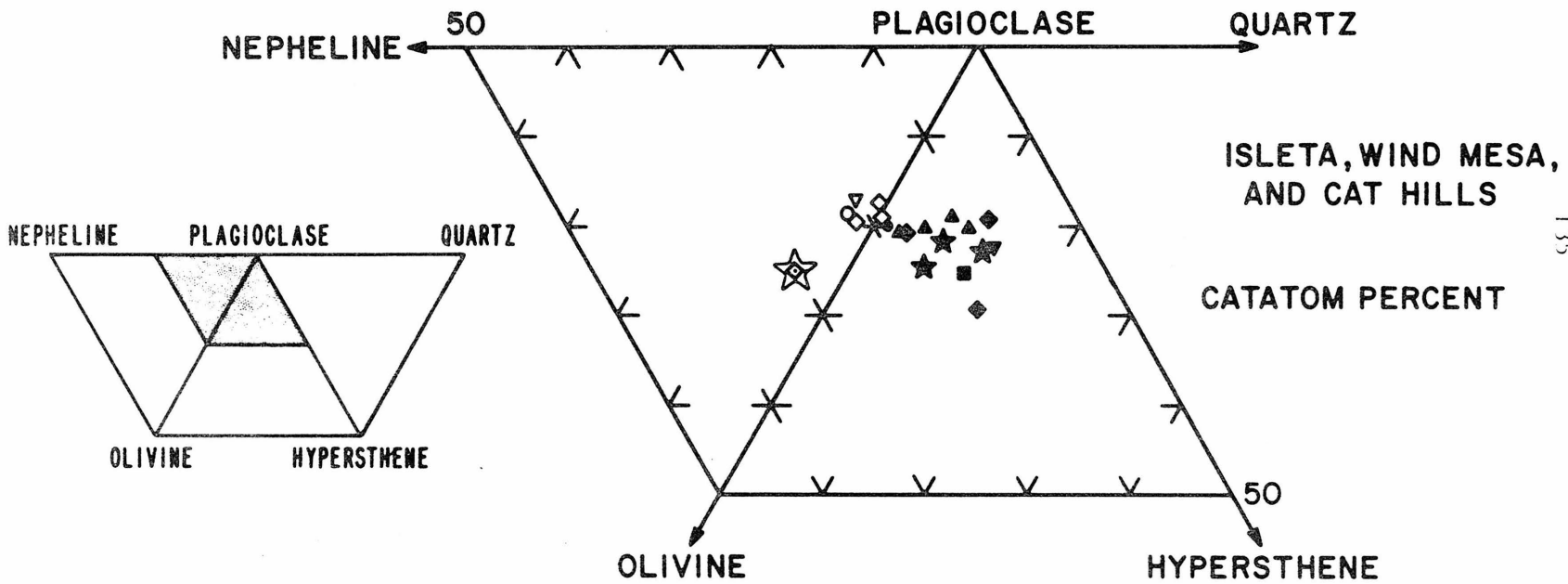


Figure 27



135

Figure 28

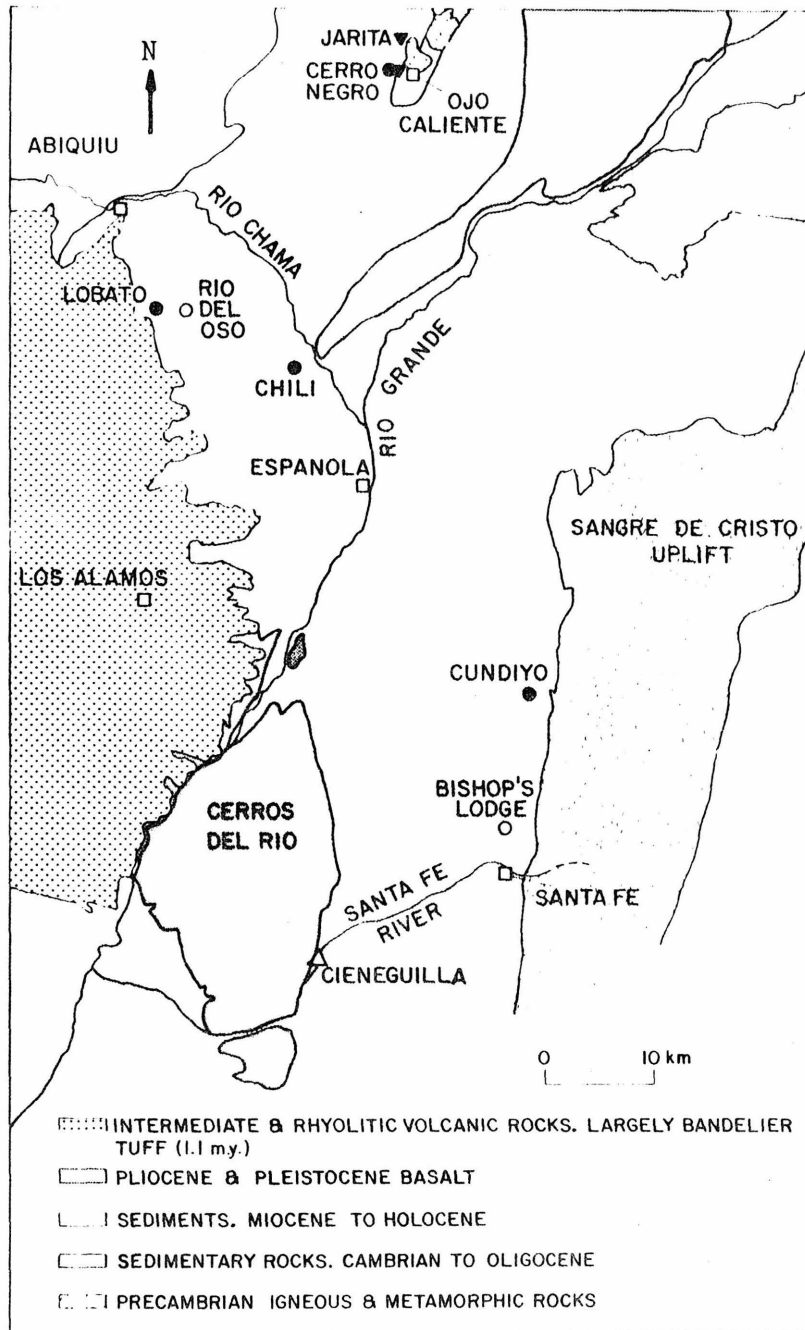


Figure 29

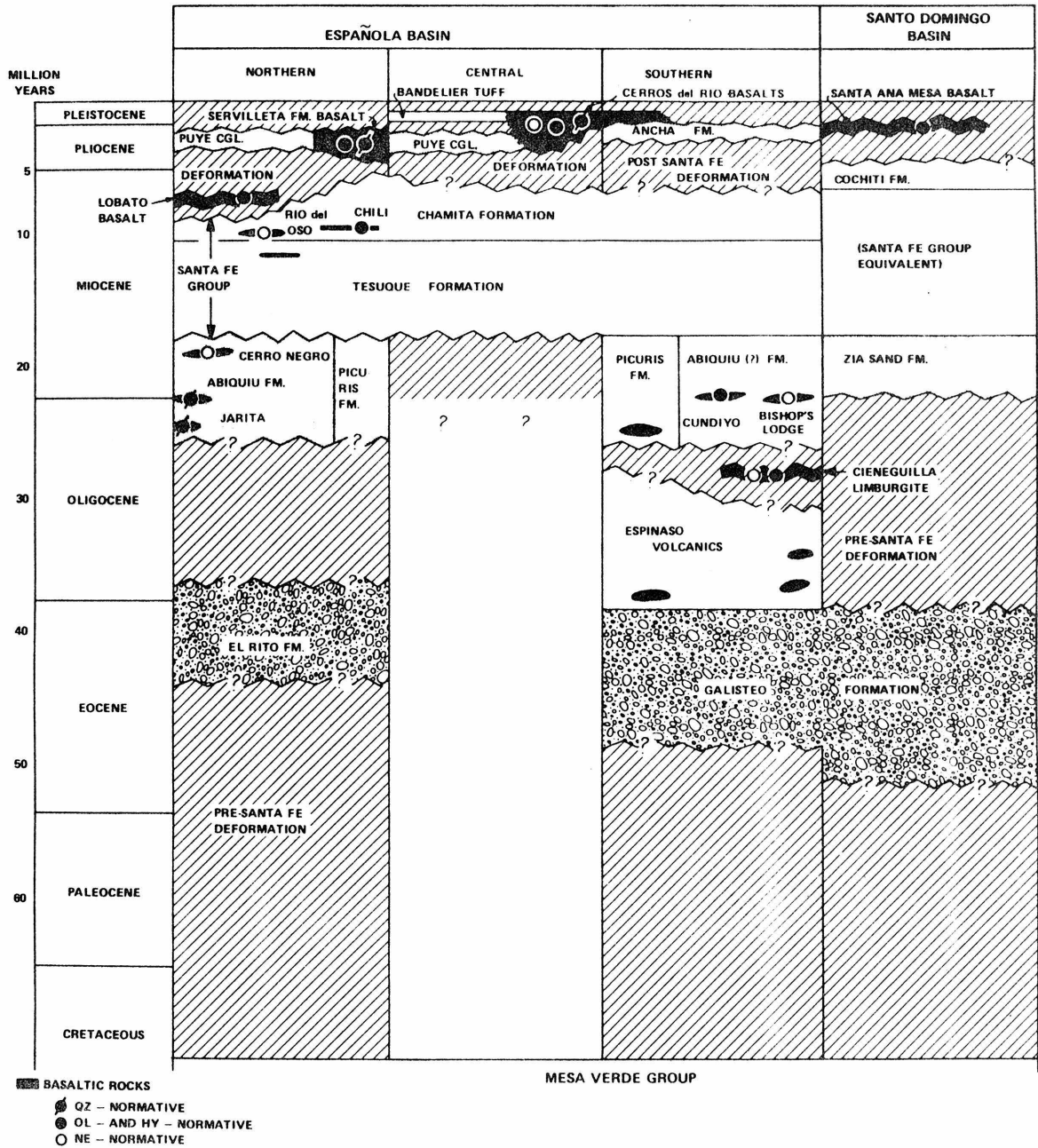


Figure 30

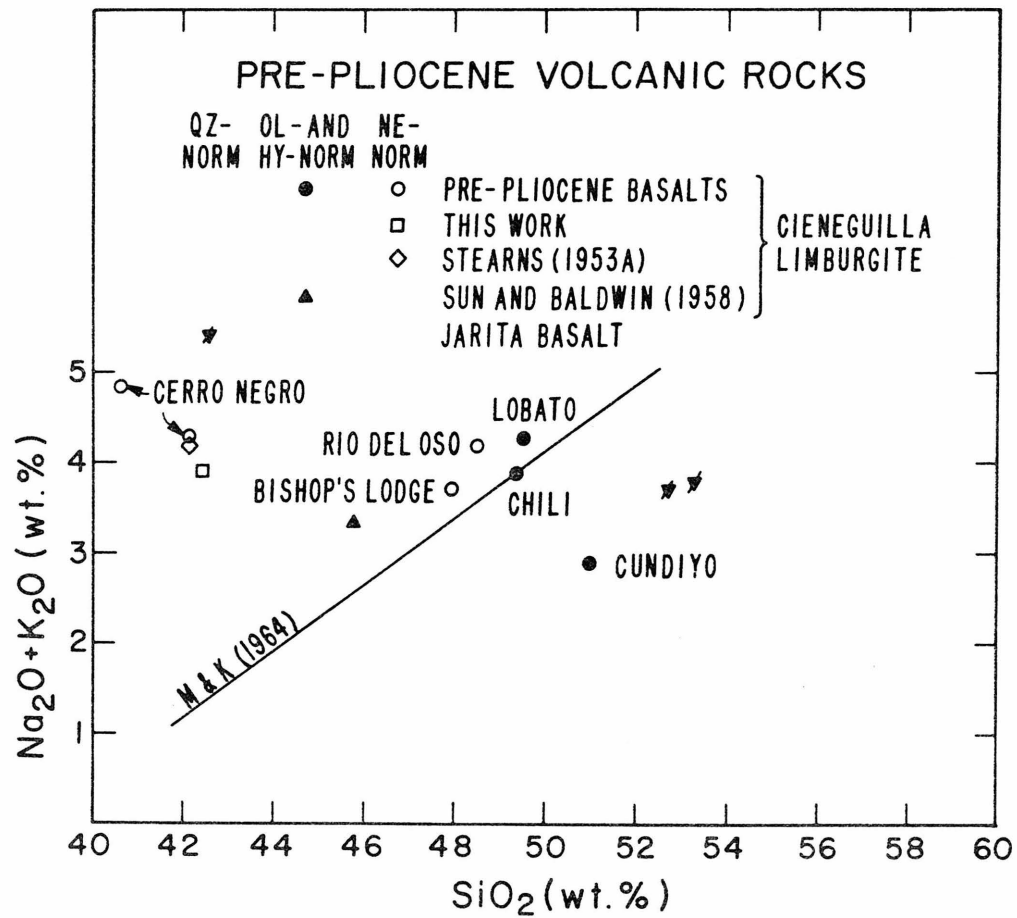


Figure 31

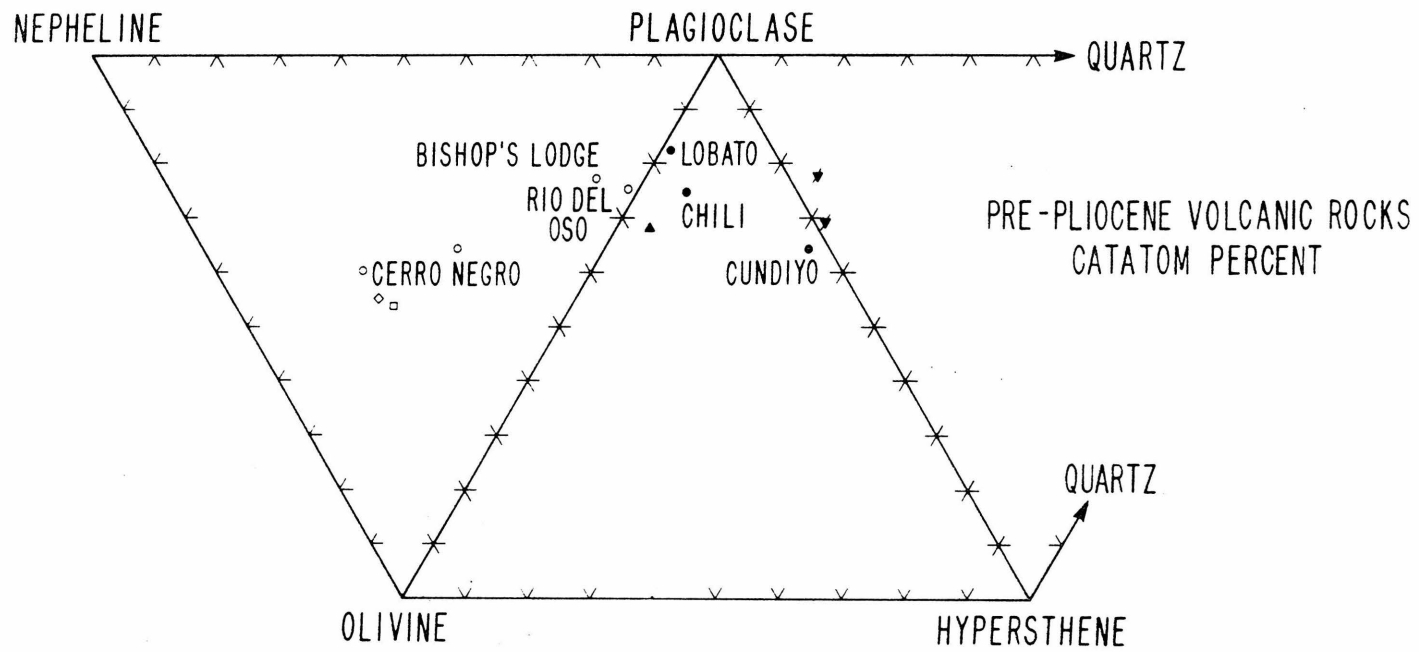
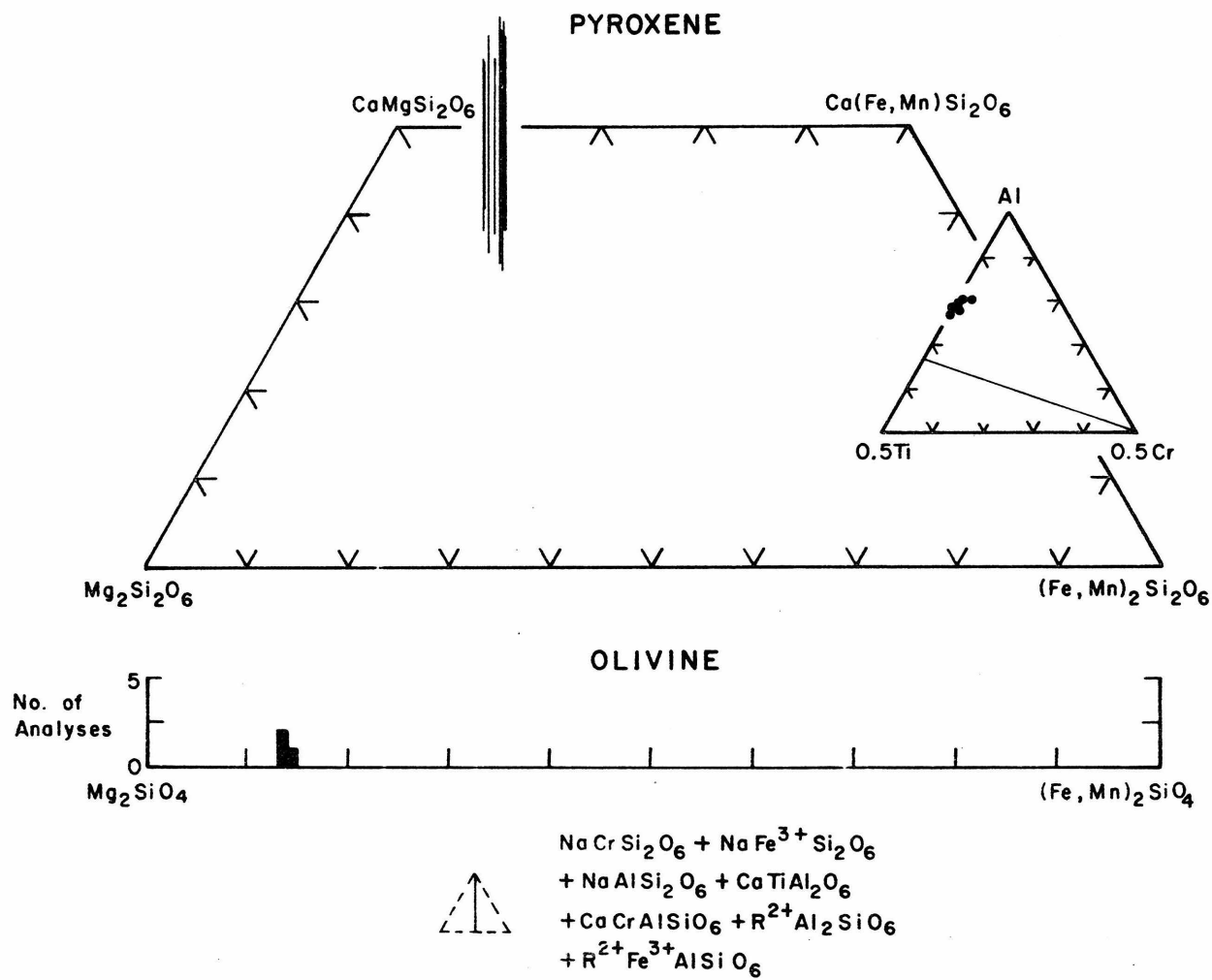


Figure 32

76-A271-JM-WSB



140

Figure 33

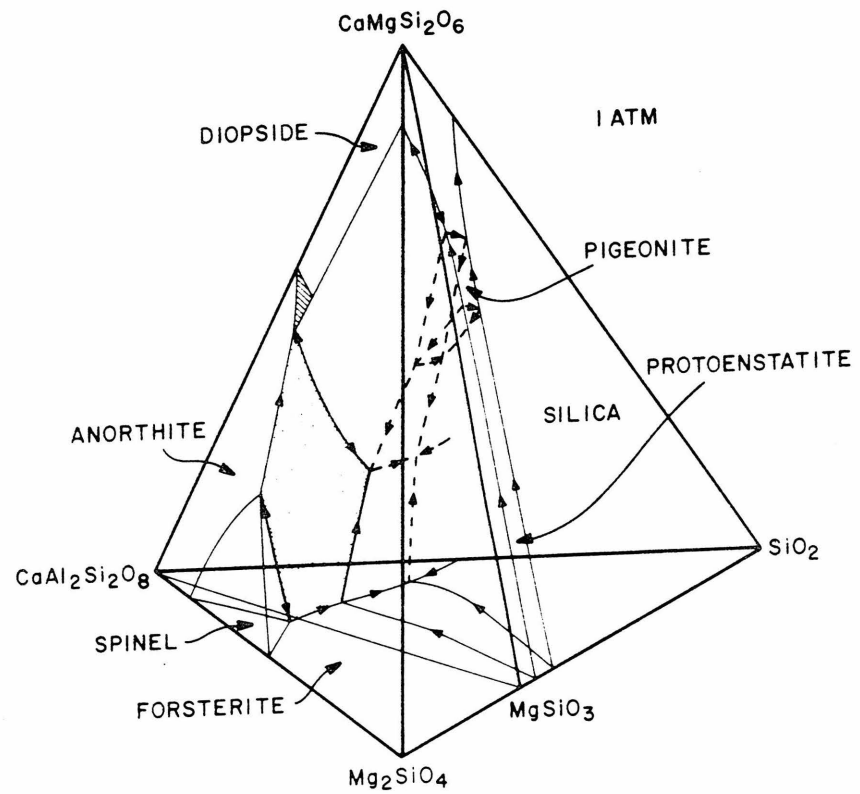


Figure 34

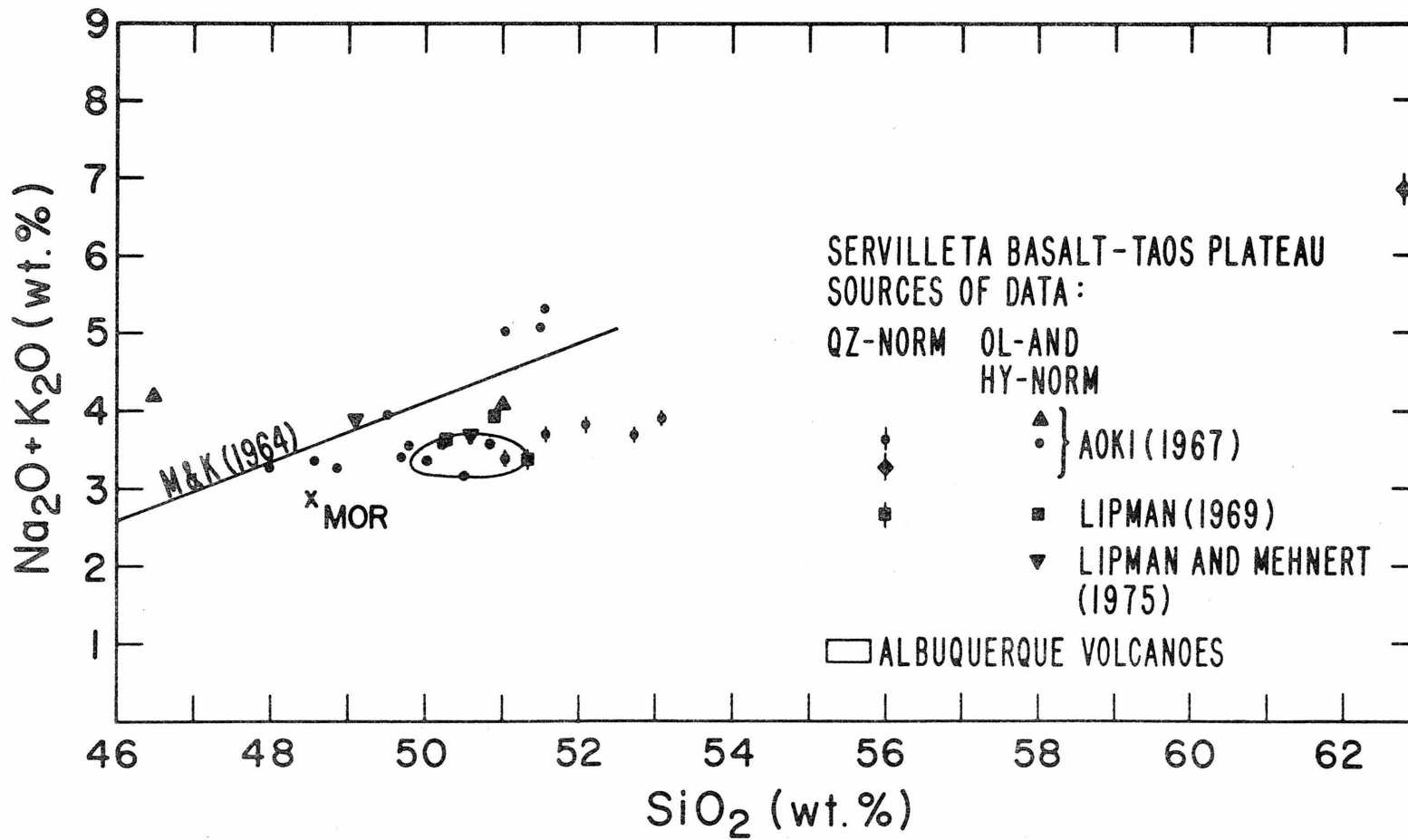


Figure 35

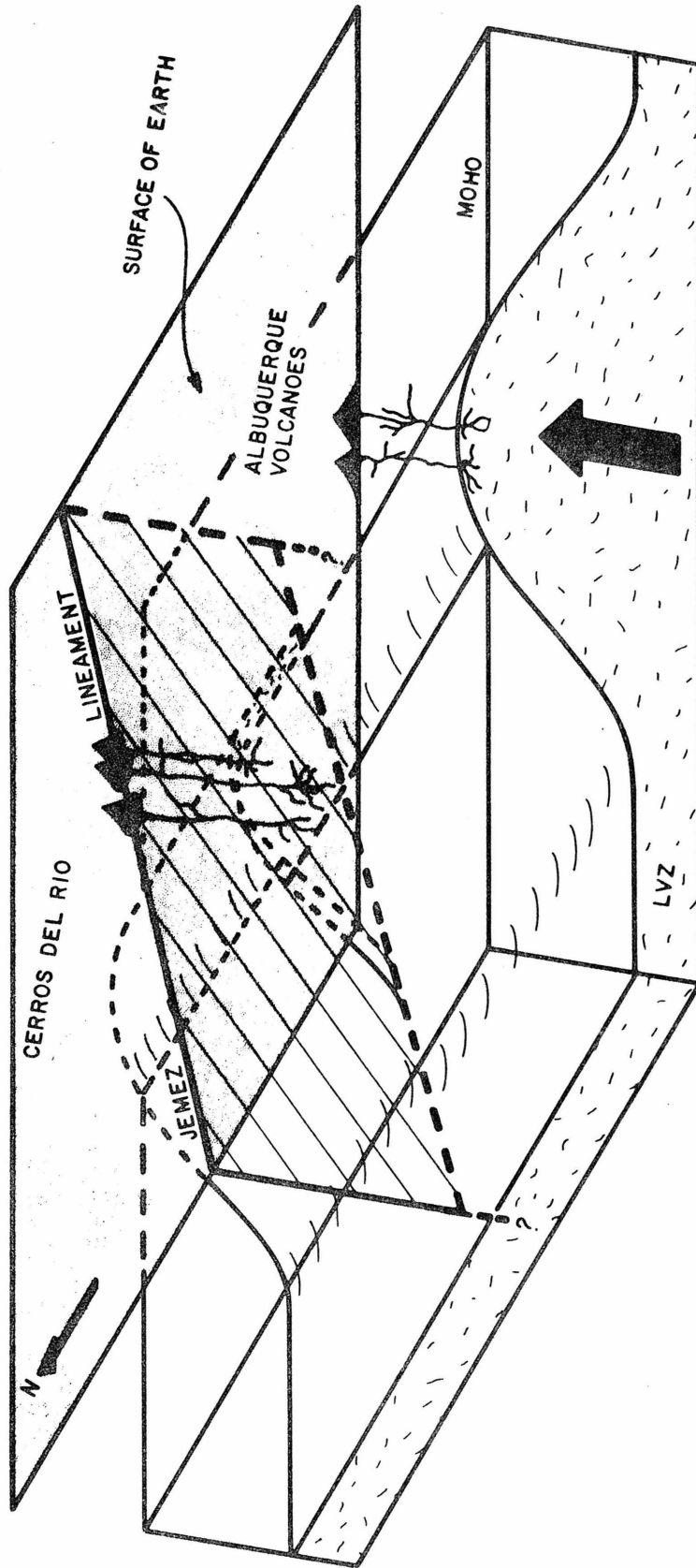


Figure 36

APPENDIX 1.

Group A olivine tholeiites

- 74-004-JM-WSB Vallecitos Quadrangle. Cinder cone of Los Cerritos, top of 8290' hill.
- 009 Vallecitos Quadrangle. 50 m from top of cinder cone (hill 8452') on Rinco de Mora.
- 049 Otowi flow. White Rock Quadrangle. 5 km north of White Rock at point where Rt. 4 crosses basalt.
- 057 San Felipe Pueblo Quadrangle. 1.6 km south-southwest of San Felipe Pueblo on road to Santa Ana. Sample from 1/2 m above base of flow capping mesa.
- 058 San Felipe Pueblo Quadrangle. Same locality. From 2 m above base of same flow as -057.
- 064 San Felipe Pueblo Quadrangle. T14N, R4E, section 23; 4.2 km west of San Felipe Pueblo, on road to Santa Ana. Top of mesa-capping flow.
- 065 San Felipe Pueblo Quadrangle. Bomb from cinder cone, 8 km northeast of San Felipe Pueblo. T15N, R4E, section 27.
- 087 White Rock Quadrangle. Ancho Canyon, at point where 6120' contour crosses gully.
- 232 White Rock Quadrangle. 1.2 km northeast of White Rock at point where 6170' contour crosses old Buckman Bridge road. Uppermost of four flows exposed in this canyon.

- 261 White Rock Quadrangle. Ancho Canyon at point where 6170' contour crosses canyon. Next flow overlying -087.

Group B basaltic andesites and related basaltic andesites and latite-andesites

- 001 Frijoles Quadrangle. Cinder cone 1.1 km northeast of Bandelier National Monument headquarters.
- 021 Canones Quadrangle. Near top of 8225' hill, 3.8 km north of Cerro Pelon.
- 023 Canones Quadrangle. Base of cinder cone, 1.9 km northeast of Cerro Pelon.
- D031 Montosa Peak Quadrangle. Non-vesicular plug of cinder cone, from northerly of two Twin Hills.
- 036 White Rock Quadrangle. Flow exposed in ravine 0.2 km north of Stoney Tank.
- 038 White Rock Quadrangle. North end of Ortiz Tank.
- A039 White Rock Quadrangle. 0.4 km east of Ortiz Tank, at point where 6560' contour crosses gully.
- 044 White Rock Quadrangle. Along Rio Grande at mouth of Ancho Canyon. Lowermost flow exposed in White Rock Canyon.
- 045 White Rock Quadrangle. From 5700' level at east end of point immediately south of Ancho Canyon. From lowermost flow of sequence of flows stratigraphically below -087 and above -044.

- 062 Cochiti Dam Quadrangle. T17N, R6E, section 28.
4.5 km north of Cochiti Dam. Top of cliff (5600') on west side of Rio Grande. Tank Nineteen basaltic andesite of Smith, Bailey and Ross (1970).
- 063 Cochiti Dam Quadrangle. T17N, R6E, section 28. Top of eroded cinder cone (5700') on west side of Rio Grande.
- 230 White Rock Quadrangle. 2.2 km east-northeast of White Rock at point where 5970' contour crosses old Buckman Bridge road. Lowermost of 4 flows exposed along this road (stratigraphically below -231, -233, and -232).
- 231 White Rock Quadrangle. 1.9 km east-northeast of White Rock. Next flow above -230.
- 262 White Rock Quadrangle. Dike exposed in Ancho Canyon approximately 1.5 km from Rio Grande.

Group C basanites

- 034 Montosa Peak Quadrangle. Bomb from south flank of Cerro Rito.
- 269 Tetilla Peak Quadrangle. Flow capping east edge of La Bajada mesa, 1.1 km northeast of Canon T16N, R8E, section 30.

Group D alkali olivine basalts and related basalts and hawaiites

- 005 Vallecitos Quadrangle. Cinder Cone of Los Cerritos, top of 7796' hill. Adjacent to -004.
- 006 Vallecitos Quadrangle. From deeply eroded cinder cone (hill 7789') 1.2 km north of Rinco de Mora.
- 024 Montosa Peak Quadrangle. Lithified ash from cinder cone 1.1 km southeast of Twin Hills.
- 028 Montosa Peak Quadrangle. Dike 1.5 km southeast of Twin Hills.
- 029 Montosa Peak Quadrangle. Bomb from rim of small crater 0.6 km southeast of Twin Hills.
- 042 Montosa Peak Quadrangle. Basalt from top of Montosa Peak.
- 061 Cochiti Dam Quadrangle. From rim of canyon on west side of Rio Grande, 3.1 km north of Cochiti Dam.
- F212 Abiquiu Quadrangle. 5.3 km south-southwest of Abiquiu at point where road to El Alto meadows crosses flow capping Mesa de Abiquiu.
- 213 Abiquiu Quadrangle. 5.6 km south-southwest of Abiquiu. Flow overlying -F212.
- 233 White Rock Quadrangle. Overlook Park at White Rock. Sample from third (from bottom) of four flows exposed along this canyon. This flow overlies -230 and -231, and underlies -232.

- 281 Española Quadrangle. Southwest corner of Black Mesa
 at San Ildefonso Pueblo.
- 283 Horcado Ranch Quadrangle. East side of Pankey Mesa
 (at 6380'), 2.0 km south of intersection of Calabasa
 Arroyo and Canada Ancha.

APPENDIX 2

Albuquerque Volcanoes

- 75-093-AV-WSB La Mesita Negra SE Quadrangle. Near base of uppermost of two flows exposed along edge of mesa, 5.2 km west of intersection of Coors Road and Interstate Rt. 40.
- 095 La Mesita Negra SE Quadrangle. Near base of lowermost of two flows, same location as -093.
- 105 Volcano Ranch Quadrangle. Northernmost of well-developed cinder cones, 2.6 km north of Vulcan cone. T11N, R2E, section 19.
- 106 Los Griegos Quadrangle. Lower flow or flow unit exposed along edge of mesa, 4.4 km northwest of St. Joseph College. T11N, R2E, section 22.
- 108 Los Griegos Quadrangle. Upper flow or flow unit exposed along edge of mesa. Same location as -106.
- 110 Los Griegos Quadrangle. Upper of two flows exposed along edge of mesa, 2.0 km west-northwest of St. Joseph College, T11N, R2E, section 34.

Isleta

- 75-111-IS-WSB Isleta Quadrangle. Northwest corner of Black Mesa, from capping flow.
- 114 Isleta Quadrangle. From near top of Parea Mesa (Isleta Volcano).

Wind Mesa

- 75-116-WM-WSB Wind Mesa Quadrangle. Lava flow from west side of mesa, 2.1 km southeast of survey point 5937' on Wind Mesa.
- 122 Wind Mesa Quadrangle. 0.7 km east of survey point 5937' on Wind Mesa.
- 129 Wind Mesa Quadrangle. From survey point 5937' highest point on Wind Mesa.
- 131 Wind Mesa Quadrangle 1.0 km southwest of survey point 5937', west side of Wind Mesa.

Cat Hills

- 75-132-WM-WSB Dalies Quadrangle. Cinder cone (Blackbird Hill).
- 133 Dalies Quadrangle. Cinder cone (hill 5701'), 2.4 km south of Blackbird Hill.
- 135 Dalies Quadrangle. Lava flow 0.5 km south-southeast of hill 5701'.
- 136 Dalies Quadrangle. Cinder cone 0.8 km south of hill 5701'.
- 140 Dalies Quadrangle. Cinder cone 4.9 km south of Blackbird Hill.

PART II

MAFIC AND ULTRAMAFIC INCLUSION SUITES FROM
THE RIO GRANDE RIFT (NEW MEXICO) AND THEIR
BEARING ON THE COMPOSITION AND
THERMAL STATE OF THE LITHOSPHERE

by

W. S. Baldrige
Division of Geological and Planetary Sciences*
California Institute of Technology
Pasadena, California 91125 USA

ABSTRACT

Mafic and ultramafic inclusions from Abiquiu, from Cieneguilla, and from Elephant Butte in the northern and central Rio Grande rift in New Mexico have been examined in detail. The type and variety of inclusions differ greatly at each site: at Abiquiu, the inclusions consist of pyroxenite and megacrysts of plagioclase and orthopyroxene; at Cieneguilla, primarily harzburgite, minor granulite, and megacrysts of magnetite and clinopyroxene are present; and at Elephant Butte spinel lherzolite, granulite, clinopyroxenite, and megacrysts of spinel, magnetite, clinopyroxene, olivine, and plagioclase occur. Mineral chemistry and textures indicate that the lithic inclusions (excluding lherzolite and harzburgite) represent fragments of several separate intrusive bodies of different bulk composition located at different depths in the lithosphere.

Inclusions with igneous textures were plainly derived from mafic intrusions in the lower crust or upper mantle. Such intrusions may be part of a wedge of mafic rocks emplaced into the lithosphere above a mantle diapir associated with rifting. Granulite with metamorphic texture was probably derived from the uppermost mantle and may have been part of the pre-existing lithosphere, or possibly was an early component of the mafic wedge which was subsequently recrystallized. Spinel-bearing lherzolite and harzburgite are probably accidental fragments of mantle country rock. Megacrysts have compositions similar to the same phases in associated pyroxenite and granulite. Their origin is related to high-pressure crystallization

of mafic magmas, but whether as phenocrysts from their host or as (now disaggregated) pegmatites from magmas of the same eruptive episode, cannot in general be determined.

(P,T) conditions at depth can best be estimated for the Elephant Butte suite of inclusions. Spinel lherzolite indicates equilibration temperatures of 935-1030°C at pressures of 14-20 kb; spinel-two-pyroxene granulite yields 900-980°C at 6-13 kb. A best fit geothermal gradient passes through 1000°C at 50 km. This geotherm is higher than the oceanic geotherm but lower than geotherms calculated from surface heat flow data in the Rio Grande rift, suggesting that these calculated gradients reflect transient heat flow from shallow (<30 km) crustal intrusions.

INTRODUCTION

Suites of mafic and ultramafic inclusions occur at several localities within the Rio Grande rift of New Mexico. This paper reports on three such suites, those occurring at Abiquiu, at Cieneguilla, and at Elephant Butte (figure 1). The first two of these suites were previously unknown, and none has been described in the literature. The well-known Kilbourne Hole xenolith locality in the southern Rio Grande rift is currently under investigation by Reid (1976), Reid and Woods (1978), and Padovani and Carter (1977a, b), and will not be discussed here. The purpose of this paper is to examine the major inclusion types at each locality. Representative samples of each type were chosen for analysis. In this paper the general term

"inclusion" will refer both to lithic inclusions (i.e., rocks) and to megacrysts (large single crystals). The terms xenolith and xenocryst will be reserved specifically for rock fragments and single crystals, respectively, not directly related comagmatically to their host magmas.

These suites encompass diverse assemblages of inclusions, the proportions of which differ greatly among the suites. The Abiquiu suite consists mainly of pyroxenite and megacrysts of pyroxene and plagioclase. No lherzolite is present (see figure 2 for explanation of terminology). Inclusions from Cieneguilla consist predominantly of harzburgite, with megacrysts of magnetite and clinopyroxene. The suite from Elephant Butte encompasses the greatest diversity of material, including several clinopyroxene-rich rock types, granulite, and spinel lherzolite; and spinel, magnetite, clinopyroxene, olivine, and plagioclase megacrysts. Spinel-bearing two-pyroxene granulite is a particularly prominent rock type at this locality.

Although differing greatly from each other in types and variety of inclusions, these localities are considered together because they come from a single structural setting, the Rio Grande continental rift. These suites are important to a general understanding of the rift in that inclusions constitute our only available samples of the lower crust and upper mantle in this region. Comparison of the suites from these three localities yields a more comprehensive picture regarding the rift than study of each suite separately. These

inclusions provide firm compositional constraints for petrological and geophysical models. Their phase compositions record the pressure and temperature conditions existing in their source regions, enabling the geothermal gradient to be estimated and, in a gross way at least, providing the stratigraphy of the source lithologies.

ANALYTICAL PROCEDURES

Mineral analyses were performed with a Materials Analysis Corporation model 5-SA3 electron microprobe controlled by a Digital Equipment Corporation 12K PDP-8/L computer. Operating techniques were similar to those described by Chodos and Albee (1972), with an updated program (Chodos et al., 1973). Standard operating conditions were 15 kv accelerating potential, 0.05 μ A sample current on brass, and 15-micron beam diameter, with beam current integration and pulse height selection. The beam diameter was decreased to 5 microns or less as required where grains were compositionally inhomogeneous or very small. Analyses are accurate to 1-2 relative % for oxides constituting more than 10% of the sample and 2-5 relative % for most oxides constituting 1-10% of the sample (e.g., Champion et al., 1975).

All formula compositions and elemental ratios used in the text and diagrams are in molecular proportions. Olivine compositions are reported as %Fo = $100 \times [\text{Mg}/(\text{Mg} + \text{Fe} + \text{Mn})]$. Feldspar compositions are reported as %An = $100 \times [\text{Ca}/(\text{Ca} + \text{Na} + \text{K})]$, %Ab = $100 \times [\text{Na}/(\text{Ca} + \text{Na} + \text{K})]$, %Or = $100 \times [\text{K}/(\text{Ca} + \text{Na} + \text{K})]$. Pyroxene compositions are reported as

$\%Wo = 100 \times [Ca / (Ca + Mg + Fe + Mn)]$, $\%En = 100 \times [Mg / (Ca + Mg + Fe + Mn)]$, $\%Fs = 100 \times [(Fe + Mn) / (Ca + Mg + Fe + Mn)]$. Pyroxene formulas were calculated by assuming that $Fe^{3+} = 12 - [4(Si + Ti) + 3(Al + Cr) + 2(Ca + Mg + Fe + Mn) + Na]$, normalizing the sum of the cations to four, and sequentially calculating $(Fe, Mn)_2Si_2O_6$, $NaCrSi_2O_6$, $NaFe^{3+}Si_2O_6$, $NaAlSi_2O_6$, $CaTiAl_2O_6$, $CaCrAlSiO_6$, $R^{2+}Al_2SiO_6$, $Ca_2Si_2O_6$, $R^{2+}Fe^{3+}AlSiO_6$, and $Mg_2Si_2O_6$. Ilmenite and spinel (including magnetite) formulas were calculated by assuming that the difference of $[4(Si + Ti + Zr) + 3(Al + Cr + Nb) + 2(Mg + Fe + Mn + Zn)]$ from six and eight, respectively, was equal to Fe^{3+} ; normalizing the sum of the cations to two and three, respectively; and sequentially calculating $(Mg, Zn)TiO_3$, $MnTiO_3$, $FeTiO_3$, and Fe_2O_3 for ilmenite, and $(Mg, Fe, Mn)Cr_2O_4$, $(Mg, Fe, Mn)_2TiO_4$, $(Mg, Fe, Mn)Al_2O_4$, and $(Mg, Fe, Mn)Fe_2^{3+}O_3$ for spinel. Appendices of all analyses may be obtained from the author.

Whole-rock analyses were obtained by electron microprobe analysis of glass beads fused from whole-rock powders on an Ir-strip furnace. The techniques used were similar to those described by Brown (1976) except that beads were homogenized by grinding and re-fusing prior to microprobe analysis. All analyses were run in duplicate. Analyses are accurate to 1/2-2 1/2 relative % for oxides present in >10% abundance and 2-8 relative % for oxides constituting 1-10% of the sample.

DESCRIPTION AND CHEMISTRY

Abiquiu localityGeologic setting; host rock

The inclusion suite from Abiquiu occurs in the lava flow capping Mesa de Abiquiu, directly south of the town of Abiquiu (U. S. Geological Survey 7 1/2 minute topographic map: Abiquiu, New Mexico). This flow belongs to a group of late Pliocene to Pleistocene flows and cinder cones located about 20 km north-northeast of the Valles Caldera along the western bounding faults of the Rio Grande rift (Smith et al., 1970). Inclusions were examined in fresh outcrops at both the upper and lower ends of Mesa de Abiquiu. Most of the inclusions were collected from the former locality, where the flow is exposed in an 8 x 200 m outcrop along a Forest Service road to El Alto meadows. No differences were observed between the two localities.

The host rock is an alkali olivine basalt. Its chemical analysis and norm are presented in table 1 (analysis 1). The rock contains about 5% olivine phenocrysts (Fo_{71-77}), 1% plagioclase phenocrysts ($\text{An}_{66-63}\text{Ab}_{33-36}\text{Or}_1$), <1% augite microphenocrysts ($\text{Wo}_{42}\text{En}_{45}\text{Fs}_{13}$), and sparse quartz xenocrysts (?) in a slightly vesicular, granular groundmass of plagioclase ($\text{An}_{59}\text{Ab}_{39}\text{Or}_2$), augite ($\text{Wo}_{45}\text{En}_{41}\text{Fs}_{14}$), olivine (Fo_{70}), magnetite, and sanidine ($\text{An}_7\text{Ab}_{51}\text{Or}_{42}$). Mineral compositions are included in figures 3 and 4.

Description of inclusions

The dominant inclusions occurring in the Mesa de Abiquiu flow are pyroxenites (orthopyroxenite, websterite) and plagioclase

megacrysts, constituting approximately 60 and 25%, respectively, of the inclusions. Additional types include plagioclase-bearing pyroxenite and pyroxene megacrysts. Most of the pyroxenite inclusions consist of websterite (80%), with the remainder orthopyroxenite. Clinopyroxenite has not been identified. A total of approximately 35 inclusions were collected. Of these, 20 of the most representative and least altered were examined in thin section and 12 (listed in appendix 1) were analyzed with the microprobe. The estimated modal compositions of these inclusions are indicated in figure 2. The inclusions tend to be concentrated toward the center 3-4 m of this 10 m-thick flow. Within this zone the density of inclusions is about one per cubic meter. The inclusions are rounded to subrounded, commonly with very ragged edges. Their maximum size is about 3 cm, but most are in the range 1/2-1 cm. The average grain size of the lithic inclusions is between 1/2 and 2 mm (minimum of approximately 50 grains per inclusion). Within the pyroxenite inclusions pyroxene grains tend to be equigranular to elongate or (rarely) tabular in shape, generally with irregular boundaries (figure 3A). Exsolution lamellae of orthopyroxene and clinopyroxene are typically present in clino- and orthopyroxene, respectively. These lamellae are commonly restricted to cores of grains and are surrounded by narrow rims free of lamellae. However, in some grains the distribution of exsolution lamellae is irregular throughout the grain, and in some grains they are absent completely. Frequently associated with these exsolution lamellae are tiny ($< 50 \mu$) acicular grains of

ilmenite and/or rutile, sometimes with both phases present in the same needle (figure 3A). These are probably also exsolution features.

Plagioclase is a minor phase in some websterite and orthopyroxenite inclusions. In one sample (C212) plagioclase occurs as a single inhomogeneous, interstitial, poikilitic grain. This texture [resembling cumulate texture (Jackson, 1961; Wager, 1968; Best, 1975)] and the tabular habit (relict euhedral?) of pyroxene in some inclusions suggest igneous textures. However, in general well-defined igneous textures are absent and some recrystallization may have occurred.

The megacrysts occurring at Abiquiu consist of plagioclase and orthopyroxene, all of which are rounded to subrounded, prismatic grains about 1 cm in longest dimension. Some plagioclase "megacrysts" actually consist of two or more large plagioclase grains. Some orthopyroxene megacrysts contain short (< 0.2 mm), lath-shaped, oriented inclusions of titaniferous magnetite, possibly also the result of exsolution.

Mineral chemistry

Pyroxene compositions for these inclusions are presented in figure 4. Selected individual analyses are given in table 2. Clinopyroxene has $\text{Al}_2\text{O}_3 = 2.6-6.9$ weight percent, $\text{TiO}_2 = 0.4-1.1\%$, $\text{Cr}_2\text{O}_3 = 0.2-0.6\%$, and $\text{Na}_2\text{O} = 0.6-0.9\%$; and orthopyroxene has $\text{Al}_2\text{O}_3 = 1.5-6.1\%$, $\text{TiO}_2 = 0.1-0.3\%$, $\text{Cr}_2\text{O}_3 = 0-0.3\%$, and $\text{Na}_2\text{O} < 0.1\%$. Thus pyroxene compositions are characterized by a very limited variation and total range, both among pyroxenite inclusions and pyroxene megacrysts. However, small but significant differences in pyroxene

chemistry do exist. Among the websterite inclusions two groups can be distinguished based on the Al content of the pyroxenes. One group includes the majority of inclusions and is characterized by lower Al_2O_3 (2.6-4.5 weight percent in clinopyroxene; 1.5-3.2% in orthopyroxene). Compositions vary slightly in $\text{Mg}/\text{Mg}+\text{Fe}^{2+}$ (figure 4). Pyroxene of the second group has higher Al_2O_3 (4.8-6.9% in clinopyroxene; 2.8-6.1% in orthopyroxene) and slightly lower $\text{Mg}/\text{Mg}+\text{Fe}^{2+}$. Orthopyroxene of the orthopyroxenite is similar in composition to that of the websterite except that it tends to be slightly higher in $\text{Mg}/\text{Mg}+\text{Fe}^{2+}$ (figure 4). Orthopyroxene of the megacrysts is most similar to that of the higher-Al websterite group. These differences in composition (reflected mainly in Al) cannot be due to differences in degree of fractionation, as from a single magma, since all pyroxenes have essentially identical $\text{Mg}/\text{Mg}+\text{Fe}^{2+}$. Therefore they are probably the result of crystallization from magmas of different bulk compositions, or to precipitation at significantly different pressures, or both.

Plagioclase compositions are shown in figure 5 (see also table 2). Compositions range from $\sim\text{An}_{56}\text{Ab}_{43}\text{Or}_1$ (in orthopyroxenite) to $\sim\text{An}_{34}\text{Ab}_{61}\text{Or}_5$ (megacrysts). Each inclusion type and the megacrysts seem to be characterized by a unique plagioclase composition, but this uniqueness may simply be due to the small number of samples analyzed.

In attempting to use inclusions to infer (P,T) conditions for the source area, data on subsolidus assemblages rather than on individual minerals become important. At Abiquiu the important assemblage is

plagioclase-orthopyroxene-clinopyroxene, which is shown in figure 11. The inset locates the positions of plagioclase and pyroxene within the tetrahedron $\text{SiO}_2\text{-CaO-(Mg,Fe)O-Al}_2\text{O}_3$. Plagioclase is shown on a portion of the plane $\text{CaSiO}_3\text{-(Mg,Fe)SiO}_3\text{-Al}_2\text{SiO}_5$ (parallel to base of tetrahedron) and the pyroxenes on a portion of the plane $\text{CaSiO}_3\text{-(Mg,Fe)SiO}_3\text{-Al}_2\text{O}_3$ (dipping diagonally to back corner of tetrahedron). This latter plane includes Ca-Tschermak's molecule $\text{CaAl}_2\text{SiO}_6$ within it, hence the amount of this component in the pyroxene is shown by the distance of the pyroxene compositions from the front face of the tetrahedron. The stability limits of this assemblage will be discussed in a later section.

Cieneguilla locality

Geologic setting; host rock

The inclusion suite from Cieneguilla occurs in a group of flows and tuffs, collectively called the Cieneguilla limburgites by Stearns (1953), which crop out over a small area 20 km southwest of Santa Fe. These flows consist of alkali olivine basalt and olivine nephelinite of Oligocene to mid (?) Miocene age, which were extruded immediately prior to the main episode of rifting in this area (Stearns, 1953; Sun and Baldwin, 1958). The inclusion suite occurs at what may be a deeply-eroded cinder cone in these limburgites (sample location: U. S. Geological Survey 7 1/2 minute topographic map, Tetilla Peak, New Mexico; T. 16 N., R. 8 E., section 30; Hill 6330 and two small hills 300 m to the south and southwest).

The host rock is a nephelinite; its analysis and norm are presented in table 1 (analysis 2). This rock contains about 10 % olivine phenocrysts (Fo_{85-87}) and 5 % clinopyroxene phenocrysts ($\text{Wo}_{51}\text{En}_{38}\text{Fs}_{11}$) in a non-vesicular, granular groundmass of olivine, clinopyroxene, nepheline, magnetite, biotite, and zeolites (natrolite and gonnardite). Pyroxene and olivine analyses are included in figure 6.

Description of inclusions

The main lithic inclusions occurring at this site consist of harzburgite, some containing a small amount (< 5 %) of clinopyroxene, and sparse granulite (not analyzed). Megacrysts consist of titaniferous magnetite and two types of clinopyroxene, black and green augite. These green augite megacrysts are very similar in appearance and chemistry to augite phenocrysts in the host nephelinite and in fact include grains of nepheline. A total of about 43 inclusions were collected. Fourteen of the most representative and least altered were examined in thin section and ten (listed in appendix 2) were analyzed with the microprobe. The estimated modes of these inclusions are indicated in figure 2.

The density of inclusions is greatest (5-10 per m^3) on the unmarked hill 300 m southeast of Hill 6330. This unmarked hill is the main sample locality. The harzburgite inclusions are angular to rounded, and range up to 10 cm in longest dimension. Grain sizes and shapes are very irregular. Orthopyroxene grains are generally relatively large (< 5 mm), and irregular in shape. Olivine grains

range in size from 0.2 to 4.6 mm. Larger grains are very irregular and are strained (kink bands), with curvilinear boundaries. Olivine usually occurs as smaller, unstrained grains (< 1 mm) of more regular (polygonal) shape. Spinel occurs as small (< 0.1 mm), rounded grains and as larger (< 0.5 mm), irregular grains typically associated with fine-grained, devitrified glass (?). Where present clinopyroxene occurs in small (< 1 mm), irregular grains. These textures are transitional protogranular to porphyroclastic (Mercier and Nicolas, 1975). Magnetite and clinopyroxene megacrysts occur as angular to rounded, prismatic grains 1/2 to 3 1/2 cm in longest dimension.

Mineral chemistry

Pyroxene compositions for these inclusions are presented in figure 6 and selected individual analyses are given in table 2. The green clinopyroxene megacrysts are characterized by high Al_2O_3 (5-6 weight percent) and TiO_2 (1 1/4-2 weight percent), moderate FeO^* (4-7 weight percent), and high Fe^{3+} ($\text{Fe}^{3+}/\text{Fe}^{2+} + \text{Fe}^{3+} \approx 0.8$; $\text{R}^{2+} \text{Fe}^{3+} \text{AlSiO}_6 + \text{NaFe}^{3+} \text{Si}_2\text{O}_6 \approx 13.5\%$ of end members) relative to the black megacrysts. Their compositions are slightly more magnesian than, but exactly continuous with, the compositions of phenocrysts in the host nephelinite. Black clinopyroxenes are compositionally distinct. They have significantly lower Al_2O_3 (< 2 weight percent) and TiO_2 (1/2 weight percent), higher FeO^* (7 1/2-8 weight percent), and lower Fe^{3+} ($\text{Fe}^{3+}/\text{Fe}^{2+} + \text{Fe}^{3+} \approx 0.3$; $\text{R}^{2+} \text{Fe}^{3+} \text{AlSiO}_6 + \text{NaFe}^{3+} \text{Si}_2\text{O}_6 \approx 6.6\%$ of end members) and $\text{Mg}/\text{Mg} + \text{Fe}^{2+}$ than the green megacrysts. Pyroxenes of the harzburgite are very magnesian (see figure 6). Orthopyroxene has Cr_2O_3 and TiO_2 < 1/2 weight

percent and $\text{Al}_2\text{O}_3 = 1/2\text{-}3$ weight percent; clinopyroxene has $\text{Cr}_2\text{O}_3 \approx 1/4\text{-}1\ 1/2$ weight percent, $\text{TiO}_2 \approx 1/4\text{-}1$ weight percent, and $\text{Al}_2\text{O}_3 = 2\ 1/2\text{-}4$ weight percent. Both pyroxenes have moderate Fe^{+3} ($\text{R}^{2+}\text{Fe}^{3+}$ $\text{AlSiO}_6 + \text{NaFe}^{3+}\text{Si}_2\text{O}_6$ generally $< 6\%$). Olivine is $\text{Fo}_{90\text{-}93}$, and is very slightly more magnesian in the clinopyroxene-free harzburgite ($\text{Fo}_{91\text{-}93}$) than in the clinopyroxene-bearing harzburgite ($\text{Fo}_{90\text{-}92}$).

The compositions of titaniferous magnetite megacrysts are shown in figure 7 (see also table 2). Core-rim relationships in one megacryst (B271) indicate that magnetite crystallizes toward increasing ulvöspinel (from 20 to 40 mole percent Fm_2TiO_4). Within the harzburgites, spinel compositions range greatly (figure 7 and table 2), from those typical of most spinel lherzolites (N271; c.f. figure 12) to very chromium-rich ($\text{Cr}_2\text{O}_3 = 52$ weight percent) compositions (in clinopyroxene-free harzburgite, H271 and J271). Cr in spinel correlates positively with Mg in olivine and pyroxene and inversely with Al in pyroxene.

Elephant Butte locality

Geologic setting; host rock

The inclusion suite from Elephant Butte occurs in an extensive Quaternary volcanic field east of Elephant Butte reservoir (Loeber, 1976), 15 km northeast of Truth or Consequences. Localities from which inclusions were examined in this study are: (1) locality 234 - lava flow capping south end of mesa, 4.5 km east-southeast of Elephant Butte (Elephant Butte 7 1/2 minute quadrangle), (2) locality 244 - cinder cone 5.1 km east of Kettle Top Butte (Engle 15 minute quadrangle),

(3) locality 245 - cinder cone 6.1 km northwest of Engle, and (4) locality 247 - lava flow capping mesa 7.7 km west-northwest of Engle. At sites 234 and 247 the inclusions are uniformly distributed throughout the flows, both vertically over the 6-10 m thickness of the flows and laterally at least 50-100 m along the exposures. At 247 unweathered samples are exposed in a relatively young rock fall. The density of inclusions exceeds 10 per m³.

The host rock is an alkali olivine basalt. Chemical analyses and normative compositions of the basalts at localities 234 and 247 are presented in table 1 (analyses 3 and 4). At these two localities the rock contains about 5% olivine phenocrysts in a fine-grained, granular groundmass of plagioclase microlites, olivine, magnetite, and interstitial feldspar and glass.

Description of inclusions

The inclusions at Elephant Butte constitute the most diverse of these three suites. Lithic inclusions consist of clinopyroxenite, two-pyroxene granulite, and spinel lherzolite. They are angular to rounded in shape and range in size up to at least 15 cm.

Clinopyroxenite. Two clinopyroxenite types occur, one an orthopyroxene-ulvöspinel-clinopyroxenite and the other a spinel-olivine-clinopyroxenite. This latter consists of about 90% dark green, zoned, anhedral to polygonal clinopyroxene grains, 8-9% Fe-rich spinel, and 1-2% anhedral, interstitial olivine. Clinopyroxene grains poikilitically enclose spinel. Anhedral olivine is interstitial to

clinopyroxene, and poikilitically encloses both euhedral to subhedral spinel and clinopyroxene (figure 3B). This texture, which is very similar to cumulate textures pictured by Jackson (1961), Hess (1960), Wager (1968), and Best (1975), is the only clearly igneous-appearing texture in the inclusions from Elephant Butte.

Granulite. The most common granulite present is a spinel-two-pyroxene granulite consisting of 30 to 60% plagioclase and 5 to 10% deep green to opaque spinel (figure 3C). These are commonly foliated. Average grain size is 1 to 2 mm. All phases are characterized by equant grains and polygonal textures. Plagioclase is very commonly untwinned or discontinuously twinned and may be slightly continuously zoned. In several of the inclusions orthopyroxene is surrounded by reaction rims of fine-grained olivine, sodic plagioclase, and potassium feldspar, or is completely reacted away to aggregates of these minerals (figure 3D). Several other inclusions resemble these spinel-two-pyroxene granulites in every petrographic detail except that they lack spinel. Additional granulite lithologies include an apatite-rutile-two-pyroxene granulite, petrographically similar to the spinel-two-pyroxene granulite, and a slightly more Fe-rich, ilmenite-two-pyroxene granulite.

Spinel lherzolite. Spinel lherzolite inclusions are common throughout the Elephant Butte field. These have an average grain size of $< 1/2$ -3 mm and are typically slightly foliated (figure 3E). Olivine grains range in size from $< 1/2$ to 4 mm. Large olivine grains are irregular in shape and are strained (kink bands), and have curvilinear boundaries; smaller grains are strain-free and tend to have polygonal

textures. Spinel occurs as very irregular grains along boundaries of olivine and pyroxene, elongated in the direction of the foliation. The overall textures are transitional between protogranular and porphyroclastic (Mercier and Nicolas, 1975).

Megacrysts consist of clinopyroxene, plagioclase, spinel, and ulvöspinel-magnetite. These are angular to subrounded and up to about 5 cm in size. Clinopyroxene is by far the most abundant megacryst type. These are black and vitreous in appearance and commonly have a prismatic habit.

Altogether more than 130 inclusions were collected from nine localities within the Elephant Butte volcanic field. From this collection 28 of the most representative and least altered from the four previously mentioned localities were examined in thin section. Twenty six inclusions (listed in appendix 3) were analyzed in detail with the microprobe. The estimated modal compositions of the lithic inclusions examined in thin section are indicated in figure 2.

Mineral chemistry

Pyroxene and olivine compositions for these inclusions and megacrysts are shown in figure 8. Representative individual analyses are presented in table 2. Distinct differences in pyroxene compositions exist both among and within the main inclusion types. Among the clinopyroxenite inclusions, clinopyroxene compositions correlate with the two modal types discussed above. Clinopyroxene of the spinel-olivine-clinopyroxenite is characterized by higher Al_2O_3 (8.5-9.0 weight percent), TiO_2 (~ 1.5%), and Na_2O (~ 1.4%) and by lower Fe^{3+} (R^{2+} Fe^{3+})

AlSiO₆+NaFe³⁺Si₂O₆ ~ 9% of end members) relative to clinopyroxene of the orthopyroxene-ulvöspinel-clinopyroxenite (6.0-6.4, ~1.0, ~1.0, and 10% for Al₂O₃, TiO₂, Na₂O, and R²⁺Fe³⁺AlSiO₆+NaFe³⁺Si₂O₆, respectively). In addition this group has a lower Mg/Mg+Fe²⁺ (figure 8).

Similarly pyroxene compositions in the granulites also correlate with the three modal groups: (1) two-pyroxene (± spinel) granulite, in which clinopyroxene is characterized by Al₂O₃ = 5.5-9.0 weight percent, TiO₂ = 0.5-1.5%, Na₂O = 0.7-1.4%, and Cr₂O₃ ≈ 0.2%; and orthopyroxene by Al₂O₃ = 4.0-6.6%, TiO₂ = 0.1-0.3%, Na₂O < 0.1%, and Cr₂O₃ < 0.2%. Within this group, pyroxene from spinel-free granulite is lower in Al₂O₃ (average for clinopyroxene and orthopyroxene is 6.0 and 4.2 weight percent, respectively) than pyroxene from spinel-bearing granulite (8.0 and 5.9 weight percent, respectively). (2) Apatite-rutile-two-pyroxene granulite, in which clinopyroxene and orthopyroxene are characterized by lower Al₂O₃ (~4.6 and 3.1 weight percent, respectively) and approximately similar Ti, Na, and Cr as group (1). (3) Ilmenite-two-pyroxene granulite, in which clinopyroxene has distinctly lower Al₂O₃ (3.2 weight percent), TiO₂ (0.4%), and Na₂O (0.7%) and orthopyroxene by lower Al₂O₃ (1.9%), TiO₂ (0.2%), and Na₂O (< 0.1%) than either group. In addition this granulite has lower Mg/Mg+Fe²⁺ than other granulites. Clinopyroxene megacrysts are characterized by Al₂O₃ ≈ 9.0 weight percent, TiO₂ ≈ 1.5%, Na₂O ≈ 1.4%, and Cr₂O₃ < 0.1%.

Clinopyroxene of the spinel lherzolite has Al₂O₃ = 6.6-8.0 weight percent, TiO₂ = 0.4-0.7%, and Na₂O = 1.5-2.1%. However, the high Cr₂O₃

(0.5-0.9%) and higher $\text{Mg}/\text{Mg}+\text{Fe}^{2+}$ (see figure 9) best distinguishes this group. Orthopyroxene has $\text{Al}_2\text{O}_3 = 3.3-5.1\%$, $\text{TiO}_2 \approx \text{Na}_2\text{O} \leq 0.2\%$, and $\text{Cr}_2\text{O}_3 = 0.3-0.6\%$. Discontinuous granular rims up to approximately $100\ \mu\text{m}$ thick around clinopyroxene grains in some inclusions have slightly lower Al_2O_3 (5.7%) and Na_2O (0.6-1.0%) than the cores of the grains.

Interstitial olivine from the clinopyroxenite has a narrow compositional range from Fo_{74} to Fo_{77} . Olivine from the spinel lherzolite is Fo_{88-92} .

Compositions of feldspar in the granulite inclusions are shown in figure 9 (see also table 2). Plagioclase in all of the granulites falls in the range An_{46-68} except for the ilmenite-orthopyroxene granulite. In this rock plagioclase is significantly more sodic (An_{37}). Compositions of sodic plagioclase and K-spar from the fine-grained olivine-feldspar intergrowths surrounding or replacing orthopyroxene are also shown in figure 9. These intergrowths probably result from reaction of orthopyroxene with a small amount of the host basalt introduced along grain boundaries. Orthopyroxene is particularly susceptible to alteration because it is not a liquidus phase in alkali olivine basalts at low pressures.

Figure 10 (also table 2) shows the compositions of the oxide minerals occurring in the Elephant Butte suite. For most of the clinopyroxenite, granulite, and spinel megacrysts the dominant oxide phase is pleonaste with $\text{Fe}^{2+}/\text{Mg}+\text{Fe}^{2+}$ between 0.36 and 0.52. However the presence of ulvöspinel ($\text{Fm}_2\text{TiO}_4:\text{FmFe}_2^3\text{O}_4 > 2.5$) with ilmenite

exsolution lamellae in one clinopyroxenite distinguishes this sub-type, as discussed above. These ulvöspinel grains are zoned to slightly higher Fm_2TiO_4 at the margins, and are most titaniferous adjacent to ilmenite lamellae. Ilmenite with lamellae of ulvöspinel and of potassium feldspar (figure 3F), which occurs in an Fe-rich two-pyroxene granulite, is probably not primary to the inclusion. It is associated with fine-grained reaction products, in part surrounding orthopyroxene, which include potassium feldspar, olivine, ilmenite needles, and a second, Mg-rich orthopyroxene. Hence it is likely that the ilmenite and the fine-grained reaction material are derived from the breakdown of orthopyroxene and/or from partial melting of the inclusion, in combination with contamination along grain boundaries by the host basalt. Within these ilmenite grains the ratio ilmenite:K-feldspar is approximately 4:1. The composition of this feldspar is plotted in figure 9. The large amount of additional components is due to fluorescence of adjacent ilmenite and to beam damage resulting from the small beam size used (1-2 μm). Hence the ilmenite/K-feldspar grains represent intergrowths of phases rich in incompatible elements. Similar textures in clinopyroxene-ilmenite intergrowths have been produced experimentally by eutectic crystallization (Wyatt, 1977).

In one spinel-two-pyroxene granulite inclusion (C247) ulvöspinel-rich magnetite coexists with pleonaste spinel. In addition, rims consisting of small (< 30 μm) granules of ulvöspinel commonly surround spinel grains. The pyroxenes of clinopyroxenite and granulite containing ilmenite or ulvöspinel-magnetite solid solution have lower $\text{Mg}/\text{Mg}+\text{Fe}^{2+}$

than other clinopyroxenite or granulite sub-types (figure 8). A second granulite sub-type is distinguished by the presence of rutile (not plotted) rather than pleonaste as the oxide phase.

Both spinel and ulvöspinel-magnetite solid solution (Fm_2TiO_4 : $\text{FmFe}_2^{3+}\text{O}_4 = 1$) occur as megacrysts. This ulvöspinel is similar in composition to that occurring as rims around spinel in granulite C247.

Cr-rich magnesian spinel characterizes the spinel lherzolite. The Cr_2O_3 -content is variable, ranging from 6.7 weight percent (H245) to 22.1 weight percent (E247). In general Cr in spinel correlates with $\text{Mg}/\text{Mg}+\text{Fe}^{2+}$ of pyroxene and olivine.

ORIGIN OF INCLUSIONS

Pyroxenite and granulite

Inclusions of pyroxenite (clinopyroxenite, orthopyroxenite, websterite) and of granulite are diverse both mineralogically and texturally. Where textures are well-defined they can be divided into either (1) igneous (cumulate), or (2) metamorphic (recrystallized). Group (1) includes the spinel-olivine-clinopyroxenite from Elephant Butte in which euhedral to subhedral spinel and clinopyroxene grains are poikilitically enclosed by intercumulus olivine (figure 3B). Also one orthopyroxenite inclusion from Abiquiu has a possible cumulate origin but the texture is not completely distinctive.

Group (2) is comprised of the two-pyroxene granulite inclusions from Elephant Butte. Most of these have unambiguous metamorphic textures

(figure 3C). They are characterized by equigranular, polygonal textures, with grain boundaries meeting at 120° triple points. A few plagioclase grains preserve relicts of twin lamellae and (minor) concentric zoning.

Some differences in mineral chemistry exist among these. For example, spinel-bearing granulite can be distinguished from spinel-free types based on the Al-content of the pyroxene; and pyroxene of ilmenite-two-pyroxene granulite and apatite-rutile-two-pyroxene granulite is characterized by high-Fe and low-Al, respectively (see previous section and figure 8). These pyroxene compositions cannot be related to each other by fractional crystallization from a single magma at a single depth. Therefore, even though the bulk compositions of all of these granulite inclusions are fundamentally basaltic (e.g., analysis no. 5, table 1), these inclusions probably represent fragments of at least four separate metamorphosed mafic intrusive bodies and are not cognate to their hosts. Orthopyroxene-ulvöspinel-clinopyroxenite also has a recrystallized texture, and in addition, has a relatively Fe- and Al-rich pyroxene (figure 8), hence may represent part of an additional metamorphosed intrusive body.

Most of the websterite and orthopyroxenite inclusions from Abiquiu have textures which are less well-defined. Some pyroxene grains are tabular (figure 3A) suggesting they crystallized from a melt. However, generally cores of grains contain exsolution lamellae whereas rims are free of them. The lamellae-free rims could result either from an initial compositional zoning due to down-temperature crystallization (as for example in adcumulate growth), or to an incomplete metamorphic

recrystallization. Whatever their origin the two distinct pyroxene compositions (figure 4) require that the inclusions be derived from at least two different intrusive bodies.

Megacrysts

Megacrysts of a variety of minerals occur nearly ubiquitously at mafic and ultramafic inclusion localities throughout the world (e.g., Binns et al., 1970; Irving, 1974; Wilkinson, 1975; Stuckless and Irving, 1976; Stuckless and Ericksen, 1976). The compositions of these phases indicate that they crystallized at relatively high pressures from magmas of approximately basaltic composition. They may form by one or more of several mechanisms: (1) Early interpretations favored formation of megacrysts by high pressure crystallization from their host magmas (summarized in Binns et al., 1970; also Laughlin et al., 1971). Recently Wilkinson (1975) and Ellis (1976) again emphasized the cognate nature of megacrysts suites.

(2) Recent chemical (Irving, 1974) and isotopic studies (summarized in Stuckless and Irving, 1976) showed that the megacrysts are not always strictly cognate with respect to their present hosts, although in general the range in chemical and isotopic composition for both the megacrysts and hosts is the same. To explain this similarity, Irving (1974) and Stuckless and Irving (1976) proposed that megacrysts crystallized from one magma could be entrained by a later pulse of magma (belonging to the same eruptive episode) of slightly different composition. The host lavas would then not be strictly cogenetic with the megacrysts, yet would have

similar ranges in chemical and isotopic composition due to similar conditions of origin. The mechanism by which this entrainment could occur presents a problem if megacrysts represent phenocrysts, for then large-scale and widespread magma mixing must be invoked.

(3) Irving (1974) suggested that megacrysts may represent disaggregated coarse-grained, polycrystalline aggregates (pegmatites). They need not necessarily be cogenetic with their host magma. A problem with this mechanism is that such coarse-grained aggregates are seldom observed, certainly not as frequently as should be expected considering the general abundance of megacrysts.

(4) Finally, Stuckless and Ericksen (1976) have suggested that megacrysts are formed by reaction between the host magma and included material.

Hence, although the specific mechanism(s) of megacryst formation remains problematic, the general interpretation that emerges from studies of megacrysts and their host basalts is that megacrysts are genetically related to their "host" magmas (when considered as an entire eruptive episode), either as high pressure crystallization products or by reaction between the magma and inclusions.

For the inclusions examined in this study, phases occurring as megacrysts are in general very similar in composition to the same phases in the associated mafic inclusions (especially granulite), and very different from those phases in associated lherzolite or harzburgite. The typical clinopyroxene megacrysts are very aluminous ($\text{Al}_2\text{O}_3 \approx 8 \frac{1}{2}$ - $9 \frac{1}{2}$ weight percent, sodic ($\text{Na}_2\text{O} \approx 1$ - $1 \frac{1}{2}$ weight percent), and

titaniferous ($\text{TiO}_2 \sim 1-1\ 1/2$ weight percent) augites. At Elephant Butte these are nearly identical in composition to clinopyroxene in some inclusions of the granulite (see figure 8). Clinopyroxene megacrysts from Cieneguilla are different from those at Elephant Butte. Two types are present, characterized megascopically by their color. Black megacrysts are similar to those of Elephant Butte but are much lower in Na, Al, and Ti. Green megacrysts are very clearly a phenocryst phase of their present host since their chemical trend is continuous with the trend observed in smaller, abundant, unambiguous phenocrysts (figure 6). Orthopyroxene megacrysts at Abiquiu are similar in composition to orthopyroxene of the websterite inclusions (see figure 4).

At Elephant Butte spinel and ulvöspinel-magnetite are nearly identical to these same phases occurring in the granulites (figure 9). At Cieneguilla megacrysts of magnetite with 10-25 mole percent dissolved ulvöspinel occur, similar though much lower in Al_2O_3 than the ulvöspinel-magnetite of Elephant Butte (figure 7).

Plagioclase megacrysts ($\sim\text{An}_{30-35}$) from Abiquiu are similar to, but slightly more sodic than, plagioclase occurring in websterites (figure 5), but much more sodic than phenocrysts of the host magma ($\sim\text{An}_{60-65}$).

The general chemical similarity between the megacrysts and granulites indicates only that the parental compositions are approximately the same (i.e., basaltic) and that the depth of origin is comparable. The megacrysts could be cogenetic in the narrow sense (i.e., related specifically to the host magma) but need not necessarily be. Neither the textures nor the major element compositions of the megacrysts

allows their origin to be unambiguously determined.

Lherzolite and harzburgite

Although differing from each other in modal and phase compositions both the spinel lherzolite from Elephant Butte and the harzburgite from Cieneguilla belong to the Cr-diopside ultramafic group of Wilshire and Shervais (1975). The harzburgite differs from the lherzolite in its lower abundance or absence of clinopyroxene, by the slightly higher Fo-content of the olivine (figures 6 and 8), and by the fact that clinopyroxene in the harzburgite contains more Cr_2O_3 (< 1.5 weight percent vs. 0.9 weight percent) and less Na_2O , Al_2O_3 , and TiO_2 (0.7, 3.7, and 0.3 vs. 2.1, 8.0, and 0.6%, respectively) than the clinopyroxene in lherzolite from Elephant Butte. Spinel compositions also differ between the two suites. The spinel from the Cieneguilla harzburgite has significantly higher $\text{Cr}/\text{Cr}+\text{Al}+\text{Fe}^{3+}$ than spinel from the Elephant Butte lherzolite (cf. figures 7 and 10). This greater depletion in the components of basaltic melt of the Cieneguilla harzburgite relative to the Elephant Butte lherzolite (of which Cr in spinel is the most sensitive indicator) is compatible with the harzburgite representing the residual material from a greater amount of partial melting (e.g., Ringwood, 1975; Reid and Woods, 1978).

Similar though less pronounced variations (seen primarily in the Fo-content of olivine and in the FmCr_2O_4 of spinel) occur among the inclusions of the Elephant Butte and (especially) the Cieneguilla suites. These variations show that the degree of depletion not only differs

between the two suites but varies substantially among the inclusions of a single suite, as shown for example by Reid and Woods (1978) at Kilbourne Hole.

It is generally accepted that lherzolites represent the most abundant material present in the upper mantle (e.g., Ringwood, 1975) and also that they, in general, bear no cogenetic relation to their host magmas (e.g., Frey and Green, 1974). Accordingly the lherzolite/harzburgite material from Cieneguilla and Elephant Butte is interpreted here as wall rock which was randomly incorporated as accidental xenoliths by the ascending mafic magmas. The difference in degree of depletion between the two localities is probably inherited from some earlier crust-forming event(s).

ESTIMATION OF GEOTHERMAL GRADIENT

The compositions of coexisting minerals in appropriate assemblages can be used to infer (P,T) conditions of the latest equilibration of that assemblage. If it is assumed that the inclusions equilibrated along a geothermal gradient, then the (P,T) regions define or place constraints on that geotherm. The following inclusion assemblages were used to derive pressure and temperature estimates:

- (1) clinopyroxene-orthopyroxene-plagioclase (websterite, Abiquiu)
- (2) clinopyroxene-orthopyroxene-plagioclase-spinel
(granulite, Elephant Butte)
- (3) clinopyroxene-orthopyroxene-olivine-spinel (harzburgite, Cieneguilla; and lherzolite, Elephant Butte).

Temperatures of equilibrium were determined from compositions of coexisting pyroxenes according to Wells (1977). Wells' calibration incorporates recent experimental re-determinations of the diopside-enstatite miscibility gap and its extension into the iron-bearing system. For Mg-rich pyroxene compositions, this calibration yields temperatures which are approximately 50-100°C lower than those of Wood and Banno (1973), which are based on the experiments of Davis and Boyd (1966). For the temperature calculations individual representative analyses were used and the results averaged. These average values and the range in temperatures determined from different individual pyroxene analyses in a given rock are presented in table 3. The error on the temperature calculations is approximately 70°C (Wells, 1977). The temperature regions defined by each assemblage are shown in figure 13.

Pressure limits must be determined differently for each of the different assemblages. For the plagioclase-bearing websterite from Abiquiu the important assemblage is plagioclase+clinopyroxene+orthopyroxene (figure 11). This assemblage can in principle coexist with either olivine (low pressure), spinel (intermediate pressure), or garnet (high pressure), provided the bulk composition lies sufficiently below the plane $\text{CaSiO}_3\text{-FmSiO}_3\text{-Al}_2\text{SiO}_5$ (see figure 11 for phase compositions in the simplified mafic system $\text{CaO-Al}_2\text{O}_3\text{-SiO}_2\text{-FmO}$) to be interior to all four phases. Since however a fourth phase is not present in the Abiquiu plagioclase-bearing websterite, it is not possible to estimate the pressure very precisely. The maximum pressure to which this three phase assemblage is stable is given by the breakdown of plagioclase, shown as

plagioclase-out line on figure 13 (Green and Ringwood, 1967), and the minimum pressure is atmospheric. The region of (P,T) space defined by the plagioclase-bearing websterite assemblage is shown in figure 13.

For the spinel-two-pyroxene granulites from Elephant Butte (figure 11), the presence of a fourth phase (spinel) provides a significant pressure constraint. The minimum pressure at which this assemblage is stable is governed by the reaction anorthite (plagioclase)+olivine = Al-clinopyroxene+Al-orthopyroxene+spinel and the maximum pressure by the reaction anorthite (plagioclase)+Al-clinopyroxene+Al-orthopyroxene +spinel = garnet (figure 12). In figure 13 these reaction boundaries are given by the olivine-out and garnet-in boundaries, respectively (Green and Ringwood, 1967). The greater alumina content of the pyroxenes in this assemblage possibly reflects the higher pressures of equilibration and certainly the more aluminous bulk composition.

To estimate the pressure (depth) of equilibration for the (clinopyroxene-bearing) harzburgite of Cieneguilla and the spinel lherzolite of Elephant Butte, the alumina content of orthopyroxene (0.7-2.9 and 4.4-5.1 weight percent, respectively; see table 3) was referred to the Al-isopleths recently determined by Dixon and Presnall (1977). Their experiments are actually valid only for Fe-free systems but are probably applicable to lherzolite with low Fe. These Al values are lower than experimental values, hence pressure can only be estimated. For the Cieneguilla harzburgite a minimum pressure is given by the plagioclase pyroxene to spinel pyroxene transition (shown on figure 13). The maximum pressure can in principle be determined from the Al-content of

the orthopyroxene. Direct extrapolation from the data of Dixon and Presnall (1977) suggests that a reasonable maximum is 15 kb. As has already been discussed however, the low Al_2O_3 content is due to the significant depletion which this entire suite has undergone. Therefore application of Dixon and Presnall's (1977) data is not valid. Instead the only reasonable pressure maximum for this suite is given by the spinel- to garnet pyrolite transition. For the Elephant Butte lherzolites, extrapolation from Dixon and Presnall (1977) suggests that a reasonable minimum pressure is about 14 kb; a maximum is given again by the spinel pyrolite to garnet pyrolite transition.

The regions of (P,T) space defined by each assemblage are shown in figure 13. Each region is essentially an area of uncertainty, hence the exact (P,T) conditions of equilibration of the particular assemblage could lie anywhere within that region. If at any given locality each assemblage has equilibrated along a geothermal gradient, then that geotherm must pass through the (P,T) regions defined by each assemblage. The position of a geotherm is most tightly constrained by the granulite and lherzolite assemblages from Elephant Butte (figure 13). It must pass through the lowermost part of the granulite region and the uppermost part of the lherzolite region. These regions themselves need not overlap. These (P,T) regions constrain the geotherm to pass through approximately 1000°C at 14 kb (50 km). Hence in figure 13 a "best fit" gradient (curve 1) has been constructed through this point and parallel to the oceanic gradient (curve 2). It is not expected that the geotherm at Abiquiu and at Cieneguilla should necessarily be the same as at Elephant Butte,

particularly since the assemblage at Cieneguilla represents a Miocene geotherm. However the data summarized on figure 13 do not justify constructing additional geotherms for these localities and in fact the Elephant Butte geotherm (curve 1) adequately fits all the data.

The Elephant Butte geotherm is significantly higher than the oceanic geotherm (curve 2) (Ringwood, 1975), yet lower than geotherms calculated for the Rio Grande rift on the basis of surface heat flow. Curve 3 is calculated for the northern rift (near Abiquiu) based on a two-dimensional fit to a surface heat flow of 2.8 HFU (1 HFU=1 $\mu\text{cal}/\text{cm}^2\cdot\text{s}$) (Bridwell, 1976). Curve 4 was calculated for the southern Rio Grande rift (south of Elephant Butte) for a surface heat flow of 2.4 HFU (Decker and Smithson, 1975). Both curves agree well with each other but are too high to be compatible with the assemblage data. (P,T) gradients determined from different inclusion assemblages from Kilbourne Hole in the southern Rio Grande rift give conflicting results. The gradient which Reid (1976) estimated from the compositions of spinel lherzolites (curve 5) fits the Elephant Butte data most closely, although his geotherm would be lowered somewhat by recalculation of pyroxene temperatures according to Wells (1977). In contrast a geotherm estimated by Padovani and Carter (1977 a,b) from various granulite facies assemblages coincides with the calculated geotherm of Decker and Smithson (1975).

The most likely cause for the high calculated geotherms is probably that the surface heat flow reflects transient thermal pulses from shallow intrusions. Reiter et al. (1978) calculate that a heat flow of about 2.5 HFU and somewhat greater could be induced by the introduction of

magma bodies of sufficient size at a depth of 15-30 km. In this case the calculated geotherms would be correct at shallow (< 30 km) depths, and lower geotherms would be correct at greater depths. This explanation may account for the higher temperatures apparently associated with the shallower crustal inclusions of Padovani and Carter (1977 a,b).

LITHOSPHERIC STRUCTURE BENEATH THE RIO GRANDE RIFT

The overall picture that emerges then is one in which lavas arriving at the surface have passed through and sampled a variety of rocks of different compositions, textures, and origins. Some of these are mafic to ultramafic igneous rocks, including cumulates; others are metamorphic rocks of basaltic composition. Depths of origin cannot be determined for many of the lithologies, although it is most likely that pyroxenite and at least some granulite is of crustal origin, whereas spinel-two-pyroxene granulite is probably of mantle derivation.

The presence of inclusions with igneous textures suggests that these rocks are widespread components of the lithosphere beneath the rift and that recent intrusive activity has occurred prior to, and is perhaps related to, the eruptive event that carried the inclusions to the surface. The presence of these inclusions is compatible with, although does not necessarily require, a wedge of intrusive mafic rocks emplaced into the lithosphere above a rising sub-lithospheric diapir, as elaborated for example by Ramberg (1976) for the Oslo rift. Indeed recent geophysical work suggests that such a wedge of intrusive rocks is present above anomalous mantle in the Rio Grande rift (Bridwell, 1976; McCullar and

Smithson, 1977; Olsen et al., 1977; Ramberg et al., 1978). The ages of these intrusive bodies probably spans the entire range of time over which the rift has been active -- from 25 m.y. (Lipman and Mehnert, 1975; Chapin and Seager, 1975) to the present. Rocks with clearly metamorphic textures (mainly two-pyroxene granulite) may represent rocks intruded early in the intrusive episode and subsequently metamorphosed and recrystallized by exposure to later intrusions, or alternatively, may have been part of the pre-existing lithosphere.

Inclusions of lherzolite and harzburgite probably represent sub-crustal wall rock material incorporated as accidental fragments in the ascending magmas. The spinel lherzolite at Elephant Butte was probably derived from depths greater than 50 km and the harzburgite from Cieneguilla from at least 30 km. These depths are compatible with recent seismic refraction studies (McCullar and Smithson, 1977; Olsen et al., 1977), which show the Moho to be at 27-35 km under the central and southern rift, and also with the preliminary COCORP data (Oliver and Kaufman, 1976), which suggests that the Moho is at about 36 km depth beneath the central rift.

Similarly the spinel-two-pyroxene granulite was probably derived from near 40 km depth, which means that it too was part of the upper mantle. Intrusions of granulite may correspond to reflectors seen well within the mantle by the COCORP profiling (Oliver and Kaufman, 1976). It is likely that much heterogeneity in composition exists within the uppermost mantle, particularly in regions of extensive, recent volcanism.

ACKNOWLEDGMENTS

Discussions with T. R. McGetchin and R. J. Bridwell have yielded continuing stimulation for this work. This manuscript has been considerably improved by discussions with A. L. Albee. T. R. McGetchin and R. Riecker have provided much support through the facilities of the Los Alamos Scientific Laboratory of the University of California both for field work and for electron microprobe analysis at Caltech. Additional support has been provided by a grant from the Caltech Ford/Exxon Energy Research Program and by National Science Foundation Grant EAR75-03416 A03 to A. L. Albee.

REFERENCES

- Best, M. G., 1975. Amphibole-bearing cumulate inclusions, Grand Canyon, Arizona and their bearing on silica-undersaturated hydrous magmas in the upper mantle. *J. Petrol.*, 16: 212-236.
- Binns, R. A., Duggan, M. B., and Wilkinson, J. F. G., 1970. High pressure megacrysts in alkaline lavas from northeastern New South Wales. *Am. J. Sci.*, 269: 132-168.
- Bridwell, R. J., 1976. Lithospheric thinning and the late Cenozoic thermal and tectonic regime of the northern Rio Grande rift. *New Mex. Geol. Soc. Guidebook, 27th Field Conf.*, 283-292.
- Brown, R. W., 1976. A sample fusion technique for whole rock analysis with the electron microprobe. *Geochim. Cosmochim. Acta*, 41: 435-438.
- Carmichael, I. S. E., Turner, F. J., and Verhoogen, J., 1974. *Igneous Petrology*. McGraw-Hill, New York, 739 pp.
- Champion, D. E., Albee, A. L., and Chodos, A. A., 1975. Reproducibility and operator bias in a computer-controlled system for quantitative electron microprobe analysis. *Proc. 10th Ann. Microbeam Anal. Soc. Conf.*, pp. 55A-55F.
- Chapin, C. E., and Seager, W., 1975. Evolution of the Rio Grande rift in the Socorro and Las Cruces area. *New Mex. Geol. Soc. Guidebook, 26th Field Conf.*, 297-322.
- Chodos, A. A., and Albee, A. L., 1972. Automated microprobe analysis and applications to analysis of exotic lunar phases. *Proc. 6th Internat. Conf. X-ray Optics and Microanalysis*, pp. 779-784.
- Chodos, A. A., Albee, A. L., Gancarz, A. J., and Laird, J., 1973. Optimization of computer-controlled quantitative analysis of minerals. *Proc. 8th Nat. Conf. Electron Probe Anal.*, pp. 45A-45C.
- Coombs, D. S., and Wilkinson, J. F. G., 1969. Lineages and fractionation trends in undersaturated volcanic rocks from the East Otago volcanic province (New Zealand) and related rocks. *J. Petrol.*, 10: 440-501.
- Davis, B. T. C., and Boyd, F. R., 1966. The join $Mg_2Si_2O_6$ - $CaMgSi_2O_6$ at 30 kilobars pressure and its application to pyroxenes from kimberlites. *J. Geophys. Res.*, 71: 3567-3576.
- Decker, E. R., and Smithson, S. B., 1975. Heat flow and gravity interpretation across the Rio Grande rift in southern New Mexico and west Texas. *J. Geophys. Res.*, 80: 2542-2552.

- Dixon, J. R., and Presnall, D. C., 1977. Geothermometry and geobarometry of synthetic spinel lherzolite in the system $\text{CaO-MgO-Al}_2\text{O}_3\text{-SiO}_2$ (abstr.). Second Internat. Kimberlite Conf., Santa Fe, N. Mex.
- Ellis, D. J., 1976. High pressure cognate inclusions in the Newer Volcanics of Victoria. *Contr. Mineral. Petrol.*, 58: 149-180.
- Frey, F. A., and Green, D. H., 1974. The mineralogy, geochemistry, and origin of lherzolite inclusions in Victorian basanites. *Geochim. Cosmochim. Acta*, 38: 1023-1059.
- Green, D. H., and Ringwood, A. E., 1967. An experimental investigation of the gabbro to eclogite transformation and its petrological applications. *Geochim. Cosmochim. Acta*, 31: 767-833.
- Hess, H. H., 1960. Stillwater igneous complex, Montana. *Geol. Soc. Amer. Mem.*, 80: 230pp.
- IUGS Subcommittee on the Systematics of Igneous Rocks, 1973. Classification and nomenclature of plutonic rocks: recommendations. *N. Jb. Mineral. Mh.*, H. 4, 149-164.
- Irving, A. J., 1974. Megacrysts from the Newer Basalts and other basaltic rocks of southeastern Australia. *Geol. Soc. Amer. Bull.*, 85: 1503-1514.
- Jackson, E. D., 1961. Primary textures and mineral associations in the ultramafic zone of the Stillwater complex, Montana. *U. S. Geol. Surv. Prof. Paper*, 358, 106pp.
- Laughlin, A. W., Brookins, D. G., Kudo, A. M., and Causey, J. D., 1971. Chemical and strontium isotopic investigations of ultramafic inclusions and basalt, Bandera Crater, New Mexico. *Geochim. Cosmochim. Acta*, 35: 107-113.
- Lipman, P. W., and Mehnert, H. H., 1975. Late Cenozoic basaltic volcanism and the development of the Rio Grande depression in the southern Rocky Mountains. *Geol. Soc. Amer. Mem.*, 144: 119-154.
- Loeber, K. N., 1976. Cenozoic volcanic geology of the Truth or Consequences-Engle area, New Mexico (abstr.). *Abstracts with Programs, Geol. Soc. Am. Rocky Mtn. Sec. Ann. Mtg.*, 8: 601-602.
- McCullar, D. B., and Smithson, S. B., 1977. Unreversed seismic crustal refraction profile across the southern Rio Grande rift (abstr.). *EOS, Trans. Am. Geophys. Union*, 58: 1184.
- Mercier, J.-C. C., and Nicolas, A., 1975. Textures and fabrics of upper-mantle peridotites as illustrated by xenoliths from basalts. *J. Petrol.*, 16: 454-487.

- Oliver, J., and Kaufman, S., 1976. Profiling the Rio Grande rift. *Geotimes*, 21: 20-23.
- Olsen, K. H., Keller, G. R., Stewart, J. N., Homuth, E. F., Cash, D. J., and Newton, C. A., 1977. A seismic refraction study of crustal structure in the central Rio Grande rift, New Mexico (abstr.). *EOS, Trans. Am. Geophys. Union*, 58:1184.
- Padovani, E. R., and Carter, J. L., 1977a. Aspects of the deep crustal evolution beneath south central New Mexico. Pp. 19-55 in *The Earth's Crust* (eds. Heacock, J. G., Keller, G. V., Oliver, J. E., and Simmons, G.). *Amer. Geophys. Union Mono.*, 20.
- Padovani, E. R., and Carter, J. L., 1977b. Granulite facies xenoliths from Kilbourne Hole maar, New Mexico, and their bearing on deep crustal evolution (abstr.). *Second Internat. Kimberlite Conf.*, Santa Fe, N. Mex.
- Ramberg, I. B., 1976. Gravity interpretation of the Oslo Graben and associated igneous rocks. *Norges Geol. Unders.*, 325: 1-94.
- Ramberg, I. B., Cook, F. A., and Smithson, S. B., 1978. Structure of the Rio Grande rift in southern New Mexico and West Texas based on gravity interpretation. *Geol. Soc. Am. Bull.*, 89: 107-123.
- Reid, J. B., Jr., 1976. Upper and lower constraints to the geothermal gradient beneath the southern Rio Grande rift (abstr.). *Abstracts with Programs, Geol. Soc. Am. Rocky Mtn. Sec. Ann. Mtg.*, 8: 621.
- Reid, J. B., Jr., and Woods, G. A., 1978. Oceanic mantle beneath the southwestern U. S. *Subm. Earth Planet. Sci. Lett.*
- Reiter, M., Shearer, C., and Edwards, C. L., 1978. Geothermal anomalies along the Rio Grande rift in New Mexico. *Geol.*, 6: 85-88.
- Ringwood, A. E., 1975. *Composition and Petrology of the Earth's Mantle*. McGraw-Hill, New York, 618pp.
- Smith, R. L., Bailey, R. A., and Ross, C. S., 1970. *Geologic Map of the Jemez Mountains, New Mexico*. U. S. Geol. Surv. Map, I-571.
- Stearns, C. E., 1953. Tertiary geology of the Galisteo-Tonque area, New Mexico. *Geol. Soc. Am. Bull.*, 64: 459-508.
- Stuckless, J. S., and Ericksen, R. L., 1976. Strontium isotope geochemistry of the volcanic rocks and associated megacrysts and inclusions from Ross Island and vicinity, Antarctica. *Contr. Mineral. Petrol.*, 58: 111-126.

- Stuckless, J. S., and Irving, A. J., 1976. Strontium isotope geochemistry of megacrysts and host basalts from southeastern Australia. *Geochim. Cosmochim. Acta*, 40: 209-213.
- Sun, M., and Baldwin, B., 1958. Volcanic rocks of the Cienega area, Santa Fe County, New Mexico. *New Mex. Bur. Mines Miner. Res. Bull.*, 54: 80pp.
- Wager, L. R., 1968. Rhythmic and cryptic layering in mafic and ultramafic plutons. In: H. H. Hess and A. Poldervaart (Editors), *Basalts*. Interscience, New York, pp. 573-622.
- Wells, P. R. A., 1977. Pyroxene geothermometry in simple and complex systems. *Contr. Mineral. Petrol.*, 62: 129-139.
- Wilkinson, J. F. G., 1975. An Al-spinel ultramafic-mafic inclusion suite and high pressure megacrysts in an analcimite and their bearing on basaltic magma fractionation at elevated pressures. *Contr. Mineral. Petrol.*, 53: 71-104.
- Wilshire, H. G., and Shervais, J. W., 1975. Al-augite and Cr-diopside ultramafic xenoliths in basaltic rocks from western United States. *Phys. Chem. Earth*, 9: 257-272.
- Wood, B. J., and Banno, S., 1973. Garnet-orthopyroxene and Orthopyroxene-clinopyroxene relationships in simple and complex systems. *Contr. Mineral. Petrol.*, 42: 109-124.
- Wyatt, B. A., 1977. The melting and crystallization behavior of a natural clinopyroxene-ilmenite intergrowth. *Contr. Mineral. Petrol.*, 61: 1-9.

TABLE 1

Chemical compositions (weight %) and Barth-Niggli cation norms (cation %) of host volcanic rocks and granulite inclusion. *Fe₂O₃ calculated from Fe³⁺/Fe²⁺+Fe³⁺ = 0.1 for volcanic rocks.

	1	2	3	4	5
SiO ₂	52.25	42.46	47.73	48.98	49.75
TiO ₂	1.48	1.88	2.09	2.06	0.15
Al ₂ O ₃	16.80	11.40	16.52	16.59	21.61
Fe ₂ O ₃ *	1.42	1.83	1.90	1.85	
FeO	7.12	9.17	9.50	9.27	6.41
MgO	5.84	15.54	6.53	6.63	9.48
CaO	8.45	12.98	8.28	7.85	9.13
Na ₂ O	4.46	3.09	5.07	5.45	3.27
K ₂ O	1.53	0.81	2.21	1.47	0.29
P ₂ O ₅	0.64	1.01	0.59	0.35	0.04
TOTAL	99.99	100.17	100.42	100.50	100.13
Mg-value	59.4	62.9	55.1	56.0	
or	8.95	0	12.82	8.50	1.66
ab	38.31	0	18.13	25.90	28.47
an	21.10	14.41	15.52	16.13	42.13
ne	0.80	16.15	15.95	13.21	0
di	13.01	32.30	16.84	15.81	1.23
hy	0	0	0	0	2.33
ol	13.00	26.60	14.71	15.03	23.90
cs	0	0.39	0	0	0
mt	1.47	1.86	1.96	1.90	0
ilm	2.04	2.54	2.86	2.81	0.20
ap	1.32	2.05	1.21	0.72	0.08

Sample key:

1. 75-F212-JM-WSB (host rock), Alkali olivine basalt, Mesa de Abiquiu flow.
2. 76-A271-JM-WSB. Nephelinite. Cieneguilla Limburgite.
3. 75-234-EB-WSB. Alkali olivine basalt. Elephant Butte volcanic field.
4. 75-247-EB-WSB. Alkali olivine basalt. Elephant Butte volcanic field.
5. 75-A247-EB-WSB. Spinel-two-pyroxene granulite. Elephant Butte volcanic field.

TABLE 2. Representative individual chemical analyses of major phases in most abundant inclusion types.

	Abiquiu				Cieneguilla						
	Websterite		Megacrysts		Harzburgite				Megacrysts		
	B271		P212	D212	L271				C271	E271	D271
	CPX	OPX	PLAG	OPX	OL	OPX	CPX	SP	MT	CPX	CPX
1-2	5-1	1-2	1-4	9-1	4-2	7-1	2-1	1-4	1-2	2-1	
SiO ₂	51.91	53.53	59.21	51.10	40.65	56.61	53.45	0.07	0.13	52.57	48.94
TiO ₂	0.38	0.12	0.00	0.23	0.00	0.00	0.03	0.02	13.94	0.55	1.66
Al ₂ O ₃	2.62	1.57	25.55	5.32	0.02	2.41	2.57	35.94	4.24	1.68	5.01
Cr ₂ O ₃	0.15	0.08		0.00	0.03	0.33	0.22	29.39	0.00	0.00	0.45
MgO	14.93	27.68	0.00	25.22	51.35	34.46	17.99	17.46	4.82	14.19	14.16
CaO	22.07	0.71	7.49	1.33	0.04	0.50	22.62			23.28	24.29
BaO			0.03								
FeO*	6.58	15.43	0.17	16.61	8.77	5.60	2.46	16.92	74.11	7.44	5.48
MnO	0.22	0.33		0.27	0.21	0.13	0.07	0.10	0.56	0.18	0.07
NiO					0.42						
Na ₂ O	0.63	0.00	6.96	0.07		0.01	0.49			0.60	0.43
K ₂ O			0.78								
ZrO ₂								0.04	0.02		
Nb ₂ O ₃								0.00	0.00		
ZnO								0.08	0.07		
Total	99.49	99.45	100.19	100.15	101.49	100.05	99.90	100.02	97.89	100.49	100.49
MOLECULAR END MEMBERS											
An			35.0								
Ab			59.9								
Or			4.4								
Wo	40.2	0.0		0.0		0.0	40.3			43.5	39.8
En (Fo)	41.1	72.7		63.0	91.1	86.4	48.4			39.0	38.7
Fs (Fa)	7.1	20.9		21.6	8.9	8.0	0.9			8.4	2.5
Pleo								60.0	8.8		
Mt								7.1	54.3		
Chr								32.9	0.0		
Ulv								0.0	36.9		
Other	11.6	6.4	0.7	15.4		5.6	10.4			9.1	19.0

TABLE 2 (cont.) Representative individual chemical analyses of major phases in most abundant inclusion types.

Elephant Butte														
	Clinopyroxenite			Granulite				Megacrysts			Lherzolite			
	D245			A247				B244	C244	B234	A245			
	CPX	OL	SP	PLAG	CPX	OPX	SP	CPX	SP	MT	CPX	OPX	OL	SP
	2-1	1-3	5-2	8-2	12-1	13-1	4-1	1-4	1-5	1-4	5-2	1-1	4-3	11-3
SiO ₂	48.59	38.82	0.15	56.00	50.25	51.62	0.09	49.01	0.14	0.15	52.59	56.02	41.35	0.06
TiO ₂	1.47	0.02	1.15	0.00	0.42	0.10	0.12	0.98	0.95	15.14	0.56	0.09	0.00	0.05
Al ₂ O ₃	8.69	0.04	55.65	27.64	7.44	5.45	61.34	8.67	55.60	9.54	6.93	4.18	0.03	56.89
Cr ₂ O ₃	0.04	0.03	0.05		0.02	0.00	0.00	0.02	0.13	0.03	0.85	0.33	0.00	11.70
MgO	13.23	39.51	15.27	0.02	13.90	27.55	16.22	14.01	15.99	3.36	15.64	33.14	50.28	21.51
CaO	19.18	0.18		10.03	19.93	0.83		19.91			21.46	0.75	0.06	
BaO				0.07										
FeO*	7.79	22.81	27.88	0.14	6.94	14.74	22.75	6.60	26.83	69.71	2.63	6.41	10.27	10.19
MnO	0.22	0.25	0.21		0.08	0.22	0.11	0.08	0.23	0.42	0.09	0.16	0.23	0.03
NiO		0.07											0.31	
Na ₂ O	1.39			5.55	1.21	0.07		1.21			1.67	0.00		
K ₂ O				0.51										
ZrO ₂			0.00				0.00		0.00	0.01				0.00
Nb ₂ O ₃			0.04				0.00		0.00	0.00				0.00
ZnO			0.06				0.00		0.34	0.07				0.13
Total	100.60	101.73	100.46	99.96	100.19	100.58	100.63	100.49	100.21	98.43	102.42	101.08	102.53	100.56
MOLECULAR END MEMBERS														
An				47.8										
Ab				48.5										
Or				2.9										
Wo	28.1				31.2	0.0		29.1			33.7	0.0		
En(Fo)	36.0	75.3			37.8	66.2		37.9			41.0	81.4	89.5	
Fs(Fa)	7.4	24.7			6.9	16.8		5.1			0.4	9.4	10.5	
Pleo			87.2				93.8		87.0	19.5				85.9
Mt			10.4				6.0		11.0	40.9				2.1
Chr			0.1				0.0		0.1	0.0				11.9
Ulv			2.3				0.2		1.9	39.6				0.1
Other	28.5			0.8	24.1	17.0		27.9			24.9	9.2		

TABLE 3

Calculated temperatures from compositions of coexisting clinopyroxene and orthopyroxene (Wells, 1977). Numbers in parentheses are variations from average temperatures obtained by using alternate individual analyses. Error is approximately 70°C (Wells, 1977). For harzburgite and lherzolite Al_2O_3 (weight %) in orthopyroxene is also given.

<u>Sample</u>	<u>T ± 70°C</u>	<u>(Al₂O₃)_{opx}</u>	
B212	887(5)		cpx-opx-plag
C214	907(11)		(websterite, Abiquiu)
A247	959(28)		
C247	912(4)		cpx-opx-plag-sp
H247	921(18)		(granulite, Elephant Butte)
L247	972(1)		
K271	943(1)	0.70	
L271	992(1)	2.48	cpx-opx-ol-sp
N271	987(15)	2.90	(harzburgite, Cieneguilla)
R271	972(42)	2.46	
A245	962(28)	4.41	
B245	969(20)	4.85	cpx-opx-ol-sp
C245	1029(4)	4.53	(lherzolite, Elephant
H245	1002(1)	5.05	Butte)
G247	934(19)	4.58	

FIGURE CAPTIONS

- Figure 1. Reference map of Rio Grande rift in New Mexico. Inclusion localities described in this paper are denoted by open circles.
- Figure 2. Terminology, after recommendations by the IUGS Subcommittee on the Systematics of Igneous Rocks (1973), except that the term "granulite" is preferred to "norite" or "gabbro" because these inclusions have metamorphic rather than igneous textures. Estimated modal compositions of lithic inclusions from each locality are shown.
- Figure 3. Photomicrographs. Length of bar is 1 mm unless indicated.
- A. Websterite (F212). Two large grains (left and right) are clinopyroxene. Discontinuous orthopyroxene lamellae and short (0.1 mm), oriented needles of rutile/ilmenite are visible. Exsolution lamellae of clinopyroxene are prominent in orthopyroxene (lower center and small grains in center). Rims are free of lamellae. Crossed nicols.
- B. Cumulate texture in clinopyroxenite (D245). Poikilitic olivine (partly iddingsitized) includes spinel (lower left) and nearly completely surrounds clinopyroxene (center). Partly crossed nicols.
- C. Polygonal texture in granulite (H245). Twin lamellae are nearly completely annealed out of plagioclase (left). Some alteration is visible along grain boundaries and in upper right. Partly crossed nicols.

D. Granulite (C247). Orthopyroxene (left center) is completely altered to fine-grained olivine (iddingsitized), plagioclase, and potassium feldspar. Clinopyroxene is in right center, plagioclase in top center. Plane-polarized light. Length of bar is 0.5 mm.

E. Spinel lherzolite (A245). Kink band is visible in large olivine grain on left. Spinel is in upper left (dark grain), orthopyroxene in upper right (medium gray grain). Partly crossed nicols.

F. Two-pyroxene granulite (D234). Lamellae of potassium feldspar (dark gray) in ilmenite (white). Thin ($\sim 5 \mu\text{m}$) lamellae of ulvöspinel (very light gray) are also visible. Reflected light. Length of bar is 0.2 mm.

Figure 4. Pyroxene and olivine compositions of inclusions and host basalt from Abiquiu.

Figure 5. Feldspar compositions of inclusions and host basalt from Abiquiu.

Figure 6. Pyroxene and olivine compositions of inclusions and host basalt from Cieneguilla.

Figure 7. Compositions of spinel and titaniferous magnetite of inclusions from Cieneguilla.

Figure 8. Pyroxene and olivine compositions of inclusions from Elephant Butte.

- Figure 9. Feldspar compositions of granulite inclusions from Elephant Butte.
- Figure 10. Compositions of spinel, ilmenite, and ulvöspinel-magnetite of inclusions from Elephant Butte. C = core, R = rim, E = analysis from near exsolution lamellae.
- Figure 11. The assemblage clinopyroxene-orthopyroxene-plagioclase from Abiquiu (left) and clinopyroxene-orthopyroxene-plagioclase-spinel from Elephant Butte (right). Inset shows phase compositions in the mafic tetrahedron $\text{Al}_2\text{O}_3\text{-CaO-(Mg,Fe)O-SiO}_2$. Plagioclase is plotted on the plane $\text{Al}_2\text{SiO}_5\text{-CaSiO}_3\text{-(Mg,Fe)SiO}_3$ (parallel to base) and pyroxene on the plane $\text{Al}_2\text{O}_3\text{-CaSiO}_3\text{-(Mg,Fe)SiO}_3$ (dipping diagonally from front face to back corner).
- Figure 12. Phase relations in the mafic system $\text{Al}_2\text{O}_3\text{-CaO-(Mg,Fe)O-SiO}_2$. Assemblages shown are for intermediate to high-pressure granulites (Green and Ringwood, 1967). The assemblage plagioclase-clinopyroxene-orthopyroxene-spinel is not stable because of presence of quartz. See text for details.
- Figure 13. Regions of (P,T) space defined by various inclusion assemblages (see text). Curve 1 is geothermal gradient which best fits Elephant Butte data (this paper). Curve 2 is the oceanic geotherm (Ringwood, 1975). Curves 3 and 4 are geotherms calculated for the Rio Grande rift based on

surface heat flow of 2.8 HFU (Bridwell, 1976) and 2.4 HFU (Decker and Smithson, 1975). Curve 5 is geotherm estimated from spinel lherzolites of Kilbourne Hole by Reid (1976).

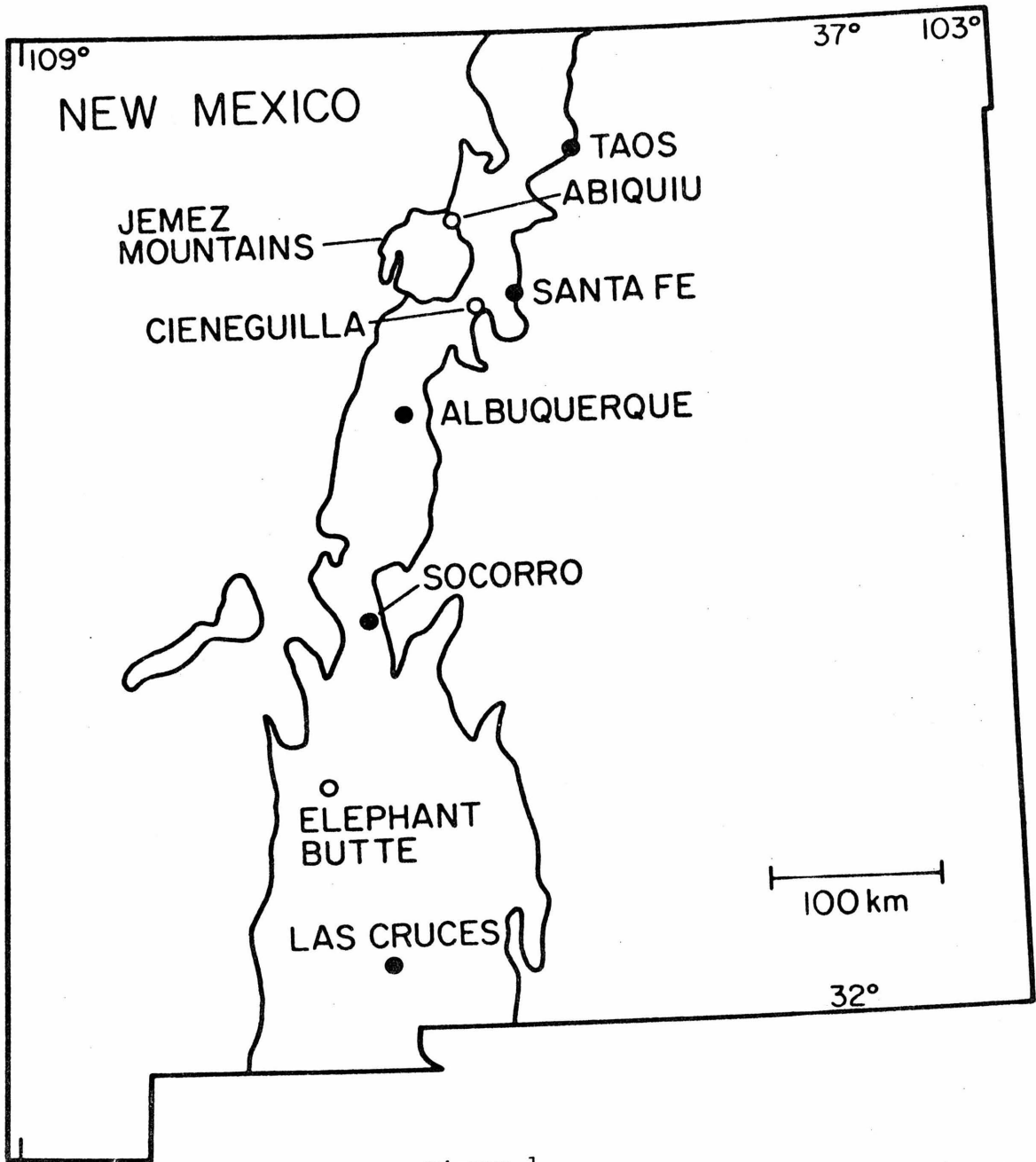


Figure 1

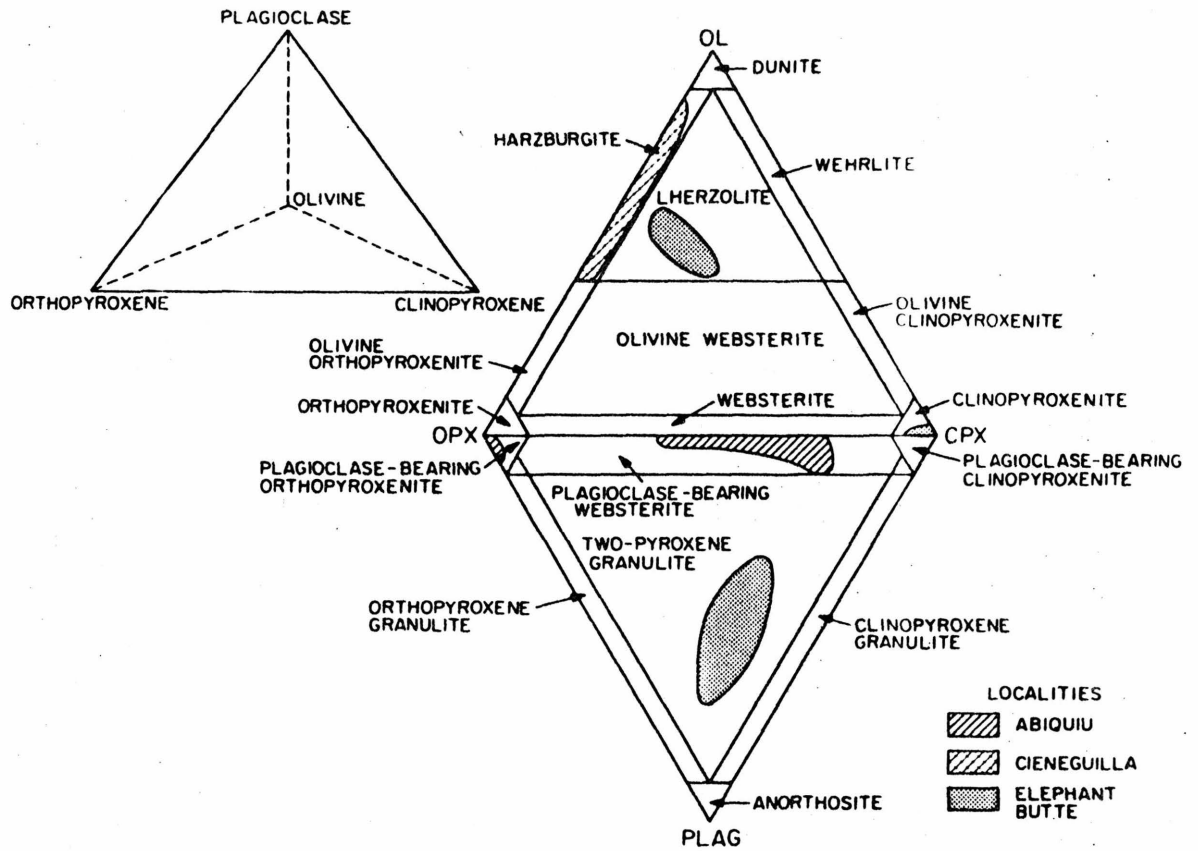


Figure 2

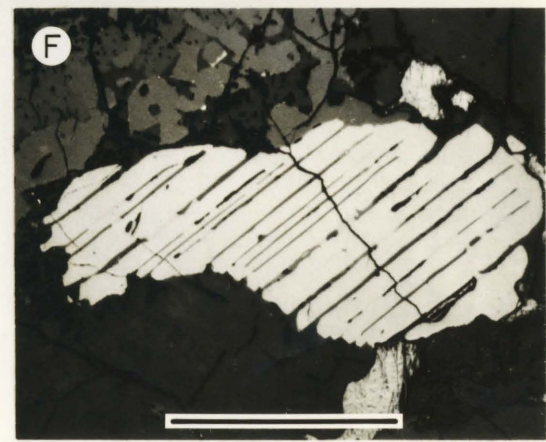
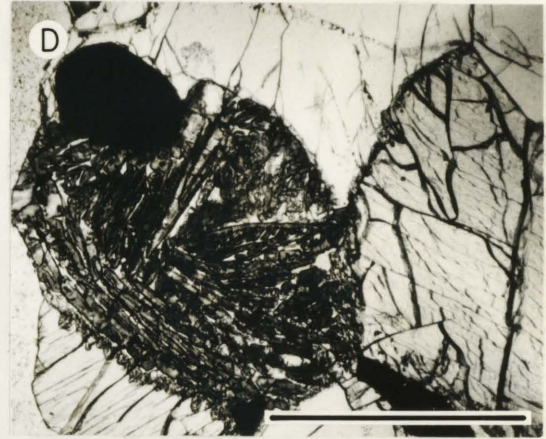
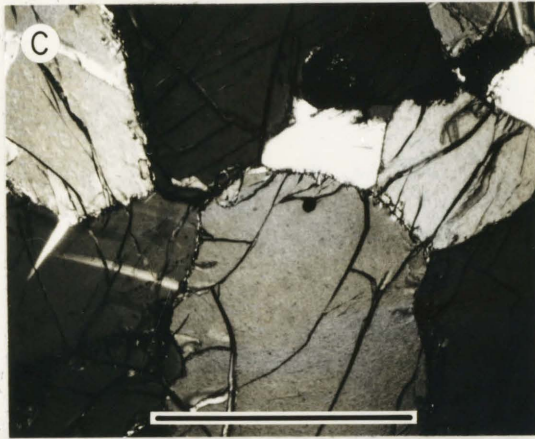
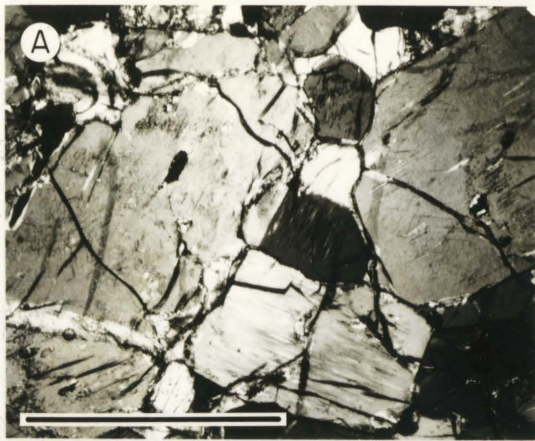


Figure 3

ABIQUIU INCLUSION SUITE
PYROXENE

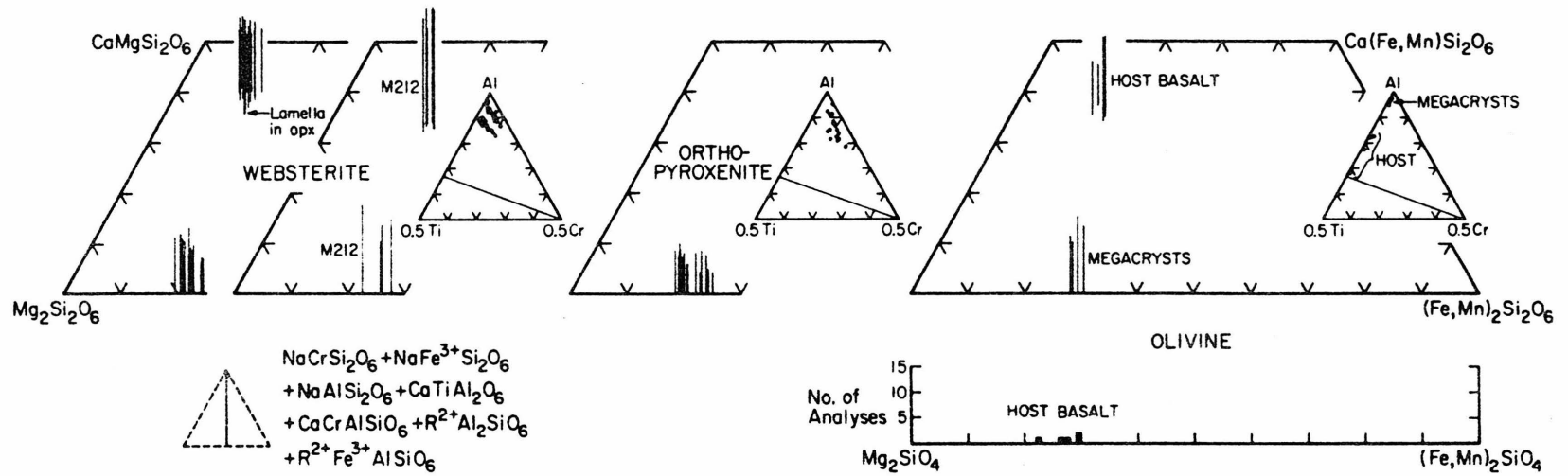


Figure 4

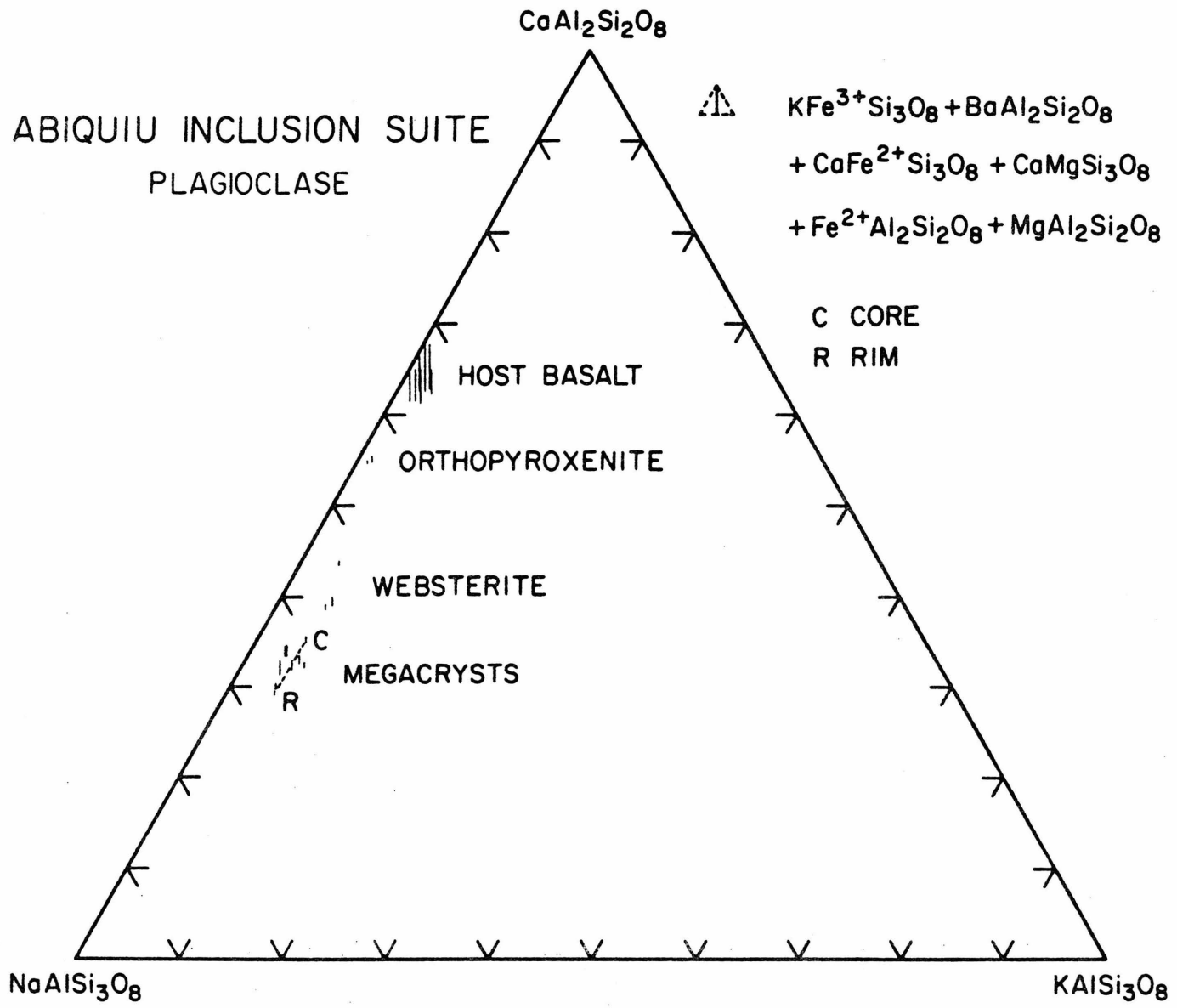


Figure 5

CIENEGUILLA INCLUSION SUITE
PYROXENE

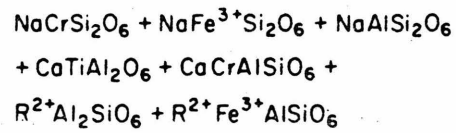
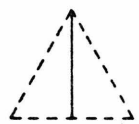
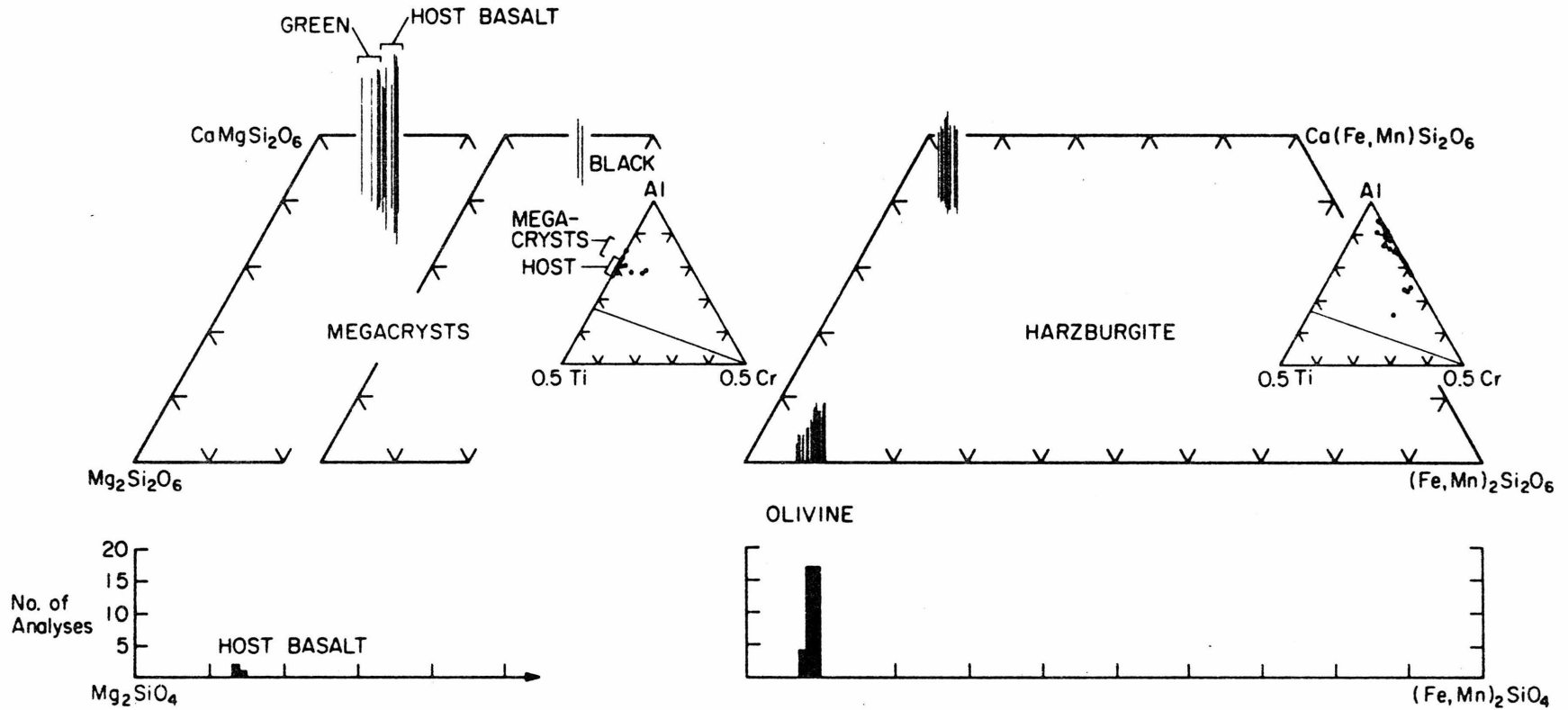
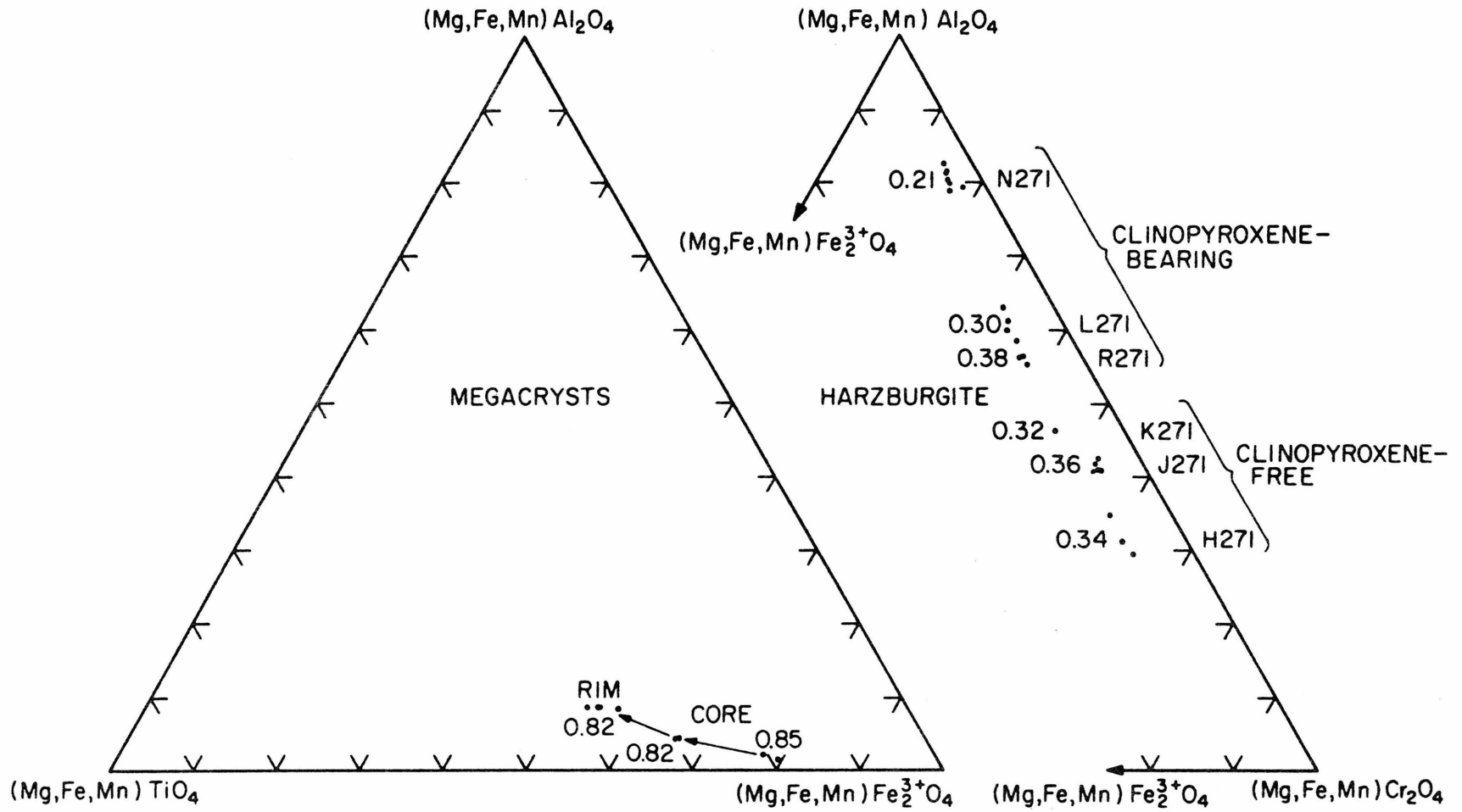


Figure 6

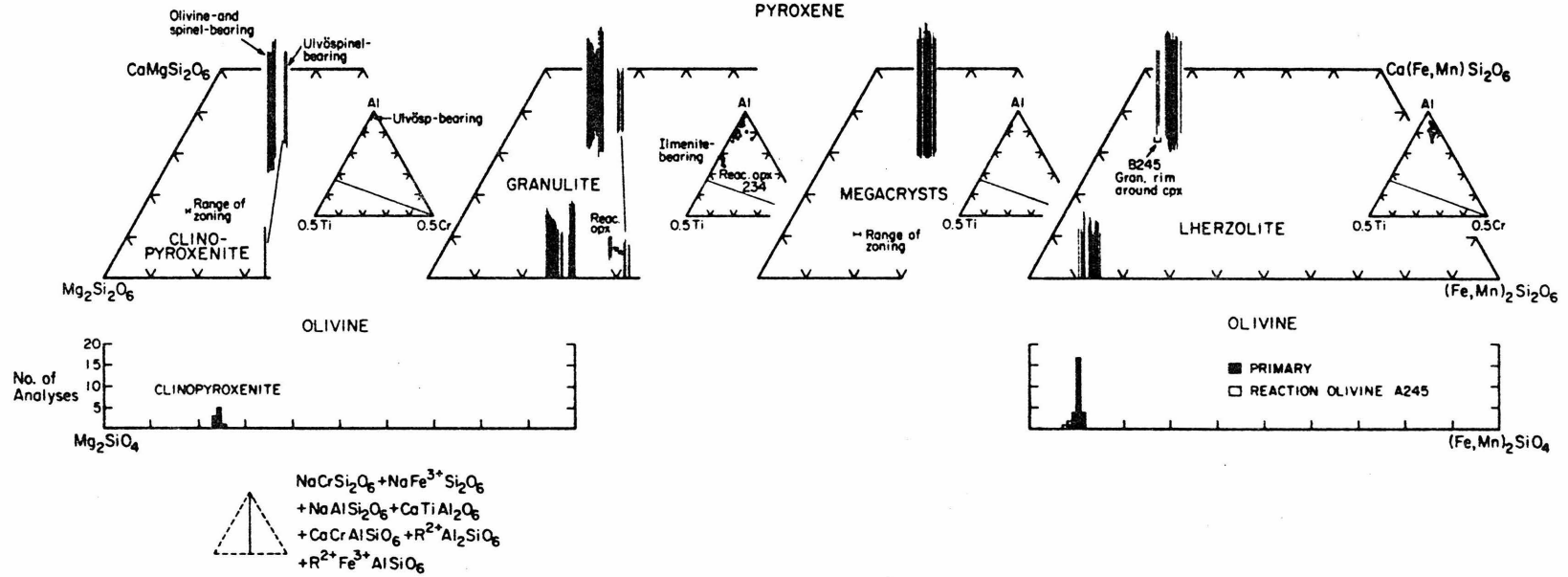
CIENEGUILLA INCLUSION SUITE
OXIDE MINERALS



No. is $\text{Fe}^{2+}/\text{Mg} + \text{Fe}^{2+}$

Figure 7

ELEPHANT BUTTE INCLUSION SUITE



204

Figure 8

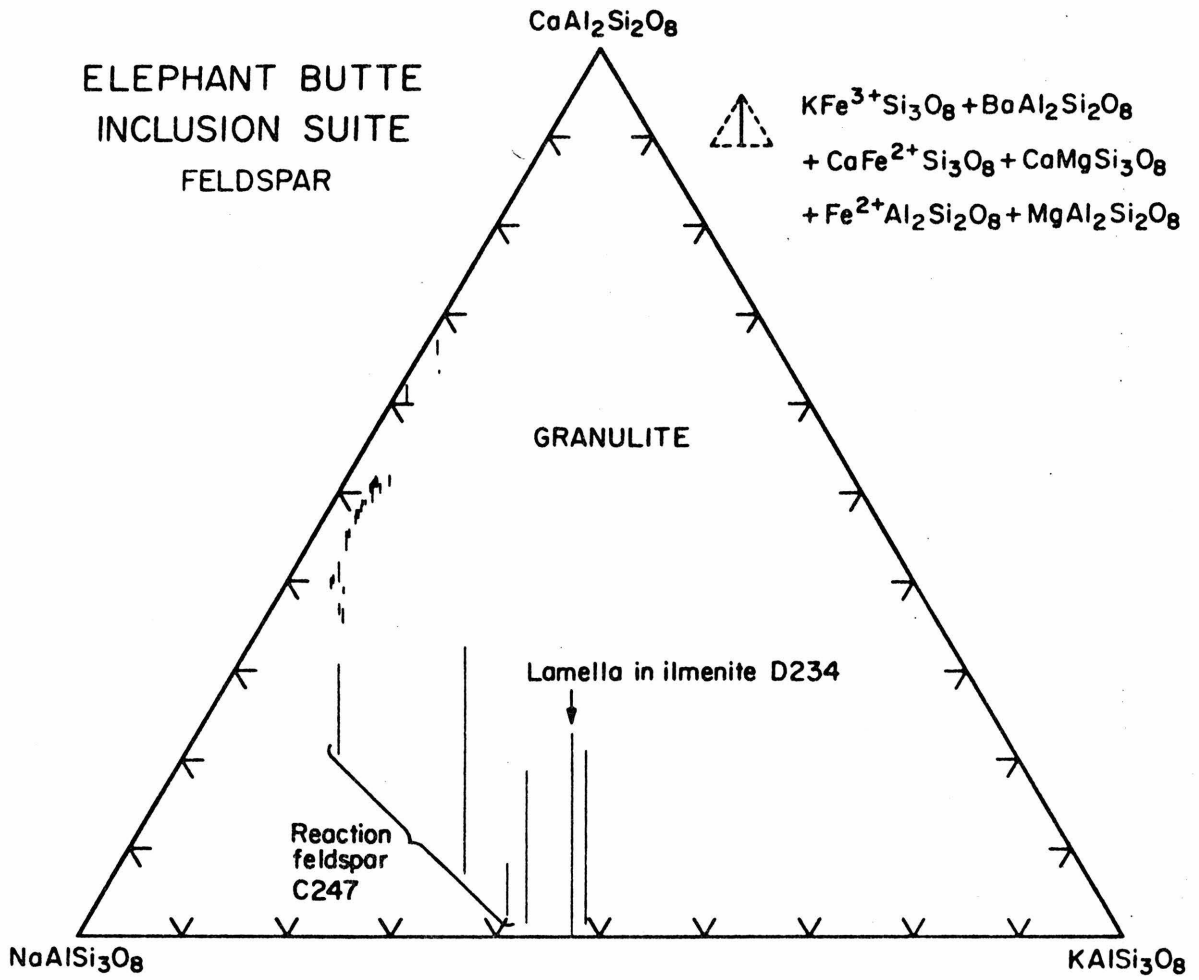


Figure 9

ELEPHANT BUTTE INCLUSION SUITE

OXIDE COMPOSITIONS

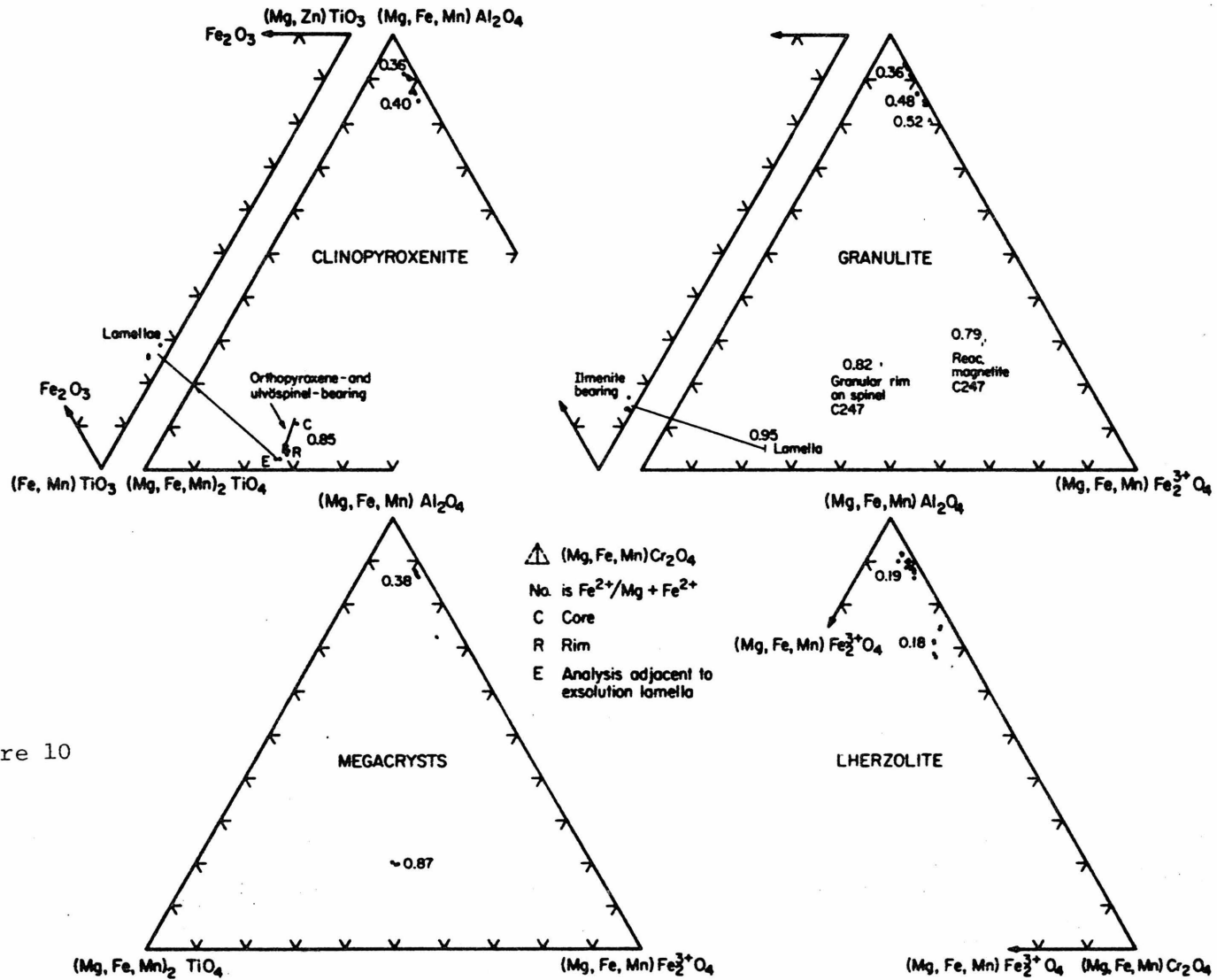


Figure 10

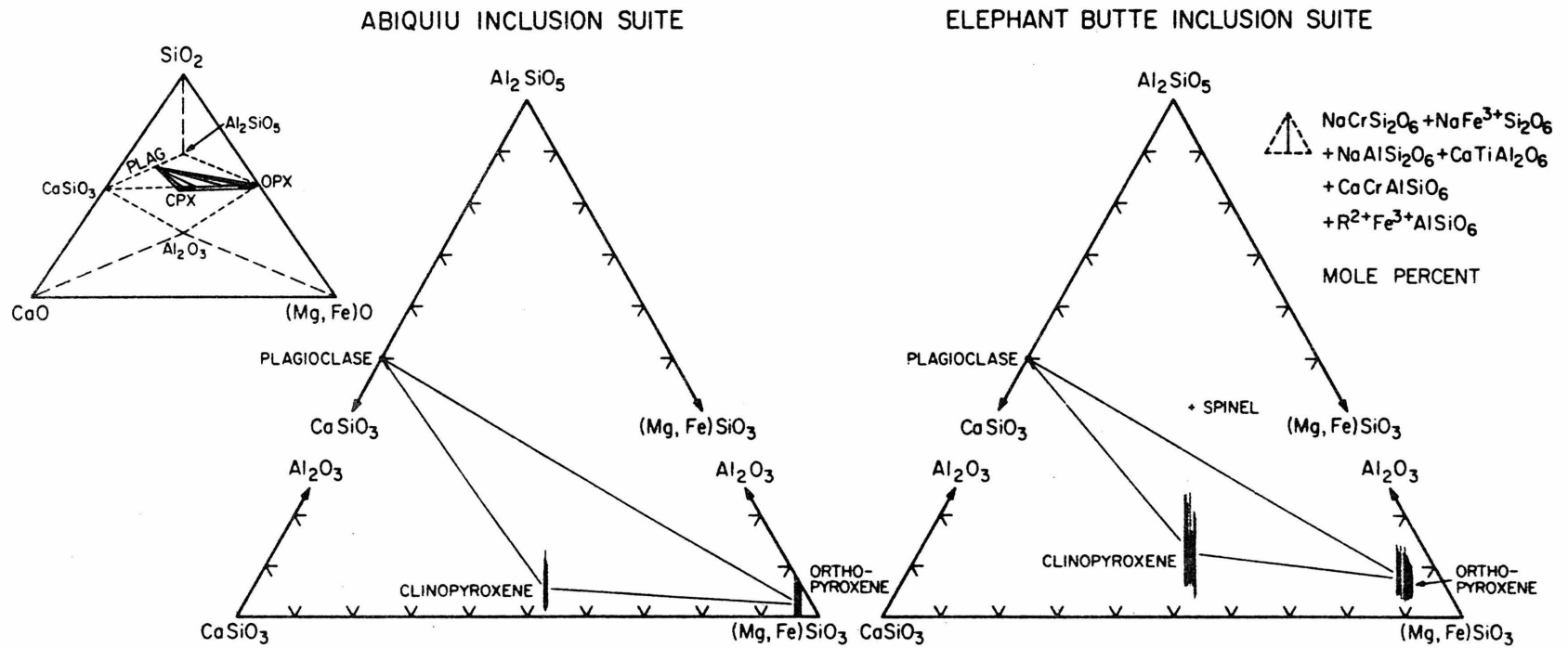


Figure 11

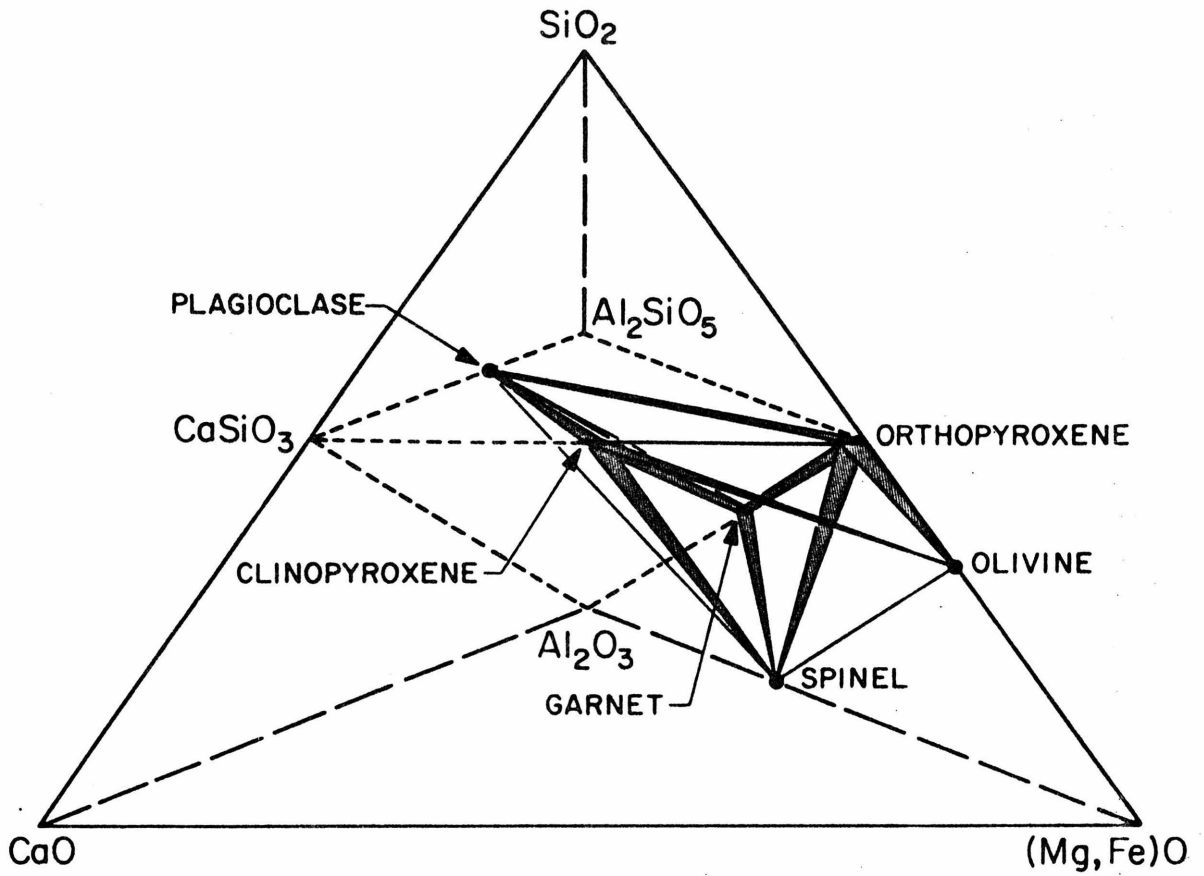


Figure 12

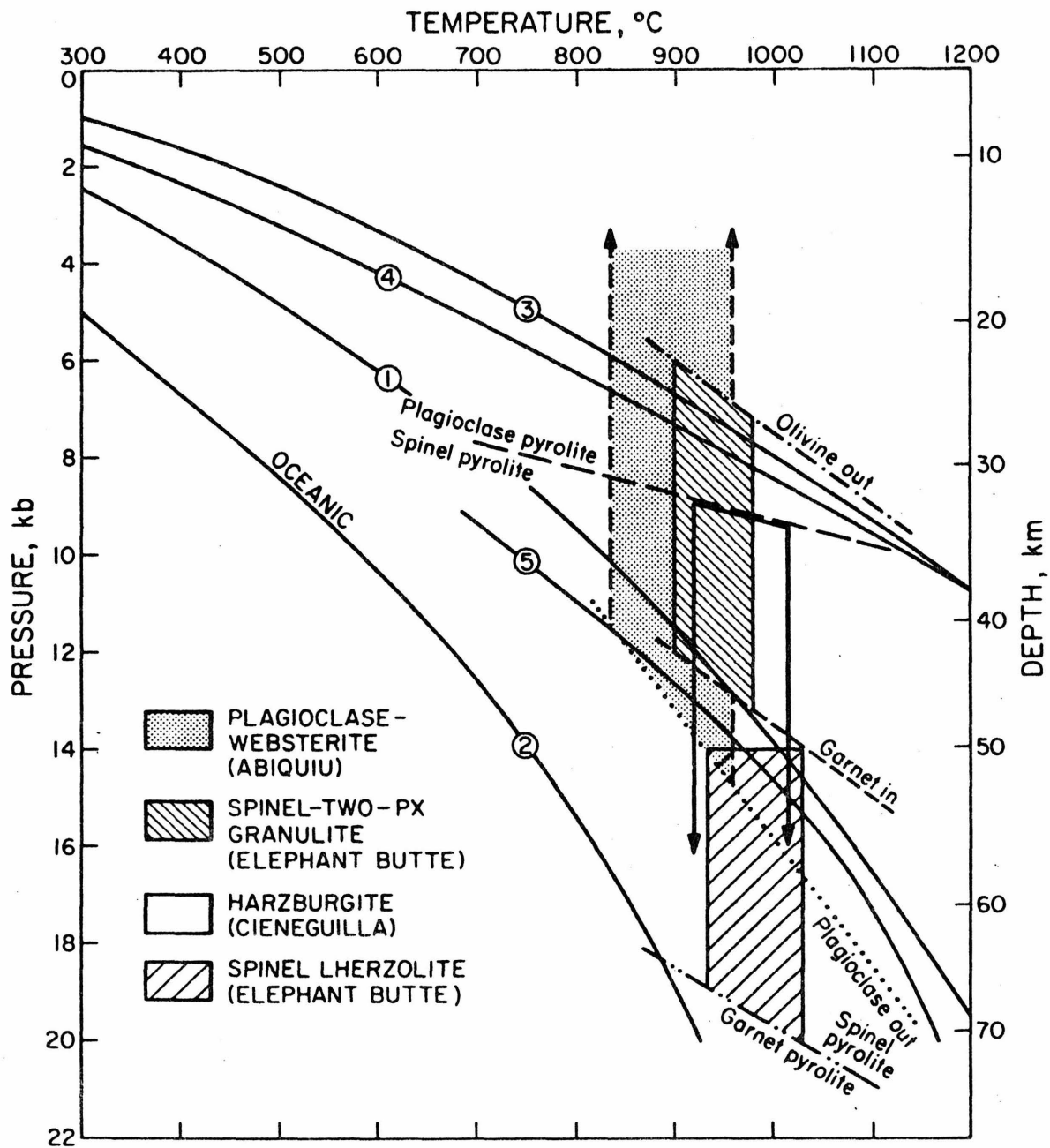


Figure 13

PART III

PETROLOGY OF FOUR LEUCITITES FROM
THE ROMAN REGION, ITALY

ABSTRACT

Four leucitites from Italy, described originally by Washington (1906), have been re-examined with the aid of the electron microprobe. One rock contains the four-phase assemblage plagioclase-sanidine-nepheline-leucite which corresponds to an invariant point assemblage in the liquidus tetrahedron $\text{SiO}_2\text{-NaAlSiO}_4\text{-KAlSiO}_4\text{-CaAl}_2\text{Si}_2\text{O}_8$. Additional phases in these rocks are Al-rich calcic clinopyroxene, melilite, sodalite, aluminous magnetite, and trace amounts of olivine, biotite, and apatite.

The felsic phases in these rocks commonly have unusually high Sr, Ba, and Rb contents. For example, sanidine contains as much as 6 weight percent BaO and 3 1/2 weight percent SrO; plagioclase as much as 4 weight percent BaO and 6 weight percent SrO; leucite up to 0.3 weight percent Rb_2O , 0.7 weight percent BaO, and 0.2 weight percent SrO; and nepheline as much as 0.08 weight percent BaO. Strontium is partitioned preferentially into plagioclase relative to sanidine, but barium is less distinctive.

Numerous buffer reactions relate the compositions of the solid phases to the melt composition and indicate that during crystallization the activity of silica in these melts was buffered at about 10^{-1} , the activity of alumina at about 10^{-4} , and the fugacity of oxygen at about 10^{-12} . Such reactions show that, for example, aluminous and

titaniferous pyroxenes and aluminous magnetites are a necessary consequence of low-silica melts (at an approximately constant alumina content). In addition they furnish a means of determining the activities of various pyroxene components and provide a rationale for the choice of end members.

Published oxygen- and strontium-isotope data indicate that these leucitites have interacted strongly with a crustal component. Melting experiments by Thompson (1977) suggest that they are derived directly from the mantle. Hence these melts may have acquired their crustal components from partial fusion of ocean floor sediments subducted beneath Italy.

INTRODUCTION

Nearly 70 years ago Henry S. Washington (1906) published his classical descriptions of the potassium-rich lavas which occur in the Roman Region of Italy. Among the rocks he described are several which contain the four-phase salic assemblage leucite-nepheline-sanidine-plagioclase. As far as is known this assemblage has not been reported from other alkalic provinces. Since Washington's descriptions form the basis for our present knowledge of the unusual rock types found in this volcanic region and since little detailed petrographic work has been done subsequent to Washington's time, it was felt that a re-examination of Washington's samples, using the electron microprobe, would be valuable.

More importantly, the assemblage leucite-nepheline-sanidine-plagioclase could represent crystallization at an isobaric invariant point in the system $\text{SiO}_2\text{-NaAlSiO}_4\text{-KAlSiO}_4\text{-CaAl}_2\text{Si}_2\text{O}_8$. Experimental studies of

various subsystems of this liquidus tetrahedron (e.g., Schairer and Bowen, 1947; Schairer, 1950, 1957; Yoder et al., 1957; Tuttle and Smith, 1958; Tuttle and Bowen, 1958; Fudali, 1963; Hamilton and MacKenzie, 1965; Morse, 1970) have delineated the field boundaries, but data on compositions of coexisting minerals are sparse. In the anorthite-free system only Fudali (1963) and Hamilton and MacKenzie (1965) have experimentally determined tie lines. From mineral analyses Tilley (1954, 1958) has inferred tie lines for a suite of nepheline-alkali feldspar rocks and for a leucite-nepheline dolerite. Tie lines between feldspars have been determined experimentally by Yoder et al. (1957), Iiyama (1966), and Seck (1971a,b). Data on compositions of coexisting feldspars from rocks have been presented by numerous authors including Tuttle and Bowen (1958, 130 ff), Carmichael (1963, 1965), Rahman and MacKenzie (1969), Nicholls and Carmichael (1969), and Carmichael et al. (1974, figures 5-2, 5-4). It was desired to determine the compositions of all four phases leucite-nepheline-sanidine-plagioclase which coexist with liquid at the isobaric invariant point.

The presence of the assemblage leucite-nepheline-sanidine-plagioclase was confirmed in only one (NMNH-99024) of the four samples selected for study from Washington's collection of the Roman Region. However, the strontium and barium contents of some of these phases are so high that the assemblage probably does not correspond closely to the invariant point of the simple system. Hence the original objectives were expanded to pursue the partitioning of Sr and Ba between the phases and to evaluate the effect of the low SiO_2 content of the melt upon the compositions of the phases.

DESCRIPTION OF SAMPLES

Washington's (1906) purposes in studying the leucite-bearing rocks of the Roman Region were to understand better the physio-chemical conditions under which leucite forms and also to characterize chemically the Roman Region as a whole. He presented more than 20 "superior" new bulk chemical analyses and described in great detail over 30 rock types. From his descriptions four rocks were selected, described below, which seemed likely to contain the assemblage leucite-nepheline-sanidine-plagioclase. These were furnished by Dr. W. G. Melson from the Smithsonian Institute, which now houses Washington's collection.

The Roman Region consists of eight volcanic centers of Plio-Pleistocene age lying to the west of the Apennine Mountains of central Italy. The lavas from this region are abnormally enriched not only in K but also in a suite of associated elements including Ba, Rb, Sr, Th, U, P, and the rare earths. Although they have been the subject of many geochemical studies (e.g., Hurley et al., 1966; Savelli, 1967; Locardi and Mittempergher, 1967; Appleton, 1972) little detailed petrology has been done since Washington's time. It is now recognized that the volcanic rocks of the Roman Region can be separated into two chemically distinct series on the basis of their potassium contents (Appleton, 1972). The four rocks studied in this present work all belong to the High-K series of lavas as defined by Appleton (1972) and fall very close to his inferred potassium-enriched "primitive" lavas in composition.

NMNH-99024.

Leucitite (Washington, 1906, pp. 108-111: Galeral Braccianose). Flow west of Crocicchie, south of Lake Bracciano, Sabatinian district. Zoned euhedral phenocrysts of pyroxene, < 2.2mm in length, comprising 2-3% of the rock and phenocrysts of leucite, < 2.5 mm in diameter, comprising ~ 1% of the rock are set in a groundmass dominated by equant or rounded microphenocrysts of leucite, 0.1 to 0.3 mm in diameter, which comprise ~ 30% of the rock (figure 1a). Washington (1906, p. 109) applied the term "clathrate" (meaning "latticed") to the distinctive texture produced by these leucite microphenocrysts. Between the microphenocrysts are grains of acicular to granular pyroxene spar (< 0.2 mm); magnetite (< 0.02 mm); and euhedral to anhedral interstitial feldspar (< 0.2 mm), nepheline (< 0.1 mm), and leucite (< 0.1 mm). A small amount of inclusion-filled, devitrified glass is interstitial to all other phases. Leucite phenocrysts and microphenocrysts are polysynthetically twinned, and the microphenocrysts contain abundant concentrically-arranged inclusions¹. Flow structure is evidenced by subparallel acicular groundmass pyroxene crystals.

NMNH-99055.

Melilite leucitite (cecilite) (Washington, 1906, pp. 138-141: Boval Albanose). Capo di Bove, Alban Hills. Rare phenocrysts of leucite, < 5 mm in diameter, and slightly zoned phenocrysts of pyroxene, < 0.8 mm in length, occur in a slightly vesicular groundmass dominated

¹Several inclusions were shown by electron beam scans to be calcium-rich pyroxene.

by equant or rounded microphenocrysts of leucite, 0.5 to 0.1 mm in diameter, which comprise ~ 40% of rock (clathrate texture). Between the leucite microphenocrysts occur laths of pyroxene (< 0.1 mm), granules of magnetite (< 0.05 mm), subhedral grains of nepheline and leucite (< 0.2 mm), and a trace of interstitial, inclusion-filled glass (?). Melilite occurs interstitially as anhedral, irregularly-shaped poikilitic grains (< 2 mm) filled with abundant leucite, pyroxene, and magnetite grains. Melilite possesses the characteristic peg (Washington: "pflock") structure² (figure 1b). Nepheline occurs with melilite and glass as an interstitial groundmass phase and also as subhedral to euhedral crystals along margins of vesicles (figure 1c). Rare biotite (< 0.1 mm) and olivine (< 0.05 mm) grains are scattered through the groundmass. Phenocrysts and microphenocrysts of leucite are prominently twinned and the microphenocrysts characteristically contain abundant, concentrically-arranged inclusions. Calcite was deposited in the vesicles subsequent to crystallization of nepheline.

NMNH-99071.

Leucitite (Washington, 1906, pp. 111-115: Hernical Braccianose). Rocca di Papa, Alban Hills. Zoned pyroxene, leucite, and rare, poikilitic plagioclase grains (< 1 mm) occur in a groundmass dominated by equant or rounded to angular leucite microphenocrysts, which range in diameter from

²El Goresy and Yoder (1974) have recently determined that the peg structure they examined is probably produced by exsolution of (and subsequent alteration of) kalsilite and nepheline from åkermanite rich in sodium melilite and its potassium analogue.

< 0.05 mm to ~ 0.2 mm and which comprise 40% of the rock. The texture is not distinctly clathrate because of the lower abundance of the larger, more rounded leucite microphenocrysts. Both pyroxene and plagioclase display a pronounced seriate texture. Between leucite microphenocrysts occur grains of acicular to granular pyroxene (< 0.1 mm), granules of magnetite (< 0.05 mm), and sub- to anhedral interstitial leucite (< 0.05 mm) and (commonly poikilitic) feldspar (< 0.2 mm) (figure 1d). Leucite microphenocrysts are polysynthetically twinned and commonly contain concentrically-arranged inclusions.

NMNH-99097

Leucitite (Washington, 1906, pp. 117-121: Scalal Vesuviose-Braccianose). Historic flow of 1631, La Scala, Mount Vesuvius. Zoned pyroxene phenocrysts (< 2.6 mm) comprising ~5% of the rock and equant or rounded microphenocrysts of leucite (< 0.8 mm) comprising 5 to 10% of the rock occur in a much finer-grained groundmass of pyroxene, leucite, feldspar, sodalite, and olivine (trace). Larger leucite microphenocrysts tend to show glomeroporphyritic texture. Leucite possesses a pronounced seriate texture. The groundmass consists of angular to rounded leucite, 0.1 to 0.2 mm in diameter, but the texture is not clathrate, primarily because of the lower abundance of the larger, equant leucite microphenocrysts. Leucite phenocrysts and microphenocrysts are polysynthetically twinned but essentially inclusion-free. Between the leucite microphenocrysts occur abundant granules of magnetite (0.03 mm); acicular pyroxene (0.1 mm); and anhedral, interstitial leucite, feldspar, and sodalite (0.1 mm). Rare olivine grains (0.1 mm) occur in the groundmass.

Chemical and modal data for these four samples are given in tables 1 and 2. It is virtually impossible to measure a mode in such fine-grained rocks as these. From his chemical analyses Washington (1906) calculated a "mode", based presumably on ideal mineral compositions. His results are compared in table 2 to a "mode" obtained by a least-squares solution of the mass balance equations distributing each oxide among the various observed phases (Reid et al., 1973). The microprobe analyses of tables 3-7 were averaged to obtain the mineral compositions used in the solution. Visual estimates of the phase abundances served as additional weak constraints on the solution. All phases used in these calculated modes were identified by both optical methods and by probe analyses, and in some rocks they differ from the phases used by Washington. In particular no plagioclase was found in the melilite leucitite, NMNH-99055. In NMNH-99055, magnetite is considerably less abundant than in Washington's "mode", where he probably assumed an iron-free composition for melilite. Magnetite of NMNH-99071 is very aluminous, accounting for its greater abundance than in Washington's "mode". In NMNH-99055 melilite and pyroxene are highly correlated, hence it is difficult to determine a unique solution. It is likely that pyroxene is somewhat more abundant and melilite less abundant than the least-squares solution.

ANALYTICAL TECHNIQUE

Analyses were made with a Materials Analysis Corporation model 5-SA3 electron microprobe interfaced with a Digital Equipment Corporation PDP-8/L computer. Operating techniques were similar to those described thoroughly by Chodos and Albee (1972) with an updated program (Chodos

et al., 1973). All analyses were completed and calculated into formula proportions for comparison before leaving the point of analysis. This feature of the computer control is a distinct advantage in analyzing fine-grained volcanic rocks.

Standard operating conditions were 15 kV accelerating potential, 0.05 μ A sample current, and a 15 μ beam diameter. The beam diameter was increased and the sample current decreased to 0.01 μ A when volatilization became a problem as was the case for nepheline and sodalite. Sodalite in particular suffered some loss of Na even with this reduced sample current and with a 25-30 micron beam diameter. Stability tests for K, Ca, Na, Si, and Al on the interstitial glass of NMNH-99024 showed no measurable loss of these elements with a beam diameter of approximately 30 microns and a sample current of 0.01 microamps. Hence the deficiency of the analytical sum from 100 percent is attributed to water. Analyses are accurate to about 2 to 5% for oxides constituting less than 10 weight percent of the sample and 1-2% for oxides over 10 weight percent (Champion et al., 1975).

ANALYTICAL RESULTS

Electron microprobe analyses of the minerals NMNH-99024, -055, -071, and -097 are presented in tables 3-6, respectively. These tables also include end members and formula proportions, based on normalization of the sum of the cations to 5 for feldspar and melilite; 4 for leucite and pyroxene; 3 for nepheline, olivine, and magnetite; and 20 for sodalite. As indicated near the bottom of each table some analyses are averages of several points, whereas others are analyses of single points where zoning or variable compositions are evident.

A striking feature of these analyses is the high content of SrO, BaO, and Rb₂O in many of the felsic phases -- so high as to permit study of these elements using electron microprobe analyses. Sanidine contains as much as 6 weight percent BaO and 3 1/2 weight percent SrO; plagioclase as much as 4 weight percent BaO and 6 weight percent SrO; and leucite up to 0.3 weight percent Rb₂O, 0.7 weight percent BaO, and 0.2 weight percent SrO. In rock NMNH-99055, which contains no feldspar, nepheline has as much as 0.08 weight percent BaO and nearly 8 weight percent K₂O, and melilite has up to 1.8 weight percent SrO. Sodalite in -097 contains Cl but no F or SO₃.

The pyroxene in these rocks is relatively aluminous, commonly containing 6 weight percent or more Al₂O₃. The Al₂O₃ content increases from core to rim and in general is highest in groundmass grains. Pyroxene typically contains 0.1 to 0.2 weight percent SrO. The magnetite has an extremely high Al and Ti content. Grains in -071 contain more than 20 weight percent Al₂O₃ and 10 weight percent TiO₂, and a grain in -097 contains more than 17 weight percent TiO₂.

DISCUSSION

Phase relations

Carmichael et al. (1974) have discussed crystallization within the system NaAlSi₃O₈-KAlSi₃O₈-NaAlSiO₄-KAlSiO₄-CaAl₂Si₂O₈ in some detail. The leucite-bearing rocks of this study all began crystallizing within the leucite volume, as indicated by the abundant and ubiquitous leucite phenocrysts and/or microphenocrysts. Further cooling caused the feldspars to crystallize. The liquid composition, now in equilibrium with leucite

and two feldspars, moved along a univariant line toward the isobaric invariant (reaction) point (see Carmichael et al., 1974, figures 5-10). For melts in which the fugacities of Cl_2 or SO_2 did not become high enough to cause sodium to crystallize as sodalite or hatyne, respectively, crystallization of leucite and two feldspars continued until nepheline was precipitated.

Stormer and Carmichael (1971) and Carmichael et al. (1974) have discussed the effect of sodalite in preventing the crystallization of nepheline. Essentially if f_{Cl_2} attains high enough values during crystallization, sodalite becomes a stable crystallizing phase. Sodalite is stable at silica activities well above those at which nepheline begins to crystallize. Sodalite thereby consumes Na and thus may prevent nepheline from ever crystallizing. Rock NMNH-99097 is an example where this effect may have occurred. Limiting values of $f_{\text{F}_2}/f_{\text{Cl}_2}$ and $f_{\text{SO}_2}/f_{\text{Cl}_2}$ for the stability of sodalite as a function of t and f_{O_2} have been calculated by Stormer and Carmichael (1971). A similar effect could occur where f_{SO_2} is high. High f_{SO_2} stabilizes nosean or hatyne which precedes nepheline in the crystallization sequence and may prevent precipitation of nepheline altogether.

The feldspar analyses are plotted in figure 2 in terms of end member proportions (given in tables 3-6). The sum of the minor components $\text{SrAl}_2\text{Si}_2\text{O}_8$, $\text{BaAl}_2\text{Si}_2\text{O}_8$, $\text{MgAl}_2\text{Si}_2\text{O}_8$ and $\text{FeAl}_2\text{Si}_2\text{O}_8$ is given by the size of the triangle representing each analysis. Since the proportions of Mg-feldspar and Fe-feldspar are relatively constant the variation in the size of the triangles is due mainly to differences in Sr- and Ba-

feldspar. Tie lines between coexisting plagioclase and sanidine can only be inferred, because of the difficulty of determining which grains coexist in equilibrium in such fine-grained rocks. However three tentative tie lines are shown, our criterion being that the analyzed plagioclase and sanidine grains are actually in contact with each other.

Even though the three feldspar-bearing samples NMNH-99024, -071, and -097 all come from different volcanic centers, compositional differences among them correspond in detail to those expected in a fractional crystallization sequence with the high- to low-temperature sequence -097, -071, and -024. As shown in figure 2 the plagioclase and sanidine become progressively more sodic and the Ba and Sr contents increase greatly from rock -097 to -024. An anorthoclase with the highest Ba and Sr contents occurs interstitially in -024. The pronounced enrichment of $\text{BaAl}_2\text{Si}_2\text{O}_8$ and $\text{SrAl}_2\text{Si}_2\text{O}_8$ in the feldspars in this sequence is a function of the concomitant crystallization of leucite and pyroxene, which enriches the remaining melt (and hence the feldspars) in Sr and Ba. Olivine is present in -097 and -071, the earlier rocks of the sequence, and the two feldspar-two feldspathoid assemblage only occurs in -024, the latest in the sequence. The values of Mg/Fe in clinopyroxene have overlapping ranges but tend to be lowest in rock -024.

The high Ba and Sr contents of the melts stabilized unusual feldspar compositions. The dashed line on figure 2 indicates the limit of ternary solid solution for naturally-occurring feldspars (Carmichael, 1963). In rock NMNH-99024 coexisting plagioclase and sanidine both have compositions exceeding the limit of ternary solid solution and lying within the normal

two-phase field. The presence of barium and strontium raises the intersection of the solidus with the solvus, thus expanding the field of ternary solid solution. This is compatible with the high melting point of $\text{SrAl}_2\text{Si}_2\text{O}_8$ (1660°C; Goldsmith, 1950) and $\text{BaAl}_2\text{Si}_2\text{O}_8$ (1760°C; Lin and Foster, 1968) and with the probable existence of a melting loop between $\text{BaAl}_2\text{Si}_2\text{O}_8$ and KAlSi_3O_8 (Rudert, 1972) and between $\text{BaAl}_2\text{Si}_2\text{O}_8$ and KAlSi_3O_8 (Mall and Rudert, 1974) (the analogous melting relationships involving $\text{SrAl}_2\text{Si}_2\text{O}_8$ are not known).

In figure 3 the four phase volume defined by the salic assemblage leucite-nepheline-sanidine-plagioclase of NMNH-99024 is shown in an orthographic projection of the tetrahedron NaAlSiO_4 - KAlSiO_4 - CaAl_2O_4 - SiO_2 (inset) onto the base NaAlSiO_4 - KAlSiO_4 - CaAl_2O_4 . For simplicity the feldspar compositions have been omitted and only the single tentative two-feldspar tie line (figure 2) has been shown. The cation proportions of NaAlSiO_4 , KAlSiO_4 , CaAl_2O_4 , and SiO_2 in the glass are 6.6, 25.0, 9.8, and 58.6, respectively, and the glass composition lies just within the above four phase volume. The projection of this point is shown in figure 3. The high water content of the glass analysis indicates that the glass has undergone significant alteration. The large amount of silica probably indicates that the above proportions are no longer representative of the silicate liquid in equilibrium with these solid phases.

It is believed that analyses of coexisting leucite-nepheline-sanidine-plagioclase have not previously been published. However, Tilley (1958) has analyzed the compositions of coexisting leucite-nepheline-sanidine from a leucite nepheline dolerite. In comparison to his data

sanidine of -024 has higher CaO; nepheline has lower Na_2O and K_2O , and higher SiO_2 and CaO; and leucite has lower Na_2O . In fact the leucite of all these rocks is virtually sodium-free. This composition is anomalous with respect to the experimental work of Fudali (1963), who has shown that substantial substitution of $\text{NaAlSi}_2\text{O}_6$ for KAlSi_2O_6 (approximately 40 weight percent at 1 atm pressure and 1000°C) should occur. He explained the usually sodium-free composition of volcanic leucites by suggesting that the sodium content of the magma was too low or that the crystallization temperature was too high. However neither explanation is adequate in the case of these rocks since (1) in many of these samples a sodium phase (nepheline, sodalite, or hatyne) has crystallized concurrently with leucite, and (2) in all cases the temperature was low enough that the rocks are holocrystalline or nearly so. In such rapidly quenched rocks as these, then, sodium-rich leucite grains ought to be present. Therefore to explain the sodium-enrichment of leucite under experimental conditions and the formation of pseudoleucite, the subsolidus ion-exchange mechanism as proposed by Taylor and MacKenzie (1975) whereby rapid subsolidus exchange of K and Na ions between leucite and hydrous glass produces a metastable leucite-analcite solid solution, is favored.

The assemblage of figure 3 may be taken as approximately representing the compositions of the solid phases in equilibrium with a silicate liquid at an isobaric invariant point in the system $\text{NaAlSi}_4\text{O}_{10}$ - $\text{KAlSi}_4\text{O}_{10}$ - CaAl_2O_4 - SiO_2 . The representation is necessarily only approximate because (1) the additional phases pyroxene, olivine, magnetite, etc., involving additional components, are also present as part of the system;

(2) the range of feldspar compositions present in the groundmass indicates some amount of disequilibrium; and (3) the high SrO and BaO contents of the feldspars indicate that even with respect to the salic phases the above four-component system is a simplification.

The compositions of the mafic silicate minerals of these rocks and the corresponding whole rock compositions are plotted in figure 4 in terms of their normative amounts of Ca_2SiO_4 - $(\text{Mg,Fe})_2\text{SiO}_4$ - SiO_2 . For pyroxene, only groundmass compositions are plotted because melilite and olivine occur only as groundmass phases. SrO is included with CaO. The bulk composition for rock NMNH-99055 falls within the three-phase **triangle** melilite-clinopyroxene-olivine. The compositions of the other rocks should fall on the clinopyroxene-olivine tie line (-071 and -097) or in the clinopyroxene field (-024), but are slightly shifted probably due to the presence of other components in the melt. Washington (1906) gave calculated modes of three rocks containing both melilite and plagioclase. Yoder (1973) re-examined two of these, finding only plagioclase, and concluded from these and other occurrences that melilite and plagioclase are incompatible in volcanic rocks. Sample NMNH-99055 is the third and contains melilite but no plagioclase (table 2).

Strontium and barium partitioning in feldspar

Existing data on the partition of strontium between coexisting feldspars has been critically summarized by Smith (1974, Chap. 14, pp. 23-24, 79-88). Strontium is found to partition preferentially into either plagioclase or potassium feldspar, depending upon a variety of factors. Smith (1974, p. 88) states: "The factors which control the Sr distribution

are not known, and it is certain... that there are no easy answers. In addition to temperature and pressure, it will be necessary to consider the effects of the major-element concentration of the feldspars, the order-disorder of the T atoms, the extent of unmixing, the nature of the coexisting minerals, and the bulk composition of the host rock." Relevant to the determination of strontium partitioning from natural rocks is the recognition by Berlin and Henderson (1968) and by Brooks (1968) that the strontium concentration of feldspar reflects the effect that the crystallization of other phases has on the strontium content of the melt. It is essential then, not only that both plagioclase and potassium feldspar are present, but that they were in equilibrium with a given melt at the same time during its cooling history in order to determine a true partition coefficient from concentration data.

The data in tables 3, 5, and 6 clearly show that in these leucitites strontium fractionates preferentially into plagioclase rather than into sanidine (see also figure 2). SrO has a concentration of about 6 weight percent in the plagioclase of both -024 and -071, whereas SrO in sanidine is significantly lower. Strontium is much lower in the feldspar of -097, but still appears to be more concentrated in the plagioclase (although only one grain of sanidine has been located for comparison). Partition coefficients have not been calculated because of the uncertainty of establishing which plagioclase-sanidine pair coexisted with liquid simultaneously. Only three tentative two-feldspar tie lines have been drawn. However the possibility that one feldspar appeared significantly earlier on the liquidus than the second and thereby enriched or depleted the

liquid in strontium before crystallization of the second is unlikely in these rocks because both feldspars are groundmass phases and have crystallized over essentially the same temperature interval.

The increase in SrO (and BaO) in feldspar in the fractional crystallization sequence from NMNH-99097 to -024 (figure 2) reflects the concomitant crystallization of leucite and pyroxene, which enriches the melt in SrO and BaO and results in a higher concentration of these components in the later-crystallizing feldspars. This effect can also be seen in rock NMNH-99024, as an inverse correlation between SrO vs. CaO in figure 5. It is not evident however in -071 or -097 where SrO is lower and the feldspars do not have such a range of compositions.

It is apparent from these analyses and from previous work that the partitioning of strontium between coexisting feldspars is not well characterized. The work of Barth (1961), Virgo (1968), and Scotford (1973) may have defined a real temperature-dependence of the partitioning. The pressure dependence of the partitioning, though probably small, cannot be evaluated without accurate volume or density data on strontium feldspars. In all previous investigations of strontium partitioning between coexisting feldspars, strontium was present in only trace amounts. However in these rocks strontium abundances are several orders of magnitude greater and in fact, SrO is a major element oxide in these feldspars. Consequently, it is possible that the strontium feldspar component behaves very non-ideally.

Most studies of the partitioning of barium between coexisting feldspars have shown that its behavior is better defined than that of strontium

(Smith, 1974, Chap. 14, pp. 23-24, 88-97). Because its ionic radius is close to that of potassium ($\text{Ba}^{+2}=1.35 \text{ \AA}$; $\text{K}^{+1}=1.33 \text{ \AA}$), barium tends to be concentrated in K-feldspar. A notable exception is the experimental work of Iiyama (1968) who found that at low concentrations (less than approximately 3000 ppm) barium fractionated preferentially into plagioclase.

The partitioning of barium in NMNH-99071 follows the usual pattern in that the sanidine is richer in barium (4 to 5 mole % $\text{BaAl}_2\text{Si}_2\text{O}_8$) than the plagioclase (approximately 1 to 2 mole % $\text{BaAl}_2\text{Si}_2\text{O}_8$). However the partitioning in -024 is more ambiguous. Examination of Table 3 shows that for this rock the five sanidines which are lowest in sodium (i.e., earliest in the crystallization sequence) have a smaller amount of barium (less than 2 mole % $\text{BaAl}_2\text{Si}_2\text{O}_8$) than the plagioclase, but that the two sanidines most enriched in albite-component (i.e., latest in the crystallization sequence) have a larger amount (6 1/2 to 10 1/2 mole % $\text{BaAl}_2\text{Si}_2\text{O}_8$) as expected a priori. The explanation for this apparent reversal in partition is not evident. As is the case for strontium, the absolute abundance of barium is much less in the feldspar of NMNH-99097, and barium appears to be more concentrated in plagioclase than in sanidine.

The amount of barium generally increases, parallel to the trend for strontium in the crystallization sequence from NMNH-99097 to -024. As for strontium, this trend is also well defined for NMNH-99024 alone, manifested as an inverse correlation of BaO vs. CaO (figure 5) and is less well defined for -071 and -097. Core-rim relationships in -024 and -071 show a consistent enrichment of the rim in BaO. No correlation of either the barium or strontium content of the feldspars with grain size has been discerned.

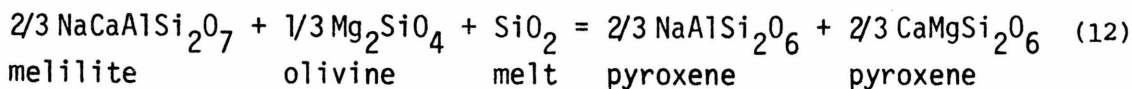
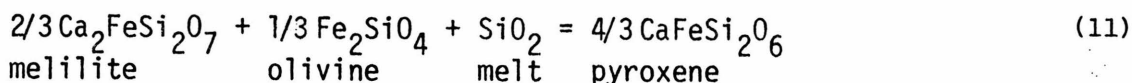
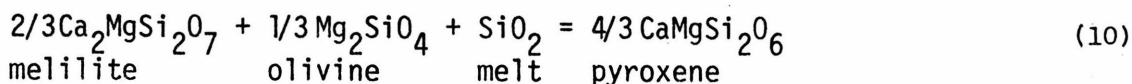
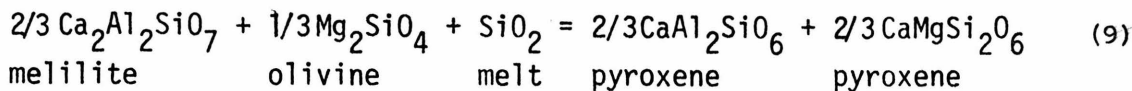
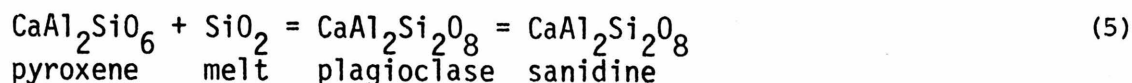
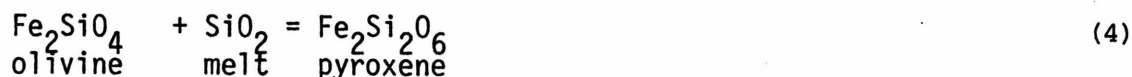
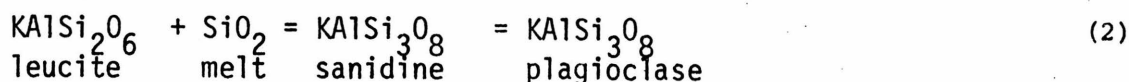
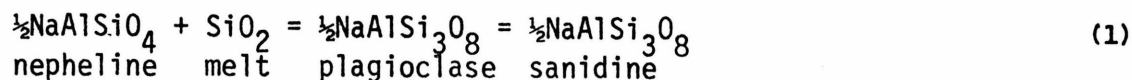
Strontium-rich (and barium-rich) feldspars may be no more rare than are major occurrences of potassium-rich rocks. It is well-known that K-rich lavas are also highly enriched in certain associated elements including Sr and Ba (e.g., Hurley et al., 1966; Locardi and Mittempergher, 1967; Appleton, 1972; Savelli, 1967; Higazy, 1954; Washington, 1920). Electron probe wavelength scans of several rocks from the Highwood Mountains of Montana were made in a reconnaissance-style search for strontium and barium. Groundmass sanidine in two rocks, one from the transition zone of the Shonkin Sag laccolith and the other from the transition zone of Square Butte, contained about half a percent of SrO and over a percent of BaO. From this same area Nakamura and Yoder (1974) report Ba-rich alkali feldspar and hyalophane, with BaO ranging up to 20 weight percent. Also Nicholls (1969) reports several feldspar analyses from rocks of the Navajo and Hopi volcanic fields which contain on the order of half a percent (1.13% maximum) of SrO and half a percent to a percent (2.96% maximum) of BaO. It is likely that many more examples of Sr- and Ba-rich feldspars (and Rb-rich leucites, etc.) will be found when more detailed analyses are made of similar rocks from such other potassic provinces of the world as the Western Rift (Africa); West Kimberly region (Australia); and the Leucite Hills (Wyoming).

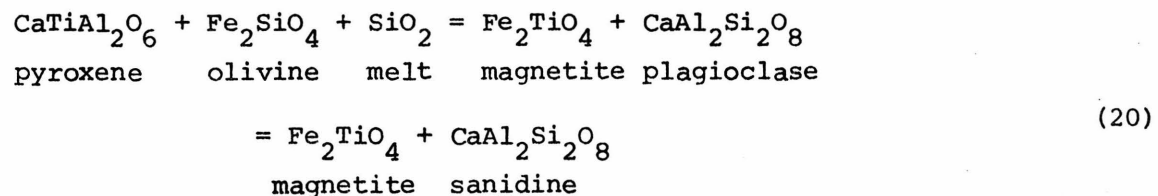
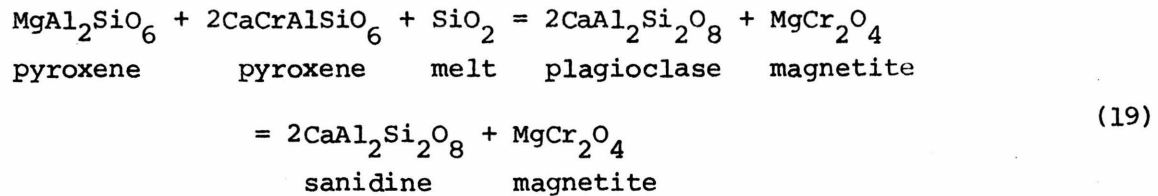
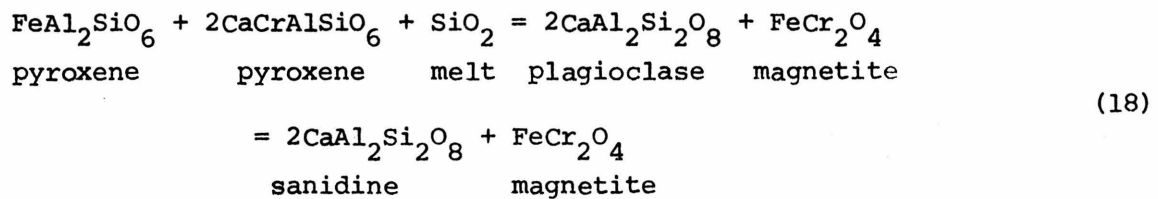
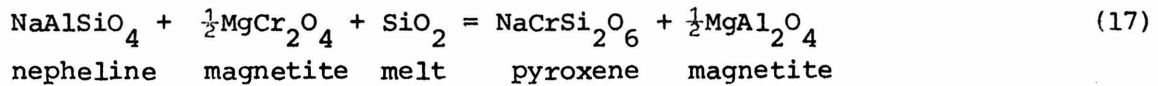
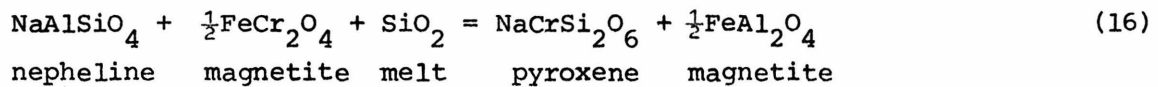
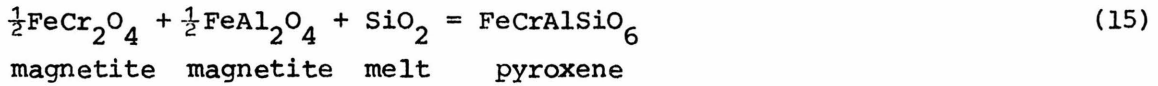
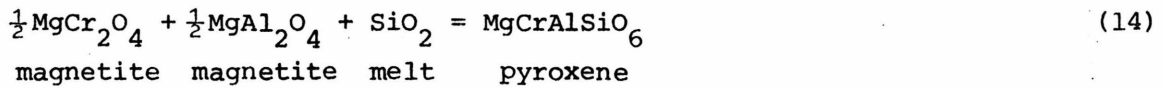
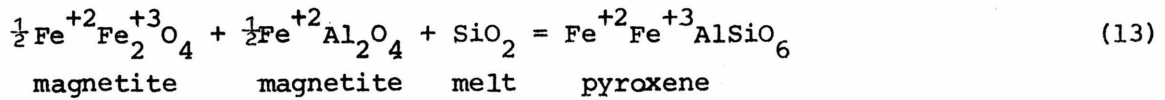
Silica and alumina activity; oxygen fugacity; pyroxene components

It is desirable to be able to determine specifically the effects of the melt composition on the compositions of the coexisting solid phases. This may be achieved by writing suitable buffer reactions. These four leucitites contain an unusually large number of phases which serve to buffer the activity of silica, alumina, and oxygen in the melt.

In theory the silica activity of the melts corresponding to these rocks may be determined (at equilibrium) from each of the following reactions, where the component is given by a formula with the phase indicated

below:





For example, for reaction (1)

$$K(T,P) = \frac{(a_{\text{plagioclase}})_{\text{NaAlSi}_3\text{O}_8}^{1/2}}{(a_{\text{nepheline}})_{\text{NaAlSiO}_4}^{1/2} \cdot a_{\text{SiO}_2}^{\text{melt}}}$$

and

$$\log a_{\text{SiO}_2}^{\text{melt}} = \frac{\Delta G_r^{\circ}}{2.303 RT} - 1/2 \log a_{\text{NaAlSiO}_4}^{\text{nepheline}} + 1/2 \log a_{\text{NaAlSi}_3\text{O}_8}^{\text{plagioclase}},$$

where $K(T,P)$ is the equilibrium constant (a function of temperature and pressure), R is the gas constant, ΔG_r° is the standard state Gibb's free energy of reaction, and $a_{\text{NaAlSi}_3\text{O}_8}^{\text{plagioclase}}$, etc., is the activity of albite component in plagioclase, etc. $\log a_{\text{SiO}_2}^{\text{melt}}$ at 1300°K has been evaluated from reactions (1), (2), (3), (5), (9), and (10) (table 7) using thermodynamic data from Robie and Waldbaum (1968), Kelly (1962)³, and Bacon and Carmichael (1973) (for ΔH_f° of diopside). Activities were calculated assuming ideal mixing of ions on each equivalent site in the various mineral structures (Wood and Banno, 1973; Bacon and Carmichael, 1973).

For example, pyroxene activities were calculated by normalizing the sum of all catatoms to 4, filling the tetrahedral sites with Si and Al, assigning remaining Al, Cr, and Ti to M_1 , assigning Ca and Na to M_2 ,

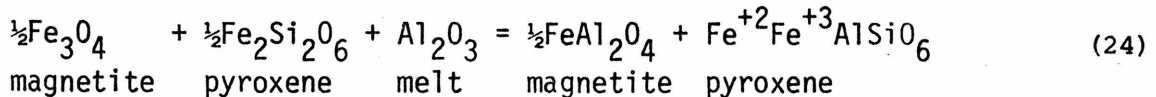
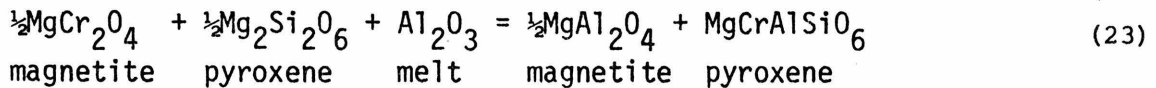
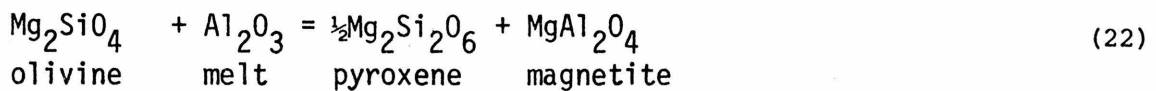
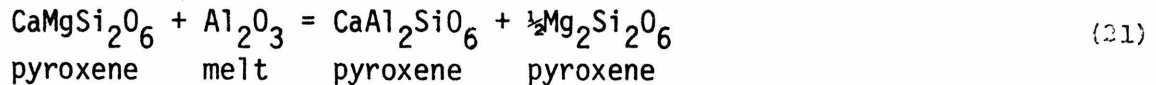
and allowing Fe, Mg, and Mn to fill M_1 and M_2 randomly. Hence $a_{\text{CaAl}_2\text{SiO}_6}^{\text{pyroxene}} = x_{\text{Ca}}^{M_2} \cdot x_{\text{Al}}^{M_1}$, $a_{\text{Mg}_2\text{Si}_2\text{O}_6}^{\text{pyroxene}} = x_{\text{Mg}}^{M_2} \cdot x_{\text{Mg}}^{M_1}$, etc.

These calculated values are all in good agreement with each other and with the silica buffer curves of Carmichael et al. (1970) and Nicholls et al. (1971), which were based on the compositions of pure phases, with the exception of reaction (3), reaction (5) for rock NMNH-99097, and reaction (10) for NMNH-99055. Values of $a_{\text{SiO}_2}^{\text{melt}}$ determined from reaction (3) are extremely low (approximately 10^{-3}) probably because the activity

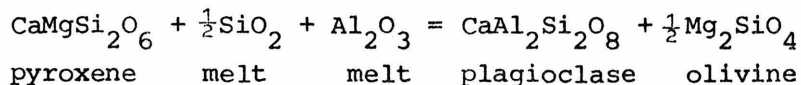
³More recent enthalpy and entropy data for leucite by Pankratz (1968) leads to values of $a_{\text{SiO}_2}^{\text{melt}}$ which are lower than is geologically reasonable, hence have not been used.

coefficient of enstatite in clinopyroxene differs significantly from unity. For NMNH-99097, the activity of Ca-Tschermak's molecule used in reaction (5) was based on only two groundmass pyroxene compositions. It is possible that these are not representative of the groundmass pyroxene in this rock in general. For reaction (10), the value of $a_{\text{SiO}_2}^{\text{melt}}$ determined for NMNH-99055 is much too high. This discrepancy could result from a value of G_f° , 1300°K for åkermanite that is approximately 4 kilocalories too large or from a significant non-ideality of åkermanite component in melilite, or both. The best value of $\log a_{\text{SiO}_2}^{\text{melt}}$ is estimated to be essentially -1 for each rock.

A similar set of buffer reactions can be written for alumina, several of which are listed below:



Following Nicholls and Carmichael (1972) a reaction may be written

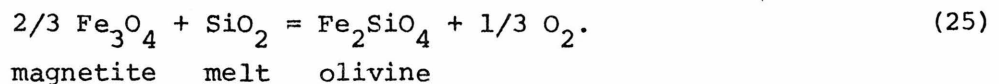


for which

$$\log a_{\text{Al}_2\text{O}_3}^{\text{melt}} = \frac{\Delta G_r^\circ}{2.303 RT} + \log a_{\text{CaAl}_2\text{Si}_2\text{O}_8}^{\text{plagioclase}} + 1/2 \log a_{\text{Mg}_2\text{SiO}_4}^{\text{olivine}} \\ - \log a_{\text{CaMgSi}_2\text{O}_6}^{\text{pyroxene}} - 1/2 \log a_{\text{SiO}_2}^{\text{melt}}$$

This reaction has been evaluated for NMNH-99097, using $\log a_{\text{SiO}_2}^{\text{melt}} = -0.95$ (table 7), G_f° , 1300°K for Al_2O_3 (liquid) = -282,459 cal. (Nicholls and Carmichael, 1972), and the activity models previously mentioned, with the result that $\log a_{\text{Al}_2\text{O}_3}^{\text{melt}} = -4.02$. This value is slightly higher (0.2 to 0.5 log units) than the alumina activity of kenyte and an alkali olivine basalt magma obtained by Nicholls and Carmichael (1972) and Bacon and Carmichael (1973) using the same reaction. The alumina activity may also be calculated from reactions (21) and (22). The resulting values however are significantly lower, probably, as previously mentioned, because of the non-ideality of enstatite component in clinopyroxene. In general it is more difficult to characterize quantitatively the alumina activity of igneous melts than it is the silica activity, primarily because of the uncertainty regarding the mixing properties of the appropriate components. However these alumina buffer reactions when taken in conjunction with reactions (1) through (20) do serve to illustrate the complexity of buffering relationships in a natural silicate melt.

Oxygen fugacities of the melts are buffered by the reaction



The activity of Fe_3O_4 in magnetite was specified as follows: After normalizing the sum of all cations to 3, the amount of Fe^{+3} was assumed equal to 2 minus all the Cr, Al, Ti, and the amount of Mg, Mn, and Zn (in the proportions occurring in the formula) which combine with Ti. The remaining Fe is Fe^{+2} . Thus $a_{\text{Fe}_3\text{O}_4}^{\text{magnetite}}$ is $x_{\text{Fe}^{+2}} \cdot (x_{\text{Fe}^{+3}})^2$. Then, using the free energy of reaction, the average groundmass phase compositions, and the activities of silica given in table 7, it is determined that for rocks NMNH-99055 and -097 (olivine of -071 was not analyzed) $\log f_{\text{O}_2} = -11.8$ and -12.5 , respectively. These values of the oxygen fugacity are unusually low, reflecting the low silica activity, and fall near the bottom of the field for the oxygen fugacity of mafic lavas (Carmichael et al., 1974, figures 6-13).

Many of the above equations involve the components of pyroxene and serve to place constraints on the "reasonableness" of certain choices of end members in these low silica, relatively high alumina melts. For example, reaction (5) was written by Carmichael et al. (1970) to express the increase of Al_2O_3 in calcium-rich pyroxenes with decreasing silica activity of the melt. Similarly reaction (20) expresses the increase of titanium in pyroxene in low- SiO_2 melts according to the suggestion of Verhoogen (1962). $\text{CaAl}_2\text{SiO}_6$ is also favored by high $a_{\text{Al}_2\text{O}_3}^{\text{melt}}$ (reaction (21)). Further, by combining reactions (14) and (23) the following can be written

$$a_{\text{MgCrAlSiO}_6}^{\text{pyroxene}} = K(T,P) \left(a_{\text{MgCr}_2\text{O}_4}^{\text{magnetite}} \right)^{\frac{1}{2}} \left(a_{\text{Mg}_2\text{Si}_2\text{O}_6}^{\text{pyroxene}} \right)^{\frac{1}{4}} \left(a_{\text{Al}_2\text{O}_3}^{\text{melt}} \right)^{\frac{1}{4}} \left(a_{\text{SiO}_2}^{\text{melt}} \right)^{\frac{1}{4}}$$

and, by combining (13) and (24)

$$a_{\text{pyroxene}}^{\text{Fe}^{+2}\text{Fe}^{+3}\text{AlSiO}_6} = K(T,P) (a_{\text{magnetite}}^{\text{Fe}^{+2}\text{Fe}^{+3}\text{O}_4})^{\frac{1}{2}} (a_{\text{pyroxene}}^{\text{Fe}_2\text{Si}_2\text{O}_6})^{\frac{1}{4}} (a_{\text{SiO}_2}^{\text{melt}})^{\frac{1}{2}} (a_{\text{Al}_2\text{O}_3}^{\text{melt}})^{\frac{1}{2}}.$$

These equations indicate that the amounts of Cr and Fe⁺³ in pyroxene are a function of the activities of both silica and alumina, and that the components MgCrAlSiO₆ and Fe⁺²Fe⁺³AlSiO₆ are most stable when both $a_{\text{SiO}_2}^{\text{melt}}$ and $a_{\text{Al}_2\text{O}_3}^{\text{melt}}$ are high.

An important use of these buffer reactions is to check the assumptions involved in constructing activity models, and to calculate pyroxene end members which correspond with thermodynamic components. For example, in recasting the pyroxene analyses of tables 3-6 into end members it was assumed that no Al^{VI} was present as MgAl₂SiO₆ or FeAl₂SiO₆. This assumption is not strictly valid because at least a small amount of these components will be produced by reactions such as (6), (7), and (25). It is possible to determine, say, $a_{\text{MgAl}_2\text{SiO}_6}^{\text{pyroxene}}$ from these reactions and to compare it to the activity based on the exchange-site model discussed previously. However, at present, the data are not good enough to allow inference of more realistic models for the activities (i.e., for the mixing properties) of the pyroxene components.

A goal of this section has been to evaluate the effects of the melt composition on the compositions of the solid phases, especially the abundant and compositionally complex pyroxenes. The above reactions indicate the complexities of buffering relationships in a natural silicate melt and provide some guidance for the choice of components. Further precise characterization of the melts and the components of the solid phases must await more and better thermodynamic data.

PETROGENESIS

No completely satisfactory explanation for the origin of potassic mafic lavas exists. Some experimental data are available on these rocks from other areas. For example, Edgar et al. (1976) studied experimentally the melting behavior of a highly potassic mafurite (modal olivine + clinopyroxene + kalsilite + perovskite + biotite) from Uganda, and determined that it could not be derived from partial melting of pyrolite. In particular, the melt is not saturated with orthopyroxene at any P, T, or H₂O content. Instead they suggest that the mafurite could be derived from an olivine + clinopyroxene + phlogopite + ilmenite assemblage occurring as enriched patches in the upper mantle. Their results may not be generally applicable to K-rich mafic rocks since the mafurite they examined is unusually mafic. Also they did not examine the effect of CO₂ on the near-liquidus phases. For an olivine melilitite Brey and Green (1975) found for example that under dry conditions or with various water contents the melt coexists with olivine and clinopyroxene but not with orthopyroxene. However the effect of increased CO₂ is to cause orthopyroxene and garnet to appear on or near the liquidus. To explain the extreme light REE enrichment and the high concentration of incompatible elements of a variety of potassic basalts, Kay and Gast (1973) proposed that these basalts formed by approximately 0.5 percent partial melting of alkali feldspar-bearing garnet peridotite. For Colorado Plateau minette this model is supported by the presence of garnet lherzolite xenoliths in these potassium-rich basalts (Baldrige et al., 1975; Ehrenberg, 1978).

The applicability of these results to the Italian potassic rocks is at best uncertain. As Thompson (1977) has pointed out, although potassic mafic lavas are commonly treated together in discussions of their origin, very significant chemical differences exist among potassic rocks from various regions. Turi and Taylor (1976) measured $^{18}\text{O}/^{16}\text{O}$ on potassium-rich volcanic rocks from the Roman Province of Italy and found that many of these lavas were very enriched in ^{18}O (up to approximately 12 per mil). From these data and from strontium isotope data they concluded that these magmas have interacted strongly with high- ^{18}O continental crust. Thompson (1977) conducted anhydrous melting experiments on a leucitite from the Alban Hills. He found that this magma was in equilibrium with clinopyroxene and leucite, both of which occur as phenocrysts, at about 14 kb and 1260°C. He therefore concluded that this magma was erupted directly from a depth of 50 km. Under anhydrous conditions this leucitite could not be in equilibrium with an olivine-bearing peridotite at any depth. Thompson's (1977) data constrain the depth at which these magmas interacted with crustal material to greater than 50 km. He suggests that these magmas derived their crustal component, including their high Sr, Rb, $^{18}\text{O}/^{16}\text{O}$, and $^{87}\text{Sr}/^{86}\text{Sr}$, from partial fusion of ocean floor sediments subducted beneath Italy. Additional experiments on compositions corresponding to various potassic lava types, along with more complete trace element and REE data on carefully chosen samples, are required to elucidate further the origin of these lavas.

REFERENCES

- Appleton, J. D., 1972. Petrogenesis of potassium-rich lavas from the Roccomonfina volcano, Roman Region, Italy. *J. Petrol.*, 13: 425-456.
- Bacon, C. R., and Carmichael, I. S. E., 1973. Stages in the P-T path of ascending magma: An example from San Quintin, Baja California. *Contr. Mineral. Petrol.*, 41: 1-22.
- Baldrige, W. S., Ehrenberg, S. N., and McGetchin, T. R., 1975. Ultramafic xenolith suite from Shiprock, N. Mex. (abstr.). *EOS Trans. Am. Geophys. Union*, 56: 464-465.
- Barth, T. F., 1961. The feldspar lattices as solvents of foreign ions. *Inst. Lucas Mallada Cursillos y Conferencias, Fasc. 8, Madrid*, p. 3-8.
- Berlin, R., and Henderson, C. M. B., 1968. A reinterpretation of Sr and Ca fractionation trends in plagioclases from basic rocks. *Earth Planet. Sci. Lett.*, 4: 79-83.
- Brey, G., and Green, D. H., 1975. The role of CO₂ in the genesis of olivine melilitite. *Contr. Mineral. Petrol.*, 49: 93-103.
- Brooks, C. K., 1968. On the interpretation of trends in element ratios in differentiated igneous rocks, with particular reference to strontium and calcium. *Chem. Geol.*, 3: 15-20.
- Carmichael, I. S. E., 1963. The crystallization of feldspar in volcanic acid liquids. *Quart. J. Geol. Soc. London*, 119: 95-131.
- Carmichael, I. S. E., 1965. Trachytes and their feldspar phenocrysts. *Min. Mag.* 34: 107-125.
- Carmichael, I. S. E., Nicholls, J., and Smith, A. L., 1970. Silica activity in igneous rocks. *Amer. Mineralogist*, 55: 246-263.
- Carmichael, I. S. E., Turner, F. J., and Verhoogen, J., 1974. *Igneous Petrology*. McGraw-Hill, New York, 739 pp.
- Champion, D. E., Albee, A. L., and Chodos, A. A., 1975. Reproducibility and operator bias in a computer-controlled system for quantitative electron microprobe analysis. *Proc. 10th Ann. Microbeam Anal. Soc. Conf.*, pp. 55A-55F.

- Chodos, A. A. and Albee, A. L., 1972. Automated microprobe analysis and applications to analysis of exotic lunar phases. Proc. 6th Internat. Conf. X-ray Optics and Microanalysis, pp. 779-784.
- Chodos, A. A., Albee, A. L., Gancarz, A. J., and Laird, J., 1973. Optimization of computer-controlled quantitative analysis of minerals. Proc. 8th Nat. Conf. Electron Probe Anal., pp. 45A-45C.
- Edgar, A. D., Green, D. H., and Hibberson, W. O., 1976. Experimental petrology of a highly potassic magma. J. Petrol., 17: 339-356.
- Ehrenberg, S. N., 1978. Petrology of potassic volcanic rocks and ultramafic xenoliths from the Navajo volcanic field, New Mexico and Arizona. Ph.D. Thesis, Univ. Calif., Los Angeles.
- El Goresy, A., and Yoder, H. S., Jr., 1974. Natural and synthetic melilite compositions. Carnegie Inst. Washington Year Book 1973-1974, 73: 359-371.
- Eskola, P., 1922. The silicates of strontium and barium. Am. J. Sci. (Fifth Series), 4: 331-375.
- Fudali, R. F., 1963. Experimental studies bearing on the origin of pseudoleucite and associated problems of alkalic rock systems. Geol. Soc. Amer. Bull., 74: 1101-1126.
- Goldsmith, J. R., 1950. Gallium and germanium substitutions in synthetic feldspars. J. Geol., 58: 518-536.
- Hamilton, D. L., and MacKenzie, W. S., 1965. Phase-equilibrium studies in the system $\text{NaAlSi}_3\text{O}_8$ (nepheline) - KAlSi_3O_8 (kalsilite) - SiO_2 - H_2O . Mineral. Mag., 34: 214-231.
- Higazy, R. A., 1954. Trace elements of volcanic ultrabasic potassic rocks of Southwestern Uganda and adjoining parts of the Belgian Congo. Geol. Soc. Amer. Bull., 65: 39-70.
- Hurley, P. M., Fairbairn, H. W., and Pinson, W. H., 1966. Rb-Sr isotopic evidence in the origin of potash-rich lavas of western Italy. Earth Planet. Sci. Lett., 5: 301-306.
- Iiyama, J. T., 1966. Contribution à l'étude des équilibres sub-solidus du système ternaire orthose-albite-anorthite à l'aide des réactions d'échange d'ions. Na-K au contact d'une solution hydrothermale. Bull. Soc. Franc. Miner. Crist., 89: 442-454.
- Iiyama J. T., 1968. Étude expérimentale de la distribution d'éléments en traces entre deux feldspaths. Feldspath potassique et plagioclase coexistants. I. Distribution de Rb, Cs., Sr, et Ba à 600°C. Bull. Soc. Franc. Miner. Crist., 91: 130-140.

- Kay, R. W., and Gast, P. W., 1973. The rare earth content and origin of alkali-rich basalts. *J. Geol.*, 81: 653-682.
- Kelley, K. K., 1962. Heats and free energies of formation of anhydrous silicates. U. S. Bur. Mines, Rept. Invest. 5901.
- Lin, H. C., and Foster, W. R., 1968. Studies in the system $\text{BaO-Al}_2\text{O}_3\text{-SiO}_2$. I. The polymorphism of celsian. *Amer. Mineralogist*, 53: 134-144.
- Locardi, E., and Mitterpergher, M., 1967. Relationship between some trace elements and magmatic processes. *Geol. Rundschau*, 57: 313-334.
- Mall, A. P., and Rudert, V., 1974. Studies in the system $\text{KAlSiO}_4\text{-BaAl}_2\text{Si}_2\text{O}_8\text{-SiO}_2\text{-H}_2\text{O}$. *Contr. Mineral. Petrol.*, 48: 81-88.
- Morse, S. A., 1970. Alkali feldspars with water at 5 kb pressure. *J. Petrol.*, 11: 221-251.
- Nakamura, Y., and Yoder, H. S., Jr., 1974. Analcite, hyalophane, and phillipsite from the Highwood Mountains, Montana. *Carnegie Inst. Washington Year Book 1973-1974*, 73: 354-358.
- Nicholls, J., 1969. Studies of the volcanic petrology of the Navajo-Hopi area, Arizona. Ph.D. Thesis, Univ. Calif., Berkeley, 107 p.
- Nicholls, J., and Carmichael, I. S. E., 1969. A commentary on the absarokite-shoshonite-banakite series of Wyoming, U. S. A. *Schweiz. Min. Petrol. Mitt.*, 49: 47-64.
- Nicholls, J., Carmichael, I. S. E., and Stormer, J. C., 1971. Silica activity and P total in igneous rocks. *Contr. Mineral. Petrol.*, 33: 1-20.
- Nicholls, J., and Carmichael, I. S. E., 1972. The equilibration temperature and pressure of various lava types with spinel- and garnet-peridotite. *Amer. Mineralogist*, 57: 941-959.
- Pankratz, L. B., 1968. High-temperature heat contents and entropies of dehydrated analcite, kaliophilite, and leucite. U. S. Bur. Mines, Rept. Invest. 7073.
- Rahman, S., and MacKenzie, W. S., 1969. The crystallization of ternary feldspars: A study from natural rocks. *Amer. J. Sci.*, 267A: 391-406.
- Reid, M. J., Gancarz, A. J., and Albee, A. L., 1973. Constrained least-squares analysis of petrologic problems with an application to lunar sample 12040. *Earth Planet. Sci. Lett.*, 17: 433-445.

- Robie, R. A., and Waldbaum, D. R., 1968. Thermodynamic properties of minerals and related substances at 298.15°K (25.0°C) and one atmosphere (1.013 bars) pressure and at higher temperatures. U. S. Geol Surv. Bull. 1259.
- Rudert, V., 1972. Das system $\text{NaAlSi}_3\text{O}_8\text{-H}_2\text{O}$ bei 1 Kbar. Contr. Mineral. Petrol., 35: 313-329.
- Savelli, C., 1967. The problem of rock assimilation by Somma-Vesuvius magma. I. Composition of Soma and Vesuvius lavas. Contr. Mineral. Petrol., 16: 328-353.
- Schairer, J. F., 1950. The alkali-feldspar join in the system $\text{NaAlSiO}_4\text{-KAlSiO}_4\text{-SiO}_2$. J. Geol., 58: 512-517.
- Schairer, J. F., 1957. Melting relations of the common rock-forming oxides. J. Amer. Ceram. Soc., 40: 215-235.
- Schairer, J. F., and Bowen, N. L., 1947. The system anorthite-leucite-silica. Bull. Comm. Geol. Finlande, 24: 67-87.
- Scotford, D. M., 1973. Strontium partitioning between coexisting K-feldspar and plagioclase as an indicator of metamorphic grade in southwestern New Hampshire. Geol. Soc. Amer. Bull., 84: 3985-3994.
- Seck, H. A., 1971a. Koexistierende alkalifeldspäte und plagioklase im system $\text{NaAlSi}_3\text{O}_8\text{-KAlSi}_3\text{O}_8\text{-CaAl}_2\text{Si}_2\text{O}_8\text{-H}_2\text{O}$ bei temperaturen von 650°C bis 900°C. N. Jb. Miner. Abh., 115: 315-345.
- Seck, H. A., 1971b. Der einfluss des drucks auf die zusammensetzung koexistierender alkalifeldspäte und plagioklase im system $\text{NaAlSi}_3\text{O}_8\text{-KAlSi}_3\text{O}_8\text{-CaAl}_2\text{Si}_2\text{O}_8\text{-H}_2\text{O}$. Contr. Mineral. Petrol. 31: 67-86.
- Smith, J. V., 1974. Feldspar Minerals. 2. Chemical and Textural Properties. Springer-Verlag, 690 p.
- Stormer, J. C., and Carmichael, I. S. E., 1971. The free energy of sodalite and the behavior of chloride, fluoride, and sulfate in silicate magmas. Amer. Mineralogist, 56: 292-306.
- Taylor, D., and MacKenzie, W. S., 1975. A contribution to the pseudo-leucite problem. Contr. Mineral. Petrol., 49: 321-333.
- Thompson, R. N., 1977. Primary basalts and magma genesis. IV. Alban Hills, Roman comagmatic province, central Italy. Contr. Mineral. Petrol., 60: 91-108.
- Tilley, C. E., 1954. Nepheline-alkali feldspar paragenesis. Amer. J. Sci., 252: 65-75.

- Tilley, C. E., 1958. The leucite nepheline dolerite of Meiches, Vogelsberg, Hessen. *Amer. Mineralogist*, 43: 758-761.
- Turi, B., and Taylor, H. P., Jr., 1976. Oxygen isotope studies of potassic volcanic rocks of the Roman Province, central Italy. *Contr. Mineral. Petrol.*, 55: 1-31.
- Tuttle, O. F., and Bowen, N. L., 1958. Origin of granite in the light of experimental studies in the system $\text{NaAlSi}_3\text{O}_8$ - KAlSi_3O_8 - SiO_2 - H_2O . *Geol. Soc. Amer. Mem.*, 74: 153p.
- Tuttle, O. F., and Smith, J. V., 1958. The nepheline-kalsilite system. II. Phase relations. *Amer. J. Sci.*, 256: 571-589.
- Verhoogen, J., 1962. Distribution of titanium between silicates and oxides in igneous rocks. *Amer. J. Sci.*, 260: 211-220.
- Virgo, D., 1968. Partition of strontium between coexisting K-feldspar and plagioclase in some metamorphic rocks. *J. Geol.*, 76: 331-346.
- Washington, H. S., 1906. The Roman Comagmatic Region. *Carnegie Inst. Washington Publ. No. 57*, 199 p.
- Washington, H. S., 1920. The chemistry of the earth's crust. *J. Franklin Inst.*, 190: 757-815.
- Wood, B. J., and Banno, S., 1973. Garnet-orthopyroxene and orthopyroxene-clinopyroxene relationships in simple and complex systems. *Contr. Mineral. Petrol.*, 42: 109-124.
- Yoder, H. S., Jr., Stewart, D. B., and Smith, J. R., 1957. Ternary feldspars. *Carnegie Inst. Washington Year Book*, 1956-1957, 56: 206-214.
- Yoder, H. S., Jr., 1973. Melilite stability and paragenesis. *Fortschr. Miner.*, 50: 140-173.

TABLE 1. Chemical analyses from Washington (1906) and CIPW norms.
 -- indicates oxide or element not analyzed for.

	<u>NMNH-99024</u>	<u>NMNH-99055</u>	<u>NMNH-99-071</u>	<u>NMNH-99097</u>
SiO ₂	47.89	45.99	47.20	47.71
Al ₂ O ₃	17.87	16.56	17.66	17.61
Fe ₂ O ₃	4.93	4.17	3.51	2.46
FeO	3.64	5.38	4.50	5.68
MgO	3.68	5.30	4.20	4.80
CaO	8.70	10.47	9.52	9.42
Na ₂ O	2.60	2.18	2.25	2.75
K ₂ O	8.23	8.97	7.63	7.64
H ₂ O ⁺	0.65	0.45	0.72	tr.
H ₂ O ⁻	-	-	0.57	n.d.
CO ₂	none	none	none	none
TiO ₂	0.77	0.37	1.19	0.37
ZrO ₂	0.02	-	0.04	0.06
P ₂ O ₅	0.36	0.56	0.58	0.77
SO ₃	0.06	-	none	none
S	-	-	none	none
BaO	0.28	0.25	0.19	0.26
SrO	-	none	-	-
TOTAL	99.68	100.65	99.76	99.53
or	19.02	0.00	16.85	11.27
an	12.94	8.91	15.81	13.23
ne	12.06	9.99	10.48	12.68
lc	23.68	41.53	22.72	26.77
wo	0.13	0.00	0.00	0.00
di	22.55	20.33	22.97	23.82
ol	0.00	6.64	2.22	5.99
cs	0.00	4.52	0.00	0.00
mt	7.23	6.04	5.17	3.59
il	1.48	0.70	2.30	0.71
ap	0.88	1.35	1.42	1.86
z	0.03	0.00	0.06	0.09

TABLE 2. Comparison of "calculated modes" given by Washington (1906) with those determined in this work. Numbers are in weight percent. Error is 1 σ formal error of curve fitting.

	NMNH-99024 <u>Leucitite</u>		NMNH-99055 <u>Melilite leucitite</u>		NMNH-99071 <u>Leucitite</u>		NMNH-99097 <u>Leucitite</u>	
	WASHINGTON		WASHINGTON		WASHINGTON		WASHINGTON	
Orthoclase	5.5 Or ₁ Ab ₁		--		6.5 Or ₃ Ab ₂		--	
Plagioclase	13.9 Ab ₂ An ₃		3.6 anorthite		15.0 Ab ₁ An ₃		13.8 Ab ₂ An ₃	
Leucite	36.2		41.9		32.5		35.6	
Nepheline	8.3		7.3		6.8		9.9	
Augite	30.4		22.6		32.0		31.8	
Olivine	--		6.8		2.3		6.1	
Melilite	--		12.6		--		--	
Ores	4.7		4.0 magnetite		2.6 magnetite		1.0	
Apatite	1.0		1.2		1.3		1.8	
TOTAL	100.0		100.0		100.0		100.0	
	THIS WORK		THIS WORK		THIS WORK		THIS WORK	
Sanidine	8.4 \pm 8.6		--		9.6 \pm 4.8		4.2 \pm 15.7	
Plagioclase	13.2 10.8		--		25.8 5.6		18.3 10.3	
Leucite	32.8 8.7		44.4 \pm 5.2		27.6 4.1		35.1 13.6	
Nepheline	12.4 5.8		12.5 2.7		--		--	
Pyroxene	24.7 5.4		14.6 9.1		28.0 4.7		23.6 7.3	
Olivine	--		5.5 2.7		-2.0 2.5		4.9 2.7	
Melilite	--		18.8 7.1		--		--	
Magnetite	7.7 1.6		2.8 1.0		9.5 1.4		2.2 1.0	
Sodalite	--		--		--		9.8 3.0	
Glass	-0.1 0.9		--		--		--	
Apatite	0.9 0.5		1.4 0.4		1.4 0.3		1.9 0.4	

TABLE 3. Microprobe analyses of NMNH-99024 (weight percent). 0.00 indicates element not present at level of detectability. - indicates element not analyzed for. Textural notation: P indicates phenocryst, Mp microphenocryst, G groundmass grain (subhedral or equant), I interstitial grain (anhedral), R rim, Im intermediate, C core.

	PLAGIOCLASE								
	3-6/7	3R	40	2-3/7	2-6	53	52P	55-6	48-3
SiO ₂	50.87	51.98	52.38	51.22	51.77	50.60	50.70	53.00	51.93
Al ₂ O ₃	29.06	27.58	26.05	28.18	26.81	28.92	29.18	24.41	27.03
TiO ₂	0.00 [†]	-	0.00 [†]	-	-	0.00 [†]	-	-	0.00 [†]
FeO*	0.66	0.59	0.56	0.67	0.55	0.91	0.87	0.62	0.68
MgO	0.15	0.15	0.14	0.15	0.15	0.20	0.16	0.16	0.17
CaO	9.18	7.17	5.50	8.72	5.97	10.82	10.83	4.00	6.41
BaO	1.00	1.82	3.03	1.00	3.01	0.52	0.49	3.97	2.63
SrO	4.50	5.30	5.35	4.70	5.72	3.99	3.95	6.17	6.03
Na ₂ O	3.98	4.44	4.39	4.26	4.55	3.77	3.83	4.16	4.14
K ₂ O	0.71	1.16	2.53	0.99	1.55	0.44	0.44	3.33	1.51
Rb ₂ O	0.00	0.00	0.00	0.00	0.00	0.00	0.00	0.00	0.00
TOTAL	100.11	100.19	99.93	99.89	100.08	100.17	100.45	99.82	100.53

Formula Proportions

Si	2.369	2.434	2.478	2.389	2.448	2.349	2.344	2.542	2.451
Al	1.595	1.522	1.453	1.549	1.494	1.582	1.590	1.380	1.503
Ti	0.000	0.000	0.000	0.000	0.000	0.000	0.000	0.000	0.000
Fe*	0.026	0.023	0.022	0.026	0.022	0.035	0.034	0.025	0.027
Mg	0.010	0.010	0.010	0.010	0.011	0.014	0.011	0.011	0.012
Ca	0.458	0.360	0.279	0.436	0.302	0.538	0.537	0.206	0.324
Ba	0.018	0.033	0.056	0.018	0.056	0.009	0.009	0.075	0.049
Sr	0.122	0.144	0.147	0.127	0.157	0.107	0.106	0.172	0.165
Na	0.359	0.403	0.403	0.386	0.417	0.339	0.343	0.387	0.379
K	0.042	0.069	0.153	0.059	0.093	0.026	0.026	0.204	0.091
Rb	0.000	0.000	0.000	0.000	0.000	0.000	0.000	0.000	0.000
Or**	4.1	6.6	14.3	5.5	8.8	2.4	2.4	18.9	8.7
Ab	34.7	38.7	37.7	36.3	39.5	31.8	32.2	35.8	36.2
An	44.2	34.5	26.1	41.0	28.6	50.2	50.5	19.1	31.0
Ce	1.8	3.2	5.2	1.7	5.3	0.9	0.8	6.9	4.6
Sr-F	11.7	13.8	13.7	12.0	14.8	10.1	9.9	15.9	15.8
Mg-F	1.0	1.0	0.9	1.0	1.0	1.3	1.0	1.1	1.1
Fe-F	2.5	2.2	2.1	2.5	2.0	3.3	3.2	2.3	2.6
No. Analyses	2	4	3	2	1	4	2	1	1
Texture	G,C	G,R	G	G	G	I	I	I	G
Size (mm)	0.30		0.10	0.20		0.05	0.05	0.05	0.08

*Total iron as FeO; **end members in mole percent; †separate determinations; ††includes Sr with Ca.

TABLE 3 (continued)

	SANIDINE						
	57	52-3/5	54	56-2	49-1	43	33-2
SiO ₂	59.03	64.78	63.13	63.91	56.65	62.93	63.81
Al ₂ O ₃	21.24 [†]	18.64 [†]	19.83	19.18	21.96	19.75	19.01
TiO ₂	0.00 [†]	0.00 [†]	0.00 [†]	0.00 [†]	0.00 [†]	0.00 [†]	-
FeO*	0.45	0.40	0.47	0.42	0.55	0.46	0.59
MgO	0.14	0.12	0.21	0.16	0.17	0.14	0.24
CaO	1.12	0.50	0.67	0.87	1.11	0.97	0.24
BaO	3.88	0.06	0.87	0.14	5.95	0.75	0.09
SrO	2.18	0.11	0.58	0.29	3.42	0.47	0.10
Na ₂ O	4.12	2.64	2.33	3.07	3.77	2.93	1.92
K ₂ O	8.33	12.35	11.74	11.32	6.60	10.97	14.55
Rb ₂ O	0.00	0.00	0.00	0.00	0.00	0.00	0.00
TOTAL	100.49	99.60	99.83	99.36	100.18	99.37	100.55

Formula Proportions

Si	2.752	2.978	2.920	2.941	2.711	2.911	2.908
Al	1.167	1.010	1.081	1.040	1.239	1.077	1.021
Ti	0.000	0.000	0.000	0.000	0.000	0.000	0.000
Fe*	0.018	0.015	0.018	0.016	0.022	0.018	0.022
Mg	0.010	0.008	0.014	0.011	0.012	0.010	0.016
Ca	0.056	0.025	0.033	0.043	0.057	0.048	0.012
Ba	0.071	0.001	0.016	0.003	0.112	0.014	0.002
Sr	0.059	0.003	0.016	0.008	0.095	0.013	0.003
Na	0.372	0.235	0.209	0.274	0.350	0.263	0.170
K	0.495	0.724	0.693	0.665	0.403	0.647	0.846
Rb	0.000	0.000	0.000	0.000	0.000	0.000	0.000

Or**	45.7	71.6	69.3	65.2	38.5	64.3	79.1
Ab	34.5	23.3	21.0	26.9	33.3	25.9	15.9
An	5.2	2.4	3.3	4.2	5.4	4.7	1.1
Ce	6.6	0.1	1.6	0.2	10.6	1.3	0.2
Sr-F	5.5	0.3	1.6	0.8	9.0	1.2	0.2
Mg-F	0.9	0.8	1.4	1.1	1.1	0.9	1.4
Fe-F	1.6	1.5	1.8	1.6	2.1	1.7	2.1

No. Analyses	6	2	3	1	1	2	1
Texture	Mp	I	I	I	G	G	G
Size (mm)	0.15	0.05	0.10	0.06	0.06	0.10	0.07

*Total iron as FeO; **end members in mole percent; †separate determinations; ††includes Sr with Ca.

TABLE 3 (continued)

	LEUCITE							
	1	59-1/2	60-1	50	55-3/4	56-4	46-3	42-2
SiO ₂	55.02	54.21	53.67	54.70	55.11	54.90	55.31	54.69
Al ₂ O ₃	22.69	22.68	22.20	22.53	22.46	22.70	22.81	22.40
TiO ₂	0.00 [†]	-	-	0.00 [†]	0.00 [†]	-	0.00 [†]	0.00 [†]
FeO*	0.62	0.80	0.75	0.79	0.84	0.69	0.79	0.77
MgO	0.14	0.11	0.12	0.14	0.13	0.14	0.14	0.12
CaO	0.00	0.00	0.03	0.01	0.02	0.01	0.00	0.00
BaO	0.05	0.05	0.00	0.00	0.05	0.05	0.00	0.00
SrO	0.09	0.08	0.09	0.09	0.10	0.10	0.10	0.10
Na ₂ O	0.22	0.19	0.19	0.22	0.19	0.16	0.21	0.22
K ₂ O	21.26	22.84	22.12	21.45	20.56	20.56	21.05	21.05
Rb ₂ O	0.07	0.08	0.13	0.08	0.02	0.12	0.06	0.25
TOTAL	100.16	101.04	99.30	100.01	99.48	99.43	100.47	99.60

Formula Proportions

Si	2.000	1.947	1.962	1.989	2.019	2.012	2.004	1.999
Al	0.971	0.960	0.957	0.965	0.970	0.981	0.974	0.965
Ti	0.000	0.000	0.000	0.000	0.000	0.000	0.000	0.000
Fe*	0.019	0.024	0.023	0.024	0.026	0.021	0.024	0.024
Mg	0.008	0.006	0.007	0.008	0.007	0.008	0.008	0.007
Ca	0.000	0.000	0.001	0.000	0.001	0.000	0.000	0.000
Ba	0.001	0.001	0.000	0.000	0.001	0.001	0.000	0.000
Sr	0.002	0.002	0.002	0.002	0.002	0.002	0.002	0.002
Na	0.015	0.013	0.013	0.016	0.014	0.011	0.015	0.016
K	0.985	1.046	1.032	0.995	0.961	0.961	0.973	0.982
Rb	0.002	0.002	0.003	0.002	0.000	0.003	0.001	0.006

No. Anal.	7	2	1	3	2	1	1	1
Texture	P	Mp	G	G	G	G	G	Mp
Size (mm)	0.80	0.20	0.06	0.18	0.18	0.10	0.15	0.35

*Total iron as FeO; **end members in mole percent; †separate determinations; ††includes Sr with Ca.

TABLE 3 (continued)

	NEPHELINE			GLASS
	29-3	33-1	43	45
SiO ₂	46.63	47.84	46.26	26.66
Al ₂ O ₃	31.65	31.37	32.02	8.85
TiO ₂	0.01	0.18	0.00	0.35
FeO*	0.58	0.39	0.57	4.45
MgO	0.00	0.01	0.03	2.68
CaO	1.06	0.68	1.21	4.70
BaO	0.00	0.00	0.05	0.15
SrO	0.11 [†]	-	0.11 [†]	-
Na ₂ O	14.80	12.81	12.51	1.02
K ₂ O	3.70	3.63	3.95	3.89
Rb ₂ O	0.00 [†]	-	0.00 [†]	-
TOTAL	98.54	96.91	96.71	52.75

Formula Proportions

Si	1.175	1.243	1.205
Al	0.940	0.960	0.983
Ti	0.000	0.004	0.000
Fe*	0.012	0.008	0.012
Mg	0.000	0.000	0.001
Ca	0.029	0.019	0.034
Ba	0.000	0.000	0.001
Sr	0.002	0.000	0.002
Na	0.723	0.645	0.632
K	0.119	0.120	0.131
Rb	0.000	0.000	0.000

Or**
Ab
An
Ce
Sr-F
Mg-F
Fe-F

No. Analyses	1	1	3	1
Texture	I	I	I	I
Size (mm)	0.16	0.05	0.09	0.18

*Total iron as FeO; **end members in mole percent; †separate determinations; ††includes Sr with Ca.

TABLE 3 (continued)

	PYROXENE				
	58-5	47-1	34-3	34-11	34-12
SiO ₂	50.47	43.53	47.32	46.85	48.96
Al ₂ O ₃	3.02	8.71	5.90	6.19	3.94
TiO ₂	0.52	1.71	0.90	0.91	0.62
FeO*	4.69	10.32	8.06	8.13	6.97
MgO	15.53	10.91	12.79	12.74	14.10
CaO	24.39	23.11	24.08	24.03	23.96
MnO	0.06	0.13	0.17	0.20	0.15
SrO	0.15	0.18	0.16	0.26	0.14
Na ₂ O	0.12	0.28	0.19	0.18	0.17
Cr ₂ O ₃	0.09	0.00	0.00	0.00	0.00
TOTAL	99.04	98.88	99.57	99.49	99.01

Formula Proportions

Si	1.868	1.651	1.766	1.751	1.828
Al	0.132	0.389	0.260	0.273	0.173
Ti	0.014	0.049	0.025	0.026	0.017
Fe*	0.145	0.327	0.252	0.254	0.218
Mg	0.857	0.617	0.712	0.710	0.785
Ca	0.967	0.939	0.963	0.962	0.959
Mn	0.002	0.004	0.005	0.006	0.005
Sr	0.003	0.004	0.003	0.006	0.003
Na	0.009	0.021	0.014	0.013	0.012
Cr	0.003	0.000	0.000	0.000	0.000

(Fe,Mn) ₂ Si ₂ O ₆ **	7.2	15.7	12.3	12.4	10.7
Mg ₂ Si ₂ O ₆	41.7	29.1	34.1	33.9	37.8
NaCrAlSiO ₆	0.2	0.0	0.0	0.0	0.0
CaTiAl ₂ O ₆	1.4	4.6	2.4	2.4	1.7
NaAlSi ₂ O ₆	0.6	1.9	1.3	1.3	1.2
CaAl ₂ SiO ₆	4.6	12.8	9.4	10.0	6.1
Ca ₂ Si ₂ O ₆ ††	44.3	35.9	40.5	40.0	42.5

No. Analyses	1	1	1	1	1
Texture	P,C	G	P,R	P,Im	P,C
Size (mm)	0.9	0.09	1.10		

*Total iron as FeO; **end members in mole percent; †separate determinations; ††includes Sr with Ca.

TABLE 3 (continued)

	MAGNETITE		
	70-11	70-13	70-14
SiO ₂	1.00	0.95	0.86
Al ₂ O ₃	4.83	4.87	3.19
TiO ₂	7.54	8.10	9.52
FeO*	76.71	75.09	75.41
MgO	1.08	0.45	0.35
MnO	1.02	1.11	1.01
ZnO	0.36	0.18	0.20
ZrO ₂	0.02	0.04	0.11
Cr ₂ O ₃	0.00	0.00	0.01
Nb ₂ O ₅	0.00	0.00	0.00
TOTAL	92.56	90.79	90.66

Formula Proportions

Si	0.038	0.037	0.034
Al	0.215	0.223	0.148
Ti	0.215	0.236	0.281
Fe*	2.428	2.436	2.475
Mg	0.061	0.026	0.021
Mn	0.033	0.036	0.034
Zn	0.010	0.005	0.006
Zr	0.000	0.001	0.002
Cr	0.000	0.000	0.000
Nb	0.000	0.000	0.000

FMCr ₂ O ₄ **	0.0	0.0	0.0
FM ₂ TiO ₄	21.8	23.9	28.4
FMA ₂ O ₄	10.9	11.3	7.5
FMO·Fe ₂ O ₃	67.3	64.8	64.1

FM = Fe + Mg + Mn + Zn

No. Analyses	1	1	1
Texture	G	G	G
Size (mm)	0.05	0.05	0.05

*Total iron as FeO; **end members in mole percent; †separate determinations; ††includes Sr with Ca.

TABLE 4. Microprobe analyses of NMNH-99055 (weight percent). 0.00 indicates element not present at level of detectability. Textural notation: P indicates phenocryst, G groundmass grain (subhedral or equant), I interstitial grain (anhedral), Pk poikilitic, R rim, C core.

	LEUCITE						
	1	10-1	11-1	6-5	21-1	27-1	29-2
SiO ₂	55.38	55.24	56.92	54.50	55.02	53.97	54.77
Al ₂ O ₃	22.72	23.37	23.36	23.10	22.92	22.47	22.71
FeO*	0.59	1.07	0.93	0.48	0.88	1.34	0.95
MgO	0.15	0.21	0.14	0.12	0.17	0.23	0.14
CaO	0.01	0.00	0.03	0.00	0.00	0.18	0.00
BaO	0.04	0.37	0.37	0.67	0.07	0.22	0.27
SrO	0.10	0.11	0.11	0.07	0.12	0.19	0.10
Na ₂ O	0.08	0.02	0.00	0.00	0.03	0.07	0.05
K ₂ O	21.35	20.64	18.63	21.88	22.04	20.62	22.05
Rb ₂ O	0.18	0.14	0.19	0.30	0.12	0.16	0.23
TOTAL	100.60	101.17	100.68	101.12	101.37	99.45	101.27

Formula Proportions

Si	2.005	1.997	2.078	1.969	1.976	1.983	1.972
Al	0.970	0.996	1.005	0.984	0.971	0.973	0.964
Fe*	0.018	0.032	0.028	0.015	0.026	0.041	0.029
Mg	0.008	0.011	0.007	0.006	0.009	0.013	0.008
Ca	0.000	0.000	0.001	0.000	0.000	0.007	0.000
Ba	0.001	0.005	0.005	0.009	0.001	0.003	0.004
Sr	0.002	0.002	0.002	0.002	0.003	0.004	0.002
Na	0.006	0.001	0.000	0.000	0.002	0.005	0.004
K	0.986	0.952	0.868	1.008	1.010	0.967	1.013
Rb	0.004	0.003	0.004	0.011	0.003	0.004	0.005

No. Analyses	5	1	1	1	1	1	1
Texture	P	G	G	G	G	G	G
Size (mm)	4.3	0.08	0.08	0.08	0.10	0.06	0.02

*Total iron as FeO; **end members in mole percent; †includes (Sr,Ba) with Ca; ††includes Sr with Ca.

TABLE 4. (continued)

	NEPHELINE						MELILITE	
	18-1/2	6-2/4	22	23-1/2	4-3/4	29-3	7	16-1
SiO ₂	41.80	41.25	41.50	41.67	41.77	41.91	42.43	42.09
Al ₂ O ₃	33.85	33.80	34.13	33.62	34.31	33.47	6.22	7.38
FeO*	0.73	0.74	0.75	0.79	0.78	0.97	4.72	5.63
MgO	0.20	0.19	0.19	0.21	0.19	0.25	7.70	6.55
CaO	1.06	1.03	1.05	1.11	1.09	1.12	36.16	33.48
BaO	0.00	0.08	0.01	0.03	0.05	0.04	0.02	0.03
SrO	0.83	0.83	0.82	0.80	0.80	0.74	1.44	1.81
Na ₂ O	13.86	13.67	13.57	13.73	13.34	13.25	2.58	3.11
K ₂ O	7.30	7.62	7.61	7.35	7.67	7.43	0.21	0.26
Rb ₂ O	0.00	0.00	0.00	0.00	0.00	0.00	0.00	0.00
TOTAL	99.63	99.21	99.63	99.31	100.00	99.18	101.48	100.34

Formula Proportions

Si	1.041	1.033	1.035	1.042	1.040	1.053	1.928	1.939	
Al	0.994	0.997	1.003	0.991	1.007	0.992	0.333	0.401	
Fe*	0.015	0.015	0.016	0.017	0.016	0.020	0.179	0.217	
Mg	0.007	0.007	0.007	0.008	0.007	0.009	0.521	0.450	
Ca	0.028	0.028	0.028	0.030	0.029	0.030	1.760	1.652	
Ba	0.000	0.001	0.000	0.000	0.000	0.000	0.000	0.001	
Sr	0.012	0.012	0.012	0.012	0.012	0.011	0.038	0.048	
Na	0.670	0.664	0.656	0.666	0.644	0.646	0.227	0.277	
K	0.232	0.243	0.242	0.235	0.244	0.238	0.012	0.015	
Rb	0.000	0.000	0.000	0.000	0.000	0.000	0.000	0.000	
							Åker**	51.2	45.1
							Na-mel	23.5	29.3
							Fe-åker	17.6	21.8
							Gehl†	7.7	3.8

No. Analyses	2	2	2	2	2	1	5	1
Texture	G	G	G	G	G	I	Pk	Pk
Size (mm)	0.25	0.11	0.08	0.11	0.15	0.06	1.1	>0.1

*Total iron as FeO; **end members in mole percent; †includes (Sr,Ba) with Ca; ††includes Sr with Ca.

TABLE 4 (continued)

	PYROXENE				OLIVINE
	3R	3-7	14-1	20-1	15-1
SiO ₂	46.52	51.89	47.55	47.76	37.08
Al ₂ O ₃	6.79	2.11	5.21	6.25	0.00
TiO ₂	1.24	0.47	1.04	1.18	0.03
FeO*	7.52	4.14	7.80	7.12	22.94
MgO	12.71	15.49	13.22	12.79	37.27
CaO	24.13	24.64	23.78	24.08	1.45
MnO	0.05	0.11	0.10	0.08	0.75
SrO	0.18	0.18	0.18	0.18	0.09
Na ₂ O	0.19	0.11	0.22	0.20	0.00
Cr ₂ O ₃	0.01	0.02	0.03	0.01	0.02
TOTAL	99.34	99.16	99.13	99.65	99.63

Formula Proportions

Si	1.738	1.920	1.781	1.779	0.975
Al	0.299	0.092	0.230	0.275	0.000
Ti	0.035	0.013	0.029	0.033	0.001
Fe*	0.235	0.128	0.244	0.222	0.504
Mg	0.708	0.854	0.738	0.710	1.461
Ca	0.966	0.977	0.954	0.961	0.041
Mn	0.002	0.003	0.003	0.003	0.017
Sr	0.004	0.004	0.004	0.004	0.001
Na	0.014	0.008	0.016	0.015	0.000
Cr	0.000	0.001	0.001	0.000	0.000
(Fe,Mn) ₂ Si ₂ O ₆ **	11.4	6.5	11.9	10.9	Fo** 74.3
Mg ₂ Si ₂ O ₆	34.0	42.2	35.5	34.5	Fa 25.7
NaCrAlSiO ₆	0.0	0.1	0.1	0.0	
CaTiAl ₂ O ₆	3.3	1.3	2.8	3.2	
NaAlSi ₂ O ₆	1.3	0.7	1.4	1.4	
CaAl ₂ SiO ₆	10.3	2.9	7.5	9.4	
Ca ₂ Si ₂ O ₆ ††	39.7	46.3	40.8	40.6	

No. Analyses	3	1	1	1	1
Texture	P,R	P,C	G	G	G
Size (mm)	0.75		0.08	0.13	0.05

*Total iron as FeO; **end members in mole percent; †includes (Sr,Ba) with Ca; ††includes Sr with Ca.

TABLE 4 (continued)

	MAGNETITE			
	91-1	93-1	94-1	95-2
MgO	0.85	0.98	1.28	0.98
Al ₂ O ₃	8.35	6.74	7.24	4.35
SiO ₂	0.53	0.47	0.49	0.62
TiO ₂	9.88	11.93	9.94	12.77
Cr ₂ O ₃	0.08	0.02	0.03	0.09
MnO	0.61	0.74	0.72	0.73
FeO*	73.01	76.25	75.56	75.46
ZrO ₂	0.02	0.06	0.01	0.00
ZnO	0.26	0.27	0.10	0.11
Nb ₂ O ₅	0.00	0.00	0.00	0.00
TOTAL	93.59	97.46	95.37	95.11

Formula Proportions

Mg	0.047	0.052	0.070	0.054
Al	0.365	0.285	0.311	0.190
Si	0.020	0.017	0.018	0.023
Ti	0.275	0.323	0.273	0.357
Cr	0.002	0.001	0.001	0.003
Mn	0.019	0.023	0.022	0.023
Fe*	2.264	2.291	2.303	2.347
Zr	0.000	0.001	0.000	0.000
Zn	0.007	0.007	0.003	0.003
Nb	0.000	0.000	0.000	0.000
FMCr ₂ O ₄ **	0.1	0.0	0.1	0.1
FM ₂ TiO ₄	27.7	32.4	27.4	36.0
FMA ₂ O ₄	18.4	14.4	15.6	9.6
FMO·Fe ₂ O ₃	53.8	53.2	56.9	54.3

FM = Fe + Mg + Mn + Zn

No. Analyses	1	1	1	1
Texture	G	G	G	G
Size (mm)	0.02	0.02	0.03	0.02

*Total iron as FeO; **end members in mole percent; †includes (Sr,Ba) with Ca; ††includes Sr with Ca.

TABLE 5. Microprobe analyses of NMNH-99071 (weight percent). 0.00 indicates element not present at level of detectability. - indicates element not analyzed for. Textural notation: P indicates phenocryst, Mp microphenocryst, G groundmass grain (subhedral or equant), Pk poikilitic, R rim, Im intermediate, C core.

	PLAGIOCLASE							
	8P	9-1/4	10-4	10-5/6	10-8	80	80-8/9	81
SiO ₂	54.58	56.99	50.47	52.40	54.83	52.89	50.68	53.21
Al ₂ O ₃	26.57	25.23	29.29	27.53	26.38	27.11	28.98	27.77
FeO*	0.56	0.48	0.54	0.50	0.58	0.54	0.60	0.55
MgO	0.15	0.14	0.17	0.08	0.15	0.15	0.16	0.15
CaO	8.65	6.57	11.29	8.68	7.03	6.40	9.76	7.23
BaO	0.65	0.99	0.54	0.76	0.92	1.19	0.39	0.76
SrO	2.84	2.16	4.53	4.86	3.70	5.97	4.39	5.02
Na ₂ O	5.14	5.98	3.63	4.37	5.83	4.77	3.78	4.75
K ₂ O	0.89	1.54	0.58	1.07	1.21	1.43	0.63	1.12
Rb ₂ O	0.00	0.00	0.00	0.00	0.00	-	-	-
TOTAL	100.03	100.08	101.04	100.25	100.63	100.45	99.37	100.56

Formula Proportions

Si	2.507	2.601	2.328	2.434	2.503	2.463	2.371	2.457
Al	1.438	1.357	1.592	1.507	1.419	1.488	1.598	1.511
Fe*	0.022	0.018	0.021	0.019	0.022	0.021	0.023	0.021
Mg	0.010	0.010	0.012	0.006	0.010	0.010	0.011	0.010
Ca	0.426	0.321	0.558	0.432	0.344	0.319	0.489	0.358
Ba	0.012	0.018	0.010	0.014	0.016	0.022	0.007	0.014
Sr	0.076	0.057	0.121	0.131	0.098	0.161	0.119	0.134
Na	0.458	0.529	0.325	0.394	0.516	0.431	0.343	0.428
K	0.052	0.090	0.034	0.063	0.070	0.085	0.038	0.066
Rb	0.000	0.000	0.000	0.000	0.000	0.000	0.000	0.000
Or**	5.0	8.6	3.2	6.0	6.6	8.1	3.7	6.4
Ab	43.4	50.7	30.0	37.1	47.9	41.1	33.2	41.3
An	40.3	30.8	51.6	40.9	31.9	30.4	47.4	34.8
Ce	1.1	1.7	0.9	1.3	1.5	2.1	0.7	1.3
Sr-F	7.2	5.5	11.2	12.3	9.1	15.3	11.6	13.1
Mg-F	1.0	0.9	1.1	0.5	0.9	1.0	1.1	1.0
Fe-F	2.0	1.8	2.0	1.9	2.1	2.0	2.3	2.1

No. Analyses	2	2	1	2	1	4	2	3
Texture	G	G	G,C	G, Im	G,R	G,Pk	G,Pk	G,Pk
Size (mm)	0.13	0.08	0.20		0.13		0.60	

*Total iron as FeO; **end members in mole percent; †includes Sr with Ca.

TABLE 5 (continued)

	SANIDINE		LEUCITE				
	8S	9-2/3	4-6/8	5-2/3	51.1	2-3/4	12-2
SiO ₂	62.44	62.02	55.02	55.89	55.06	55.24	55.17
Al ₂ O ₃	19.80	19.66	23.18	22.88	22.80	22.89	22.83
FeO*	0.38	0.70	0.47	0.70	0.77	0.65	0.69
MgO	0.14	0.18	0.13	0.12	0.14	0.12	0.14
CaO	0.63	0.58	0.00	0.00	0.01	0.00	0.00
BaO	2.31	2.69	0.11	0.04	0.11	0.04	0.04
SrO	0.59	0.63	0.09	0.10	0.15	0.09	0.11
Na ₂ O	2.88	3.07	0.32	0.16	0.17	0.15	0.12
K ₂ O	10.63	10.30	20.79	20.92	21.08	21.57	21.53
Rb ₂ O	0.00	0.00	0.12	0.15	0.26	0.24	0.13
TOTAL	99.80	99.83	100.23	100.96	100.55	100.99	100.76

Formula Proportions

Si	2.908	2.893	1.996	2.018	1.997	1.991	1.993
Al	1.087	1.081	0.991	0.974	0.974	0.972	0.972
Fe*	0.015	0.027	0.014	0.021	0.023	0.020	0.021
Mg	0.010	0.013	0.007	0.006	0.008	0.006	0.008
Ca	0.031	0.029	0.000	0.000	0.000	0.000	0.000
Ba	0.042	0.049	0.002	0.001	0.002	0.001	0.001
Sr	0.016	0.017	0.002	0.002	0.003	0.002	0.002
Na	0.260	0.278	0.023	0.011	0.012	0.010	0.008
K	0.631	0.613	0.962	0.964	0.975	0.992	0.992
Rb	0.000	0.000	0.003	0.003	0.006	0.006	0.003
Or**	62.9	59.7					
Ab	25.8	27.1					
An	3.1	2.8					
Ce	4.2	4.8					
Sr-F	1.6	1.7					
Mg-F	0.9	1.2					
Fe-F	1.5	2.7					

No. Analyses	3	2	2	2	1	2	1
Texture	G	G	P	Mp	G	Mp	Mp
Size (mm)	0.06	0.04	1.10	0.22	0.07	0.22	0.17

*Total iron as FeO; **end members in mole percent; †includes Sr with Ca.

TABLE 5 (continued)

	PYROXENE					
	6-1	1-6/7	1-8/9	3-2/3	52-1	53-1/2
SiO ₂	53.31	51.54	51.98	49.78	48.04	48.62
Al ₂ O ₃	1.89	3.78	2.65	4.50	6.91	6.20
TiO ₂	0.31	0.51	0.36	0.72	1.12	0.88
FeO*	3.36	4.50	3.61	4.97	6.33	6.25
MgO	16.59	15.75	16.51	15.05	13.80	13.92
CaO	24.85	24.00	24.02	24.33	23.47	23.82
MnO	0.07	0.06	0.04	0.08	0.09	0.07
SrO	0.12	0.13	0.12	0.13	0.15	0.15
Na ₂ O	0.10	0.14	0.13	0.15	0.19	0.15
Cr ₂ O ₃	0.25	0.16	0.35	0.23	0.05	0.04
TOTAL	100.85	100.57	99.77	99.94	100.15	100.10

Formula Proportions

Si	1.931	1.877	1.901	1.829	1.769	1.792
Al	0.081	0.162	0.114	0.195	0.300	0.269
Ti	0.008	0.014	0.010	0.020	0.031	0.024
Fe*	0.102	0.137	0.110	0.153	0.195	0.193
Mg	0.896	0.855	0.900	0.824	0.758	0.765
Ca	0.964	0.936	0.941	0.958	0.926	0.940
Mn	0.002	0.002	0.001	0.002	0.003	0.002
Sr	0.003	0.003	0.003	0.003	0.003	0.003
Na	0.007	0.010	0.009	0.011	0.014	0.011
Cr	0.007	0.005	0.010	0.007	0.001	0.001
(Fe,Mn) ₂ Si ₂ O ₆ **	5.1	6.9	5.5	7.6	9.6	9.5
Mg ₂ Si ₂ O ₆	44.4	42.1	44.4	40.1	36.9	37.2
NaCrAlSiO ₆	0.7	0.4	1.0	0.6	0.1	0.1
CaTiAl ₂ O ₆	0.8	1.4	1.0	1.9	3.0	2.3
NaAlSi ₂ O ₆	0.0	0.5	0.0	0.4	1.2	1.0
CaAl ₂ SiO ₆	2.8	6.2	4.1	7.1	10.9	10.2
Ca ₂ Si ₂ O ₆ †	46.2	42.5	44.0	42.3	38.3	39.7

No. Analyses	1	2	2	2	1	2
Texture	G	P,R	P,C	G	G	G
Size (mm)	0.26	0.90		0.50	0.33	0.38

*Total iron as FeO; **end members in mole percent; †includes Sr with Ca.

TABLE 5 (continued)

	MAGNETITE				
	70-1	72-1	73-1	74-1	75-1
SiO ₂	0.62	0.66	0.64	0.60	0.72
Al ₂ O ₃	16.31	20.20	20.94	20.61	14.89
TiO ₂	9.92	9.77	10.37	10.03	12.11
FeO*	67.48	62.76	62.45	61.41	66.42
MgO	0.59	0.91	1.39	1.42	1.12
MnO	1.05	1.22	0.47	0.80	0.46
ZnO	0.22	0.49	0.00	0.11	0.05
ZrO ₂	0.00	0.00	0.02	0.06	0.00
Cr ₂ O ₃	0.08	0.07	0.10	0.01	0.07
Nb ₂ O ₅	-	-	0.00	0.00	0.00
TOTAL	96.27	96.08	96.38	95.05	95.84

Formula Proportions

Si	0.022	0.023	0.022	0.021	0.025
Al	0.673	0.820	0.842	0.841	0.619
Ti	0.261	0.253	0.266	0.261	0.321
Fe*	1.975	1.808	1.782	1.777	1.959
Mg	0.031	0.047	0.071	0.073	0.059
Mn	0.031	0.036	0.014	0.023	0.014
Zn	0.006	0.013	0.000	0.003	0.001
Zr	0.000	0.000	0.000	0.001	0.000
Cr	0.002	0.002	0.003	0.000	0.002
Nb	0.000	0.000	0.000	0.000	0.000
FMCr ₂ O ₄ **	0.1	0.1	0.2	0.0	0.1
FM ₂ TiO ₄	26.3	25.5	26.8	26.3	32.4
FMA ₂ O ₄	33.9	41.3	42.4	42.4	31.2
FMO·Fe ₂ O ₃	39.7	33.1	30.6	31.3	36.3

FM = Fe + Mg + Mn + Zn

No. Analyses	1	1	1	1	1
Texture	G	G	G	G	G
Size (mm)	0.015	0.02	0.025	0.025	0.03

*Total iron as FeO; **end members in mole percent; †includes Sr with Ca.

TABLE 6. Microprobe analyses of NMNH-99097 (weight percent). 0.00 indicates element not present at level of detectability. - indicates element not analyzed for. Textural notation: P indicates phenocryst, G groundmass grain (subhedral or equant), I interstitial grain (anhedral), R rim, Im intermediate, C core.

	PLAGIOCLASE					
	1-3/4	7	12-2	15-1	17-1	20-1
SiO ₂	48.43	49.08	48.30	50.92	50.12	49.74
Al ₂ O ₃	31.54	30.85	31.43	29.98	30.16	30.82
TiO ₂	-	-	-	-	-	-
FeO*	0.93	0.87	0.98	0.79	1.08	0.91
MgO	0.16	0.19	0.16	0.14	0.22	0.14
CaO	15.48	14.83	15.73	12.21	13.88	14.08
BaO	0.14	0.24	0.09	0.88	0.32	0.23
SrO	0.78	0.91	0.78	0.88	0.80	0.81
Na ₂ O	2.47	2.77	2.27	3.05	3.03	2.94
K ₂ O	0.37	0.30	0.38	0.97	0.62	0.38
Rb ₂ O	0.00	0.00	0.00	0.00	0.00	0.00
TOTAL	100.30	100.04	100.12	99.82	100.23	100.05
Formula Proportions						
Si	2.222	2.257	2.223	2.353	2.299	2.285
Al	1.706	1.672	1.705	1.633	1.630	1.668
Ti	0.000	0.000	0.000	0.000	0.000	0.000
Fe*	0.036	0.033	0.038	0.031	0.041	0.035
Mg	0.011	0.013	0.011	0.010	0.015	0.010
Ca	0.761	0.731	0.776	0.604	0.682	0.693
Ba	0.003	0.004	0.002	0.016	0.006	0.004
Sr	0.021	0.024	0.021	0.024	0.021	0.022
Na	0.220	0.247	0.203	0.273	0.269	0.262
K	0.022	0.018	0.022	0.057	0.036	0.022
Rb	0.000	0.000	0.000	0.000	0.000	0.000
Or**	2.0	1.7	2.1	5.6	3.4	2.1
Ab	20.5	23.0	18.9	26.9	25.2	25.0
An	71.1	68.2	72.4	59.7	63.6	66.2
Ce	0.2	0.4	0.2	1.6	0.5	0.4
Sr-F	1.9	2.3	1.9	2.3	2.0	2.1
Mg-F	1.0	1.2	1.0	0.9	1.4	0.9
Fe-F	3.3	3.2	3.5	3.0	3.9	3.3
No. Analyses	2	4	1	1	1	1
Texture	G	G	G	G	G	G
Size (mm)	0.03	0.22	0.06	0.03	0.02	0.01

*Total iron as FeO; **end members in mole percent; † separate determinations; †† includes Sr with Ca.

TABLE 6. (continued)

	LEUCITE				SANIDINE
	13-1/2	22-1	36-1	19-1	16-1/2
SiO ₂	55.70	55.80	55.69	55.66	64.86
Al ₂ O ₃	22.84	23.04	23.00	22.17	19.12
TiO ₂	-	-	0.05 [†]	-	-
FeO*	0.63	0.48	0.63	0.67	0.54
MgO	0.13	0.14	0.15	0.12	0.13
CaO	0.00	0.04	0.02	0.04	0.75
BaO	0.08	0.00	0.00	0.05	0.14
SrO	0.12	0.07	0.12	0.05	0.20
Na ₂ O	0.04	0.05	0.03	0.07	1.69
K ₂ O	20.54	20.25	20.57	20.02	12.08
Rb ₂ O	0.12	0.04	0.17	0.11	0.00
TOTAL	100.20	99.91	100.43	98.96	99.51

Formula Proportions

Si	2.029	2.036	2.024	2.055	3.011
Al	0.981	0.991	0.985	0.964	1.046
Ti	0.000	0.000	0.001	0.000	0.000
Fe*	0.019	0.015	0.019	0.021	0.021
Mg	0.007	0.008	0.008	0.007	0.009
Ca	0.000	0.002	0.001	0.002	0.037
Ba	0.001	0.000	0.000	0.001	0.003
Sr	0.003	0.001	0.003	0.001	0.005
Na	0.003	0.004	0.002	0.005	0.152
K	0.955	0.943	0.953	0.943	0.715
Rb	0.003	0.001	0.004	0.003	0.000
Or**					75.9
Ab					16.1
An					3.9
Ce					0.3
Sr-F					0.6
Mg-F					0.9
Fe-F					2.3

No. Analyses	2	1	1	1	2
Texture	I	G	G	G	G
Size (mm)	0.10	0.10	0.10	0.10	0.02

*Total iron as FeO; **end members in mole percent; †separate determinations; ††includes Sr with Ca.

TABLE 6. (continued)

	PYROXENE						OLIVINE
	45-1	45-2	45-3	3-4/6	21-1/3	35-1	14-1/2
SiO ₂	50.45	51.12	51.03	45.39	48.15	44.57	36.29
Al ₂ O ₃	3.71	3.37	3.38	7.20	5.82	8.05	0.00
TiO ₂	0.67	0.64	0.62	1.61	1.21	1.87	0.02
FeO*	5.86	5.05	4.95	8.73	6.53	8.68	33.37
MgO	15.19	15.65	15.50	12.03	13.66	11.57	30.36
CaO	23.43	23.37	23.29	24.01	24.16	23.79	0.54
MnO	0.12	0.12	0.07	0.16	0.09	0.12	0.78
SrO	0.14	0.13	0.13	0.15	0.15	-	0.13
Na ₂ O	0.18	0.22	0.16	0.28	0.22	0.30	0.07
Cr ₂ O ₃	0.07	0.19	0.14	0.00	0.05	0.01	0.01
TOTAL	99.82	99.86	99.27	99.56	100.04	98.96	101.57

Formula Proportions

Si	1.859	1.877	1.886	1.700	1.779	1.680	0.981
Al	0.161	0.146	0.147	0.318	0.253	0.358	0.000
Ti	0.019	0.018	0.017	0.045	0.034	0.053	0.000
Fe*	0.181	0.155	0.153	0.273	0.202	0.274	0.755
Mg	0.834	0.857	0.854	0.672	0.752	0.650	1.224
Ca	0.925	0.920	0.922	0.963	0.956	0.961	0.016
Mn	0.004	0.004	0.002	0.005	0.003	0.004	0.018
Sr	0.003	0.003	0.003	0.003	0.003	0.000	0.002
Na	0.013	0.016	0.011	0.020	0.016	0.022	0.004
Cr	0.002	0.006	0.004	0.000	0.001	0.000	0.000
(Fe,Mn) ₂ Si ₂ O ₆ **	9.0	7.8	7.6	13.2	9.9	13.2	Fo** 61.8
Mg ₂ Si ₂ O ₆	40.8	42.1	42.2	31.9	36.4	31.0	Fa 38.2
NaCrAlSiO ₆	0.2	0.5	0.4	0.0	0.1	0.0	
CaTiAl ₂ O ₆	1.8	1.7	1.7	4.3	3.2	5.0	
NaAlSi ₂ O ₆	1.1	1.0	0.8	2.0	1.4	2.1	
CaAl ₂ SiO ₆	5.4	4.7	5.0	9.9	8.3	10.9	
Ca ₂ Si ₂ O ₆ ††	41.7	42.2	42.3	38.7	40.7	37.8	

No. Analyses	1	1	1	2	2	1	2
Texture	P,R	P,Im	P,C	G	P,R	G	G
Size (mm)		2.0		0.17	0.4	0.06	0.06

*Total iron as FeO; **end members in mole percent; †separate determinations; ††includes Sr with Ca.

TABLE 6. (continued)

	SODALITE		MAGNETITE	
	24-2	39-7	92-3	
SiO ₂	39.08	39.28	SiO ₂	0.38
Al ₂ O ₃	30.70	31.63	Al ₂ O ₃	3.87
FeO*	0.25	0.22	TiO ₂	17.11
MgO	0.01	0.03	FeO*	73.42
CaO	0.24	0.23	MgO	0.68
MnO	0.00	0.05	MnO	0.72
Na ₂ O	23.08	20.95	ZnO	0.53
K ₂ O	1.10	1.48	ZrO ₂	0.08
Cr ₂ O ₃	0.01	0.00	Cr ₂ O ₃	0.07
Cl	6.22	6.59	Nb ₂ O ₅	0.00
F	0.00	0.00	TOTAL	96.86
SO ₃	0.00	0.00		
Σ	100.69	100.46		
O≡Cl	1.39	1.50		
TOTAL	99.30	98.96		

Formula Proportions

Si	6.412	6.570
Al	5.936	6.235
Fe*	0.034	0.031
Mg	0.002	0.007
Ca	0.042	0.041
Mn	0.000	0.007
Na	7.342	6.793
K	0.230	0.316
Cr	0.001	0.000

Si	0.014
Al	0.168
Ti	0.475
Fe*	2.265
Mg	0.037
Mn	0.022
Zn	0.014
Zr	0.001
Cr	0.002
Nb	0.000

FMCr ₂ O ₄ **	0.1
FM ₂ TiO ₄	47.7
FMA ₂ O ₄	8.5
FMO·Fe ₂ O ₃	43.7

$$FM = Fe + Mg + Mn + Zn$$

No. Analyses	1	1
Texture	I	I
Size (mm)	0.08	0.10

1
G
0.05

*Total iron as FeO; **end members in mole percent; †separate determinations; †† includes Sr with Ca.

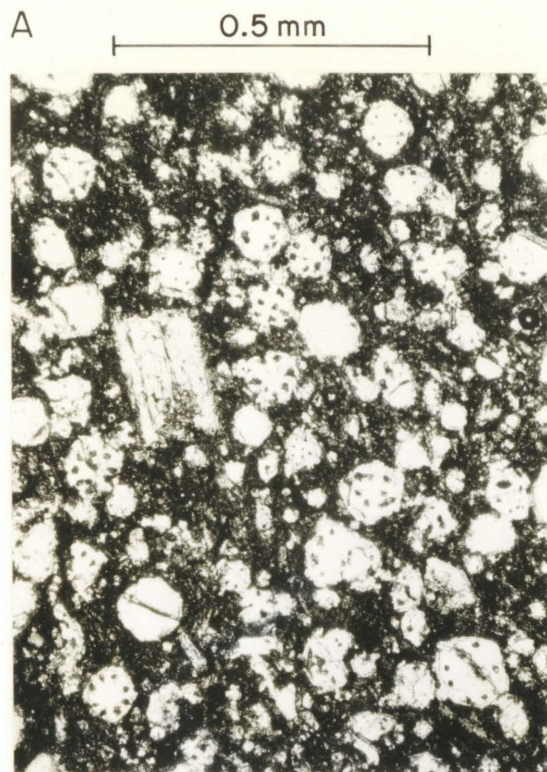
FIGURE CAPTIONS

- Figure 1. (a) NMNH-99024. Illustrating "clathrate" texture produced by rounded microphenocrysts of leucite. Inclusions in leucite are calcium-rich pyroxene.
- (b) NMNH-99055. Interstitial, poikilitic melilite displaying characteristic "peg" structure (fine, parallel lines).
- (c) NMNH-99055. Euhedral crystal of nepheline (grain 18 1/2, see table 4) growing along wall of vesicle (now filled with calcite). Nepheline is crystallographically continuous with anhedral groundmass nepheline. Polarizers slightly off crossed position.
- (d) NMNH-99071. Poikilitic, interstitial plagioclase (grain 81, see table 5). Polarizers slightly off crossed position.
- Figure 2. Ternary feldspar diagrams for NMNH-99024, NMNH-99071, and NMNH-99097. Size of triangle for each analysis indicates amount of $(\text{SrAl}_2\text{Si}_2\text{O}_8 + \text{BaAl}_2\text{Si}_2\text{O}_8 + \text{FeAl}_2\text{Si}_2\text{O}_8 + \text{Mg}_2\text{Al}_2\text{Si}_2\text{O}_8)$ in analysis. Dashed line is limit of ternary solid solution for naturally-occurring feldspars of normal composition (Carmichael, 1963). Tie lines are drawn for feldspar pairs in contact with each other (see text) and endpoint analyses are identified. Triangles with patterned borders indicate multiple analyses of single grains (one grain for -024, two grains for -071) and C, M, and R indicate core, intermediate, and rim composition, respectively, where zoning is apparent. Figure is in mol. percent.

Figure 3. Orthographic projection of the tetrahedron NaAlSiO_4 - KAlSiO_4 - CaAl_2O_4 - SiO_2 (inset) onto the base NaAlSiO_4 - KAlSiO_4 - CaAl_2O_4 . Four phase volume defined by coexisting plagioclase-sanidine-leucite-nepheline of NMNH-99024 is shown in inset by shaded region and in projection by approximate tie lines. Plagioclase-sanidine tie line is that of figure 3 (the validity of the tie lines is discussed in the text). For simplicity all other feldspar compositions have been omitted. Limits of ternary feldspar solid solution and of nepheline solid solution are schematically indicated by dashed lines. Diagram is in mole percent.

Figure 4. Ca_2SiO_4 - $(\text{Mg,Fe})_2\text{SiO}_4$ - SiO_2 ternary diagram for mafic phases. Solid lines are tie lines for NMNH-99055, dashed line is tie for NMNH-99097.

Figure 5. Plot of BaO vs. CaO and SrO vs. CaO for feldspars of NMNH-99024 and NMNH-99071. Lines connect multiple analyses from single grains. C, M, and R indicate core, intermediate, and rim compositions, respectively, where zoning is apparent.



C

0.25 mm

D

0.5 mm

Figure 1

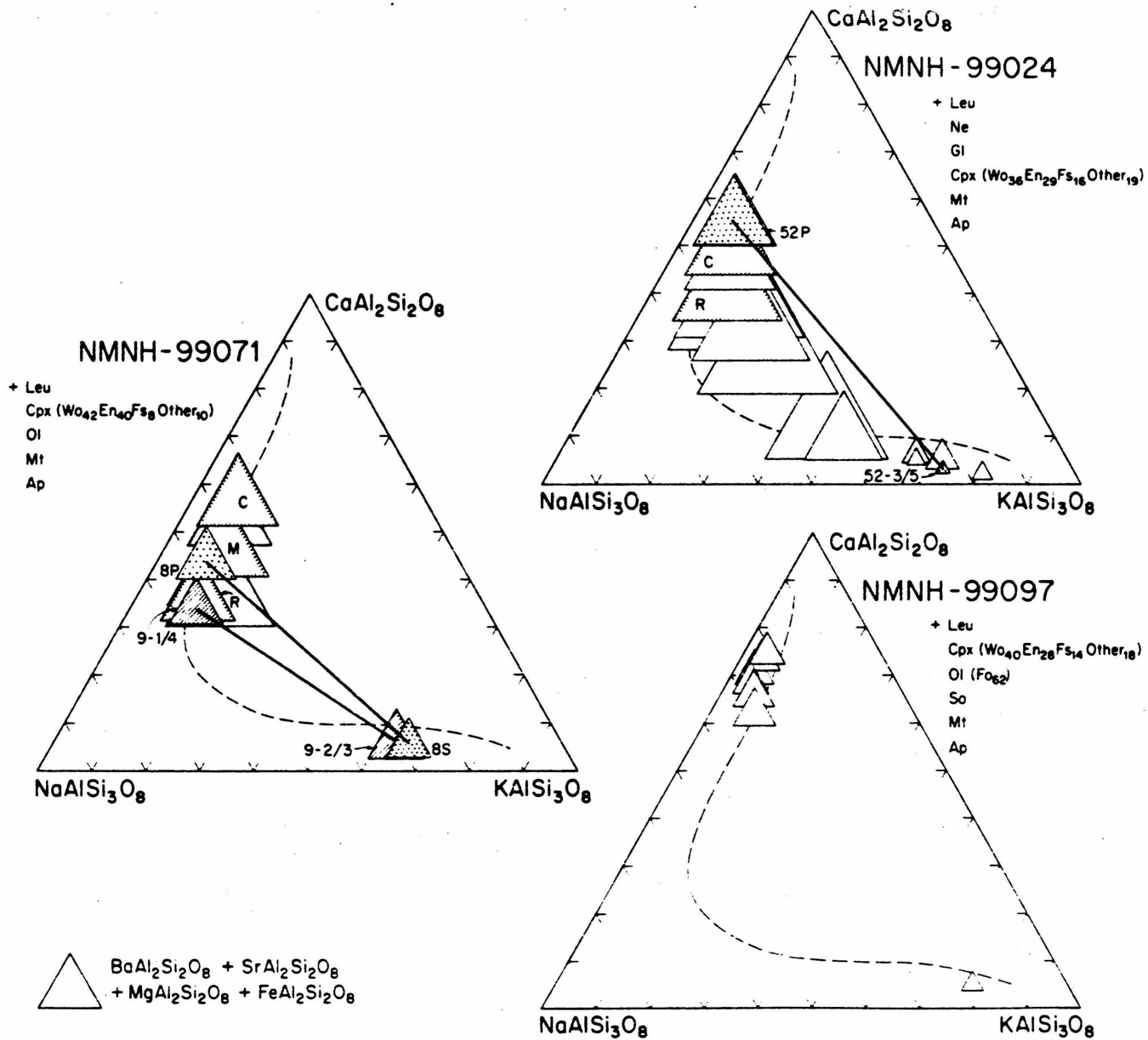
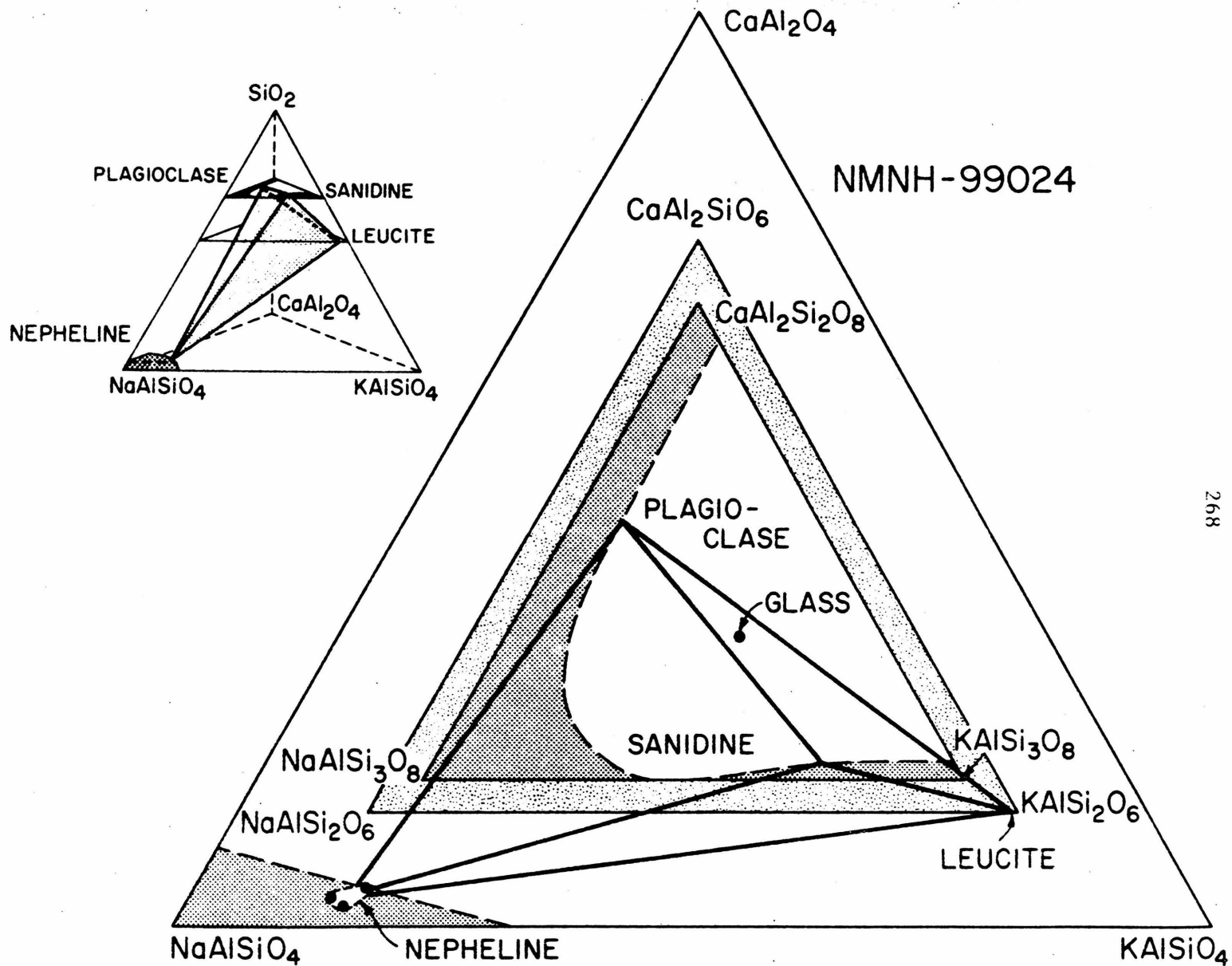


Figure 2



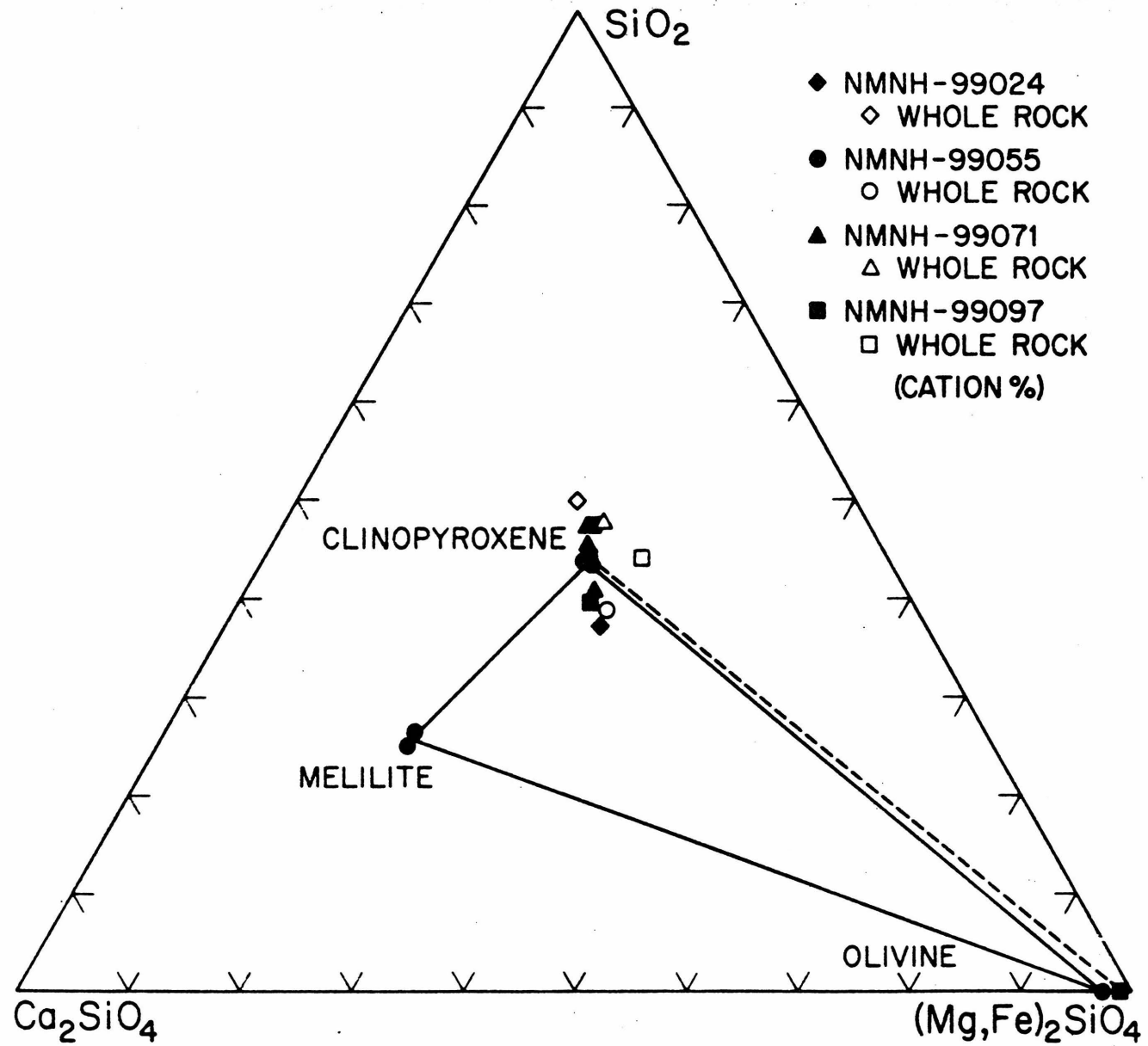


Figure 4

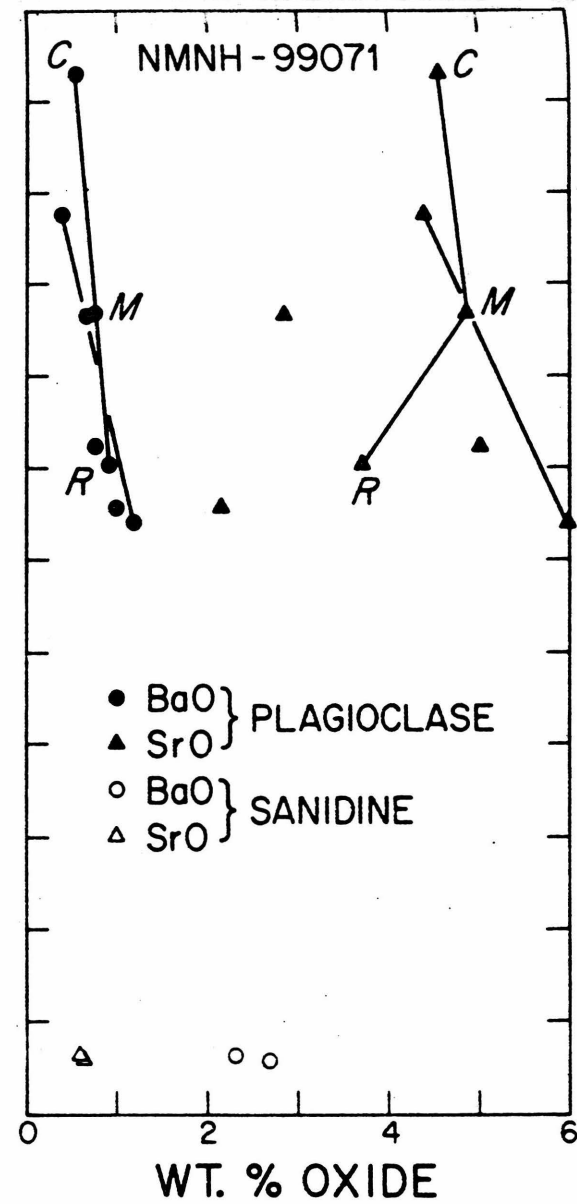
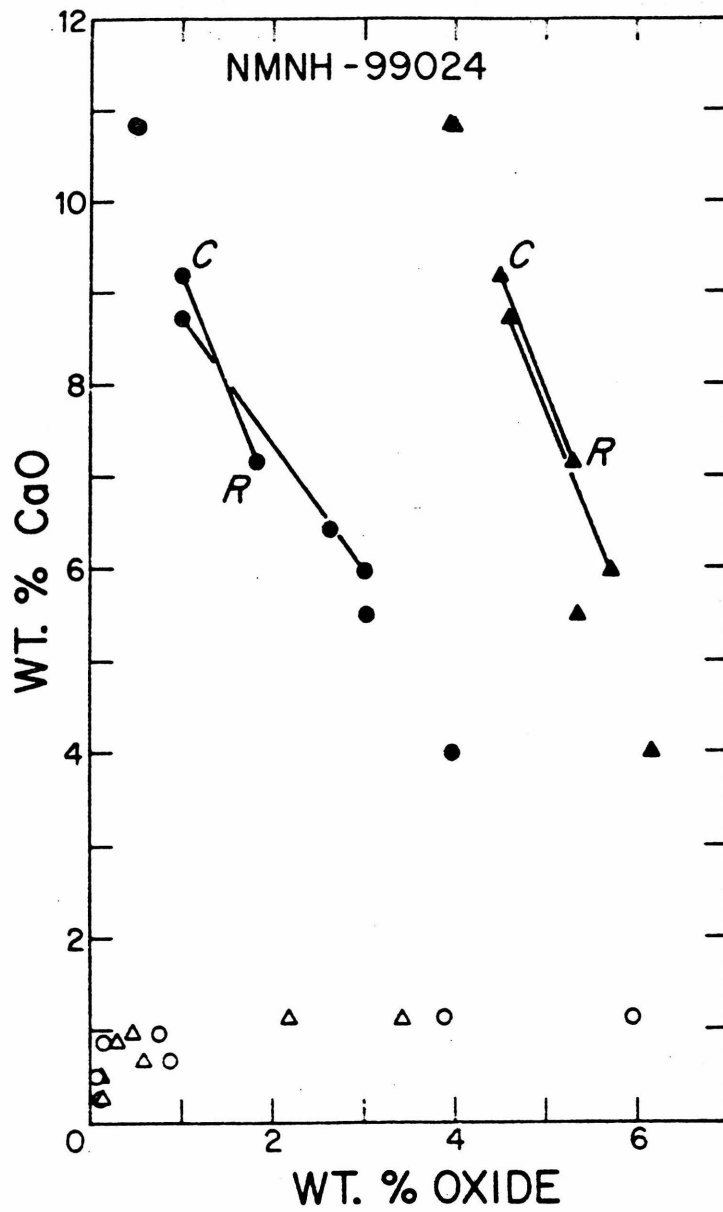


Figure 5

PART IV

PETROLOGIC EVOLUTION OF APOLLO 12 OLIVINE-PIGEONITE MARE BASALTS

By

W. S. Baldrige, A. L. Albee, A. A. Chodos, and S. Hill

Division of Geological and Planetary Sciences

California Institute of Technology

Pasadena, California 91125

ABSTRACT

The Apollo 12 olivine and pigeonite mare basalts exhibit a wide range of compositions and textures. It has become generally accepted that the pigeonite basalts are derived from the olivine basalts by fractionation of olivine, Cr-spinel, and pigeonite phenocrysts and that fractionation of these phases accounts for the range of compositions within each group. We report petrographic observations, mineral chemistry, modes, average phase compositions, and bulk compositions of five previously-unstudied rocks (12007, 12011, 12015, 12043, and 12072) which, from preliminary inspection and/or from the whole-rock data of Rhodes et al. (1977) were classified as olivine or pigeonite basalts.

Four of these rocks (12007, 12011, 12015, and 12043) are representative of the olivine and pigeonite basalt groups and allow an assessment of the fractional crystallization model. The most primitive member of this series is vitrophyre 12015, which has textures indicating that it was erupted on the lunar surface as a melt containing a small amount of olivine phenocrysts. Increasing grain size (decreasing cooling rate) correlates with more evolved mineral compositions and modal abundances. This textural and mineralogic sequence yields strong evidence that all of these rocks can be related by fractionation of early-crystallizing phases. Least-squares modeling of these rocks using the observed phenocryst compositions is completely compatible with this mechanism.

Rock 12072 is significantly higher in modal plagioclase and lower in ilmenite than the olivine and pigeonite basalts. Its composition

cannot be related in any simple way to the olivine and pigeonite basalts. Hence this rock is best classified as a feldspathic basalt. However, it is not similar to other Apollo 12 feldspathic basalts, which apparently constitute a diverse group of unrelated rock types.

INTRODUCTION

The mare basalt samples returned from the Apollo 12 site in Oceanus Procellarum were divided by James and Wright (1972) into three groups, (1) olivine-pigeonite basalts, (2) ilmenite basalts, and (3) feldspathic basalts on the basis of petrography and whole-rock chemistry. They ascribed the chemical variation within these groups to low pressure (mainly olivine) fractionation. More recently Papike et al. (1976) separated the olivine basalts from the pigeonite basalts in recognition of a distinct compositional hiatus between them. This distinction was upheld and the classification into four major basalt types confirmed by Rhodes et al. (1977). Based on additional whole-rock major and minor element chemistry in combination with textural studies they proposed that the olivine and pigeonite basalt are related to each other by fractionation of olivine (Fo_{72}), minor Cr-spinel, and (in the later stages of fractionation) pigeonite from a parental magma equivalent in composition to 12015. To explain a compositional hiatus between the most evolved of the olivine basalts and the least evolved of the pigeonite basalts, as well as an interruption in the systematic increase of grain size with degree of differentiation, they suggested that the olivine and pigeonite basalts represented two separate cooling units.

The present work was undertaken to provide an integrated set of detailed petrographic observations, mineral compositions, and whole-rock major element chemistry on a representative suite of samples from the olivine and pigeonite basalt groups in order to examine in detail their fractionation histories. The samples we have studied are 12007,9,10, and 11; 12011,7; 12015,15, and 16; 12043,6, and 8; and 12072,2.

The first four rocks were shown by Rhodes et al. (1977) to belong to the olivine and pigeonite basalt groups. The last rock, 12072, was thought on the basis of preliminary examination (Warner, 1970) also to belong to one of these groups. However, 12072 differs significantly from the olivine and pigeonite basalts in its composition and mineralogy and is classified as a feldspathic basalt. Its composition cannot be related to the olivine or pigeonite basalts by any simple process. No petrographic observations or mineral compositions for these samples have been published previously.

ANALYTICAL TECHNIQUES

The data points plotted on the various diagrams represent analyses performed consecutively on a single spot for 9-15 elements in groups of three using a MAC-5-SA3 electron microprobe interfaced to a PDP-8/L computer for control and on-line data processing. Standard operating conditions were 15 kv accelerating voltage and 0.05 μA sample current (on brass) with beam current integration and pulse height selection. For compositionally very inhomogeneous phases (especially pyroxene), a sample current of 0.005 μA was used in order to reduce the beam diameter to the smallest size possible. Reproducibility (1 σ) on two "known

unknown" secondary standards over a 13-month period ranged from 1.5% (for elements with abundances >1%) to 3% of the amount present (for elements with abundances 0.1-1.0%) (Champion et al. 1975).

Microprobe point counts were performed using a 161 eV Si(Li) detector interfaced to a NS-880 multichannel analyzer with dual floppy disks. For each sample we have measured the abundance, average composition, and range of composition of each mineral and calculated the bulk composition from the mass balance equations. Our procedure is to analyze for 10 elements with 5 sec counts at grid points on a polished thin section, identify the phase at each point to obtain the phase abundances, and accumulate an average spectrum for each phase. Identification is accomplished by a transformation of the spectrum from compositional space to phase space using preinverted matrices for minerals present in the rock. For typical basalt, $2-3 \times 10^3$ grid points are analysed on an area of about $20-100 \text{ mm}^2$. The normal running time is about 5-8 hours, and usually 98-99% of the points are identified by the program. The spectrum and identification for each point are stored sequentially on a floppy disk for subsequent reprocessing, editing, statistical analysis, and graphical display. Details of this procedure are given by Albee et al. (in press).

Each of the "average" mineral compositions given in tables 1-6 is in fact a "representative" complete microprobe analysis of a single point (or an average of several such points) that was selected from all the analyses as the best fit to the average values obtained by the point count. A computer print out of all the analyses may be obtained from A. Albee.

All mineral compositions and elemental ratios used in the text and in diagrams are in molecular proportions. Olivine compositions are reported as %Fo = $100 \times [\text{Mg}/(\text{Mg}+\text{Fe}+\text{Mn})]$; pyroxene compositions are reported as %Wo = $100 \times [\text{Ca}/(\text{Ca}+\text{Mg}+\text{Fe}+\text{Mn})]$; plagioclase compositions are reported as %An = $100 (\text{Ca}-\text{Fe}^{2+}-\text{Mg})$, where the cations are normalized to $(\text{Si}+\text{Al}+\text{Fe}^{2+}+\text{Mg}) = 4$.

Pyroxene formulas were calculated assuming that iron, titanium, and chromium are present as Fe^{2+} , Ti^{4+} and Cr^{3+} , normalizing the sum of the cations to four and sequentially calculating $(\text{Fe},\text{Mn})_2\text{Si}_2\text{O}_6$, CaCrAlSiO_6 , $\text{CaTiAl}_2\text{O}_6$, $\text{NaAlSi}_2\text{O}_6$, $\text{CaAl}_2\text{SiO}_6$, and $\text{Ca}_2\text{Si}_2\text{O}_6$ end members. The most important components not shown on the pyroxene quadrilateral are shown on an inset for Ti-Al-Cr. This triangular diagram includes the $\text{RAl}(\text{AlSiO}_6)$, $\text{RCr}(\text{AlSiO}_6)$, $\text{RTi}^{3+}(\text{AlSiO}_6)$, and $\text{RTi}^{4+}\text{Al}_2\text{O}_6$ end members. The stoichiometry of those analyses falling in the lower triangle indicates that they contain Ti^{3+} . Those analyses falling below the 0.5Ti-0.5 Cr line may contain Cr^{2+} , octahedral vacancies, or tetrahedral Ti. Spinel formulas were calculated by normalizing the sum of the cations to three and sequentially calculating $(\text{Mg}, \text{Fe}, \text{Mn})\text{Cr}_2\text{O}_4$ (chromite), $(\text{Mg}, \text{Fe}, \text{Mn})_2\text{TiO}_4$ (ulvöspinel), and $(\text{Mg}, \text{Fe}, \text{Mn})\text{Al}_2\text{O}_4$ (spinel). Cr-spinel compositions are reported as %Chr and ulvöspinel as %Ulv.

PETROGRAPHY AND MINERAL CHEMISTRY

All of these rocks are slightly vesicular, porphyritic basalts ranging in texture from vitrophyric to coarse-grained ophitic. The dominant phenocrysts are respectively olivine and pyroxene in the olivine and pigeonite basalts. In addition all rocks contain microphenocrysts

of Cr-rich spinel. The groundmasses of all samples except 12015 (vitrophyre) contain pyroxene, ilmenite, plagioclase, and cristobalite, and minor ulvöspinel, troilite, metallic Fe, high-Fe glass, high-K glass, fayalite, phosphate, and tranquillityite. The five samples we have examined in detail are described below. Olivine vitrophyre 12015 is described first, followed by the pigeonite basalts in order of increasing groundmass grain size, and finally by feldspathic basalt 12072.

12015

Rock 12015 is an olivine vitrophyre texturally similar to 12009 and 12008 (James and Wright, 1972; Dungan and Brown, 1977). It consists of phenocrysts of olivine, comprising 10-15 per cent of the rock, and microphenocrysts of olivine, pyroxene, and Cr-spinel in a nearly opaque mat of dendritic Fe-rich pyroxene and plagioclase, filamental ilmenite, cristobalite, troilite, Fe-metal, and glass. Modal abundances and average phase compositions are given in tables 1 and 2. Olivine phenocrysts occur as equant to elongate grains <1 mm in size, which typically contain slot-shaped to irregular inclusions of matrix material, with skeletal projections. Rims of olivine phenocrysts contain abundant small inclusions of euhedral Cr-spinel (<3 μm in size) and rounded grains of metallic iron (<15 μm in diameter). Olivine phenocrysts range in composition from Fo_{76} to Fo_{66} (figures 1 and 2). Cr-spinel <50 μm is a microphenocryst phase in this rock. Spinel typically includes grains of metallic iron.

The two polished thin sections which we have studied differ significantly. Olivine is present in greater abundance in 12015, 16 than in

12015, 15 (20 vs. 10 weight per cent, respectively; see tables 1 and 2). In 12015, 16 it occurs as abundant (approximately 5 per cent) skeletal microphenocrysts. As shown in figure 2 of these microphenocrysts (Fo_{69-59}) overlap phenocryst rims in composition. Some microphenocryst grains consist of hollow, hexagonal-shaped grains <0.2 mm in size. More commonly these consist of laths <1.5 mm long and $20 \mu\text{m}$ wide with chain-like skeletal forms. In some cases the chain-like grains project from the hexagonal grains, or from the olivine phenocrysts. Pyroxene also occurs as elongate, zoned microphenocrysts $<0.9 \times 0.2$ mm in size, constituting about 15 per cent of the rock. Groundmass comprises approximately 66 per cent of 12015, 16. In 12015, 15 olivine is rare as microphenocrysts. Instead pyroxene is more abundant (approximately 43 per cent) as lath-shaped or tabular, zoned microphenocrysts. Groundmass constitutes about 46 per cent of 12015, 15.

Pyroxene microphenocrysts have colorless or very pale buff-colored cores of pigeonite surrounded by rims of pinkish augite. In section 12015, 16 the pyroxene crystallization trend is continuous from pigeonite ($\text{Wo}_6\text{En}_{64}\text{Fs}_{30}$) to augite ($\text{Wo}_{36}\text{En}_{37}\text{Fs}_{27}$) (figure 2), whereas in 12015, 15 discrete rims of augite ($\text{Wo}_{22}\text{En}_{46}\text{Fs}_{32}$ - $\text{Wo}_{31}\text{En}_{25}\text{Fs}_{44}$) surround cores of pigeonite ($\text{Wo}_5\text{En}_{68}\text{Fs}_{27}$ - $\text{Wo}_9\text{En}_{58}\text{Fs}_{33}$) with a well-defined compositional break (figure 1). Pyroxene in 12015 is very aluminous (>9 weight per cent Al_2O_3). In both sections Al/Ti of pyroxene decreases continuously from about 0.80 in pigeonite to 0.75 in augite; in addition Cr decreases slightly with increasing Fe/Mg+Fe and Al/Ti (see insets, figures 1 and 2). These trends are particularly pronounced for 12015,

15. Spinel occurring as inclusions in olivine and as separate microphenocrysts has Fe/Mg+Fe between 0.60 and 0.89. The Ti/Cr increases with continued crystallization such that spinel microphenocrysts are surrounded by thin (2-5 μm) rims relatively higher in ulvöspinel-component.

An additional difference is evident in the groundmasses of these two sections. In 12015, 16 the groundmass is characterized by small (<1 μm -10 μm) grains of ilmenite (larger grains are cruciform), native Fe, and dendritic Fe-rich pyroxene, tiny dendrites (<1 μm) of plagioclase, minute grains (<1 μm) of cristobalite, and glass. By contrast, ilmenite is much more abundant in the groundmass of 12015, 15, occurring as long (50 μm), subparallel, skeletal "whiskers" 1-2 μm wide. These whiskers very commonly start at an olivine or pyroxene grain boundary and extend across the groundmass to adjacent olivine or pyroxene grains. In no case could analyses be obtained of these groundmass phases.

These textural and compositional differences indicate that 12015, 16 underwent slightly more rapid quenching than 12015, 15 although both sections are from the same sample. 12015, 15 was cut from two chips located 1/2 cm from a large (>2 cm) vesicle. This section was oriented subparallel to the vesicle wall. 12015, 16 was cut from two chips located approximately 1 cm from the vesicle and 1-1/2 cm from, 15. This section was probably oriented approximately parallel to, 15. This apparent correlation of texture with proximity to the vesicle could be misleading however, since 16 was located on the exterior of the sample and could have been affected by features not sampled. In any case we do not have a satisfactory explanation for the textural and chemical differences between these two sections.

12011

Rock 12011 is a pigeonite basalt consisting of approximately 8 per cent phenocrysts of olivine <1.1 mm, approximately 5 per cent phenocrysts of pyroxene <4 mm, and microphenocrysts of Cr-spinel in a fine-grained, variolitic-textured groundmass of pyroxene, plagioclase, ilmenite, ulvöspinel, troilite, metallic Fe, and interstitial cristobolite, glass, fayalite, phosphate, and tranquillityite. Irregular voids occur interstitially among groundmass phases. Modes, average phase compositions, and the calculated bulk composition are given in table 3. Olivine pyroxene, plagioclase, and cristobalite constitute 8, 53, 31, and 3 volume per cent of this rock, respectively. Olivine phenocrysts are euhedral to subhedral with skeletal projections. They range in composition from Fo₇₃₋₆₂ (figure 3), but some grains are zoned over almost this entire range. The phenocrysts contain equant inclusions of groundmass material, and (near the rims) euhedral inclusions of Cr-spinel <55 μm and rounded to irregular inclusions of metallic Fe <10 μm. Most phenocrysts are irregular in outline and are embayed. They are commonly overgrown by irregular pyroxene rims.

Pyroxene phenocrysts occur as elongate laths <4 mm. These laths tend to form interlocking aggregates. Pyroxene phenocrysts consist of very pale buff-colored pigeonite cores (Wo₉En₆₂Fs₂₉) surrounded by pink augite rims (Wo₂₈En₄₄Fs₂₈) (figure 3). These core-rim relationships are geometrically very complex, as if crystallization proceeded from multiple nuclei and merged to form the phenocrysts. The outer rims of phenocrysts are very irregular and they, as well as pyroxene overgrowths on olivine

phenocrysts, merge continuously with groundmass pyroxene.

Groundmass pyroxene occurs as anhedral subequant grains <4 mm and as acicular laths <0.8 mm intergrown with plagioclase in variolitic intergrowths. Compositional trends defined by groundmass pyroxene are shown on figure 3. The most magnesian groundmass pyroxene is a high-Fe pigeonite ($\text{Wo}_9\text{En}_{42}\text{Fs}_{49}$) which is zoned to high-Fe augite and subsequently to the Fe side of the quadrilateral ($\text{Wo}_{15}\text{En}_5\text{Fs}_{80}$). The minor element compositions of the pyroxene phenocrysts show a trend toward strongly decreasing Cr/Ti+Al+Cr and only very slightly decreasing Al/Ti with decreasing Fe/Mg+Fe (inset, figure 3). Separate trends differing slightly in Al/Ti can be distinguished for augite and pigeonite. At the point where pyroxene becomes a groundmass phase, corresponding to the discontinuity in major-element trend from augite to higher-Fe pigeonite, Al/Ti ratio decreases strongly with continued crystallization. No particular trend is evident once pyroxene becomes very Fe-rich (Fs <50). The large number of analyses with Al/Ti <2 indicates that Ti^{3+} is an important species in the groundmass pyroxene.

Cr-spinel occurs as euhedral to subhedral microphenocrysts, typically completely or partially including rounded to irregular grains <20 μm of metallic Fe. Spinel microphenocrysts are typically surrounded by thin (generally <5 μm but occasionally thicker) rims of ulvöspinel, except where the spinel is armored within olivine or pyroxene. Microphenocrysts range in composition from about Chr_{58-65} and are surrounded by ulvöspinel rims of approximately Ulv_{80} (figures 3 and 7).

Groundmass plagioclase occurs as anhedral, elongated acicular grains <0.8 mm and, less commonly, as anhedral, irregular interstitial grains. Acicular grains tend to be aligned subparallel to pyroxene laths. Plagioclase compositions range from An₈₂₋₇₇. Excess silica component first increases, then decreases slightly, with increasing crystallization (increasing Fe).

Ilmenite (nearly pure FeTiO₃) generally occurs as acicular grains <0.3 mm. Adjacent grains commonly are subparallel, and oriented perpendicular to boundaries of large olivine or pyroxene grains. This texture resembles the "filamental" ilmenite of 12015, 15.

Cristobalite occurs as irregular, interstitial grains comprising approximately one per cent of the groundmass. Cristobalite is characterized by a cracked, mosaic appearance due to inversion from the high to the low phase. Troilite occurs as irregular to spherical grains, typically with metallic Fe inclusions. Fe also occurs as discrete separate grains. Two glasses, a high-K and a high-Fe glass, are present, occasionally as inclusions of high-K in high-Fe glass but more commonly separately and interstitially to other phases. Fayalite, usually adjacent to pyroxene, occurs in intergrowth with either cristobalite or high-K glass. Traces of phosphate as well as of tranquillityite are also present. Because of their small size none of the phosphate grains were analyzed. By comparison to 12007, both whitlockite and apatite are probably present.

12043

Rock 12043 is a medium-grained pigeonite basalt consisting of 10 per cent large (<3.5 mm), tabular to lath-shaped phenocrysts of

pyroxene, 1 per cent irregularly-shaped grains of olivine (<1 mm) in a subophitic to variolitic groundmass of pyroxene, plagioclase, ilmenite, spinel, cristobalite, metallic Fe, troilite, tranquillityite, fayalite, and residual glass. Irregular voids are present interstitially among the groundmass phases. This groundmass is coarser-grained than that of 12011. Modes, average phase compositions, and the calculated bulk analysis are presented in table 4. Pyroxene and plagioclase constitute respectively 58 and 33 per cent of this rock. Only a small amount (about 1 per cent) of olivine is present. Olivine grains (relict phenocrysts) are deeply embayed, and are partially overgrown by pyroxene. Olivine contains euhedral inclusions of Cr-spinel <30 μm . The total range in composition is Fo_{70-65} ; individual grains have a range of up to 5 mole per cent Fo (figure 4).

Pyroxene phenocrysts are discontinuously zoned in this rock. Cores of colorless to very pale buff-colored pigeonite ($\text{Wo}_7\text{En}_{64}\text{Fs}_{29}\text{-Wo}_{13}\text{En}_{55}\text{Fs}_{32}$) are surrounded by (in sharp contact) a pinkish intermediate zone of augite ($\text{Wo}_{30}\text{En}_{44}\text{Fs}_{26}$) (figure 4). Optically this zone is typified by a very fine, parallel lamellae. Microprobe analyses of this zone show a slight dispersion toward lower -Ca augite compositions. Hence these lamellae are interpreted as exsolution lamellae of pigeonite in augite. However microprobe beam scans at high magnification fail to resolve these lamellae, indicating that their thickness is below the resolution of the beam ($\sim 2 \mu\text{m}$). Larger grains also have a pink outer rim in sharp contact with the intermediate rim. Pyroxene overgrowths on the relict olivine phenocrysts as well as the outermost rims on

pyroxene phenocrysts grade continuously into groundmass pyroxene with subophitic to variolitic texture.

Groundmass pyroxene occurs as acicular and wedge-shaped laths 0.6-0.8 mm long, intergrown with plagioclase and ilmenite in subophitic to variolitic intergrowths. Compositional trends defined by groundmass pyroxene (including overgrowths) are generally similar to those of 12011. As shown in figure 4, the most magnesian groundmass pyroxene is a high-Fe pigeonite ($Wo_{13}En_{44}Fs_{43}$). These compositions are continuously zoned to high-Fe augite ($Wo_{27}En_{28}Fs_{45}$) and subsequently to the Fe side of the quadrilateral ($Wo_{14}En_3Fs_{83}$). The minor element composition of the pyroxene is similar to 12011 in that in the phenocrysts it trends toward decreasing Cr and slightly decreasing Al/Ti with decreasing Fe/Mg+Fe. It differs slightly from 12011 in that the pigeonite and augite do not define parallel trends. The break in trend occurs with the outer rims around phenocrysts and with groundmass. Much of the groundmass pyroxene has $Al/Ti < 2$ indicating the prevalence of Ti^{3+} .

As in the other samples, Cr-spinel is a microphenocryst phase in this rock. It contains abundant inclusions of Fe-metal. These microphenocrysts have compositions that are approximately Chr_{59} with ulvö-spinel rims of Ulv_{82} (figures 4 and 7).

Groundmass plagioclase occurs as euhedral to subhedral, subequant laths and acicular grains. These grains average 0.6 to 0.8 mm in size (maximum 1.2 mm). Plagioclase composition ranges from about An_{78} to An_{88} (figure 4). Although both Fe and excess silica generally increase with increasing Na, no distinct trend exists.

Ilmenite occurs generally as acicular grains, less commonly as blocky to irregular grains, 0.3-0.5 mm in size (maximum 0.8 mm). Cristobalite occurs in irregular to elongate grains <0.5 mm in size, and comprises about 5 per cent of the groundmass. Troilite occurs as irregular to spherical grains, these latter 4 μm or less in size. Troilite typically contains spherical inclusions generally <2 μm of metallic Fe. Metallic Fe also occurs as separate grains throughout the groundmass. Ulvöspinel occurs as discrete, separate grains and also as myrmekitic intergrowths with ilmenite. Fayalite occurs in fine-grained intergrowths with cristobalite. Both high-K and high-Fe glass are present. High-K glass occurs as spherical inclusions in high-Fe glass, indicative of liquid immiscibility, but more commonly these glasses are present as separate blebs along grain boundaries of other phases. Phosphate is also present, typically associated with ilmenite and fayalite. Phosphate grains were too small to analyze, but by comparison with 12007, both apatite and whitlockite are probably present. Tranquillityite also occurs as fine-grained bladed crystals or acicular aggregates.

12007.

Rock 12007 is a relatively coarse-grained pigeonite basalt ("microgabbro"), the coarsest-grained of these three pigeonite basalts, and consists of about 15 per cent zoned phenocrysts of pyroxene in a coarse-grained (~ 1 mm) ophitic to (locally) variolitic groundmass of plagioclase, pyroxene, ilmenite and cristobalite, with minor ulvöspinel, troilite, metallic Fe, fayalite, tranquillityite, apatite, whitlockite, and

high-Fe and high-K glass. Vesicles occur interstitially to crystalline groundmass phases. Modal abundances, average phase compositions, and the calculated whole-rock analysis are presented in table 5. This rock contains 48 per cent pyroxene, 40 per cent plagioclase, and 7 per cent cristobalite. No olivine is present except for a trace amount of late-stage fayalite in the mesostasis.

Pyroxene phenocrysts range up to at least 3.2 mm in size. These are so large in comparison to our samples that we do not have whole phenocrysts and can only estimate their minimum abundance (approximately 15 per cent). As in 12043 they consist of three zones: irregular, colorless to very pale buff-colored, cores of pigeonite ($Wo_{11}En_{58}Fs_{31}$); intermediate, pale pinkish intermediate zones of augite ($Wo_{34}E_{43}Fs_{23}$) characterized by minute exsolution lamellae; and outer, very irregular rims of pink augite which, as in previous samples, merges compositionally and texturally with the groundmass pyroxene (figure 5).

Groundmass pyroxene consists of anhedral composite grains <1.5 mm interstitial to plagioclase laths. Crystallization trends of the pyroxene in this rock are more complex than in any of the others that we have studied. As shown in figure 5 several different trends are evident: (1) a high-Fe augite ($Wo_{14}En_{51}Fs_{35}-Wo_{21}En_{26}Fs_{53}$), similar to that of the other samples (except 12015); (2) a low-Ca augite trend ($Wo_{23}En_{38}Fs_{39}-Wo_{24}En_{22}Fs_{54}$); and (3) a high-Ca augite trend ($Wo_{32}En_{34}Fs_{34}-Wo_{30}En_{19}Es_{51}$). These trends all come together at about ($Wo_{28}En_{20}Fs_{52}$). Augite is zoned to pyroxferroite ($Wo_{14}En_3Fs_{83}$).

The minor element content of pyroxene (inset, figure 5) shows a similar trend as previous samples in that phenocrysts show strongly decreasing $Cr/Cr+Al+Ti$ and slightly decreasing Al/Ti with increasing $Fe/Mg+Fe$. A sharp decrease in Al/Ti appears to occur at different points for pigeonite and augite. The break in trend occurs at the point where high-Fe pigeonite begins to crystallize. As in previous samples Ti^{3+} is an important species in this groundmass pyroxene. In addition several grains have $Al/Ti < 1.0$, indicating the presence of components with Cr^{2+} , octahedral vacancies, or tetrahedral Ti.

Ilmenite occurs as acicular to irregular grains averaging about 1 mm in size. In addition ulvöspinel occurs as irregular grains < 0.5 mm.

Plagioclase generally occurs as subhedral tabular laths and anhedral interstitial grains 1.0-1.5 mm in size. It also occurs as anhedral, acicular grains, where intergrown with pyroxene in variolitic texture (rare). Its compositional range is An_{92-80} (figure 5). Excess silica generally increases with increasing Fe, but as in 12043 no well-defined trend exists.

Cristobalite, constituting about 10 per cent of the groundmass, occurs as irregular to acicular (rarely subhedral) grains generally < 0.8 mm in size. Troilite occurs as irregular to rounded grains < 0.25 mm in size, typically containing tiny ($< 2 \mu m$) spherical inclusions of metallic Fe. Metallic Fe is also present as separate grains in the groundmass. Ulvöspinel typically occurs as myrmekitic intergrowths with ilmenite, and as intergrowths with ilmenite and troilite surrounded by fayalite. In addition, fayalite also occurs in intergrowths with either

crystalite or high-K glass. High-K glass is present as spherical inclusions within high-Fe glass. However, both glasses more commonly occur separately along grain boundaries of crystalline phases. High-K glass is also associated in interstitial areas with fayalite, ilmenite, and apatite/whitlockite. Fayalite and cristobalite also occur in very fine-grained ($<1 \mu\text{m}$) intergrowths with Fe-rich pyroxene, indicating the subsolidus breakdown of pyroxferroite. Tranquillityite is present as fine-grained, acicular aggregates $\leq 1 \mu\text{m}$ in size.

Our whole-rock analysis of 12007 differs from that of Rhodes et al. (1977) primarily in having higher SiO_2 , Al_2O_3 , and CaO and lower MgO and FeO. This difference suggests that our sample is higher in modal plagioclase and lower in pyroxene than that of Rhodes et al. (1977). Such sample inhomogeneity is very plausible considering the large grain size of 12007.

12072.

Rock 12072 consists of approximately 6 per cent equant subhedral to anhedral phenocrysts of olivine ($<0.7 \text{ mm}$) and 5 per cent tabular to elongate phenocrysts of pyroxene ($\leq 1 \text{ mm}$) in a variolitic-textured groundmass of pyroxene, plagioclase, and ilmenite with minor amounts of spinel, troilite, cristobalite, Fe-metal, apatite/whitlockite, fayalite, and high-Fe and high-K glass. Irregular voids occur interstitially among the groundmass phases. Its average groundmass grain size is 0.3-0.6 mm.

Olivine phenocrysts are typically ragged and embayed, and partially or completely surrounded by irregular rims of pyroxene. These pheno-

crystals commonly contain irregular inclusions of groundmass material. Near their margins they include euhedral grains of Cr-spinel $<30 \mu\text{m}$ and rounded or ragged grains of metallic Fe $<15 \mu\text{m}$. These phenocrysts range in composition from Fo_{76} to Fo_{62} (figure 6).

Pyroxene phenocrysts consist of pinkish augite rims ($\text{Wo}_{37}\text{En}_3\text{Fs}_{24}$) grown about colorless to very pale buff-colored pigeonite cores ($\text{Wo}_{10}\text{En}_{56}\text{Fs}_{34}$) (figure 6). Pyroxene rims grade continuously into groundmass pyroxene with variolitic or (locally) subophitic texture. As shown in figure 6 these rims, together with the groundmass pyroxene, define a compositional trend extending from iron-rich pigeonite ($\text{Wo}_{13}\text{En}_{42}\text{Fs}_{45}$) to iron-rich augite ($\text{Wo}_{25}\text{En}_{18}\text{Fs}_{57}$), and then toward pyroxferroite. No distinct trend toward hedenbergite is present. Groundmass pyroxene consists of acicular, parallel to subparallel, composite laths averaging 0.4 to 0.6 mm in length intergrown with acicular plagioclase. Among the minor components of pyroxene a distinct trend toward decreasing Cr with increasing Fe/Mg+Fe is visible (inset, figure 6). The sharp decrease in Al/Ti correlates with the discontinuity in the major-component trend from augite to iron-rich pigeonite. The large number of points falling below the line from Al/Ti = 2 to Al/Cr = 1 indicates that Ti^{3+} is important in the groundmass pyroxene.

Cr-rich spinel forms equant, euhedral to subhedral microphenocrysts $<80 \mu\text{m}$. These microphenocrysts include and are intergrown with irregular grains of metallic Fe $<50 \mu\text{m}$. They are commonly surrounded by thin ($<20 \mu\text{m}$) rims of ulvöspinel except where armored within olivine or pyroxene. Spinel microphenocrysts range in composition from about

Chr₆₁ to Chr₆₅ (figures 6 and 7).

Plagioclase consists of anhedral, acicular grains averaging 0.4-0.6 mm in length (2.2 mm maximum) intergrown with pyroxene. Locally adjacent plagioclase grains are intergrown in optical continuity, giving rise to a "reverse ophitic" texture. Plagioclase is zoned from approximately An₈₅ to An₇₇. Excess silica [(Si₄O₈-component)] first increases sharply with decreasing Fe (increasing Na), then decreases gradually. This change in trend is probably associated with crystallization of cristobalite.

Cristobalite, constituting about 3 per cent of the rock, occurs as very irregular, anhedral grains generally <55 μm in size. Ilmenite (nearly pure FeTiO₃) occurs mainly as acicular grains <0.3 mm, but some occurs as more irregular, wedge-shaped, or blocky grains. Troilite forms rounded to irregular grains, typically with tiny (<2 μm) spherical inclusion of metallic Fe. However, Fe is also present as separate grains. Ulvöspinel typically occurs in myrmekitic intergrowths up to ~20 μm in size with ilmenite. Two glasses, a high-K and a high-Fe glass, are also present. The high-K glass may occur as rounded blebs in the high-Fe glass, but more typically the glasses occur separately along boundaries of crystalline phases. For example, high-K glass commonly occurs along the boundaries of plagioclase grains. Fayalite is present in intergrowths with cristobalite or high-K glass. Traces of phosphate are also present. None of the phosphate grains could be analyzed, but are assumed to consist of both apatite and whitlockite.

Phase abundances, average phase compositions, and the calculated bulk composition are given in table 6. No previous whole-rock analyses of 12072 exist. This rock is similar to pigeonite 12011 in its Mg-value (46.7) and is intermediate between 12011 and 12043 in MgO (8.57 weight per cent) and normative quartz (1.26; see table 7). Yet it is distinguished from these two basalts by its high modal plagioclase (34 weight per cent). It is distinguished from all of the pigeonite basalts by its very low modal ilmenite (1.70 weight per cent) and TiO_2 (1.81 weight per cent). Because 12072 contains high modal plagioclase relative to its Mg-value it is classified as feldspathic basalt.

COMPARATIVE PETROLOGY

Texture

These Apollo 12 basalts exhibit a variety of textures ranging from vitrophyric to micro-gabbroic. Olivine basalt 12015, a vitrophyre, was the most quickly cooled. It is characterized by olivine phenocrysts with skeletal overgrowths, by skeletal pyroxene microphenocrysts, and by skeletal, cruciform or dendritic ilmenite groundmass grains. Plagioclase occurs only as incipient crystals in the groundmass. This rock was approximately 35-55% crystallized (tables 1 and 2) when it was quenched. Slightly different textures in sections 15 and 16 indicate slightly different quenching rates within this single rock.

A continuous range in texture is present among the pigeonite basalts, formed in response to different cooling rates. The average grain size ranges from 0.4 to 1.3 mm in the following sequence: 12011 <12043 <12007.

Rock 12011 is characterized by variolitic to (rarely) subophitic texture, 12043 by subophitic to variolitic texture, and 12007 by ophitic ("micro-gabbroic") texture. Olivine phenocrysts occur in both 12011 and 12043. In 12011 these are skeletal in habit. Some are embayed and partially overgrown by pyroxene. In 12043, olivine phenocrysts are very irregular in outline, strongly embayed, and completely surrounded by overgrowths of pyroxene. Pyroxene of these overgrowths and also of the phenocrysts grades continuously into groundmass pyroxene. In 12011, plagioclase forms anhedral laths intergrown with pyroxene in variolitic texture. In 12043, which is slightly coarser-grained, plagioclase occurs in two distinct habits: as anhedral, elongate grains, intergrown with pyroxene in variolitic texture, and as euhedral to subhedral, equant laths. In the coarsest rock, 12007, plagioclase occurs dominantly as subhedral, tabular grains.

In all of these rocks ilmenite tends to be in smaller grains than the plagioclase or pyroxene. In 12011, which is the finest-grained, ilmenite occurs as acicular grains, oriented subparallel to each other and generally perpendicular to olivine and pyroxene grain boundaries. This habit strongly resembles the filamental ilmenite in vitrophyre 12015. In both 12043 and 12007, ilmenite generally occurs as elongate grains, occasionally as irregularly shaped to blocky grains. Hence among the pigeonite basalts a smooth increase in grain size and a progressive change in texture from variolitic to ophitic indicates a progressive decrease in cooling rate from 12011 through 12043 to 12007.

In the olivine and pigeonite basalts the crystallization sequence must have been the following: olivine was probably the first phase on the liquidus, followed closely by Cr-spinel. Pyroxene followed spinel closely, such that olivine, spinel, and pyroxene coprecipitated. After an interval of pyroxene crystallization, olivine began to react with the liquid to form pyroxene, and plagioclase and ilmenite began to crystallize. The sequence in which these phases precipitated is uncertain. Pyroxene, plagioclase, and ilmenite coprecipitated for the entire crystallization history of the melt, and were joined eventually by the mesostasis minerals.

Rock 12072 is similar to 12011 in its variolitic texture, but is slightly coarser-grained. Its average grain size is 0.6 mm. Olivine phenocrysts are irregular and embayed, and are partially surrounded by pyroxene overgrowths. Ilmenite grains are about the same length as in 12011, but are distinctly more equant in shape. Texturally 12072 is intermediate between 12011 and 12043. However, as will be discussed below, it can be distinguished mineralogically from the pigeonite basalts, hence does not belong to this textural series. Its crystallization history is similar to that of the olivine and pigeonite basalts.

Mineral crystallization trends

Pyroxene

Within this group of basalts, including both the olivine-pigeonite basalts and the feldspathic basalt, the pyroxene zoning trends become increasingly complex with increasing groundmass grain size (decreasing cooling rate). In the rapidly quenched olivine vitrophere 12015,

pyroxene relations are simplest, yet reflect what must be minor differences in cooling rate. Pigeonite cores, zoned slightly toward increasing Ca with increasing Fe/Mg+Fe, are overgrown by rims of augite with very little trend toward higher-Fe compositions. However in section 12015, 16 this trend is continuous from pigeonite to augite, whereas in 12015, 15 discrete rims of augite surround pigeonite with a well-defined compositional break between. We interpret this difference to indicate that 12015, 16 was quenched from a slightly higher temperature than 12015, 15. Textural differences between these two sections, such as the greater abundance of quenched olivine and the virtual absence of pyroxene microphenocrysts and groundmass "filamental" ilmenite, support this interpretation. The high Al-content (<9 weight per cent Al_2O_3) probably results from the extreme supersaturation in the components of plagioclase due to the extremely rapid quenching which 12015 has undergone. Pigeonite cores, zoned slightly toward increasing Ca with increasing Fe/Mg+Fe, are overgrown either continuously (12015, 16) or discontinuously (12015, 15) by rims of augite. Very little trend toward high-Fe augite exists. The minor element content of pyroxene shows a simple trend toward strongly decreasing Cr and slightly decreasing Al/Ti with increasing degree of crystallization (increasing Fe/Mg+Fe).

In rocks with intermediate cooling rates whose groundmass is characterized dominantly or partially by variolitic texture (12072, 12011, and 12043), the initial pyroxene trend is similar to 12015 in that phenocrysts have cores of pigeonite, zoned slightly toward higher

Ca with higher Fe/Mg+Fe, surrounded by rims of augite. However Al_2O_3 is much lower, closer to more typical values (3-5 per cent). However, following crystallization of the phenocrysts, pigeonite again crystallized. This pigeonite occurs as a groundmass phase and sometimes also as discrete (irregular) rims surrounding phenocrysts. The composition of this second pigeonite does not lie on a continuous trend with the higher-Mg pigeonite of phenocryst cores--rather a discrete compositional gap separates these two generations of pigeonite.

This break in crystallization trend from augite to pigeonite with crystallization of the groundmass probably reflects the sudden and rapid crystallization of plagioclase. The sudden appearance of plagioclase from a melt supersaturated with the components of plagioclase would deplete the melt in Ca and drive its composition back into the pigeonite field.

With continued crystallization pigeonite becomes more calcic, eventually coexisting with Fe-rich augite. The pigeonite trend appears to converge smoothly with augite at a termination of the two-pyroxene field. Further crystallization proceeds from high-Ca augite in a well-defined trend mainly to pyroxferroite, but also with the suggestion of a trend toward hedenbergite.

Minor-element crystallization trends for the phenocrysts of these three rocks are similar to 12015. However Al/Ti drops sharply (becoming <2) as pyroxene becomes a groundmass phase, correlating with the incoming of plagioclase. $\text{Al/Ti} < 2$ suggests that Ti is present in pyroxene as Ti^{3+} .

Pyroxene crystallization trends in 12007, which is characterized by ophitic textures and the coarsest grain size of any of this suite, are more complex than any other basalt of this suite. As in previous samples, phenocrysts consist of pigeonite cores overgrown by augite rims; in addition a second generation of more Fe-rich pigeonite zoned (continuously?) to Fe-rich augite is present. However in contrast to previous samples, two parallel augite trends, a high-Ca trend and a low-Ca trend, exist. Also, both trends begin at much higher Mg/Fe values than previous samples. The low-Ca augite trend merges with the pigeonite trend at the end of a two-pyroxene field. All three trends apparently merge with continued crystallization. Further crystallization leads toward pyroxferroite.

Minor element compositional trends are similar to those in finer-grained samples. Al/Ti for pyroxene with $(\text{Fe}, \text{Mn})_2\text{Si}_2\text{O}_6$ -component >50 per cent, while generally <2, show no systematic trends. A few of these analyses have Al/Ti <1, suggesting the presence of components with Cr^{2+} , octahedral vacancies, or tetrahedral Ti.

Plagioclase

In olivine vitrophyre 12015, plagioclase is present only as incipient, sub-micron-sized crystals in the glassy matrix. In the pigeonite basalts, the anorthite-content of the most calcic plagioclase increases slightly as the rock becomes coarser-grained, from An_{87} to An_{91} to An_{93} in 12011, 12043, and 12007, respectively (figures 3-5). This change in composition, which is contrary to what might be expected in a series of progressively more evolved rocks, probably results from the effect on

Ca of prior crystallization of pyroxene. Based on texture, most or all of the augite crystallized before plagioclase. Hence the amount of modal augite in tables 3-5 indicates the effect of augite crystallization on the melt prior to precipitation of plagioclase. Rock 12011 crystallized the greatest amount of augite (13.60 vol. %), and 12007 the least (7.15%). Therefore 12011 was the most depleted in Ca prior to plagioclase crystallization and 12007 the least. The composition of the first-crystallizing plagioclase reflects this relative Ca-depletion in that plagioclase is the most sodic in 12011 and least sodic in 12007. The amount of augite that crystallizes before plagioclase may reflect the amount of undercooling necessary before plagioclase becomes stable. For example, Walker et al. (1976a) have shown that the beginning of plagioclase crystallization occurs at progressively lower temperatures (i.e., more undercooled) as the cooling rate is increased. This undercooling would allow a greater interval for augite to precipitate before plagioclase.

A slight difference in the minor components of plagioclase is evident between the finer- and coarser-grained pigeonite basalts. Although not well-defined, a sharp increase in excess silica component (Si_4O_8) occurs in 12011 with early plagioclase crystallization, then decreases as crystallization continues (figure 3). In the coarser-grained pigeonite basalts, excess silica (and iron) generally increases with plagioclase crystallization. No specific decrease in excess silica is observed (figures 5 and 6).

In plagioclase basalt 12072, which is similar in grain size and texture to 12011, the most calcic plagioclase is An_{89} . Excess silica component shows a sharp increase, followed by a more gradual decrease with increasing crystallization. The reason for this fairly well-defined trend in the finer-grained Apollo 12 basalts is not known.

Olivine

In the olivine and pigeonite basalts, the compositions of the most magnesian olivine (generally cores of largest grains) become increasingly iron-rich as the grain size increases. The most magnesian olivine in 12015, 12011, and 12043 is respectively Fo_{76} , Fo_{73} , and Fo_{70} (figures 1 - 4). These compositions yield $(Fe/M+Fe)_{\text{olivine}} / (Fe/Mg+Fe)_{\text{whole rock}} = 0.28-0.33$, which are in good agreement with experimentally-determined equilibrium values of 0.30-0.33. (Longhi, 1977) (figure 8).

Rock 12072 does not fit on this trend. The most magnesian olivine of 12072 is Fo_{76} , which is the same as olivine in vitrophyre 12015. This composition yields $(Fe/Mg+Fe)_{\text{olivine}} / (Fe/Mg+Fe)_{\text{whole rock}} = 0.27$.

Spinel and ilmenite

Similarly, the compositions of the most magnesian Cr-spinel microphenocrysts (including Cr-spinel inclusions in olivine and pyroxene) become generally more Fe-rich in this same sequence: 12015 ($Fe+Mn/Mg+Fe+Mn = 0.60$), 12011 ($=.64$), 12043 ($=.72$), and 12007 (ulvöspinel; $Fe+Mn/Mg+Fe+Mn = .99$). In 12072, the most magnesian spinel has $(Fe+Mn/Mg+Fe+Mn) = 0.68$. Ilmenite, which apparently equilibrates readily with the late-stage liquid, has $Fe+Mn/Mg+Fe+Mn > 0.98$ in all rocks (figures 1-5).

Modal sequence

Among the olivine and pigeonite basalts a regular variation in modal mineralogy correlates with the increase in grain size from 12015 to 12007. For example, the amount of modal olivine decreases and the amount of modal cristobalite increases in this sequence (tables 1-6). Olivine constitutes about 15 volume per cent of 12015 (20 per cent of 12015, 16; 10 per cent of 12015, 15), 8 per cent of 12011, and 1 per cent of 12043. It is absent from 12007. Cristobalite is present in trace amounts in the groundmass of 12015, and constitutes 3, 4, and 7 per cent respectively of 12011, 12043, and 12007. The pyroxenes also show a systematic change in their composition in this sequence. Rock 12011 contains the greatest amount of augite (14 per cent) and medium-Fe pyroxene (25 per cent), whereas 12007 contains the least amount of augite (7 per cent), an intermediate amount of medium-Fe pyroxene (21 per cent), and the greatest amount of high-Fe pyroxene (13 per cent). Rock 12072 is clearly distinguished from these olivine and pigeonite basalts by its greater modal plagioclase and lower modal ilmenite (table 6). It otherwise contains intermediate amounts of olivine (6 per cent) and cristobalite (3 per cent) and is intermediate in its pyroxene composition.

GENETIC RELATIONSHIPS

Olivine and pigeonite basalts

The dominant petrographic feature of these olivine and pigeonite basalts is the correlation of more evolved modal and mineral compositions with increased grain size. All of the olivine and pigeonite basalts

are characterized by porphyritic texture, i.e., by phenocrysts of olivine and/or pyroxene, and by microphenocrysts of Cr-spinel. Separation of these phenocrysts from their melt under conditions of decreasing cooling rate constitutes a simple and plausible mechanism for relating these rocks to each other. Several previous investigators have noted the chemical variation among basalts of the olivine and pigeonite groups and suggested that this variation was due to removal of early-crystallizing phases (summarized in Rhodes et al., 1977).

Papike et al. (1976) and Rhodes et al. (1977) noted that a hiatus in $Mg/Mg+Fe$ exists among the olivine-pigeonite basalts. Rocks with $Mg/Mg+Fe > 0.54$ (1) become richer in normative olivine with increasing grain size and (2) contain olivine phenocrysts that are too Fe-rich to be in equilibrium with their host rocks. These rocks are interpreted as olivine cumulates formed at the base of a single differentiating lava flow (Walker et al., 1976b). Olivine basalts with $Mg/Mg+Fe < 0.52$ (including vitropheres 12009 and 12015) are rapidly-cooled basalts and probably have compositions close to liquid compositions. Pigeonite basalts have $Mg/Mg+Fe < 0.43$ and become richer in normative quartz as grain size increases. These rocks are interpreted as representing the upper part of a differentiating lava flow from which phenocrysts of olivine and pigeonite and microphenocrysts of Cr-spinel are being removed (Walker et al., 1976b; Rhodes et al., 1977).

Rock 12015 is texturally and compositionally similar to 12009, which has been experimentally investigated and found to be a likely parent rock for these suites (Green et al., 1971; Donaldson et al., 1975). The parental nature of 12015 is supported by the fact that the most

magnesian olivine phenocrysts in 12015 (Fo_{76}) are approximately in equilibrium with a melt equivalent in bulk composition to 12015 (figure 8). Hence in the following discussion we adopt 12015 as the parent to the olivine-pigeonite basalts.

Figure 9 shows the variation of SiO_2 , FeO , Cr_2O_3 , Al_2O_3 , CaO , and TiO_2 with MgO among the rocks we have studied. Compositions shown by solid symbols are new analyses presented in this paper. Those shown by open symbols are the data of Rhodes et al. (1977) for comparison. Our analyses of 12011 and 12043 agree well with those of Rhodes et al. (1977). Our analysis of 12015, while in agreement with that of Rhodes et al. (1977) within analytical error, is higher in SiO_2 , Al_2O_3 , and CaO and lower in MgO and FeO . This difference suggests that our sample may include more groundmass and fewer olivine phenocrysts than the sample of Rhodes et al. (1977). The difference between our analysis of 12007 and that of Rhodes et al. (1977) (figure 9 and table 7) probably results from the coarse grain size of this rock. The composition of 12072 lies significantly off these trends and is discussed in the next section.

This figure also shows the effect of subtracting phenocryst phases. Magnesian olivine (Fo_{76}) and Cr-spinel are the earliest-crystallizing phases in the olivine basalts. The removal of olivine (Fo_{76}) and Cr-spinel in the appropriate amount from a melt with the composition of 12015 will deplete the magma in FeO , Cr_2O_3 , MgO , and $\text{MgO}/\text{MgO}+\text{FeO}$, and enrich the magma in SiO_2 , Al_2O_3 , CaO , and TiO_2 , and can therefore satisfactorily account for the derivation of pigeonite basalts 12011 and 12043 from 12015. Pigeonite basalt 12007 can be derived from 12043 by removal of pigeonite, olivine, and Cr-spinel.

Least-squares calculations (Reid et al., 1973) using the compositions of the most Mg-rich olivine, pigeonite, and Cr-spinel phenocrysts and microphenocrysts observed in 12015 give similar results to those of figure 9. These calculations indicate that pigeonite basalt 12011 can be derived from olivine vitrophere 12015 by removal of about 12% olivine (Fo_{76}) and 0.3% Cr-spinel (Chr_{66} ; $\text{Fe}+\text{Mn}/\text{Mg}+\text{Fe}+\text{Mn} = 0.61$). Similarly 12043, which is a medium-grained pigeonite basalt more Fe-rich than 12011, can be derived from 12015 by removal of approximately 13.5% olivine and 0.5% Cr-spinel. However, to derive rock 12007, which is the most Fe-rich of the rocks we have studied, from 12015 requires that about 5% pigeonite ($\text{Wo}_9\text{En}_{63}\text{Fs}_{28}$) be removed in addition to 16% olivine and 0.8% Cr-spinel. These results are essentially identical to those of Rhodes et al. (1977) who used average phase composition for the Apollo 12 olivine basalts. They also found that pigeonite became a major fractionating phase after removal of about 20% crystalline material from 12015.

Hence our data on phase compositions, modal and textural sequences, and bulk compositions lead us to conclude, in concurrence with Rhodes et al. (1977), that the olivine and pigeonite basalts are comagmatic. The finest-grained pigeonite basalt 12011 can be derived from olivine vitrophyre 12015 by removal of magnesian olivine and Cr-spinel. We also conclude that the range of compositions within the pigeonite basalts results from removal of pigeonite, olivine, and Cr-spinel. The increase in grain size from 12015 to 12007 is a result of decreasing cooling rate (Walker et al., 1976a). Morphologies of olivine and pyroxene grains in 12015 suggest that this vitrophyre may have cooled at the rate of

about 500°C/hr, although differences in cooling rate existed within 12015. Rock 12007 probably cooled at a rate of substantially less than 1°C/hr (Walker et al., 1976a).

Based on a discontinuity in textural sequence from coarse-grained olivine basalts to fine-grained pigeonite basalts and on a pronounced gap in Mg/Mg+Fe Rhodes et al. (1977) suggest that the basalts represent two cooling units. Our data do not allow us to comment on this possibility. Instead all chemical and mineralogical evidence which we have examined is compatible with derivation of the olivine and pigeonite basalts by fractional crystallization within a single flow.

Feldspathic basalt 12072

Figure 9 shows that the bulk composition of rock 12072 lies significantly off the trends for the olivine and pigeonite basalts. Rock 12072 has higher SiO_2 and Al_2O_3 and lower FeO and TiO_2 . This difference is due to the higher modal plagioclase (approximately 39 per cent) and lower modal ilmenite (one per cent) of 12072 in relation to its Mg-value (46.7). Figure 9 also shows that 12072 cannot be related to the olivine and pigeonite basalts by fractionation of Cr-spinel, olivine, or pigeonite--the phases occurring as phenocrysts--or by any combination of these phases. Since 12072 cannot be related to these basalts by any simple fractionation process and since it is higher in modal and normative plagioclase (table 7 and figure 9), 12072 is classified as feldspathic basalt.

Rock 12072 is the third Apollo 12 basalt to be classified as feldspathic basalt. Previously, two other rocks, 12038 and 12031, had been

recognized as constituting a group with distinctly higher normative plagioclase than either the olivine-pigeonite basalts or the ilmenite basalts (e.g., Rhodes et al., 1977). Although these three basalts are all classified together, they are not similar in composition. Further, the new data presented in this paper, in combination with the previous data for 12031 and 12038 (e.g., Rhodes et al., 1977, figures 3-5), show that they cannot be related to each other by simple fractionation of any of the phases present as phenocrysts. For example, 12072 has the highest MgO of these feldspathic basalts and contains very magnesian olivine (Fo_{76} ; see figure 8). Yet its very low TiO_2 (1.81 weight per cent) precludes derivation of 12031 and 12038 from 12072 by fractionation of either olivine, pigeonite, or Cr-spinel. Hence at the present time the feldspathic basalts appear to represent a diverse group of basalts that do not fit into either the olivine-pigeonite or the ilmenite basalt groups. Further detailed study of 12031 and 12038 may help clarify their origin and relationship to other basalt types.

ACKNOWLEDGMENTS

This study has been supported by NASA grant NGL-05-002-338. Discussions with D. Beaty have been of continuing assistance to us in our work on these samples. We thank D. Beaty and J. Quick for critical reviews of this manuscript.

REFERENCES

- Albee, A. L., Beaty, D. W., Chodos, A. A., and Quick, J. E., in press. Quantitative analysis of petrographic properties and of mineral compositions with a computer-controlled energy-dispersive system. Subm. Proc. Nat'l. Conf. on Electron Probe Analysis, 12th.
- Champion, D. E., Albee, A. L., and Chodos, A. A., 1975. Reproducibility and operator bias in a computer-controlled system for quantitative electron microprobe analysis. Proc. 10th Ann. Microbeam Anal. Soc. Conf.: 55A-55F.
- Donaldson, C. H., Usselman, T. M., Williams, R. J., and Lofgren, C. E., 1975. Experimental modeling of the cooling history of Apollo 12 olivine basalts. Proc. Lunar Sci. Conf., 6th: 843-869.
- Dungan, M. A. and Brown, R. W., 1977. The petrology of the Apollo 12 ilmenite basalt suite. Proc. Lunar Sci. Conf., 8th: 1339-1381.
- Green, D. H., Ware, N. G., Hibberson, W. O., and Major, A. (1971). Experimental petrology of Apollo 12 basalts, 1, Sample 12009. Earth Planet. Sci. Lett., 13: 85-96.
- James, O. B., and Wright, T. L., 1972. Apollo 11 and 12 mare basalts and gabbros: Classification, compositional variations, and possible petrogenetic relations. Geol. Soc. Am. Bull. 83: 2357-2382.
- Longhi, J., 1977. Magma oceanography 2: Chemical evolution and crustal formation. Proc. Lunar Sci. Conf., 8th: 601-621.
- Papike, J. J., Hodges, F. N., Bence, A. E., Cameron, M., and Rhodes, J. M., 1976. Mare basalts: Crystal chemistry, mineralogy, and petrology. Rev. Geophys. Space Phys., 14: 475-540.
- Reid, M. J., Gancarz, A. J., and Albee, A. L., 1973. Constrained least-squares analysis of petrologic problems with an application to lunar sample 12040. Earth Planet. Sci. Lett. 17: 433-445.
- Rhodes, J. M., Blanchard, D. P., Dungan, M. A., Brannon, J. C., and Rodgers, K. V., 1977. Chemistry of Apollo 12 mare basalts: Magma types and fractionation processes. Proc. Lunar Sci. Conf., 8th: 1305-1338.
- Walker, D., Kirkpatrick, R. J., Longhi, J., and Hays, J. F., 1976a. Crystallization history of lunar picrite basalt sample 1002: Phase-equilibria and cooling rate studies. Geol. Soc. Amer. Bull., 87: 646-656.

Walker, D., Longhi, J., Kirkpatrick, R. J., and Hays, J. F., 1976b.
Differentiation of an Apollo 12 picrite magma. Proc. Lunar Sci.
Conf., 7th: 1365-1389.

Warner, J., 1970. Apollo 12 lunar-sample information. NASA Technical
Report R-353.

TABLES

- Table 1. Mode, "average" phase compositions, and bulk chemical composition of vitrophyre 12015, 15.
- Table 2. Mode, "average" phase compositions, and bulk chemical composition of vitrophyre 12015, 16.
- Table 3. Mode, "average" phase compositions, and bulk chemical composition of basalt 12011.
- Table 4. Mode, "average" phase compositions, and bulk chemical composition of basalt 12043.
- Table 5. Mode, "average" phase compositions, and bulk chemical composition of basalt 12007.
- Table 6. Mode, "average" phase compositions, and bulk chemical composition of basalt 12072.
- Table 7. Summary of whole-rock chemical and normative compositions.

TABLE 1.

12015,15: PHASE ABUNDANCES, AVERAGE "PHASE" COMPOSITIONS, AND BULK COMPOSITION

(2336 pts)	Pyroxene				Olivine	Troilite ¹	Cr-spinel	Fe-metal ¹	Meso	Bulk Comp.	σ (SDM)
	LoCaPx	Augite	HiAlPx	MedFePx							
Vol %	10.56	13.96	12.24	6.29	10.30	0.03	0.32	0.03	46.27		
σ (SDM)	0.74	0.85	0.79	0.57	1.71	0.04	0.12	0.04	1.64		
ρ	3.47	3.38	3.50	3.51	3.53	4.60	4.68	8.00	3.12		
Wt. %	11.06	14.24	12.93	6.66	10.97	0.04	0.45	0.07	43.57		
σ (SDM)	0.78	0.87	0.83	0.60	1.82	0.05	0.17	0.09	1.54		
P ₂ O ₅									0.13	0.06	0.02
SiO ₂	51.23	47.44	44.26	46.20	38.34		0.10		49.78	47.12	2.13
TiO ₂	1.02	2.84	3.87	2.99	0.05		4.72		4.26	3.10	0.25
Al ₂ O ₃	2.73	6.93	9.00	6.22	0.00		12.58		15.27	9.58	1.04
Cr ₂ O ₃	1.32	1.85	0.20	0.54	0.39		47.06		0.05	0.75	0.08
MgO	21.64	13.24	8.29	10.93	36.93		6.57		1.98	11.02	1.10
CaO	5.96	13.74	14.21	12.04	0.31				11.06	10.11	0.75
FeO	16.48	14.33	19.98	20.61	26.68	63.53	28.04	100.00	16.55	18.18	1.30
MnO	0.25	0.35	0.40	0.36	0.27		0.22		0.20	0.27	0.02
Na ₂ O	0.04	0.05	0.07	0.04					0.46	0.22	0.06
K ₂ O									0.11	0.05	0.02
BaO									0.05	0.02	0.03
ZrO ₂							0.06		0.00	<0.01	
V ₂ O ₃							1.13			0.01	0.01
Nb ₂ O ₅							0.01			<0.01	
NiO					0.13				0.03	0.03	0.02
Zn							0.06			<0.01	
S						36.47			0.19	0.10	0.06
Total	100.67*	100.77*	100.28*	99.93*	102.97	100.00	100.55**	100.00	100.12 [†]	100.62	
	Wo 7.8	Wo 19.2	Wo 19.7	Wo 17.9	Fo 70.9		Ulv 12.0		Qtz 12.8		
	En 58.8	En 38.2	En 24.6	En 32.1	Fa 29.1		Chr 62.9		Fld 47.1		
	Ps 25.5	Ps 23.8	Ps 34.0	Ps 34.6			Her 25.1		Pyx 33.2		
	Other 7.9	CaTiPx 8.3	CaTiPx 11.6	CaTiPx 8.9					Ilm 6.3		
		Other 10.5	Other 10.1	Other 6.5					Other 0.4		

* Average of three analyses.
 ** Average of ten analyses.

[†] Average of seven defocused beam analyses.
¹ Theoretical elemental abundances; converted to oxides for bulk calculation.

TABLE 2. 12015,16: PHASE ABUNDANCES, AVERAGE "PHASE" COMPOSITIONS, AND BULK COMPOSITION

(1694 pts)	Pyroxene							Meso	12015,16 area=20.0 mm ² p calc=3.30				Rhodes et al. (1977)
	LoCaPx	Augite	HiAlPx	MedFePx	Olivine	Cr-spinel	Bulk Comp.		σ (SDM)	Bulk Comp. 12015†	σ (SDM)		
Vol. %	1.42	1.59	5.58	5.05	20.42	0.24	65.70						
σ (SDM)	0.31	0.33	0.62	0.59	1.95	0.12	2.70						
ρ	3.49	3.38	3.50	3.51	3.53	4.68	3.20						
Wt. %	1.50	1.62	5.90	5.36	21.77	0.34	63.51						
σ (SDM)	0.33	0.34	0.66	0.63	2.08	0.17	2.61						
P ₂ O ₅							0.08	0.05	0.02	0.06	0.02	0.06	
SiO ₂	48.70	46.38	45.76	47.39	37.42	0.14	50.33	46.83	2.95	47.00	2.47	44.98	
TiO ₂	1.50	2.98	3.15	2.38	0.05	4.33	3.50	2.63	0.52	2.90	0.36	2.86	
Al ₂ O ₃	2.92	6.49	7.85	4.50	0.00	12.63	12.46	8.81	1.50	9.26	1.23	8.57	
Cr ₂ O ₃	0.80	1.51	0.52	0.45	0.44	48.35	0.36	0.58	0.12	0.68	0.10	0.68	
MgO	17.11	12.05	10.66	11.82	37.04	7.81	3.48	12.01	1.24	11.44	1.16	11.88	
CaO	6.19	14.22	12.65	9.61	0.35		13.48	9.90	1.20	10.02	0.94	9.21	
FeO	23.40	14.97	19.96	23.48	27.18	27.11	14.87	18.23	2.16	18.20	1.66	20.18	
MnO	0.33	0.29	0.40	0.38	0.32	0.24	0.23	0.27	0.04	0.27	0.03	0.29	
Na ₂ O	0.05	0.02	0.05	0.02			0.33	0.21	0.05	0.22	0.06	0.23	
K ₂ O							0.08	0.05	0.03	0.05	0.02	0.06	
BaO							0.03	0.02	0.02	0.02	0.03		
ZrO ₂						0.02		<0.01		<0.01			
V ₂ O ₃						0.98		<0.01		0.01	0.01		
Nb ₂ O ₅						0.01		<0.01		<0.01			
NiO					0.04		0.02	0.02	0.02	0.03	0.02		
S							0.14	0.09	0.05	0.10	0.06	0.07	
Total	101.00*	98.91*	101.00*	100.03*	102.84	101.62**	98.99†	99.70		100.26		99.07	
Wo 8.6	Wo 21.5	Wo 17.0	Wo 14.7	Fo 70.6	Ulv 10.9	Qtz 11.5							
En 47.1	En 35.6	En 30.9	En 34.7	Fa 29.4	Chr 64.1	Fld 38.2							
Fs 36.6	Fs 25.3	Fs 33.1	Fs 39.3	Her 25.0	Pyx 44.6								
Other 7.7	CaTiPx 8.9	CaTiPx 9.2	CaTiPx 7.1			Ilm 5.2							
	Other 8.7	Other 9.8	Other 4.2			Other 0.5							

*Average of three analyses.

**Average of 17 analyses.

†Average of six defocussed beam analyses.

‡Weighted average of 12015,15 and 12015,16.

TABLE 3.

12011: PHASE ABUNDANCES, AVERAGE "PHASE" COMPOSITIONS, AND BULK COMPOSITION

(2141 pts)	Plag	Pyroxene						Olivine	"SiO ₂ "	Ilmenite	Troilite ¹	Phosphate ²	Cr-spinel	Ulvöspinel ⁴	Fe-metal ¹	Fayalite	Meso ³	Bulk Comp.	σ (SDM)	Rhodes et al. (1977)
		LoCaPx	Augite	MedFePx	HiFePx	Ferrohed														
Vol %	30.63	7.82	13.60	24.68	6.66	0.16	7.64	3.37	2.89	0.53	0.07	0.47	0.12	0.08	0.08	1.20				
σ (SDM)	1.05	0.54	0.71	0.95	0.50	0.08	0.60	0.40	0.37	0.16	0.06	0.15	0.08	0.06	0.06	0.24				
σ	2.74	1.49	1.39	3.51	1.72	1.57	1.56	2.33	4.72	4.60	3.20	4.68	4.78	8.00	4.38	2.61				
wt. %	25.62	8.33	14.07	26.45	7.57	0.17	8.30	2.40	4.16	0.74	0.07	0.67	0.17	0.20	0.11	0.96				
σ (SDM)	0.88	0.58	0.73	1.02	0.57	0.09	0.65	0.28	0.53	0.22	0.06	0.21	0.11	0.15	0.08	0.19				
P ₂ O ₅											43.15					0.12	0.03	0.03	0.07	
SiO ₂	49.31	49.04	48.59	49.97	46.81	48.02	37.54	100.01	0.04			0.09			31.72	66.56	46.59	0.96	46.63	
TiO ₂	0.09	1.38	1.83	1.70	1.24	1.40	0.04	0.22	52.88			5.29	35.73		0.20	0.21	3.25	0.29	3.29	
Al ₂ O ₃	31.31	2.90	4.28	2.65	1.97	1.80	0.00	0.88	0.06			13.11			0.08	19.58	10.02	0.32	9.77	
Cr ₂ O ₃		0.84	1.16	0.40	0.15	0.16	0.30		0.25			44.21			0.35	0.00	0.68	0.10	0.59	
MgO	0.33	17.75	14.58	11.08	3.19	3.60	33.17	0.00	0.08			5.78			0.71	0.19	9.59	0.31	8.26	
CaO	17.08	6.92	14.37	10.07	9.48	14.83	0.31	0.23			54.54				0.68	10.03	10.55	0.27	10.63	
FeO	1.00	20.50	14.77	25.64	37.97	32.22	30.95	0.36	46.00	63.53		30.53	64.27	100.00	68.20	1.18	19.31	0.55	19.53	
MnO		0.37	0.24	0.49	0.51	0.41	0.37		0.40			0.22			0.60	0.13	0.28	0.02	0.29	
Na ₂ O	1.16	0.09	0.01	0.04	0.01	0.04		0.03								0.72	0.33	0.03	0.25	
K ₂ O	0.04							0.09								1.09	0.02	0.02	0.06	
BaO	0.06							0.00								0.14	0.02	0.02		
ZrO ₂									0.04			0.00				0.00	<0.01			
V ₂ O ₅									0.00			0.97					0.01	0.01		
Nb ₂ O ₅									0.00			0.00					0.00			
HfO							0.04										0.07	0.00	<0.01	
S										36.47							0.27	0.08	0.06	
F											2.31						<0.01			
Total	100.51*	99.79**	99.83**	102.04**	101.33**	102.48**	102.72*	101.82	99.75	100.00	100.00	100.20**	100.00	100.00	102.61*	99.95	100.95		99.42	
Am	78.3	Mo 10.2	Mo 23.6	Mo 17.9	Mo 18.5	Mo 29.6	Fo 65.4		Gl 0.03			Ulv 13.7			Fo 98.2					
Ab	10.3	En 49.3	En 41.2	En 32.4	En 9.8	En 10.7	Fa 34.6		Ilm 99.7			Chr 60.2			Fa 1.8					
Cr	0.2	Fs 32.6	Fs 23.8	Fs 42.9	Fs 66.6	Fs 54.6						Her 26.1								
Other	11.2	Other 7.9	Other 11.4	Other 6.8	Other 5.1	Other 5.1														

*Average of two analyses.
**Average of three analyses.

¹Theoretical elemental abundances; converted to oxides for bulk calculation.
²Assumed 1:1 mixture of fluorapatite and whitlockite.
³Composition constructed from weighted average (20:57:23) of K-glass, plagioclase and "SiO₂".
⁴Theoretical end-member oxide abundances.

12011.7 area = 43 nm²
σ calc = 3.28

TABLE 4.

12043: PHASE ABUNDANCES, AVERAGE "PHASE" COMPOSITIONS, AND BULK COMPOSITION

(367) pts) <u>Phase</u>	Pyroxene										Olivine	"SiO ₂ "	Ilmenite	Trolite ¹	Phosphate ²	Cr-spinel	OlivSpinel	Fe-metal ¹	Fayalite	Meso ³	K-Glass	Fe-Glass
	LcZaPx	Augite	MedFePx	HiFePx	Ferrohed																	
Vol %	32.87	13.86	9.85	21.83	11.72	0.44	0.95	3.70	3.45	0.22	0.14	0.15	0.12	0.04	0.07	0.52	0.05	<0.05				
wt % (SDM)	0.99	0.51	0.43	0.65	0.47	0.09	0.16	0.33	0.30	0.08	0.06	0.06	0.06	0.03	0.04	0.12	0.04					
wt %	2.74	2.88	3.39	3.52	3.73	3.57	3.56	2.33	4.72	4.60	3.20	4.68	4.76	8.00	4.38	2.59	2.85					
wt % (SDM)	0.83	0.54	0.45	0.70	0.54	0.10	0.17	0.22	0.43	0.11	0.06	0.08	0.09	0.08	0.05	0.09	0.03					
Fe ₂ O ₃												43.15				0.01	0.09	0.18				
SiO ₂	47.14	51.33	49.37	49.59	47.25	48.13	36.99	98.15	0.03			0.05	0.07		30.07	67.71	74.97	44.47				
TiO ₂	0.03	0.91	1.71	1.14	0.95	1.32	0.05	0.42	52.37			5.98	31.61		0.10	0.27	0.67	6.11				
Al ₂ O ₃	32.22	1.93	3.89	1.88	1.04	1.51	0.00	0.52	0.06			13.37	2.40		0.03	19.38	10.82	4.41				
Cr ₂ O ₃		0.81	1.23	0.40	0.05	0.11	0.33		0.38			45.32	5.81		0.00	0.02	0.16	0.17				
MgO	0.21	19.32	14.49	11.38	3.31	4.75	33.10	0.00	0.29			6.48	1.50		0.00	0.11	0.00	3.52				
CaO	17.99	5.24	15.39	10.55	8.83	14.23	0.30	0.17			54.54				0.41	9.83	1.61	10.00				
P ₂ O ₅	1.19	20.88	14.24	28.12	38.67	31.42	30.65	0.39	46.94	63.53		29.65	59.32	100.00	68.56	1.33	3.83	29.79				
MnO		0.33	0.27	0.38	0.49	0.44	0.24		0.28			0.30	0.36		0.23	0.02	0.15	0.13				
Na ₂ O	0.94	0.00	0.02	0.03	0.01	0.00		0.02								0.51	0.01	0.06				
K ₂ O	0.05							0.02								0.97	6.56	0.02				
BaO	0.00							0.01								0.37	2.47	0.00				
BaCO ₃									0.06			0.02	0.06			0.08	0.52	0.00				
V ₂ O ₅									0.00			1.12	0.12									
W ₂ O ₃									0.06			0.00	0.00									
BiO							0.00									0.00	0.00	0.02	0.00			
S									36.47								0.06	0.40	0.34			
P											2.31											
Total	100.77*	100.75**	100.61**	101.47**	100.60**	101.91**	101.66	99.70*	100.49	100.00	100.00	102.29	101.25	100.00	99.40	100.67	102.28	99.20				
As	83.9	Wo	7.8	Wo	25.9	Wo	19.4	Wo	18.4	Wo	28.5	Fe	65.6	Cl	0.8	Ulv	14.9	Ulv	85.4	Data		
Mb	8.4	En	53.7	En	40.7	En	32.8	En	10.3	En	14.1	Fe	34.4	Ilm	99.2	Chr	59.2	Chr	8.04	from		
Cr	0.3	Ps	33.1	Ps	22.9	Ps	42.8	Ps	68.1	Ps	53.1					Mer	25.9	Mer	6.0	12007		
Other	7.4	Other	5.4	Other	10.5	Other	5.0	Other	3.2	Other	4.3											

* Average of two analyses.
 ** Average of three analyses.

¹Theoretical elemental abundances; converted to oxides for bulk calculation.
²Assumed 1:1 mixture of fluorapatite and whitlockite.
³Composition constructed from weighted average (15:53:32) of K-glass, plagioclase, and "SiO₂".

12041.6 area = 18 μm ²		
12043.8 area = 59.5 μm ²		
ρ calc = 3.27		
Bulk Comp.	ρ (SDM)	Rhodes et al. (1977)
0.06	0.03	0.06
47.11	0.81	46.77
3.39	0.24	3.38
10.56	0.32	10.09
0.47	0.04	0.50
7.90	0.23	7.68
11.15	0.24	10.96
19.52	0.35	19.50
0.25	0.02	0.29
0.27	0.03	0.27
0.02	0.03	0.06
<0.01		
<0.01		
<0.01		
<0.01		
0.11	0.04	0.07
<0.01		
100.81		99.63

TABLE 6.

12072: PHASE ABUNDANCES, AVERAGE "PHASE" COMPOSITIONS, AND BULK COMPOSITION

(2585 pts)	Flag	Pyroxene					Olivine	"SiO ₂ "	Ilmenite	Troilite ¹	Phosphate ²	Cr-spinel	IlvBspinel ⁴	Fe-metal ¹	Fayalite	Meso ³	K-Glass	Bulk Comp.	g (SDM)
		LoCaPx	Augite	MedFePx	HiFePx	Ferrobhd													
Vol %	38.94	8.51	8.83	23.24	8.24	0.22	5.71	3.07	1.15	0.31	0.12	0.17	0.12	0.07	0.20	1.03	0.08		
σ (SDM)	1.07	0.76	0.78	1.26	0.75	0.12	0.47	0.34	0.21	0.11	0.07	0.08	0.07	0.05	0.09	0.20	0.06		
ρ	2.74	3.49	3.40	3.51	1.72	3.57	3.53	2.33	4.72	4.60	3.20	4.68	4.78	8.00	4.39	2.65	2.65		
Wt. %	33.36	9.29	9.38	25.51	9.59	0.25	6.31	2.24	1.70	0.45	0.12	0.25	0.18	0.18	0.28	0.85	0.07		
σ (SDM)	0.92	0.83	0.83	1.38	0.87	0.14	0.52	0.25	0.31	0.16	0.07	0.12	0.11	0.13	0.13	0.17	0.05		
P ₂ O ₅											43.15				0.33	0.64			
SiO ₂	48.91	51.10	48.57	48.65	48.18	48.65	37.43	100.45	0.06		0.08			35.06	70.41	79.75			
TiO ₂	0.29	1.01	1.56	1.53	1.16	1.25	0.01	0.40	51.88		4.71	35.73		0.18	0.45	0.58			
Al ₂ O ₃	30.39	1.91	4.04	2.55	1.06	1.14	0.02	0.60	0.08		12.67			0.34	15.65	8.07			
Cr ₂ O ₃		0.60	1.06	0.33	0.06	0.12	0.55		0.06		47.88			0.03	0.00	0.00			
MgO	0.52	17.07	15.46	10.45	3.91	4.53	36.12	0.00	0.07		6.64			1.98	0.20	0.00			
CaO	17.75	5.70	13.99	10.02	9.11	14.44	0.30	0.18			54.54			0.69	7.36	1.29			
FeO	1.12	22.53	14.18	26.28	36.83	31.03	26.85	0.29	47.16	63.53		28.73	64.27	100.00	63.87	1.89	2.79		
MnO		0.36	0.26	0.47	0.48	0.33	0.26		0.30					0.18	0.61	0.36	0.70		
Na ₂ O	0.98	0.01	0.21	0.03	0.08	0.01		0.12							0.51	0.25			
K ₂ O	0.04							0.07							2.86	5.51			
BaO	0.15							0.00							0.33	0.54			
ErO ₂									0.02			0.03			0.00	0.00			
V ₂ O ₅									0.00			1.03							
Nb ₂ O ₅									0.07			0.01							
HfO							0.05								0.00	0.00	0.00		
S										36.47					0.00	0.00			
F											2.31								
Total	100.15**	100.29**	99.13**	100.31**	100.87**	101.50**	101.59*	102.11	99.70**	100.00	100.00	101.94*	100.00	100.00	102.76*	100.35	100.12		
An 79.9	Wo 9.1	Wo 23.1	Wo 18.1	Wo 19.0	Wo 29.6	Fo 70.4		Cl 0.3			Olv 11.8			Fo 5.2		Qtz 52.1			
Ab 8.8	En 48.8	En 43.1	En 30.9	En 12.0	En 13.5	Fa 29.6		Ilm 99.7			Chr 63.3			Fa 94.8		Pld 40.1			
Cr 0.2	Fs 36.8	Fs 22.6	Fs 44.4	Fs 64.5	Fs 52.6						Mer 24.9					Pyx 4.9			
Other 11.1	Other 5.3	Other 11.2	Other 6.6	Other 4.5	Other 4.3											Other 2.9			

*Average of two analyses.
 **Average of three analyses.

¹Theoretical elemental abundances; converted to oxides for bulk calculation.
²Assumed 1:1 mixture of fluorapatite and whitlockite.
³Composition constructed from weighted average (51:38:11) of K-glass, plagioclase, and "SiO₂".
⁴Theoretical end-member oxide abundances.

12072,2 area = 11.0 mm²
 ρ calc = 3.20

Bulk Comp.	g (SDM)
0.06	0.03
48.14	1.14
1.81	0.18
11.64	0.34
0.40	0.07
8.57	0.33
11.38	0.32
17.46	0.61
0.25	0.02
0.37	0.04
0.04	0.02
0.05	0.02
<0.01	
<0.01	
<0.01	
<0.01	
0.16	
<0.01	
0.16	0.06
100.33	

313

TABLE 7. Summary of whole-rock chemical and normative compositions. Chemical analyses are in weight percent. Normative compositions are in catatom percent.

	Olivine Basalt	Pigeonite Basalt			Feldspathic Basalt
	<u>12015</u>	<u>12011</u>	<u>12043</u>	<u>12007</u>	<u>12072</u>
P ₂ O ₅	0.06	0.03	0.06	0.08	0.06
SiO ₂	47.00	46.59	47.11	48.03	48.14
TiO ₂	2.90	3.25	3.39	3.82	1.81
Al ₂ O ₃	9.26	10.02	10.56	12.13	11.64
Cr ₂ O ₃	0.68	0.68	0.47	0.24	0.40
MgO	11.44	9.59	7.90	5.67	8.57
CaO	10.02	10.55	11.15	12.07	11.38
FeO	18.20	19.31	19.52	17.85	17.46
MnO	0.27	0.28	0.25	0.22	0.25
Na ₂ O	0.22	0.33	0.27	0.40	0.37
K ₂ O	0.05	0.02	0.02	0.04	0.04
BaO	0.02	0.02	<0.01	0.01	0.05
ZrO ₂	<0.01	<0.01	0.01	0.02	0.01
V ₂ O ₃	0.01	0.01	0.01	0.01	0.01
Nb ₂ O ₅	0.01	0.01	0.01	0.01	0.01
NiO	0.03	0.01	0.01		0.01
S	0.10	0.27	0.11	0.12	0.16
F		0.01	0.01	0.01	0.01
TOTAL	100.26	100.95	100.81	100.70	100.33
Mg-value	52.8	46.9	41.9	36.1	46.7
<u>Barth-Niggli norm</u>					
Q		0.03	2.11	5.35	1.26
or	0.31	0.12	0.12	0.25	0.24
ab	2.04	3.07	2.53	3.77	3.44
an	24.95	26.77	28.78	32.76	31.08
di	20.86	21.90	22.89	23.69	21.71
hy	45.73	42.32	37.86	28.02	38.92
oi	0.94				
Chr	0.77	0.77	0.54	0.28	0.46
ilm	4.18	4.70	4.93	5.59	2.61
ap	0.13	0.07	0.13	0.18	0.13
py	0.09	0.24	0.10	0.11	0.14

FIGURE CAPTIONS

- Figure 1. Compositions of the principal silicate and oxide phases in vitrophyre 12015, 15. Vertical lines represent the altitudes of triangles that correspond to the amount of minor-element substitution. Triangular inset for pyroxene shows the relative amounts of Al-Ti-Cr in pyroxene. Inset for plagioclase shows substitution of excess silica vs. Fe.
- Figure 2. Compositions of the principal silicate and oxide phases in vitrophyre 12015, 16. Insets same as for Figure 1.
- Figure 3. Compositions of the principal silicate and oxide phases in basalt 12011. Insets same as for Figure 1.
- Figure 4. Compositions of the principal silicate and oxide phases in basalt 12043. Insets same as for Figure 1.
- Figure 5. Compositions of the principal silicate and oxide phases in basalt 12007. Insets same as for Figure 1.
- Figure 6. Compositions of the principal silicate and oxide phases in basalt 12072. Insets same as for Figure 1. Dashed line indicates probable tie line based on coexisting grains.
- Figure 7. Compositions of Cr-spinel and ulvospinel in olivine and pigeonite mare basalts 12007, 12011, 12015, 12043, and 12072. $Fm = Fe + Mg + Mn$.
- Figure 8. $(Fe/Mg+Fe)_{\text{olivine}}$ of the most magnesian phenocrysts vs. $(Fe/Mg+Fe)_{\text{whole rock}}$ for basalts 12011, 12015, and 12043. No olivine is present in 12007.
- Figure 9. Variation of SiO_2 , FeO , Cr_2O_3 , Al_2O_3 , CaO , and TiO_2 vs. MgO (weight per cent) for olivine and pigeonite basalts 12007, 12011, 12015, and 12043 and feldspathic basalt 12072. Solid symbols are new data presented in this paper. Open symbols are data from Rhodes et al. (1977). Subtraction of phases present as phenocrysts and microphenocrysts is indicated by arrows.

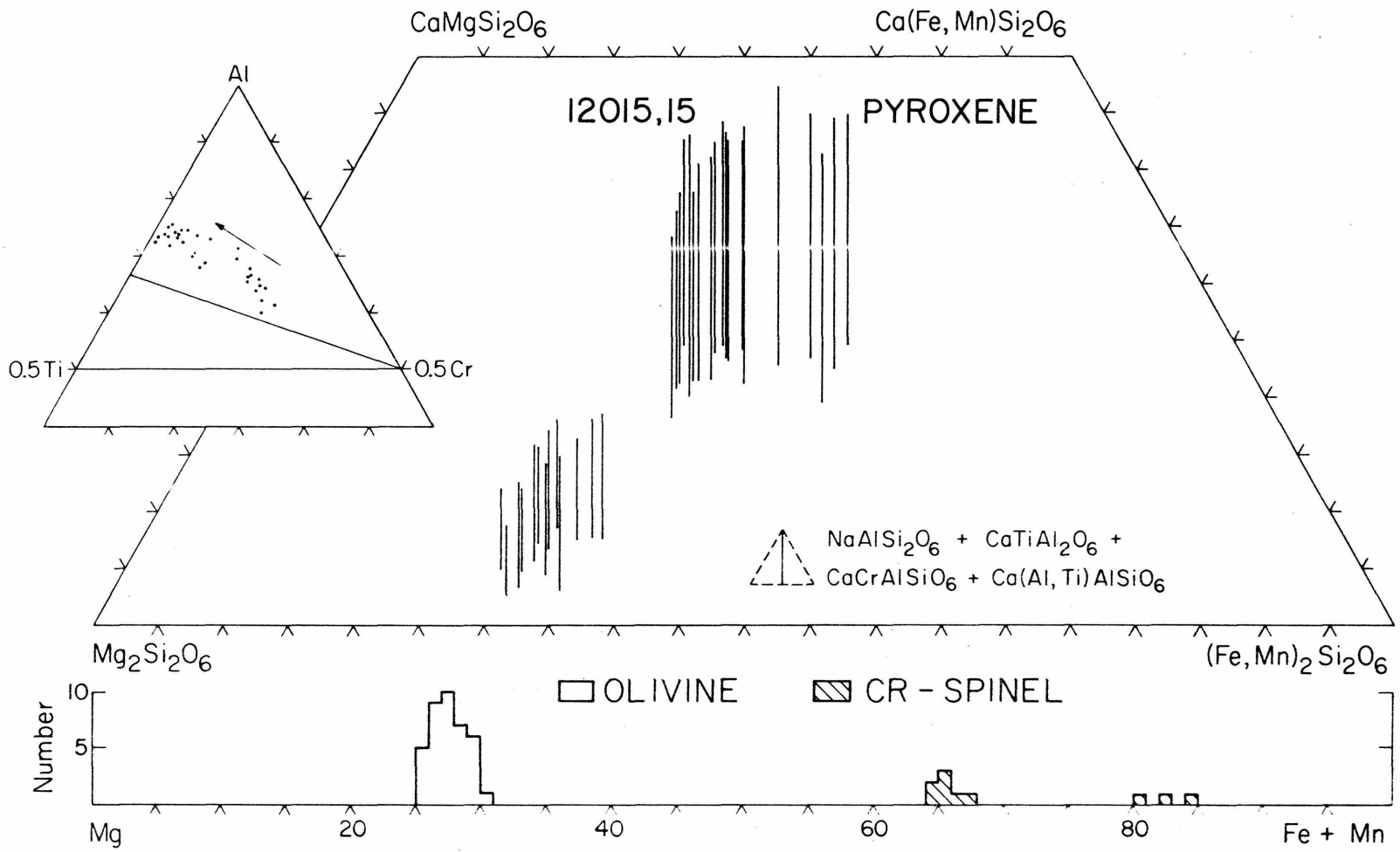


Figure 1

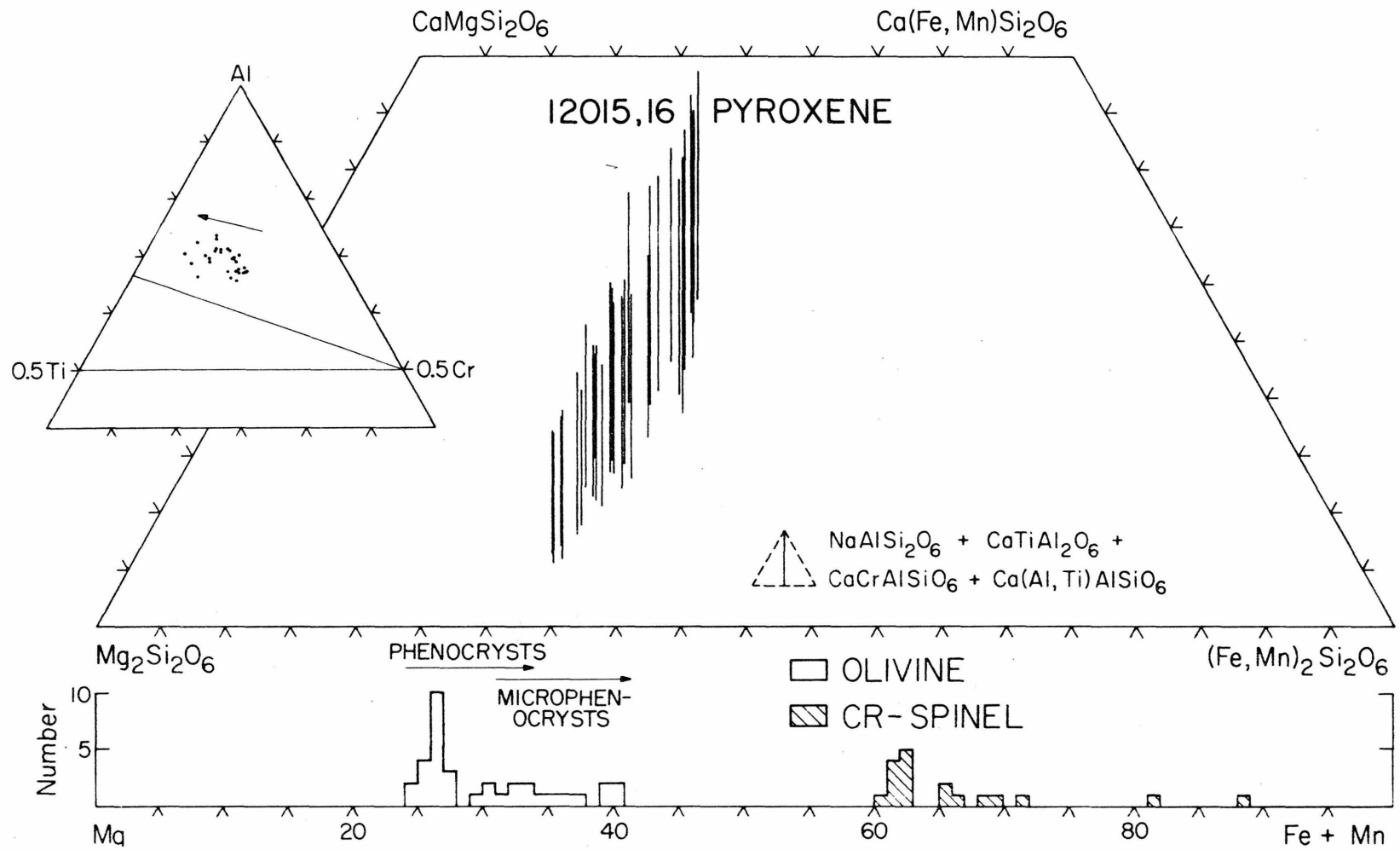


Figure 2

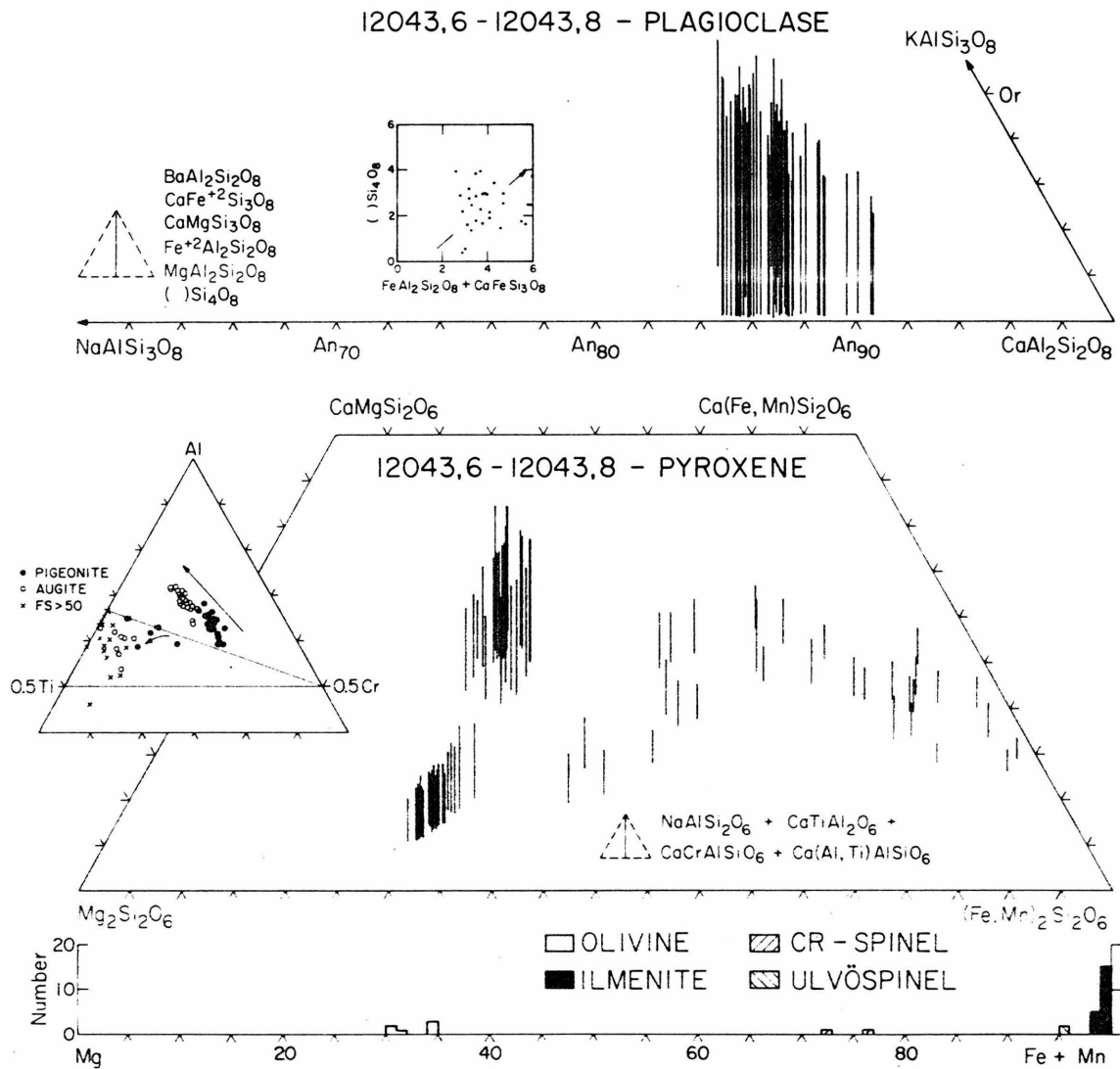


Figure 4

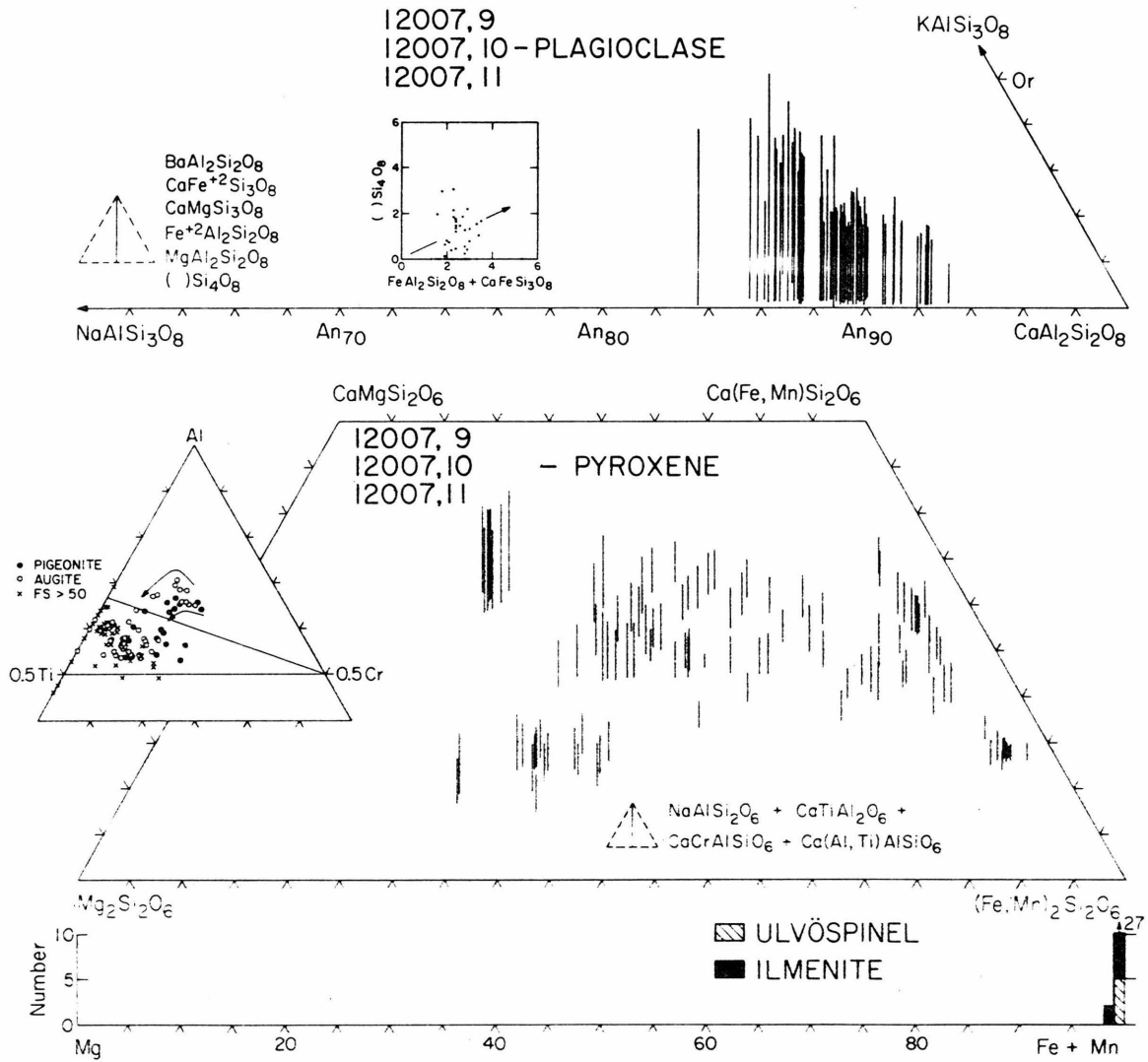


Figure 5

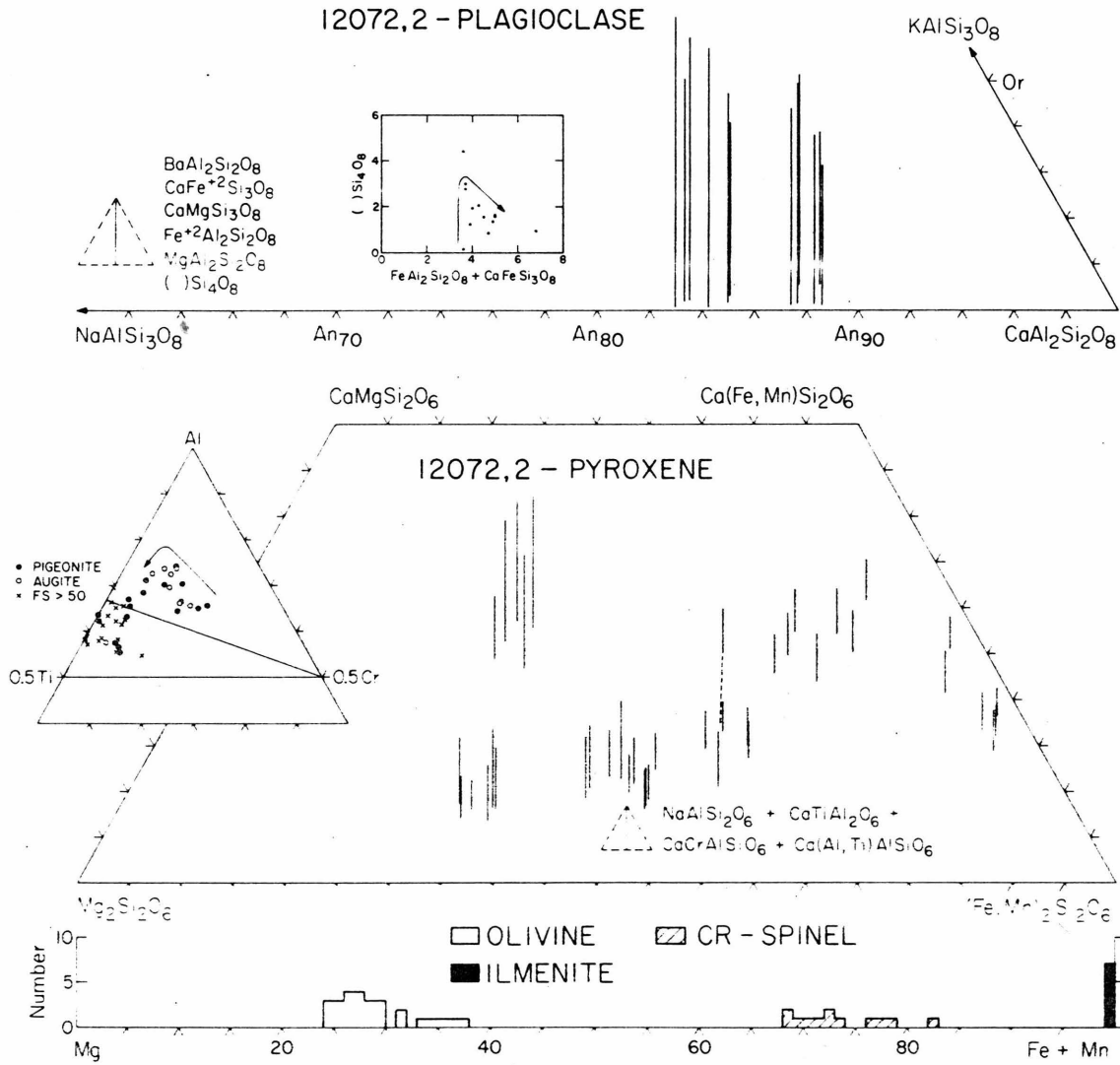


Figure 6

SPINEL

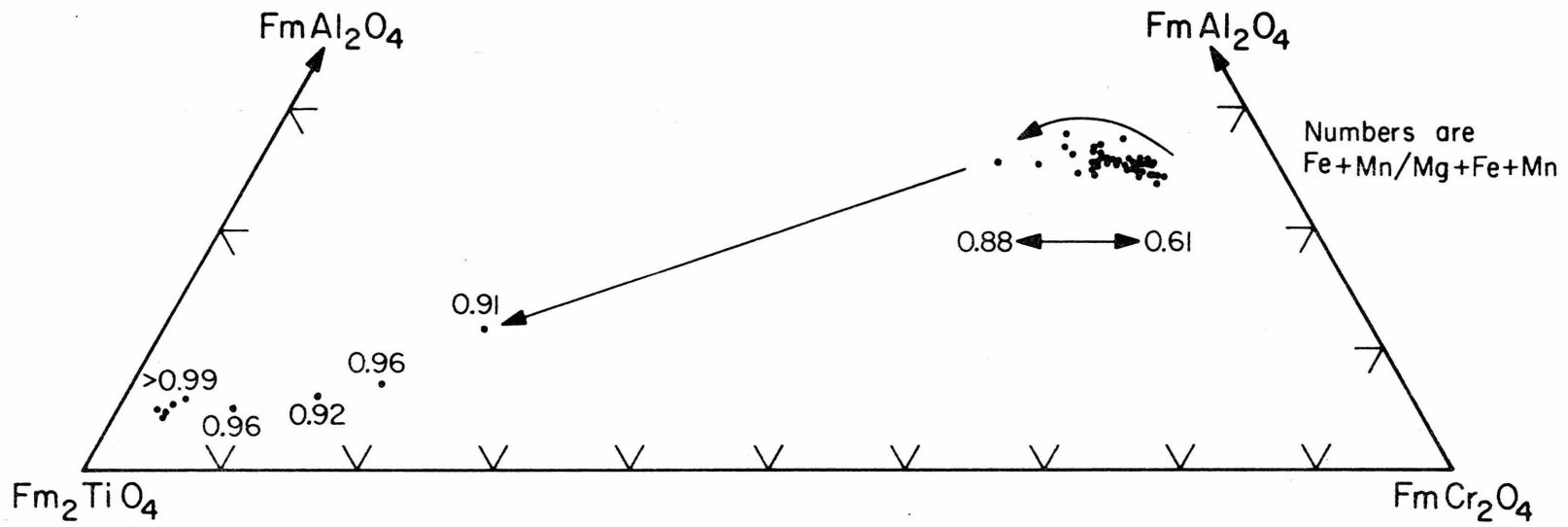


Figure 7

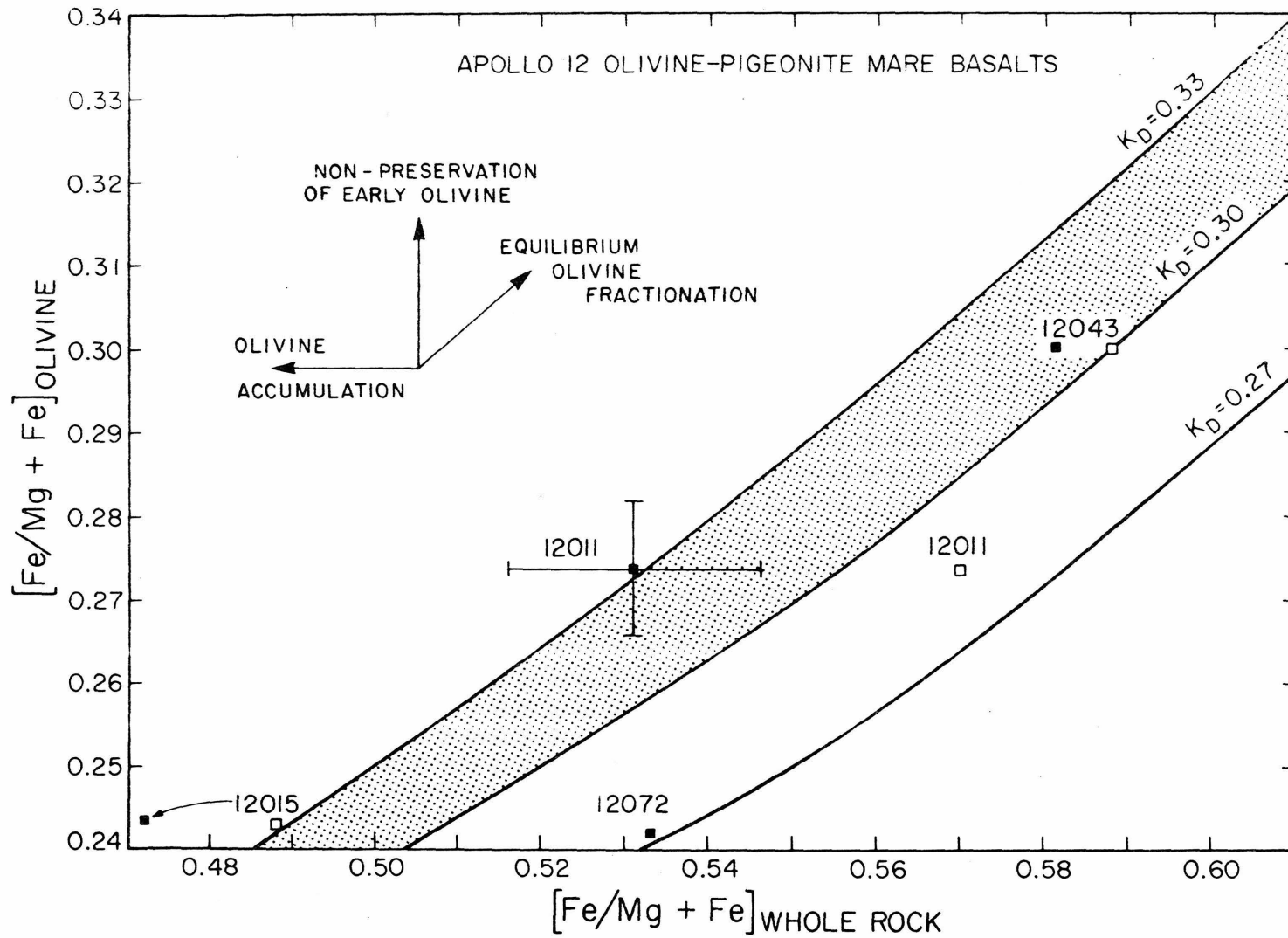


Figure 8

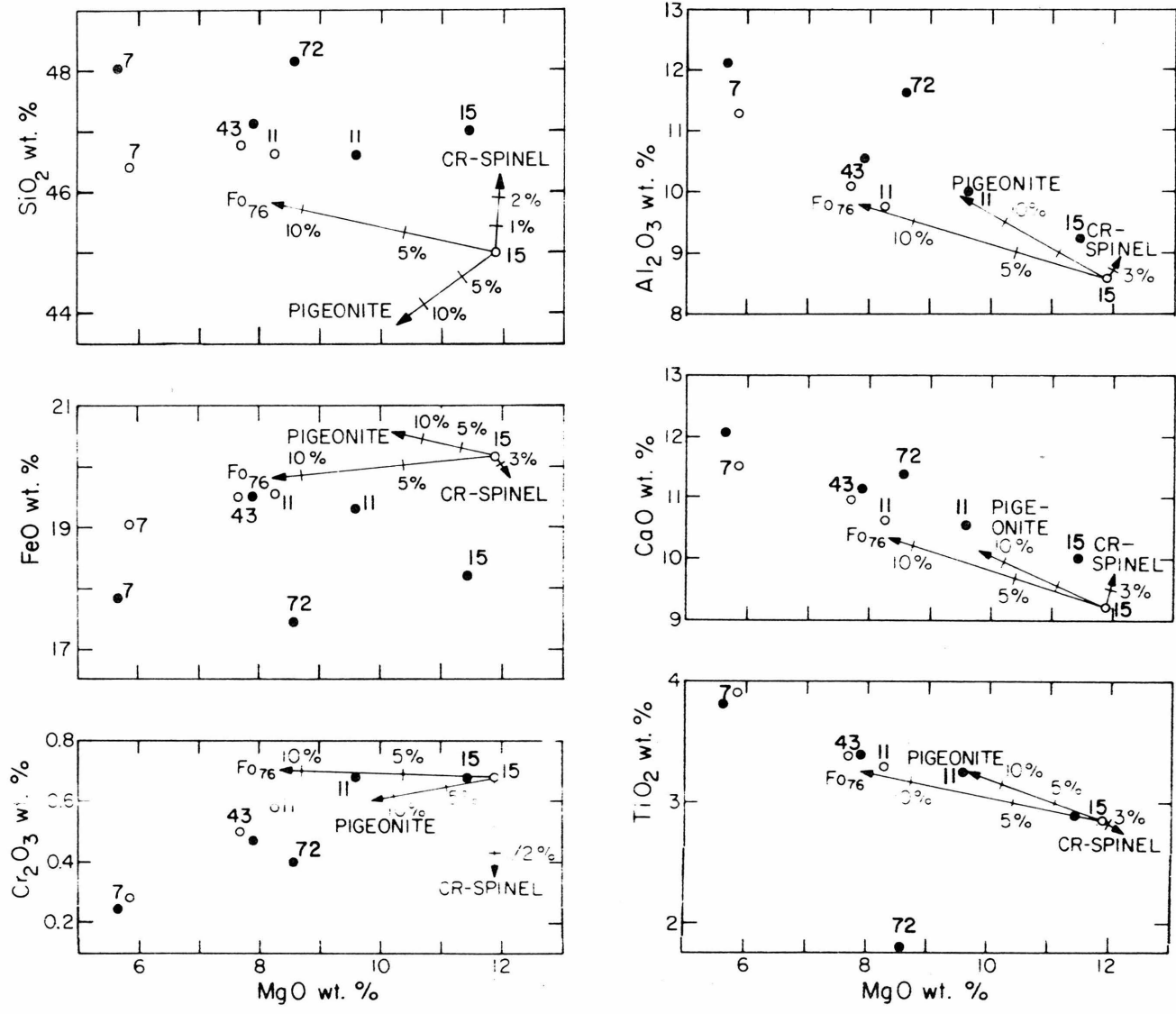


Figure 9